Dynamic Parallel Imaging for Fast MRI, and Optimization of CEST Methods for Metabolic MRI

Dissertation

der Mathematisch-Naturwissenschaftlichen Fakultät

der Eberhard Karls Universität Tübingen

zur Erlangung des Grades eines

Doktors der Naturwissenschaften

(Dr. rer. nat.)

vorgelegt von
Felix Glang
aus Nürtingen

Tübingen
2023

Abstract

Magnetic Resonance Imaging (MRI) is a fascinating example of how basic research in physics, studying nuclear spin and magnetism, has evolved into a highly successful technology that enables non-invasive medical imaging. As such, it provides insight into both anatomy and physiology, and aids in the diagnosis of a wide range of pathologies. In addition, functional MRI is a central tool for addressing neuroscientific questions that seek, for example, a better understanding of the human brain. The basic principle of Magnetic Resonance (MR) technology is that nuclear spins can be manipulated and probed by electromagnetic fields. When done properly, the interactions between the spins, as well as with their microscopic electronic environment and the external electromagnetic fields, allow a large variety of different tissue properties to be accessed and imaged without the use of harmful ionizing radiation. This makes MRI an inherently multimodal imaging technique, yielding information about, for example, proton density, relaxation times, diffusion and perfusion, blood oxygenation, molecular structure, temperature, magnetic susceptibility, electrical and even mechanical properties.

Despite the versatility and advantages of this technology, probably the most striking limitation of MRI lies in the comparatively long acquisition times required to obtain the necessary information, especially to achieve sufficient Signal to Noise Ratio (SNR). To address this problem, the aforementioned manipulation and probing of nuclear magnetization has been subject to extensive research and engineering efforts. In particular, approaches to optimize and speed up MRI can be broadly classified into three categories: 1) faster imaging sequences such as Fast Low Angle Shot (FLASH) or Echo Planar Imaging (EPI), 2) hardware-based improvements such as better gradient coils and so-called Parallel Imaging (PI), and 3) reconstruction methods based on tailored signal processing.

This thesis covers two distinct topics in the context of optimizing MRI acquisition and reconstruction. As the first topic, a novel concept for improving PI at Ultra-high Field (UHF) MRI is presented. Among all technical developments to speed up MRI acquisition, PI is one of the most successful and widely applied techniques. It relies on the additional localization information provided by the spatial sensitivity profiles of multiple Radio Frequency (RF) receive coils used to detect nuclear magnetization. However, the maximum achievable PI acceleration factor that still provides acceptable image quality is fundamentally limited by the number and spatial independence of the coil sensitivity profiles. The proposed novel concept to improve PI is based on electronically modulated time-varying receive sensitivities enabled by custom-built reconfigurable RF coils. It is investigated and demonstrated how these can be realized experimentally and used advantageously in acquisition and reconstruction. This work thus can be seen as falling into categories 2 and 3 above.

As a second topic, Chemical Exchange Saturation Transfer (CEST) is considered as one of the MRI contrast mechanisms listed above that promises to provide insights into the molecular microenvironment and to detect low concentration metabolites. Due to the required sequence structure of repeated RF-prepared readouts, CEST MRI suffers from long scan times. In addition, the extraction of the desired contrast information usually requires computationally complex processing steps. In this context, a data-driven linear projection method for CEST parameter estimation from the acquired raw data is proposed, which allows simple and fast contrast generation and a potential reduction of acquisition times by providing insight into which parts of the CEST data contain relevant information and which parts could be omitted. This project can be seen as belonging to categories 1 and 3 of the MRI optimization methods mentioned above.

Finally, a novel and experimental method of optimizing MRI contrast generation is proposed, where both acquisition and contrast mapping are treated as a joint numerical optimization problem. Departing from the conventional way of basing such optimizations on theoretical models and numerical simulations, a model-free framework is implemented here that optimizes both acquisition parameters and contrast extraction schemes purely based on automated exploratory acquisitions running on a real MRI scanner. The method can also be seen as belonging to categories 1 and 3. A proof-of-principle demonstration of this framework is given in the context of CEST MRI. The approach may be particularly useful in situations where a theoretical description of the targeted problem is not available, such as hardware system imperfections. This in turn suggests a possible link to category 2 of the MRI optimization methods mentioned above.

Overall, all of these projects highlight the potential that lies in synergistically considering all aspects of MRI related to hardware, acquisition, and reconstruction in order to strive for optimization of acquisition times and information retrieval.

Zusammenfassung

Die Magnetresonanztomographie (MRT) ist ein faszinierendes Beispiel dafür, wie sich physikalische Grundlagenforschung an Kernspin und Magnetismus zu einer äußerst erfolgreichen Technologie entwickelt hat, die eine nicht-invasive medizinische Bildgebung ermöglicht. Als solche bietet sie Einblicke in Anatomie und Physiologie, und hilft bei der Diagnose einer Vielzahl von Krankheiten. Darüber hinaus ist die funktionelle MRT ein zentrales Instrument zur Beantwortung neurowissenschaftlicher Fragestellungen, die beispielsweise auf ein besseres Verständnis des menschlichen Gehirns abzielen. Das Grundprinzip der MR-Technologie besteht darin, dass Kernspins durch elektromagnetische Felder manipuliert und untersucht werden können. Hierbei ermöglichen die Wechselwirkungen der Spins untereinander sowie mit ihrer mikroskopischen elektronischen Umgebung und den externen elektromagnetischen Feldern den Zugang zu einer großen Vielfalt unterschiedlicher Gewebeeigenschaften und deren Abbildung ohne den Einsatz schädlicher ionisierender Strahlung. Dies macht die MRT zu einem inhärent multimodalen Bildgebungsverfahren, das Informationen beispielsweise über Protonendichte, Relaxationszeiten, Diffusion und Perfusion, Sauerstoffsättigung des Blutes, molekulare Struktur, Temperatur, magnetische Suszeptibilität, elektrische und sogar mechanische Eigenschaften liefern kann.

Trotz der Vielseitigkeit und der Vorteile dieser Technologie liegt die wohl hervorstechendste Einschränkung der MRT in den vergleichsweise langen Messzeiten, die erforderlich sind, um die notwendigen Informationen zu erhalten, insbesondere um ein ausreichendes Signal-Rausch-Verhältnis (SNR) zu erzielen. Um dieses Problem zu lösen, ist die oben erwähnte Manipulation und Untersuchung der Kernmagnetisierung zum Gegenstand umfangreicher Forschungs- und Entwicklungsarbeiten geworden. Die Ansätze zur Optimierung und Beschleunigung der MRT lassen sich grob in drei Kategorien einteilen: 1) schnellere Bildgebungssequenzen wie Fast Low Angle Shot (FLASH) oder Echo Planar Imaging (EPI), 2) Hardware-basierte Verbesserungen wie bessere Gradientenspulen und so genannte Parallele Bildgebung (PI) und 3) Rekonstruktionsmethoden, die auf maßgeschneiderter Signalverarbeitung basieren.

Diese Arbeit befasst sich mit zwei verschiedenen Themen im Zusammenhang mit der Optimierung von MRT-Datenaufnahme und -Rekonstruktion. Als erstes Thema wird ein neuartiges Konzept zur Verbesserung der Parallelen Bildgebung bei der Ultra-Hochfeld-MRT vorgestellt. Unter allen technischen Entwicklungen zur Beschleunigung der MRT-Datenaufnahme ist die Parallele Bildgebung eine der erfolgreichsten und am häufigsten verwendeten Techniken. Sie basiert auf der zusätzlichen Lokalisationsinformation, die durch die räumlichen Sensitivitätsprofile mehrerer Hochfrequenz-Empfangsspulen zur Detektion der Kernmagnetisierung zur Verfügung gestellt wird. Der maximal erreichbare Beschleunigungsfaktor durch Parallele Bildgebung, der noch eine akzeptable Bildqualität

ermöglicht, ist jedoch grundsätzlich durch die Anzahl und räumliche Unabhängigkeit der Sensitivitätsprofile der Spulen begrenzt. Das vorgeschlagene neue Konzept zur Verbesserung der Parallelen Bildgebung basiert auf elektronisch modulierten, zeitlich variierenden Sensitivitätsprofilen, die durch speziell angefertigte rekonfigurierbare Hochfrequenz-Spulen ermöglicht werden. Es wird untersucht und demonstriert, wie diese experimentell realisiert und vorteilhaft bei der Datenaufnahme und Rekonstruktion eingesetzt werden können. Diese Arbeit kann somit den oben genannten Kategorien 2 und 3 zugeordnet werden.

Als zweites Thema wird Chemical Exchange Saturation Transfer (CEST) als einer der oben aufgeführten MRT-Kontrastmechanismen betrachtet, der Einblicke in die molekulare Mikro-Umgebung und die Detektion niedrig konzentrierter Metaboliten verspricht. Aufgrund der erforderlichen Sequenzstruktur von wiederholter Hochfrequenzpräparierter Signalauslese leidet die CEST MRT unter besonders langen Messzeiten. Darüber hinaus erfordert die Extraktion der gewünschten Kontrastinformation in der Regel rechnerisch komplexe Verarbeitungsschritte. In diesem Zusammenhang wird eine datengetriebene lineare Projektionsmethode zur Schätzung von CEST-Parametern aus den gemessenen Rohdaten vorgeschlagen, die eine einfache und schnelle Kontrasterzeugung und eine potenzielle Verringerung der Messzeiten ermöglicht, indem sie Aufschluss darüber gibt, welche Teile der CEST-Daten relevante Informationen enthalten und welche Teile weggelassen werden können. Dieses Projekt kann den Kategorien 1 und 3 der oben erwähnten MRT-Optimierungsmethoden zugeordnet werden.

Schließlich wird eine neuartige und experimentelle Methode zur Optimierung der MRT-Kontrasterzeugung vorgeschlagen, bei der sowohl die Datenaufnahme als auch die Kontrastberechnung als ein gemeinsames numerisches Optimierungsproblem behandelt werden. Abweichend von konventionellen Methoden, bei denen solche Optimierungen auf theoretischen Modellen und numerischen Simulationen basieren, wird hier eine modellfreie Methode implementiert, die sowohl die Datenaufnahmeparameter als auch die Schemata zur Kontrastberechnung ausschließlich auf der Grundlage automatisierter explorativer Messungen optimiert, die auf einem echten MRT-Scanner laufen. Diese Methode kann ebenfalls als zu den Kategorien 1 und 3 gehörig betrachtet werden. Eine grundlegende Demonstration dieser Methode wird im Kontext von CEST MRT durchgeführt. Der vorgestellte Ansatz könnte besonders in Situationen nützlich sein, in denen eine theoretische Beschreibung des anvisierten Problems nicht zur Verfügung steht, wie z. B. bei Imperfektionen von Hardware-Systemen. Dies wiederum legt eine mögliche Verbindung zu Kategorie 2 der oben erwähnten MRT-Optimierungsmethoden nahe.

Insgesamt unterstreichen alle diese Projekte das Potenzial, das in der synergetischen Betrachtung aller Aspekte der MRT in Bezug auf Hardware, Datenaufnahme und Rekonstruktion liegt, um eine Optimierung der Messzeiten und des Informationsgewinns anzustreben.

Contents

Acronyms and Definitions

ADC	Analog-to-Digital Converter	GRAPPA	Generalized Autocalibrating Partially Parallel Acquisitions
APT	Amide Proton Transfer	GRE	Gradient Echo
B_0	Static Magnetic Field Strength	LASSO	Least Absolute Shrinkage and Selection Operator
B_1	Magnetic Component of Radio Frequency Fields	MPRAGE	Magnetization Prepared Rapid Gradient Echo
B_1^-	counter-clockwise rotating Magnetic Component of RF Fields ("Receive Field")	MR	Magnetic Resonance
		MRI	Magnetic Resonance Imaging
B_1^+	clockwise rotating Magnetic Component of RF Fields ("Transmit Field")	MSE	Mean Squared Error
		NOE	Nuclear Overhauser Effect
CEST	Chemical Exchange Saturation Transfer	NRMSE	Normalized Root Mean Squared Error
		NUFFT	Non-Uniform Fast Fourier Transform
CAIPIRINHA	Controlled Aliasing in Parallel Imaging Results in Higher Acceleration	PCA	Principal Component Analysis
		PCB	Printed Circuit Board
CP	Circular Polarization	PE	Phase Encoding
DC	Direct Current	PI	Parallel Imaging
DFT	Discrete Fourier Transform	PSNR	Peak Signal to Noise Ratio
EPI	Echo Planar Imaging	pTx	Parallel Transmission
FA	Flip Angle	RF	Radio Frequency
FFT	Fast Fourier Transform	RMSE	Root Mean Squared Error
FLASH	Fast Low Angle Shot	rNOE	exchange-relayed NOE
FLAIR	Fluid Attenuated Inversion Recovery	RO	Readout
		ROI	Region Of Interest
FOV	Field Of View	RSC	Receive Sensitivity Configuration
GM	Gray Matter		

Contents

Constants

$$k_\mathrm{B} = \quad 1.380649\ldots \cdot 10^{-23} \qquad \tfrac{\mathrm{J}}{\mathrm{K}} \quad \text{(Boltzmann Constant)}$$

$$\gamma/2\pi \approx \quad 42.577478518\ldots \qquad \tfrac{\mathrm{MHz}}{\mathrm{T}} \quad \text{(Proton Gyromagnetic Ratio)}$$

$$\hbar \approx \quad 1.054571817\ldots \cdot 10^{-34} \quad \mathrm{Js} \quad \text{(Reduced Planck Constant)}$$

Notation

Vectors denoted with arrows correspond to physical vector quantities in $\mathbb{R}^3$ like macroscopic magnetization $\vec{M}$ or magnetic field strength $\vec{B}$.

Quantum mechanical operators are denoted with a hat, e.g. the spin $\hat{\vec{S}}$.

Boldface vectors, e.g. $\mathbf{x}$ or $\mathbf{y}$, correspond to collections of data points with variable dimension. Expectation value and covariance matrix of a random variable $\mathbf{x}$ are denoted as $\mathbb{E}(\mathbf{x})$ and $\mathrm{cov}(\mathbf{x})$, respectively.

$\mathbf{A}^T$ and $\mathbf{A}^H$ indicate the transpose and Hermitian conjugate of a matrix $\mathbf{A}$, respectively.

1. Summarized Publications

This dissertation is written in cumulative form based on the following four manuscripts, which are attached at the end of the document. In sections 4.1 to 4.4, detailed summaries of these publications are given.

Publication 1

Glang, F.; Nikulin, A. V.; Bause, J.; Heule, R.; Steffen, T.; Avdievich, N.; Scheffler, K. *Accelerated MRI at 9.4 T with Electronically Modulated Time-Varying Receive Sensitivities.* Magnetic Resonance in Medicine 2023, 88 (2), 742 - 756.
https://doi.org/10.1002/mrm.29245.

Publication 2

Nikulin, A. V.; Glang, F.; Avdievich, N.; Bosch, D.; Steffen, T.; Scheffler, K. *Reconfigurable Dipole Receive Array for Dynamic Parallel Imaging at Ultra-High Magnetic Field.* Magnetic Resonance in Medicine 2023, 90 (4), 1713-1727.
https://doi.org/10.1002/mrm.29745.

Publication 3

Glang, F.; Fabian, M. S.; German, A.; Khakzar, K. M.; Mennecke, A.; Liebert, A.; Herz, K.; Liebig, P.; Kasper, B. S.; Schmidt, M.; Zuazua, E.; Nagel, A. M.; Laun, F. B.; Dörfler, A.; Scheffler, K.; Zaiss, M. *Linear Projection-Based Chemical Exchange Saturation Transfer Parameter Estimation.* NMR in Biomedicine 2022, e4697.
https://doi.org/10.1002/nbm.4697.

Publication 4

Glang, F.; Mueller, S.; Herz, K.; Loktyushin, A.; Scheffler, K.; Zaiss, M. *MR-Double-Zero – Proof-of-Concept for a Framework to Autonomously Discover MRI Contrasts.* Journal of Magnetic Resonance 2022, Volume 341, 107237.
https://doi.org/10.1016/j.jmr.2022.107237.

2. Introduction

This chapter provides a summary of the theoretical concepts and foundations that serve as the basis for the results presented in this thesis.

First, in section 2.1, a compilation of results related to linear regression models is provided, since the underlying mathematical framework is used in different manifestations in all manuscripts included in this thesis. Then, in section 2.2, a brief introduction to the basics of MRI is provided, including a description of spatial encoding and PI. Finally, basic aspects of CEST MRI are presented in section 2.3.

2.1. Linear Models

This section provides a brief overview of the basics of linear regression models, including multiple linear regression, (generalized) least squares estimation, and estimation of parameter variance. This summary is based on the textbooks [1–4], in which a more general and comprehensive treatment of the topic can be found.

Linear models are a central tool in statistics and are ubiquitously used in virtually all quantitative fields of study, be it science, engineering, economics, etc. They are popular because they are simple, have favorable analytical properties, and often provide adequate and interpretable results. Under certain conditions, they can even surpass the predictive performance of more complicated non-linear models (chapter 3 of [1]).

First, consider the multiple linear regression model

$$y = \beta_0 + \beta_1 x_1 + \beta_2 x_2 + \ldots + \beta_k x_k + \varepsilon, \tag{2.1}$$

for which a scalar response variable y is modeled as linear combination of predictors x_i with regression coefficients β_i, up to random errors ε. Note that this model is linear in the coefficients β even if arbitrary fixed non-linear transforms of the original predictors x are included as new predictors, for instance $y = \beta_0 + \beta_1 x + \beta_2 x^2 + \beta_3 x^3 + \ldots + \varepsilon$. This forms a polynomial regression model, which is an example of the more general class of so-called basis-function methods (chapter 5 of [1]). Writing equation (2.1) for n observations in matrix forms yields

$$\begin{pmatrix} y_1 \\ y_2 \\ \vdots \\ y_n \end{pmatrix} = \begin{pmatrix} 1 & x_{11} & x_{12} & \ldots & x_{1k} \\ 1 & x_{21} & x_{22} & \ldots & x_{2k} \\ \vdots & \vdots & \vdots & \ddots & \vdots \\ 1 & x_{n1} & x_{n2} & \ldots & x_{nk} \end{pmatrix} \begin{pmatrix} \beta_0 \\ \beta_1 \\ \vdots \\ \beta_k \end{pmatrix} + \begin{pmatrix} \varepsilon_1 \\ \varepsilon_1 \\ \vdots \\ \varepsilon_n \end{pmatrix} \tag{2.2}$$

or in short

$$\mathbf{y} = \mathbf{X}\boldsymbol{\beta} + \boldsymbol{\varepsilon} \tag{2.3}$$

with the $n \times (k+1)$ design matrix $\mathbf{X}$, in which the additional column of ones accounts for the constant intercept term. A typical assumption is that the errors have zero mean ($\mathbb{E}(\boldsymbol{\varepsilon}) = 0$), are uncorrelated, and have all the same variance σ^2; the latter two conditions being summarized as $\mathrm{cov}(\boldsymbol{\varepsilon}) = \sigma^2 \mathbf{I}$ with the identity matrix $\mathbf{I}$. In this case, estimating the coefficients $\boldsymbol{\beta}$ by minimizing the residual sum-of-squares

$$\mathrm{RSS}(\boldsymbol{\beta}) = ||\mathbf{y} - \mathbf{X}\boldsymbol{\beta}||_2^2 = \sum_{i=1}^{n} \left| y_i - \beta_0 - \sum_{j=1}^{k} x_{ij}\beta_j \right|^2, \tag{2.4}$$

i.e., the least-squares approach, is guaranteed by the Gauss-Markov theorem to yield a so-called best linear unbiased estimator[1] [1], leading to the analytical solution

$$\hat{\boldsymbol{\beta}} = \arg \min_{\boldsymbol{\beta}} \{\mathrm{RSS}(\boldsymbol{\beta})\} = \mathbf{X}^+ \mathbf{y} \tag{2.5}$$

with the Moore-Penrose pseudoinverse $\mathbf{X}^+ = (\mathbf{X}^T\mathbf{X})^{-1}\mathbf{X}^T$.

Due to the randomness of $\boldsymbol{\varepsilon}$ and thus $\mathbf{y}$, the estimated regression coefficients $\hat{\boldsymbol{\beta}}$ are random variables as well, for which the covariance matrix can be shown to be

$$\mathrm{cov}(\hat{\boldsymbol{\beta}}) = \sigma^2 (\mathbf{X}^T\mathbf{X})^{-1}. \tag{2.6}$$

In case of non-spherical errors, i.e., error variances that are not identical for the different predictors and potentially correlated, the approach can be extended to the so-called generalized least squares [5]. Given the error covariance matrix $\mathrm{cov}(\boldsymbol{\varepsilon}) = \boldsymbol{\Sigma} = \sigma^2 \mathbf{V}$, with a known positive definite matrix $\mathbf{V}$, the best linear unbiased estimator of the regression coefficients is

$$\hat{\boldsymbol{\beta}} = (\mathbf{X}^T\mathbf{V}^{-1}\mathbf{X})^{-1}\mathbf{X}^T\mathbf{V}^{-1}\mathbf{y} \tag{2.7}$$

with covariance matrix

$$\mathrm{cov}(\hat{\boldsymbol{\beta}}) = \sigma^2 (\mathbf{X}^T\mathbf{V}^{-1}\mathbf{X})^{-1}. \tag{2.8}$$

This result follows from the Gauss-Markov theorem, applying a de-correlation (also called pre-whitening) step: The matrix $\mathbf{V}$ permits a decomposition as $\mathbf{V} = \mathbf{P}\mathbf{P}^T$, e.g. by Cholesky factorization or applying the matrix square root $\mathbf{P} = \mathbf{V}^{1/2}$. Multiplying equation (2.3) by $\mathbf{P}^{-1}$ from the left results in a transformed linear regression system $\tilde{\mathbf{y}} = \tilde{\mathbf{X}}\boldsymbol{\beta} + \tilde{\boldsymbol{\varepsilon}}$ with $\tilde{\mathbf{y}} = \mathbf{P}^{-1}\mathbf{y}$, $\tilde{\mathbf{X}} = \mathbf{P}^{-1}\mathbf{X}$ and de-correlated errors $\tilde{\boldsymbol{\varepsilon}} = \mathbf{P}^{-1}\boldsymbol{\varepsilon}$, for which $\mathrm{cov}(\tilde{\boldsymbol{\varepsilon}}) = \sigma^2 \mathbf{I}$, i.e., the original assumptions of spherical errors holds again. Thus, substituting the de-correlated quantities $\tilde{\mathbf{y}}$ and $\tilde{\mathbf{X}}$ into equations (2.5) and (2.6), one obtains equations (2.7) and (2.8). The same solution is obtained in the framework of maximum likelihood estimation, assuming a multivariate Gaussian distribution of the error terms [2].

---

[1]This means that among all estimators $\hat{\boldsymbol{\beta}}$ that are linear in $\mathbf{y}$ and fulfill $\mathbb{E}(\hat{\boldsymbol{\beta}}) = \boldsymbol{\beta}$, it has the lowest variance, i.e., is least sensitive to noise $\boldsymbol{\varepsilon}$.

In the case of multiple response variables, i.e., a vector-valued instead of scalar target that should be modeled by the predictors $\mathbf{X}$, the resulting general linear model for number of responses m can be formulated as

$$\mathbf{Y} = \mathbf{X}\mathbf{B} + \mathbf{E} \tag{2.9}$$

with the $n \times m$ target matrix $\mathbf{Y}$, the $(k+1) \times m$ coefficient matrix $\mathbf{B}$ and random errors $\mathbf{E}$. Applying least-squares estimation as above, the matrix of optimal regression coefficients turns out to be again given by the pseudoinverse as $\hat{\mathbf{B}} = (\mathbf{X}^T\mathbf{X})^{-1}\mathbf{X}^T\mathbf{Y}$. Thus, comparing with equation (2.5), the problem decouples into m linear regressions for each column of $\mathbf{Y}$ separately, meaning that multiple outputs do not influence regression parameter estimation among each other.

2.2. Basics of MRI

This section introduces some physical background to MRI, intended as a coarse overview of the concepts relevant to the projects that are summarized in this work. A thorough treatment of spin physics and MR imaging can be found in the textbooks [6–8], on which this chapter is based.

2.2.1. Spin

The fundamental physics underlying MRI is the interaction of nuclear spins with external magnetic fields. Spin is a property of elementary particles as well as composite particles like protons. It describes an intrinsic angular momentum that cannot be related to a mechanical rotation by classical physics; instead, it can be accurately described in the framework of quantum mechanics [6]. A particle with spin $\hat{\vec{S}}$ exhibits a magnetic moment

$$\hat{\vec{\mu}} = \gamma \hat{\vec{S}}, \tag{2.10}$$

where the so-called gyromagnetic ratio γ depends on the type of particle. In an external magnetic field $\vec{B}_0 = (0, 0, B_0)$, here assumed along the z-axis, a particle with spin quantum number s is described by the Hamiltonian $\hat{H} = -\hat{\vec{\mu}} \cdot \vec{B}_0$. This results in $2s + 1$ eigenstates with energies

$$E_s = -\gamma m_s \hbar B_0, \tag{2.11}$$

where m_s is the magnetic quantum number that assumes the values $m_s = -s, -s + 1, \ldots, s - 1, s$. The splitting of energy levels in a magnetic field is called Zeeman effect.

The hydrogen nucleus ^{1}H, which is the most abundant nucleus in the human body and consists of a single proton, has a spin quantum number of $s = {}^1/_2$ and thus $m_s = \pm {}^1/_2$. According to equation (2.11), in a magnetic field, its two eigenstates $|\uparrow\rangle = |m_s = +{}^1/_2\rangle$ and $|\downarrow\rangle = |m_s = -{}^1/_2\rangle$ have an energy difference of

$$\Delta E = \hbar \gamma B_0 = \hbar \omega_0 \tag{2.12}$$

with the Larmor frequency $\omega_0 = \gamma B_0$. This energy is absorbed or emitted during transitions between the spin states, which can be caused by time-varying magnetic fields. In a quantum electrodynamical description, this corresponds to absorption or emission of (virtual) photons [9], whose energy $E_{\mathrm{ph}} = \hbar \omega_{\mathrm{rf}}$ matches the energy difference of the spin states, equation (2.12), leading to the resonance condition $\omega_{\mathrm{rf}} = \gamma B_0$. The dynamics of the expectation value $\langle \hat{\vec{\mu}} \rangle$ of the magnetic moment (equation (2.10)) due to an external magnetic field $\vec{B}$ can be obtained from the Ehrenfest theorem [10, 11] as

$$\frac{\mathrm{d}}{\mathrm{d}t} \langle \hat{\vec{\mu}} \rangle = \gamma \langle \hat{\vec{\mu}} \rangle \times \vec{B}. \tag{2.13}$$

This expression can be identified with the equation of motion for a classical magnetic moment in an external field.

2.2.1.1. Chemical Shift

Nuclear spins in biological tissue reside in atoms and molecules, whose electronic orbitals react to the external field B_0 by inducing local magnetic fields. This causes a partial shielding or de-shielding of the external field at the location of the spin, which results in a slightly shifted Larmor frequency compared to an isolated nucleus. The resulting shift of the resonance frequency ω compared to a reference frequency ω_{ref} is conventionally stated relatively as

$$\delta = \frac{\omega_{\text{ref}} - \omega}{\omega_{\text{ref}}} \tag{2.14}$$

in units of parts per million (ppm), which is independent of B_0. This so-called chemical shift depends on the electronic environments of the considered nucleus, i.e., electron density and electronegativity of molecular groups. Consequently, it bears information about molecular structure and conformation as well as functional groups and is thus central to the analysis of MR spectroscopy and CEST MRI (section 2.3).

2.2.2. Macroscopic Magnetization and Bloch Equations

The situation encountered in MRI applied in a biophysical context always involves ensembles of a large number N (usually $N \gtrsim 10^{23}$) of nuclei. Thus, the overall behavior of the system can be expected to be well described by a classical limit of quantum statistics. It is customary to consider the macroscopic magnetization density

$$\vec{M} = \frac{1}{V} \sum_{i=1}^{N} \langle \hat{\vec{\mu}} \rangle \tag{2.15}$$

in a volume V. At temperature T, the population fraction of the two energy levels in thermal equilibrium is approximately described by the Boltzmann distribution as

$$\frac{n_\uparrow}{n_\downarrow} = \exp\left(\frac{\hbar\omega_0}{k_{\text{B}}T}\right). \tag{2.16}$$

From that, it follows that for typical body temperature ($T \approx 310\,\text{K}$) and MRI field strength ($B_0 \approx 1.5\,\text{T}$ to $9.4\,\text{T}$), thermal fluctuations strongly dominate ($k_{\text{B}}T \gg \hbar\gamma B_0$), such that only a very small excess population in the lower energy state remains (relative fraction on the order of 10^{-6}). This results in the thermal equilibrium value of the macroscopic magnetization

$$M_0 \approx \frac{1}{4} \frac{N}{V} \frac{\gamma^2 \hbar^2}{k_{\text{B}}T} B_0, \tag{2.17}$$

which is aligned along $\vec{B}_0$ [8]. From this equation it can be seen that the magnetization usable for MRI is proportional to the main magnetic field strength B_0, which underlines the advantage of UHF MRI in terms of signal strength [12]. The dynamics of the macroscopic magnetization in an external magnetic field directly follow from equations (2.13) and (2.15) as $\mathrm{d}\vec{M}/\mathrm{d}t = \gamma\vec{M} \times \vec{B}$. The same result can be derived by applying

the density matrix formalism to an ensemble of non-interacting spins [6]. However, in a realistic setting, interactions between nuclear spins cannot be neglected. To account for that, a modification of the previous equation in order to phenomenologically include typical interactions was introduced by Felix Bloch [13], leading to the Bloch equations

$$\frac{\mathrm{d}\vec{M}}{\mathrm{d}t} = \gamma \vec{M} \times \vec{B} + \frac{(M_0 - M_z)\vec{e}_z}{T_1} - \frac{M_x\vec{e}_x + M_y\vec{e}_y}{T_2} \tag{2.18}$$

$$= \begin{pmatrix} -1/T_2 & \gamma B_z & -\gamma B_y \\ -\gamma B_z & -1/T_2 & \gamma B_x \\ \gamma B_y & -\gamma B_x & -1/T_1 \end{pmatrix} \begin{pmatrix} M_x \\ M_y \\ M_z \end{pmatrix} + \begin{pmatrix} 0 \\ 0 \\ M_0/T_1 \end{pmatrix}. \tag{2.19}$$

According to these, the time evolution of $\vec{M}$ consist of rotation around $\vec{B}$ (first term in equation (2.18)) and relaxation: The longitudinal magnetization component M_z undergoes exponential recovery towards the thermal equilibrium M_0 with the Longitudinal Relaxation Constant (T_1) (second term in equation (2.18)), which accounts for energy exchange between excited nuclear spins and their surrounding atomic environment. In addition, the transversal components M_x and M_y decay exponentially with the Tranversal Relaxation Constant (T_2) (third term in equation (2.18)). On a microscopic level, this corresponds to a loss of phase coherence between spin packets due to various reasons, such as local magnetic field disturbances or spin-spin interactions. The empirical inclusion of relaxation terms in equation (2.18) can be justified and related to microscopic interactions between spins by appropriate quantum mechanical treatment [14].

2.2.3. MR imaging

Most phenomena that are relevant in the context of MRI can be comprehensively understood from the Bloch equations (equation (2.18)), and the Maxwell equations of classical electrodynamics that describe the magnetic fields involved in the excitation, encoding and detection processes.

2.2.3.1. Signal Reception

In MRI, detection of the desired signal happens through an induced voltage U_{ind} in appropriate RF receive coils close to the investigated object. This can be understood from Faraday's law of induction

$$U_{\mathrm{ind}} = -\frac{\mathrm{d}\Phi}{\mathrm{d}t} \tag{2.20}$$

with the magnetic flux $\Phi = \int_{\mathrm{coil\ area}} \vec{B} \cdot \mathrm{d}\vec{A}$ through the coil, which is equivalent to the Maxwell equation $\vec{\nabla} \times \vec{E} = -\mathrm{d}\vec{B}/\mathrm{d}t$. It can be found that the time evolution of the nuclear magnetization $\vec{M}$ causes a magnetic flux of

$$\Phi(t) = \int_{\mathrm{sample}} \vec{B}_{\mathrm{receive}}(\vec{r}) \cdot \vec{M}(\vec{r}, t) \, \mathrm{d}^3 r, \tag{2.21}$$

where $\vec{B}_{\text{receive}}$ is the hypothetical field that would be produced by the receive coil at location $\vec{r}$ when driven with a unit current [8]. This is an example of the principle of Lorentz reciprocity [15], which follows from symmetries of the Maxwell equations under certain conditions and allows reversing the roles of magnetization sources and detection coils for MR signal strength calculations. Further analysis shows [8, 15, 16] that the received signal is given by

$$s(t) \propto \int_{\text{sample}} M_+(\vec{r})\, B_1^-(\vec{r})\, e^{\mathrm{i}\phi(\vec{r},t)}\, \mathrm{d}^3 r, \tag{2.22}$$

which indicates that only the transverse component of the magnetization, here written as the complex quantity $M_+ = M_x + \mathrm{i}M_y$ with phase $\phi(\vec{r}, t)$, as well as the circularly polarized component of the hypothetical receive field $B_1^- = (B_{\text{receive},x} - \mathrm{i}B_{\text{receive},y})/2$ that rotates at the Larmor frequency in an opposite sense to the magnetization (counter-clockwise) contribute to the detectable signal. In an MRI scanner, this signal gets amplified, demodulated and digitized by an Analog-to-Digital Converter (ADC). As $B_1^-(\vec{r})$ indicates how sensitive a receive coil is to excited magnetization at a certain location, this quantity is also referred to as receive coil sensitivity. The spatial pattern of coil sensitivities depends on the electromagnetic properties of the receive coils, the RF wavelength, which in turn scales inversely with the Larmor frequency and thus B_0, and on the electrical conductivity and permittivity of the object inside the coil [17].

2.2.3.2. RF excitation

As seen in the previous section, only the transverse components of $\vec{M}$ can be detected through an induced voltage in a receive coil. To create transversal magnetization, a magnetic RF field $\vec{B}_1(\vec{r}, t) = \vec{B}_1(\vec{r})e^{\mathrm{i}\omega_{\text{RF}}t}$ is applied via a so-called transmit coil. According to equation (2.18), this field needs to have x or y components in order to deflect the magnetization from its thermal equilibrium of alignment along the z axis. It can be found that only the circularly polarized component $B_1^+ = (B_{1,x} + \mathrm{i}B_{1,y})/2$ that rotates at the Larmor frequency in the same sense of rotation as the magnetization (clockwise) effectively contributes to this deflection [8]. When applying an on-resonant ($\omega_{\text{rf}} = \omega_0$) RF pulse of duration t_{p}, the magnetization $\vec{M}$ rotates around B_1^+ and stops at the so-called flip angle $\alpha = \gamma \int_0^{t_{\text{p}}} B_1^+(t')\,\mathrm{d}t'$ between $\vec{M}$ and the z-axis. This process is often referred to as excitation of the magnetization. Following from equation (2.18), $\vec{M}$ subsequently precesses with the Larmor frequency around the z axis and undergoes the described T_1 and T_2 relaxation.

2.2.3.3. Spatial Encoding

Having created excited magnetization in the transversal plane by an excitation pulse as described in the previous section, the detected signal of the precessing and decaying magnetization according to equations (2.18) and (2.22) is a damped oscillation, a so-called free induction decay (FID). This signal results from integration over the entire

sample and thus does not yield any spatial information. In order to perform imaging, i.e., obtain spatially resolved information, most applications employ time-varying magnetic gradient fields $\vec{G}(t)$ [18] that are created by gradient coils and designed such that the z component of the magnetic field varies linearly along each spatial direction as $B_z(\vec{r}, t) = B_0 + \vec{G}(t) \cdot \vec{r}$, assuming a perfectly homogeneous main magnetic field. Consequently, the Larmor frequency becomes a function of space as $\omega_L(\vec{r}, t) = \gamma(B_0 + \vec{G}(t) \cdot \vec{r})$. Resulting from that, the phase of the transversal magnetization in equation (2.22) after an RF pulse at $t = 0$ at different locations evolves as

$$\phi(\vec{r}, t) = -\int_0^t \omega_L(\vec{r}, \tau) \, \mathrm{d}\tau = -\omega_0 t - \gamma \int_0^t \vec{G}(\tau) \cdot \vec{r} \, \mathrm{d}\tau \tag{2.23}$$

With the conventionally performed quadrature demodulation of the signal with the Larmor frequency ω_0 [8], the first term on the right in equation (2.23) vanishes. Finally, with the definition

$$\vec{k}(t) = \gamma \int_0^t \vec{G}(\tau) \, \mathrm{d}\tau, \tag{2.24}$$

equations (2.22) and (2.23) can be combined to yield the signal

$$s(t) \propto \int_{\text{sample}} \rho(\vec{r}) \, e^{-\mathrm{i}\vec{k}(t) \cdot \vec{r}} \, \mathrm{d}^3 r, \tag{2.25}$$

summarizing receive sensitivity and transversal magnetization including possible relaxation effects as the effective spin density $\rho(\vec{r})$. Equation (2.25) shows that the acquired signal $s(t)$ is the continuous Fourier transform of $\rho(\vec{r})$ evaluated at the coordinates $\vec{k}(t)$ in reciprocal space, called k-space [19–21]. Image reconstruction is thus the problem of recovering an approximation of $\rho(\vec{r})$ from samples of its Fourier transform along the k-space trajectory $\vec{k}(t)$ and is described in section 2.2.4. By controlling the gradient waveforms $\vec{G}(t)$ appropriately, a large variety of different k-space trajectories can be used for image encoding, the most common ones being rectilinear (Cartesian) [22], radial [18, 23] and spiral [19, 20, 24]. However, long trajectories are problematic due to $T_2{}^*$ decay and off-resonance effects caused by B_0 inhomogeneities, which cause image artifacts. Thus, image encoding is usually performed along multiple trajectory segments (also called shots), each following a new excitation pulse.

An example of a basic Cartesian 2D imaging sequence (spoiled GRE) with associated k-space trajectory is shown in Figure 2.1. Here, Phase Encoding (PE) is applied to one spatial axis (y by convention), which means that a trapezoidal gradient is played out before the ADC is open, traveling to a certain initial position along k_y in k-space. The other axis (here: x) is frequency encoded, which involves opening the ADC during a constant gradient, such that signal is sampled along straight lines with constant velocity in k-space. Note that for such single-line acquisitions, the time between acquisition of two data points along the PE direction (between shots) is the Repetition Time (TR) (usually on the ms scale), while along the Readout (RO) direction it is the much shorter ADC dwell time (usually μs scale). Spatial localization along the remaining z axis can
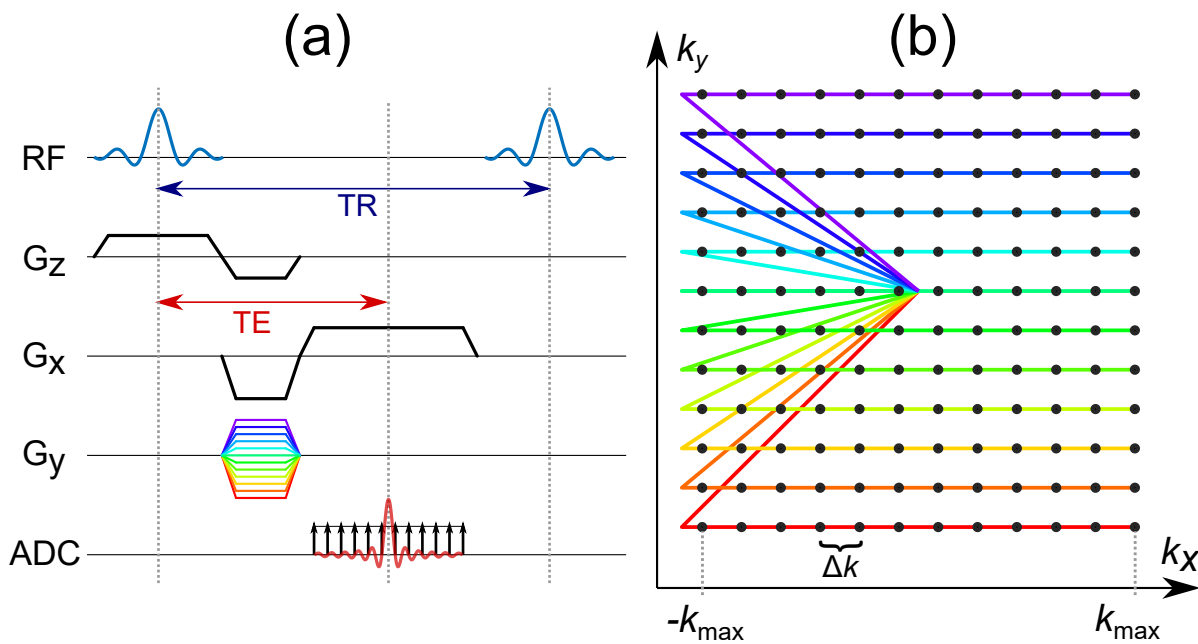
Figure 2.1.: (**a**) Examplary sequence diagram of a 2D GRE sequence (spoiling not shown for clarity). It consists of repeated slice selective excitation by combination of RF pulses and G_z gradients, phase encoding (G_y) of variable amplitude, frequency encoding (G_x) and signal sampling by the ADC. (**b**) Corresponding k-space trajectory. Data points are sampled on a Cartesian grid, enabling simple FFT reconstruction. Colors correspond to the respective phase encoding gradients in different repetitions.

be performed either by PE as well (3D encoding), or by slice-selective excitation. In the latter case (shown in the Figure), a shaped RF pulse with certain bandwidth (e.g., a sinc-shaped pulse) is applied during a constant z-gradient. Thus, only spin packets at locations for which the local Larmor frequency lies within the bandwidth of the pulse get excited, enabling selective excitation of certain slices or slabs.

2.2.3.4. Noise in MRI

Data collected at an MRI scanner are inevitably corrupted by noise of various sources, the principal contribution arising from random thermal fluctuations in the imaged sample, as well as from resistive elements in the receive coils and electronics. In most situation relevant for human MRI, the sample noise dominates [25] and can be characterized as additive, complex, and white. The standard deviation of thermal noise at temperature T is given by $\sigma_{\mathrm{noise}} = \sqrt{4k_{\mathrm{B}}T \cdot R \cdot \mathrm{BW}}$ with the effective resistance R and receiver bandwidth BW [8]. If the image reconstruction, i.e. the mapping from measured complex k-space data to the final image, is a unitary linear transform (as it is the case for a simple Fourier transform), the uniform Gaussian nature of the noise is preserved in the complex image. If magnitude images are considered, as well as for multi-coil-combined images and PI techniques, the noise statistics in image space are better described by potentially spatially varying Rician or non-central chi distributions [26]. As a central measure for image quality, the SNR being defined as the ratio of voxel signal and noise standard deviation depends on a multitude of factors such as B_0, the scanner hardware including RF coils, sample properties and sequence parameters. For the latter, the most important proportionality is given by $\mathrm{SNR} \propto V \cdot \sqrt{t_{\mathrm{acq}}}$, meaning that the SNR scales linearly with the voxel volume V and the square root of the acquisition time t_{acq} [27].

2.2.4. Sampling and Image Reconstruction

The effective spin density $\rho(\vec{r})$, i.e., the image that is ideally to be reconstructed, is a continuous function, whereas the ADC of an MRI system can only sample a finite number of discrete data points of the k-space signal $s_i = s(t_i), i = 1 \ldots N_k$ with usually equally spaced times t_i according to equation (2.25). Consequently, perfect reconstruction of $\rho(\vec{r})$ is impossible and several assumptions have to be made, e.g. the image being of finite support, called the Field Of View (FOV), and composed of a set of chosen voxel basis functions, usually a grid of Dirac peaks [28]. With that, equation (2.25) can be cast into the linear measurement model

$$\mathbf{s} = \mathbf{E}\boldsymbol{\rho} + \boldsymbol{\varepsilon} \tag{2.26}$$

with the vectors of voxel intensities $\boldsymbol{\rho} = (\rho_1, \ldots, \rho_{N_r})$ corresponding to spatial positions $\vec{r}_j$ and k-space samples $\mathbf{s} = (s_1, \ldots s_{N_k})$, related through the $N_k \times N_r$ encoding matrix $\mathbf{E}_{i,j} = e^{i\vec{k}(t_i) \cdot \vec{r}_j}$ and complex, zero-mean, uncorrelated, temporally white Gaussian noise $\boldsymbol{\varepsilon}$ [28]. Equation 2.26 can be identified with the general linear model introduced in section 2.1, equation (2.3); thus, the least-squares solution of the reconstruction problem

is given according to equation (2.5) by the pseudo-inverse of the encoding matrix as $\hat{\boldsymbol{\rho}} = (\mathbf{E}^H\mathbf{E})^{-1}\mathbf{E}^H\mathbf{s}$. However, the accuracy of this reconstruction depends strongly on the k-space trajectory used. The Nyquist–Shannon sampling theorem [29] applied to MRI states that for a faithful reconstruction, neighboring samples in k-space should be no more than $\Delta k = 2\pi/\text{FOV}$ apart. Conversely, a maximum k-space value of $k_{\max} = \pi/\Delta x$ is required to achieve a spatial resolution, i.e., voxel size of Δx along each axis. When data are acquired on such a Cartesian Nyquist-sampled k-space grid (Figure 2.1b), the encoding matrix $\mathbf{E}$ becomes a regular Discrete Fourier Transform (DFT) matrix, which is unitary up to a normalization constant ($\mathbf{E}^H = N_k\mathbf{E}^{-1}$), meaning that its pseudo-inverse is simply given by its Hermitian conjugate, $\mathbf{E}^+ = \frac{1}{N_k}\mathbf{E}^H$ [4]. Therefore, reconstruction can be performed by inverse DFT, efficiently computed by the FFT algorithm [30]. This is the most common and simple MRI reconstruction method.

A major drawback is that obtaining a Nyquist-sampled k-space is inevitably time-consuming, which is why most MRI acceleration methods involve some form of under-sampling. Regular undersampling on a Cartesian grid leads to coherent aliasing, also called ghosting, whereas irregular or non-Cartesian sampling results in incoherent aliasing that spreads over the entire image. The task of acceleration methods such as PI, which will be introduced in the next section, is then to eliminate these aliasing artifacts by filling in the missing information in k-space.

2.2.5. Parallel Imaging

The above introduction of image encoding and reconstruction assumed a single receive coil. However, for most imaging applications, it is common to use multiple receive coils connected to independent receive channels.

An illustrative example is given in Figure 2.2. The original purpose of this so-called phased array coil concept [31] was to improve the SNR by making use of small local surface coils that are less sensitive to noise compared to large volume coils, but can be combined to still yield large volume coverage. In addition, forming a central milestone in the development of rapid MRI methods, it was recognized that the sensitivity information of multiple local receive coils provides complementary spatial encoding information that can be used to partially omit the time-consuming gradient encoding introduced in section 2.2.3.3 [32–34]. This can be understood by noting that in conventional MRI (i.e., based only on gradient encoding), all information is acquired sequentially as a one-dimensional signal in time. This is manifested in equation (2.25), where by means of the integration over the sample, all direct spatial information is collapsed into a single signal value (i.e., induced voltage) at a time. Consequently, conventional gradient encoding uses only the temporal degree of freedom of the electromagnetic fields created by precessing magnetization at different locations, which makes it inherently time-consuming. However, also the spatial degrees of freedom of these electromagnetic fields carry image information. With knowledge of the sensitivity patterns $B_1^-(\vec{r})$ of multiple receive coils in equation (2.22), some information about these spatial degrees of freedom is retrieved and can be used for image reconstruction, complementary to the temporal, gradient-encoded information [35].
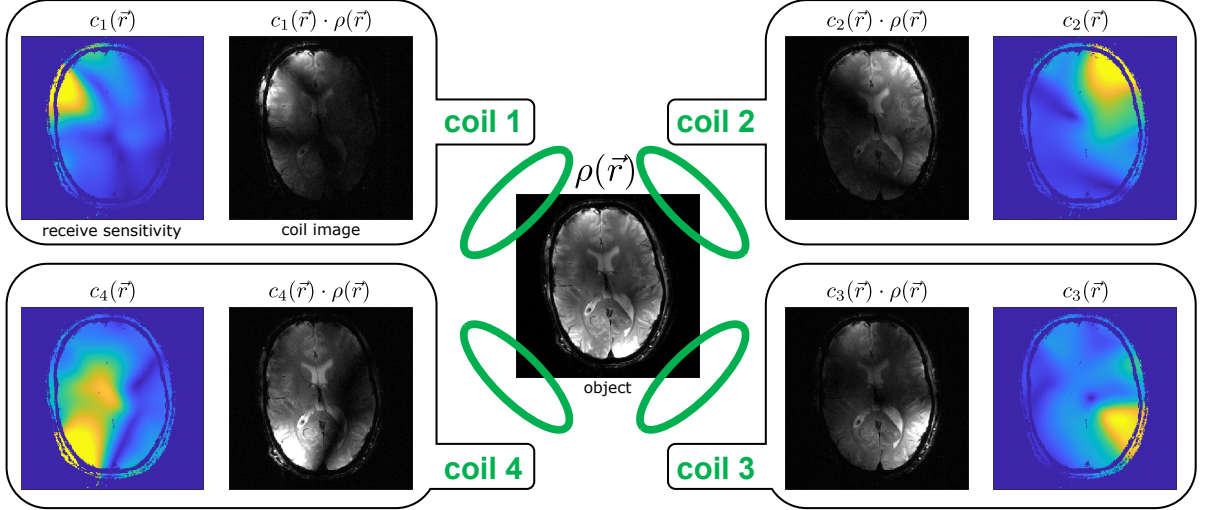
Figure 2.2.: Illustrative example of a receive array consisting of four surface loop coils. Due to the different spatial locations and electromagnetic properties of the coils, the images reconstructed from each channel are given by the underlying image $\rho(\vec{r})$ weighted by the respective coil sensitivity $c_k(\vec{r})$, according to equation (2.22). Knowledge of this spatial weighting forms the basis of PI.

An immense amount of research exists on such PI methods and algorithms, of which Sensitivity Encoding (SENSE) [34] and Generalized Autocalibrating Partially Parallel Acquisitions (GRAPPA) [36] are the most widely used. Due to its relevance for Publication 1 and 2 of this thesis, in the following, SENSE is introduced in more detail. An overview of other methods can be found in the review articles [35, 37–40].

The SENSE method can be elegantly formulated in the framework of linear least-squares reconstruction as introduced in section 2.2.4, based on the general theory of linear models outlined in section 2.1. Assuming an array of N_c receive coils and denoting their sensitivities $B_1^-(\vec{r})$ as $c_k(\vec{r})$, $k = 1, \ldots, N_c$, the signal equation (2.22) reads $s_k(t) \propto \int_{\text{sample}} c_k(\vec{r})\rho(\vec{r})\, e^{-\mathrm{i}\vec{k}(t)\cdot\vec{r}}\,\mathrm{d}^3r$. It can, equivalently to equation (2.26), be discretized to yield the linear equation system $\mathbf{s} = \mathbf{E}\boldsymbol{\rho} + \boldsymbol{\varepsilon}$, with the multi-channel encoding matrix

$$\mathbf{E}_{(ik),j} = c_k(\vec{r}_j)e^{\mathrm{i}\vec{k}(t_i)\cdot\vec{r}_j} \tag{2.27}$$

and multi-channel data vector $\mathbf{s}$ of stacked data samples from each channel. Note that in the row dimension of the encoding matrix, equation (2.27), the k-space indices i and coil indices k occur concurrently in a vectorized manner, which highlights the complementary gradient and sensitivity-based encoding. For multi-channel acquisition, the noise $\boldsymbol{\varepsilon}$ among channels is generally correlated, as fluctuating noise sources at a certain location may simultaneously affect multiple receive coils nearby [34, 41]. In this case, assuming a known receiver noise covariance matrix $\boldsymbol{\Psi}$ and following the concept of generalized least-squares introduced in section 2.1, equation (2.7), the optimal reconstruction is obtained

as $\hat{\boldsymbol{\rho}} = (\mathbf{E}^H \boldsymbol{\Psi}^{-1} \mathbf{E})^{-1} \mathbf{E}^H \boldsymbol{\Psi}^{-1} \mathbf{s}$. As the encoding matrix is now composed of coil sensitivities and Fourier terms, it is possible to violate the Nyquist criterion for pure Fourier encoding and use undersampled, thus accelerated k-space trajectories (Figure 2.3). As a drawback, $\mathbf{E}$ is no longer unitary and thus the variance of the reconstruction, i.e., the noise level in the image, will potentially be amplified and vary in space. According to equation (2.8), the corresponding covariance matrix, called image noise matrix is given by $\mathbf{X} = (\mathbf{E}^H \boldsymbol{\Psi}^{-1} \mathbf{E})^{-1}$. Application of SENSE thus leads to two distinct mechanisms of SNR degradation: One is related to the inevitably reduced noise averaging when acquiring a reduced number of k-space samples $N_{k_{\mathrm{red}}} = N_k / R$ with the acceleration factor R compared to full Nyquist sampling. The other is due to the potentially amplified and spatially varying noise level resulting from a non-unitary encoding matrix. This can concisely be written as

$$\mathrm{SNR}^{\mathrm{PI}} = \frac{\mathrm{SNR}^{\mathrm{ref}}}{g \cdot \sqrt{R}} \tag{2.28}$$

with the SNR of the PI reconstruction and Nyquist sampled reference reconstruction $\mathrm{SNR}^{\mathrm{PI}}$ and $\mathrm{SNR}^{\mathrm{ref}}$, respectively; and the so-called geometry factor or g-factor

$$g_j = \sqrt{(\mathbf{E}^H \boldsymbol{\Psi}^{-1} \mathbf{E})^{-1}_{j,j} (\mathbf{E}^H \boldsymbol{\Psi}^{-1} \mathbf{E})_{j,j}} \tag{2.29}$$

in the j-th voxel. A derivation of equation (2.29) is given in the Appendix, section C.1. Note that by a noise de-correlation step as described in section 2.1 and [42], the receiver noise covariance matrix $\boldsymbol{\Psi}$ can be eliminated from the above equations.

The g-factor is a central quality metric for PI, as it quantifies the spatial encoding capability of the combination of coil sensitivities and k-space sampling scheme. Consequently, it is frequently used to guide both receive coil design [43–46] as well as sampling pattern optimization [47–51]. The concept of the g-factor can be related to the statistical framework of Cramér-Rao lower bounds[2] [52, 53]. Additionally, it is connected to the condition number of the encoding matrix $\mathbf{E}$, which quantifies how sensitive the solution of equation (2.26) is to small perturbations (e.g., noise) of the right hand side of the equation[3]. Generally, the encoding matrix becomes increasingly ill-conditioned for stronger acceleration, since for reduced Fourier encoding, more and more spatial information needs to be encoded by the coil sensitivities. These in turn are not fully spatially independent (or, in a mathematical sense, orthogonal), as their spatial patterns are governed by electrodynamics, typically resulting in a smooth and partially overlapping behavior.

Consequently, for both stronger acceleration (Figure 2.3(a-c)) as well as more strongly overlapping sensitivity profiles (Figure 2.4), an increase in g-factors and condition num-

---

[2]In the context of statistics and estimation theory, the Cramér-Rao inequality gives a lower bound on the variance of an unbiased estimator [4]. In PI, the SENSE reconstruction is a linear estimator and its variance quantifies the image noise.

[3]The condition number of a matrix $\mathbf{A}$ with respect to a chosen norm $||\cdot||$ is given by $\kappa(\mathbf{A}) = ||\mathbf{A}|| \cdot ||\mathbf{A}^{-1}||$ [54], from which the similarity with the definition of the SENSE g-factor, equation (2.29), can be seen.

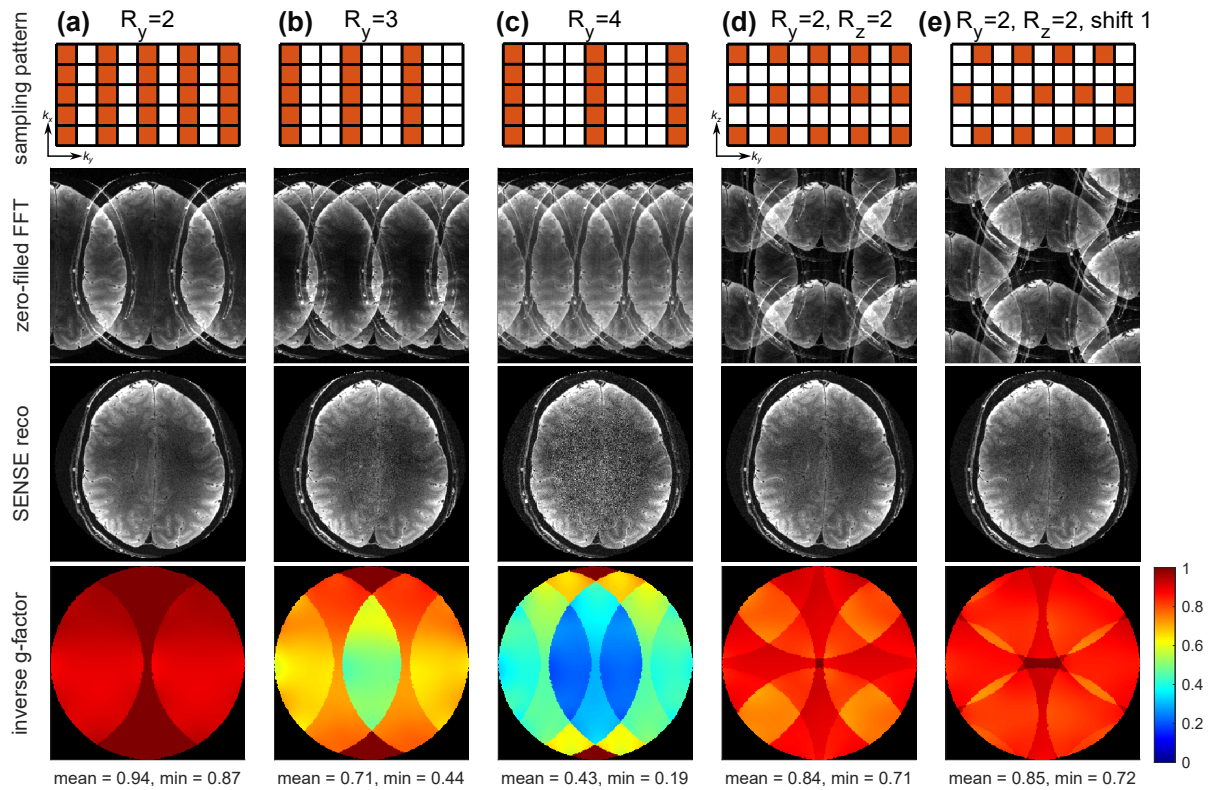Figure 2.3.: Examples of SENSE applied for different Cartesian k-space sampling patterns, namely (**a**) two-fold, (**b**) three-fold and (**c**) four-fold regular undersampling along the PE direction (k_y), as well as (**d**) 2×2 undersampling in two PE directions (k_y and k_z) of a 3D acquisition and (**e**) the same acceleration along k_y and k_z but with an additional so-called CAIPIRINHA shift [47, 55]. First row: part of the k-space sampling pattern. Second row: A zero-filled FFT reconstruction (no PI applied), showing the aliasing pattern in image space associated with the respective sampling scheme. Third row: SENSE reconstruction, showing aliasing-free images, which, however can suffer from noise amplification. Fourth row: Inverse g-factor maps (close to one means little noise amplification, while lower values indicate stronger SNR loss). For this illustrative example, 8 receive coils at $B_0 = 3\,\mathrm{T}$ were assumed.
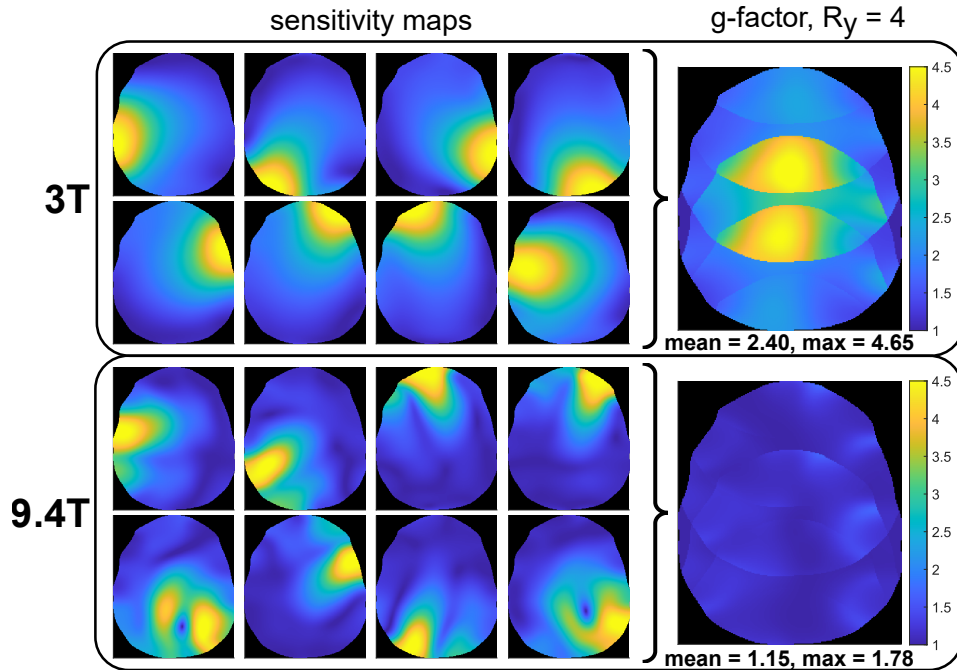
Figure 2.4.: Dependence of g-factors on spatial independence of receiver sensitivity profiles obtained at different B_0. Upper panel: Coil sensitivities at 3 T with stronger spatial overlap result in higher g-factors due to increased ill-conditioning of the matrix inversions required for SENSE reconstructions. Bottom panel: Less overlapping sensitivities at 9.4 T result in significantly lower g-factors. Cartesian undersampling along one axis with acceleration factor $R = 4$ was assumed. Sensitivity maps were acquired both on a human 3 T scanner using the vendor's 20-channel head coil and on a human 9.4 T scanner using the same phantom and a custom-built 31-channel head coil [56]. For illustration purposes, only the 8 coil elements with the highest signal in the slice are shown and used to calculate g-factors.

ber $\kappa(\mathbf{E})$ can be observed. In particular, due the lower RF wavelength at higher B_0 (see section 2.2.3.1), coil sensitivities at UHF tend to be more spatially independent and thus generally yield lower g-factors compared to e.g. 3 T. As another general observation, g-factors are higher if there are larger gaps in the k-space sampling pattern, corresponding to a large overlap of aliases in image space. Therefore, avoiding large gaps by distributing the undersampling among two PE directions of a 3D acquisition (Figure 2.3(d)) and using so-called CAIPIRINHA [47, 55] shifts (Figure 2.3(e)) is generally advantageous.

It has to be emphasized that for practical applications, storing the encoding matrix $\mathbf{E}$ in memory and performing the matrix inversion required for obtaining reconstructions
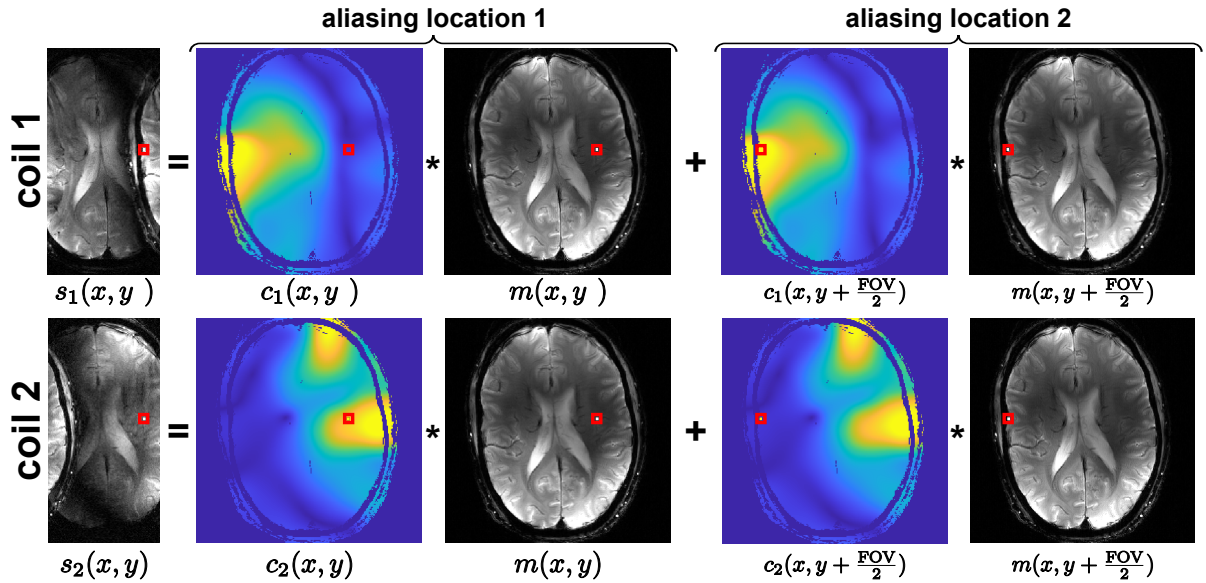
Figure 2.5.: Exemplary depiction of the linear equation system formulated for SENSE reconstruction in image space for regular Cartesian k-space undersampling (here shown for an acceleration factor of $R = 2$ and two receive coils). A voxel in the coil images of each channel s_k (leftmost column) is given by the superposition (aliasing) of image intensities at the aliased locations m (third and fifth column), weighted by the respective coil sensitivity c_k (second and fourth column). For the shown two-fold undersampling, the aliased locations have a distance of half of the FOV. As indicated by the equations below the images, this can be formulated as the linear equation system $\mathbf{s} = \mathbf{Cm}$, which can be solved for the "unfolded" image intensities $\mathbf{m}$ if the coil sensitivities in $\mathbf{C}$ are known. Figure adapted from [38].

and analytical g-factors is infeasible[4]. Therefore, for general (especially non-Cartesian) encoding, the linear reconstruction problem, equation (2.26), is commonly solved iteratively, for example with the conjugate gradient method [42, 57]. In the special case of regular Cartesian undersampling, due to the coherent aliasing (Figure 2.3), the reconstruction problem can be decomposed into small sub-problems, corresponding to unfolding of a small number of aliased voxels in image space, which can be solved individually. An illustrative example of this procedure is shown in Figure 2.5 and a detailed description of this special case is given in [34].

---

[4]For an image matrix size of 256×256, an undersampled k-space trajectory with acceleration factor $R = 2$ and $N_c = 8$ receive coils, storing the entries of the encoding matrix as complex double-precision floating point numbers in memory would consume $(256)^4/2 \cdot 8 \cdot 16$ bytes ≈ 275 gigabytes.
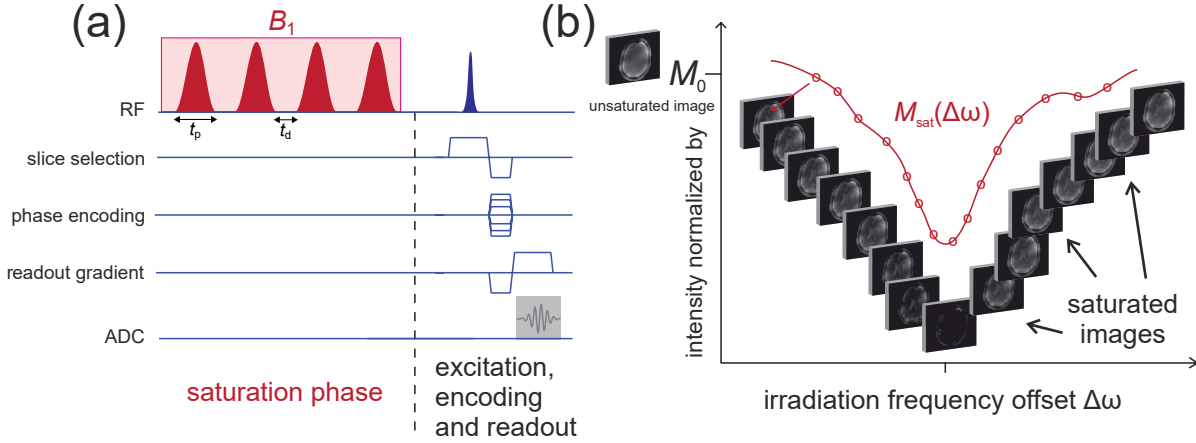
Figure 2.6.: (**a**) Schematic sequence diagram of a CEST MRI sequence, consisting of a saturation block during which a train of RF pulses of amplitude B_1, duration t_p and interpulse delay time t_d are applied, followed by a conventional imaging sequence. (**b**) If the sequence blocks displayed in (a) are repeated for different off-resonance frequencies $\Delta\omega$ of the RF pulses, a Z-spectrum in every voxel can be obtained by normalizing the acquired images $M_{sat}(\Delta\omega)$ with an unsaturated image M_0. Figure adapted from [64].

2.3. Basics of CEST MRI

CEST MRI is based on the indirect detection of labile protons within a target compound (e.g metabolite) that have a chemically shifted Larmor frequency relative to bulk water protons (section 2.2.1.1) by means of selective saturation. [58–61]. This saturation is achieved by off-resonant RF irradiation. In the microscopic picture, saturation refers to a temporarily induced equilibrium between the populations of the two spin states $|\uparrow\rangle$ and $|\downarrow\rangle$ (section 2.2.1), leaving zero net macroscopic magnetization. In the macroscopic view of the Bloch equations, saturation is modeled by relaxation during the rotation induced by an RF pulse [62].

When labile solute protons exchange with water protons (exchange rate k, typically in the range of $10\,\mathrm{Hz}$ - several kHz), the saturation is progressively transferred to the water pool, resulting in a reduced bulk water signal. If RF irradiation is applied for a sufficiently long saturation time t_{sat} (on the order of seconds for typical applications), this saturation transfer can occur multiple times, resulting in a detectable build-up of water pool saturation that can be recorded using MR imaging sequences as described in section 2.2.3. The process of accumulated saturation serves as a signal amplification mechanism for the solute target protons (concentration on the order of mM) by exploiting the much larger water proton concentration ($\sim 110\,\mathrm{M}$).

The magnetization dynamics of proton pools that are linked via exchange can be described by the Bloch-McConnell equations [63]; a detailed description of this theory is given in [64].

2. Introduction

Figure 2.6a shows a typical CEST MRI sequence. It consists of a saturation block with the RF pulse amplitude B_1 and frequency offset $\Delta\omega$ relative to the water Larmor frequency ω_0. This saturation phase is followed by an imaging sequence (c.f. Figure 2.1), acquiring one or more k-space lines. In the extreme case, an entire 2D or 3D k-space can be acquired after a single saturation phase (snapshot-CEST [65]). Repeating these blocks of saturation and image acquisition for different off-resonance frequencies $\Delta\omega$ yields a set of images, each depicting a differently altered water magnetization signal $M_{\text{sat}}(\Delta\omega)$, which is potentially affected by various exchange effects. The need for such repeated acquisitions in order to achieve high spectral resolution makes CEST MRI intrinsically lengthy. A so-called Z-value is then obtained by normalizing the M_{sat} images with a reference image acquired at a far off-resonant RF frequency, which provides the thermal-equilibrium magnetization M_0, leading to

$$Z(\Delta\omega) = \frac{M_{\text{sat}}(\Delta\omega)}{M_0}. \tag{2.30}$$

Plotting these values as a function of the off-resonance frequency (in ppm) yields so-called Z-spectra in each of the acquired voxels (Figure 2.6b). By convention, 0 ppm corresponds to the water Larmor frequency and the frequency axis is plotted from "upfield" (positive ppm values) to "downfield" (negative ppm values). Optionally, Z-spectra can be acquired at multiple saturation amplitudes B_1 to correct for B_1^+ inhomogeneities [66], which become increasingly pronounced at UHF, or for quantitative parameter estimation [67–69]. However, this necessitates even longer acquisition times.

A plethora of analysis methods and metrics have been proposed for the evaluation of CEST data. They vary in the extent to which they can provide quantitative information about the pool system, disentangle concomitant effects, as well as in their complexity, stability and computational requirements. For example, the simplest and most widely used metric is the asymmetry analysis of Z-spectra [60], which is given by $\text{MTR}_{\text{asym}}(\Delta\omega) = Z(-\Delta\omega) - Z(+\Delta\omega)$. This metric is easy to calculate, but is sensitive to B_0 inhomogeneity and fails to disentangle effects occurring on either side of the water resonance, as is the case with the complex structure of in vivo Z-spectra. On the other hand, fitting numerical or approximated analytical solutions of the Bloch-McConnell equations to acquired Z-spectra theoretically allows full quantification of exchange rates and concentrations of CEST pools [68–70]. However, such approaches are computationally expensive, susceptible to data fluctuations and the results are highly dependent on internal parameters of the fitting procedure [71]. As a compromise, semi-quantitative models such as a sum of Lorentzian peaks with different amplitudes, widths and spectral positions are often used to fit Z-spectra. These methods have proven to be useful estimators of isolated CEST effects in different settings [66, 72–74].
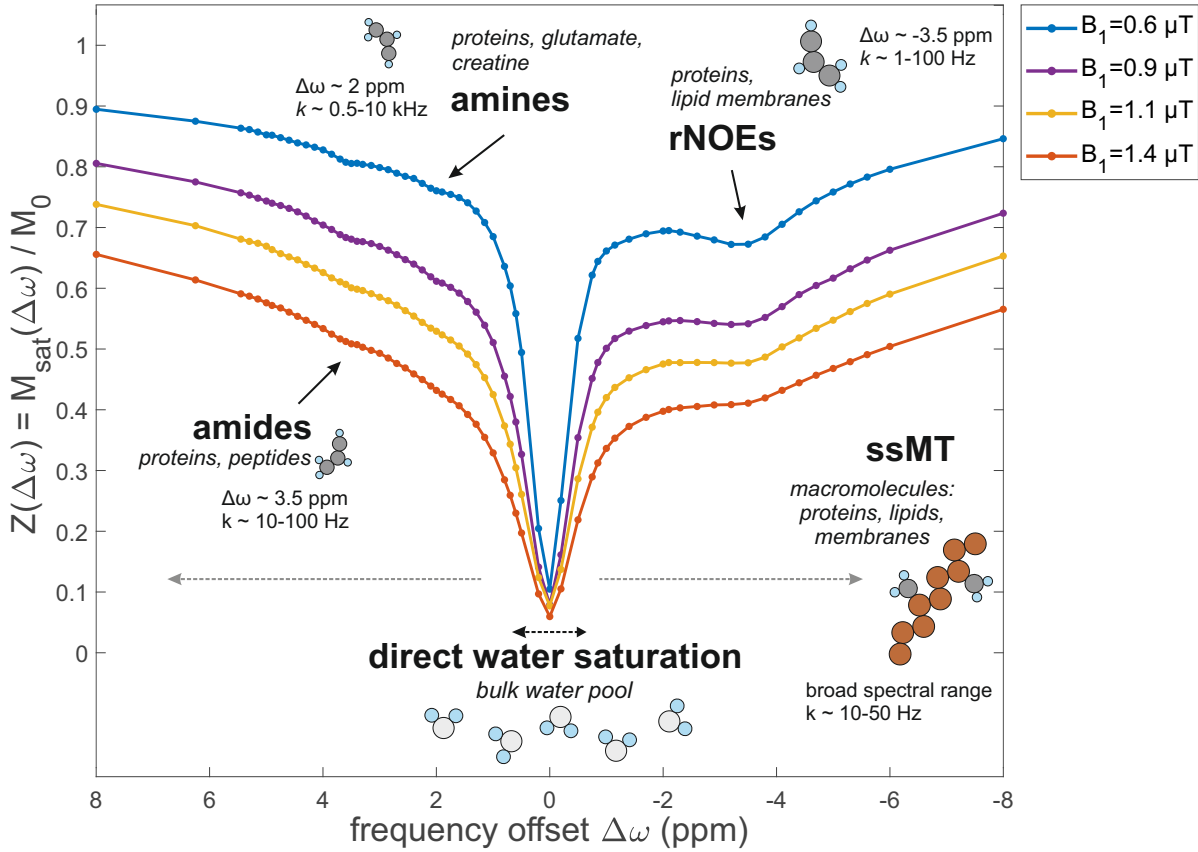
Figure 2.7.: Example of in vivo Z-spectra of the human brain (White Matter (WM)), acquired for different RF saturation amplitudes B_1 at a 9.4 T scanner. The most prominent contributions to saturation transfer observed for in vivo Z-spectra are delineated. Common to all effects is that after applying a train of off-resonant RF pulses, saturation is transferred to the bulk water pool, leading to a detectable reduction of the water signal. Saturation transfer can either happen by chemical exchange, as in the case of amide or amine systems, or by exchange-relayed dipolar cross relaxation as in the case of rNOEs and ssMT. The schematic includes typical values for chemical shifts $\Delta\omega$ and exchange rates k of the respective pools. Figure adapted from [71].

2.3.1. Contributions to the in vivo Z-spectrum in the human brain

Figure 2.7 shows in vivo Z-spectra of the human brain acquired at an UHF MRI scanner ($B_0 = 9.4\,\text{T}$) for several B_1 levels. The main effects contributing to the in vivo Z-spectrum are also shown in the Figure. As living tissue is a complex composition of different structures, compounds and molecules, in vivo Z-spectra exhibit several overlapping contributions. Therefore, it is generally not possible to clearly attribute CEST effects to specific metabolites. Still, through extensive research in model solutions and animal and human studies, certain correlations and signal origins have been identified. In the following, the most relevant effects that are observed in the human brain are briefly described.

Direct Water Saturation   The large signal drop at $0\,\text{ppm}$ is caused by direct water saturation, meaning that the bulk water pool itself is saturated by the RF irradiation. The width of the direct saturation peak increases with shorter T_2, higher RF saturation amplitude B_1 and lower static field B_0 [62].

Semi-solid Magnetization Transfer   The ssMT effect occurs due to protons bound to macromolecules, cell membranes, lipids, and other structures in a semi-solid matrix. Magnetization transfer from such protons to bulk water is caused by combinations of dipolar cross-relaxation pathways [59, 75] and chemical exchange [76, 77]. Due to the restricted mobility of the macromolecular protons, they have short T_2 of less than $1\,\text{ms}$, resulting in broad spectral linewidths. This causes a background contribution in in vivo Z-spectra that is spread across a large spectral range of several kHz.

Amide and Amine CEST   The downfield side of the in vivo Z-spectrum (positive chemical shift) shows CEST effects from several endogenous metabolites originating from exchangeable protons in functional groups such as amides and amines. The Amide Proton Transfer (APT) effect around $3.5\,\text{ppm}$ is widely studied and related to mobile tissue proteins and peptides with exchange rates around $100\,\text{Hz}$ [78]. In addition, there are various contributions from several exchangeable groups in the range of $1 - 6\,\text{ppm}$; for example, amine protons resonating around $\sim 2\,\text{ppm}$, which cause a corresponding amine CEST peak and have much higher exchange rates in the order of kHz. Amide CEST has been shown to provide interesting information in the context of brain tumors. For example, increased effect size in the tumor area has been observed [79], and isolated amide CEST contrast were shown to correlate with gadolinium ring enhancement [72, 80].

Relayed Nuclear Overhauser Effects   Besides chemical exchange of labile protons, Nuclear Overhauser Effect (NOEs) constitute another way of magnetization transfer between neighboring spins mediated by dipolar interactions. For in vivo Z-spectra, the dominant contributions are homo-nuclear (^{1}H–^{1}H) rNOEs between water and aliphatic protons that occur at the upfield side of the spectrum (negative chemical shift) in the range of -2 to $-5\,\text{ppm}$ [81]. For these rNOEs, the saturation is first relayed from

non-exchanging to exchangeable protons through dipolar coupling and is subsequently transferred to the bulk water molecules by chemical exchange [76, 82]. The strength of dipolar interaction is strongly dependent on the spatial distance between the involved protons and thus sensitive to molecular configuration. Consequently, NOEs can provide information about folding state and aggregation of proteins [83–85], which makes them an interesting subject to investigate in the context of neurodegenerative diseases [86].

3. Research Objectives

In the course of this thesis, several novel and unconventional ways to address and optimize aspects of MRI of the human brain are presented.

In the first two included publications, PI is addressed as one of the most successful techniques for reducing the inherently long acquisition times required by MRI. As described in section 2.2.5, conventional PI relies on the spatial sensitivity profiles of different RF receiver coils, which are usually constant in time. In contrast, here it is investigated whether electronically modulated time-varying receive sensitivities can be realized experimentally as a novel degree of freedom in spatial encoding for UHF MRI at 9.4 T and can improve PI, thus offering the potential to further accelerate image acquisition. In the course of this project, suitable acquisition and reconstruction methods as well as reconfigurable receive coil designs are developed and investigated. It is shown that rapid sensitivity modulation during k-space traversal can indeed reduce g-factors and enable lower reconstruction artifacts compared to conventional PI.

As a second topic, the third an fourth publication included in this thesis address contrast generation, particularly in the context of CEST MRI. Conventionally, as described in section 2.3, the extraction of the desired CEST contrasts requires repeated acquisitions while sweeping the frequency of off-resonant saturation pulses to achieve sufficient spectral resolution, which is inevitably time-consuming. The resulting spectra are then usually processed by simple normalization procedures or spectral line fitting. In contrast, here the task of CEST contrast generation is approached by a data-driven linear projection method that uses previously acquired and evaluated data to map directly to the desired contrast in a single and fast computational step, integrating field inhomogeneity compensation. In addition, this method allows for a regularization-based procedure that reduces the number of acquisitions required to map to the target contrast, offering the potential to accelerate CEST MRI acquisitions. This demonstrates that beyond direct human intuition, there is potential room for improvement in conventional MRI methods regarding the design of sequences and contrast extraction schemes for maximum information retrieval in minimum scan time. In line with this notion, in the fourth publication, a novel, experimental method for automated contrast generation is presented that minimizes human interaction to providing a representative object in the scanner, a desired target contrast, and an appropriately parameterized template sequence. The parameters of this sequence are then modified by an optimization algorithm without the necessity to provide a theoretical model of MRI, but in a data-driven manner. For this purpose, a real MR scanner is controlled by the optimization algorithm to perform exploratory acquisitions in order to achieve as good as possible mapping to the desired target contrast. A proof-of-principle for this method is carried out on the example of metabolite concentration mapping in the context of CEST MRI.

4. Publication Summaries

In this chapter, a brief summary of the included publications is given. The figures shown in this chapter are reprinted with permission of John Wiley & Sons (Publications 1–3) and Elsevier Inc. (Publication 4), respectively.

In the first publication, a novel method of improving PI (introduced in section 2.2.5) by exploiting electronically modulated time-varying receive sensitivities is introduced. In the second publication, this concept is extended from 2D to 3D imaging by using reconfigurable dipole antennas instead of loops as receive elements. For the third publication, the issue of inherently long acquisition times for CEST sequences is addressed by a linear parameter quantification method that can reduce the number of required measurements based on prior knowledge of desired target contrasts. The fourth publication demonstrates a framework for model-free, target-driven MR sequence optimization running live on a real scanner system.

4.1. Publication 1

As mentioned before, PI is one of the most successful techniques for accelerating MRI acquisitions. One reason for that is its versatility, as it can be advantageously combined with practically all MR sequences, given that suitable multi-channel receive coils [31] are available. However, higher acceleration factors and partially overlapping coil sensitivities lead to increased ill-conditioning of the reconstruction problem (see section 2.2.5). For linear reconstruction methods like SENSE, this results in noise amplification (as quantified by the g-factor, equation (2.28)) and artifacts [34].

Extensive research has been conducted on ways to improve PI, including the use of advanced, often non-linear algorithms (e.g. [87–89]) and optimized receive hardware with more coil elements [45, 46, 56, 90–92]. Another branch of research has focused on using rapid B_0 modulations to improve the conditioning of the PI reconstruction problem [48, 93, 94]. In all of these methods, the rapid modulations provide additional spatial information, which is complementary to conventional Fourier encoding (section 2.2.4). As a more exotic approach, physically rotating RF coils have been demonstrated to improve PI reconstruction due to an increased effective number of available sensitivity profiles at the different rotational positions of the coil array [95–97]. Inspired by these ideas, the underlying idea of the present work was to explore whether rapid electronic modulations of receive sensitivities (B_1^-) instead of physical rotation can be experimentally realized and utilized to improve PI. In contrast to conventional PI, for which coil sensitivities are static, here the goal was to enable time-varying coil sensitivities as a novel degree of freedom for image encoding.

4. Publication Summaries

The principle employed to dynamically modulate B_1^- is to alter the values of distributed capacitances within a receive coil loop. Conventionally, receive loop coils for UHF MRI contain a set of equal capacitors distributed symmetrically along the loops in order to reduce the electrical length [98] and thus yield a homogeneous current distribution. As described in section 2.2.3.1, according to the principle of reciprocity, the receive sensitivity of a coil, i.e., the induced voltage due to excited nuclear magnetization at a certain location is proportional to the B_1^- field component that the coil would hypothetically produce at the same location when driving it with a unit current. Thus, modulating current distributions within a loop by increasing capacitances in one arm and decreasing it in the other arm leads to distinct spatial sensitivity profiles. This could be confirmed by numerical electromagnetic simulations (Figure 4.1B and Figure 1 of the publication). Importantly, decreasing capacitances evenly on one side of a loop while increasing them on the other side by the same factor ensures a constant resonance frequency.

Preliminary investigations on this concept had been carried out using varactor diodes as adjustable capacitors [99], which allowed for continuous sensitivity modulation. With that, it was found that rapid switching between the two most distinct sensitivity profiles, i.e., highest and lowest possible capacitances, yielded the strongest potential for PI improvement. However, the required switching speed on the order of microseconds could not be realized with varactors.

Because of that, the prototype that was built for the presented work utilized fast switching PIN diodes to form two distinct RSCs. To that end, switchable units were designed that consisted of a PIN diode in series with a $20\,\mathrm{pF}$ capacitor, which were connected in parallel to a smaller $1.5\,\mathrm{pF} - 2.4\,\mathrm{pF}$ capacitor (Figure 4.1A). Depending on whether the PIN diode is being driven in forward or reverse bias, the effective capacitance of such a switchable unit becomes $\sim 22\,\mathrm{pF}$ or $\sim 2.5\,\mathrm{pF}$. Placing four switchable units on each side of a loop allows forming the distinct switchable sensitivity profiles observed in simulation (Figure 4.1B), which could subsequently confirmed in phantom measurements (Figure 4.1C and Figure 4 of the publication). Concurrently, a theoretical framework for describing PI with time-varying sensitivities was established by means of a modified SENSE [34] formulation. By explicitly incorporating a temporal degree of freedom for the coil sensitivities, the encoding operator (c.f. section 2.2.5, equation (2.27)) was formulated as

$$\mathbf{E}_{(\beta,\kappa),\rho} = c_\beta(\vec{r}_\rho, t_\kappa)e^{i\vec{k}_\kappa \cdot \vec{r}_\rho} \tag{4.1}$$

with the sensitivities of the βth coil $c_\beta(\vec{r}_\rho, t_\kappa)$ at location $\vec{r}_\rho$ and time step t_κ, and k-space trajectory $\vec{k}_\kappa = \vec{k}(t_\kappa)$. As detailed in the theory section 2.2.5, this framework allowed obtaining reconstructions for arbitrary k-space trajectories and sensitivity switching patterns. Additionally, g-factors could be calculated according to equation (2.29) for assessing the performance of a certain encoding scheme. To gain intuition of how time-varying sensitivities during gradient encoding, i.e. k-space traversal, affect image reconstruction, a series of numerical experiments with different switching patterns were conducted (Figure 5 of the publication).
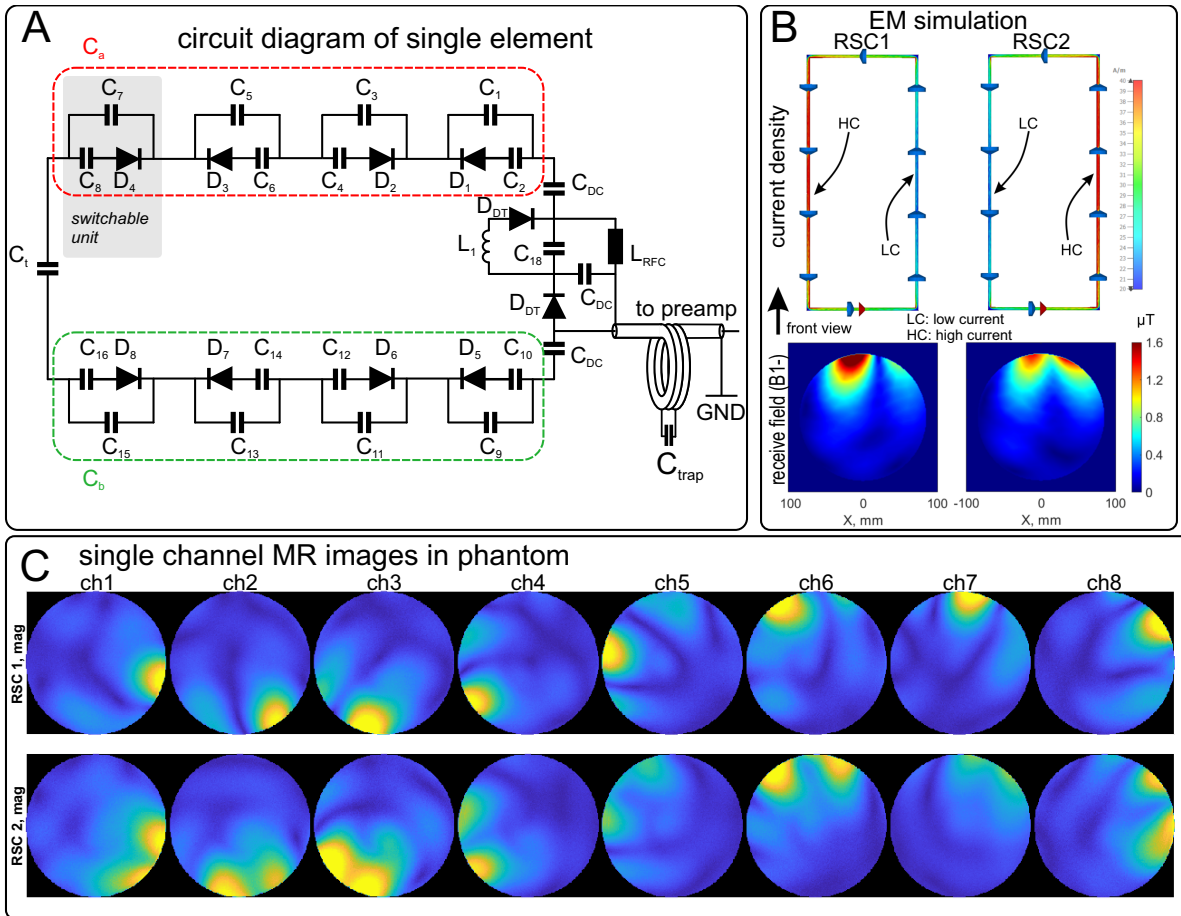
Figure 4.1.: **(A)** Circuit diagram of a single receive loop of the experimental receive array prototype, showing four switchable units, which consist of a PIN diode and two capacitors, on each arm of the loop. Alternating between forward and reverse bias of the PIN diodes yields two distinct B_1^- patterns (RSCs) that can be rapidly switched. **(B)** Surface current distribution in a loop-like coil for two configurations. Left: loop with high current (HC) in the left arm and low current (LC) in the right arm; right: loop coil with HC in the right arm. The resonance frequency of these three configurations remains about identical at 400 MHz. Below: Corresponding simulated sensitivity profiles (B_1^- field) in a central transverse plane (front view). **(C)** Fully sampled single coil images for both RSCs acquired in a homogeneous phantom. Note that additionally to the intensity weighting by the receive sensitivities (B_1^-), transmit inhomogeneity affects the spatial intensity patterns (B_1^+ pattern of CP mode). Modified and reprinted with permission of John Wiley & Sons.
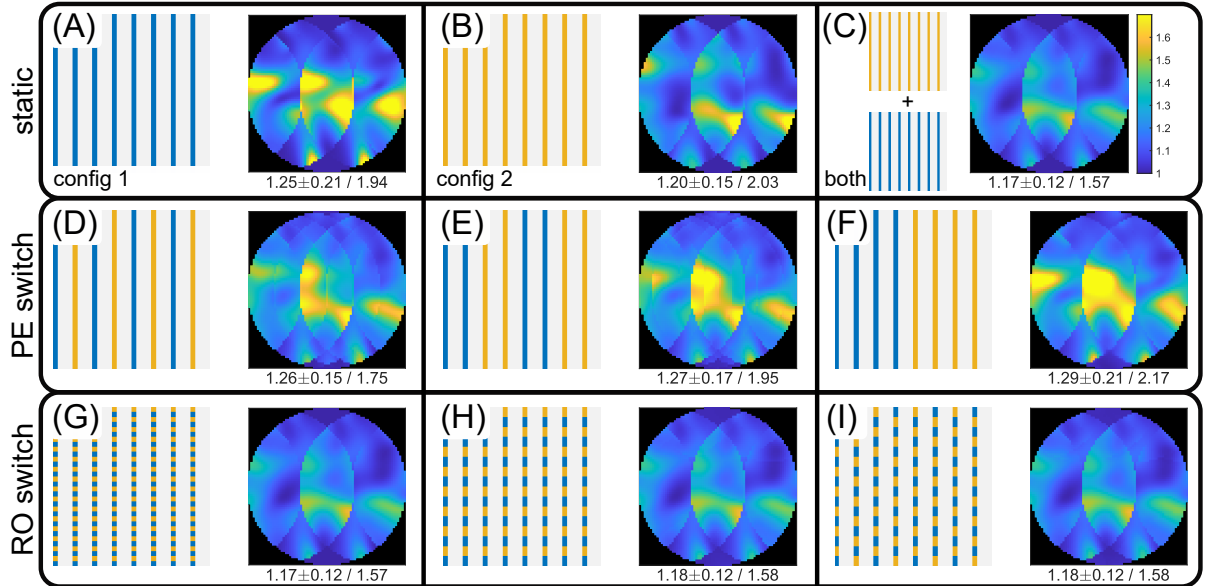
Figure 4.2.: Theoretical g-factor maps according to equation (2.29) for different RSC switching patterns and four-fold acceleration ($R = 4$) with sensitivity maps of both RSCs estimated from the phantom measurement shown in Figure 4.1C. **(A)** Only static RSC1 and **(B)** RSC2. **(C)** Hypothetical case of combining all sensitivity maps from both RSCs to effectively form a 16-element instead of the physical 8-element receive array. **(D)** PE switching for every and **(E)** every two acquired lines, as well as **(F)** switching only once in the center of k-space (similar to partial Fourier imaging for each RSC) yields worse g-factors than the static configurations. In contrast, **(G)** RO switching for every ADC sample, (**H**) for every second ADC sample or (**I**) for every second ADC sample with additional CAIPIRINHA-like shifting of the switching pattern for every second acquired line improves g-factors compared to the static configurations. In case (G), g-factors are identical to case (C), as fast RO switching with oversampling acts as time-division multiplexing of both RSCs. Labels indicate mean ± std / max of g-factor values for the respective maps. Color scales for all maps are identical. Reprinted with permission of John Wiley & Sons.

It was found that switching sensitivities between RF excitations (on the order of TR, millisecond scale), e.g. for every other k-space line along the PE direction did not yield g-factor improvements (Figure 4.2D,E,F) compared to conventional static sensitivities (Figure 4.2A,B). This could be understood from observations regarding the overlapping aliases in image space that are created by both undersampling and sensitivity switching. In contrast, rapid modulation during acquisition of a k-space line along the read direction (on the order of the ADC dwell time, microsecond scale) was found to result in lower g-factors (Figure 4.2G,H,I) than for static PI. As a central finding, switching between every k-space sample of a two-fold oversampled readout yields g-factors identical to the hypothetical case of using all sensitivity profiles of both configurations simultaneously for encoding (Figure 4.2C,G). This can be considered as a form of time-division multiplexing [96]. A theoretical proof of this result is given in Appendix C.2. Due to these insights, fast RO switching was realized experimentally. For that, a procedure was developed based on a strongly oversampled GRE readout to image periodic sensitivity modulations at $1\,\mu s$ time resolution, while switching every $10\,\mu s$ (Figure S1 and Methods section of the publication). When applying this method, it was observed that switching was accompanied by detrimental signal spikes that manifested as a line-shaped pulsating artifact of up to $8\,\mu s$ duration in the images (Figure 3 and S4 of the publication). The artifact could be corrected in post-processing by discarding corrupted data samples, which, however, reduces SNR, as there are less data points available for noise averaging. A better post-processing correction was found in applying robust Principal Component Analysis (PCA) [100, 101], which performs a matrix decomposition into a sparse component, which contains mainly the artifact, and a low-rank component, which contains mainly the desired signal.

While it was observed that robust PCA correction worked remarkably well (Figures S5 and S6 of the publication), it was concluded that a solution on the hardware level would still be favorable. In the mean time since this project was published, such a solution could indeed be found: It was noticed that the digital switching electronics on the Printed Circuit Board (PCB), which was formerly placed near to the receive elements (shown in Figure 2B of the publication), emitted the spurious signals while switching. Consequently, placing the PCB inside a shielded copper box outside of the scanner room and bringing the switching signal to the coil by means of a shielded coaxial cable could be shown to eliminate the switching artifact.

Finally, fast RO switching was applied for an in vivo measurement and retrospectively accelerated PI reconstructions were compared for the cases of conventional static and switched sensitivities (Figure 4.3). Up to an acceleration of $R = 3$, low reconstruction errors with respect to Nyquist-sampled ground truth reconstructions were observed throughout. For acceleration $R = 4$ and above, the conventional static reconstructions showed increasingly strong artifacts, which were less pronounced for the case of switched sensitivities. This could be confirmed by quantitative reconstruction metrics (Figure 9B,C,D of the publication). Similarly, g-factors were lower for the case of switched compared to static sensitivities, where the improvements due to switching were stronger at higher acceleration factors. For $R = 4$, the maximum g-factor for the better of the
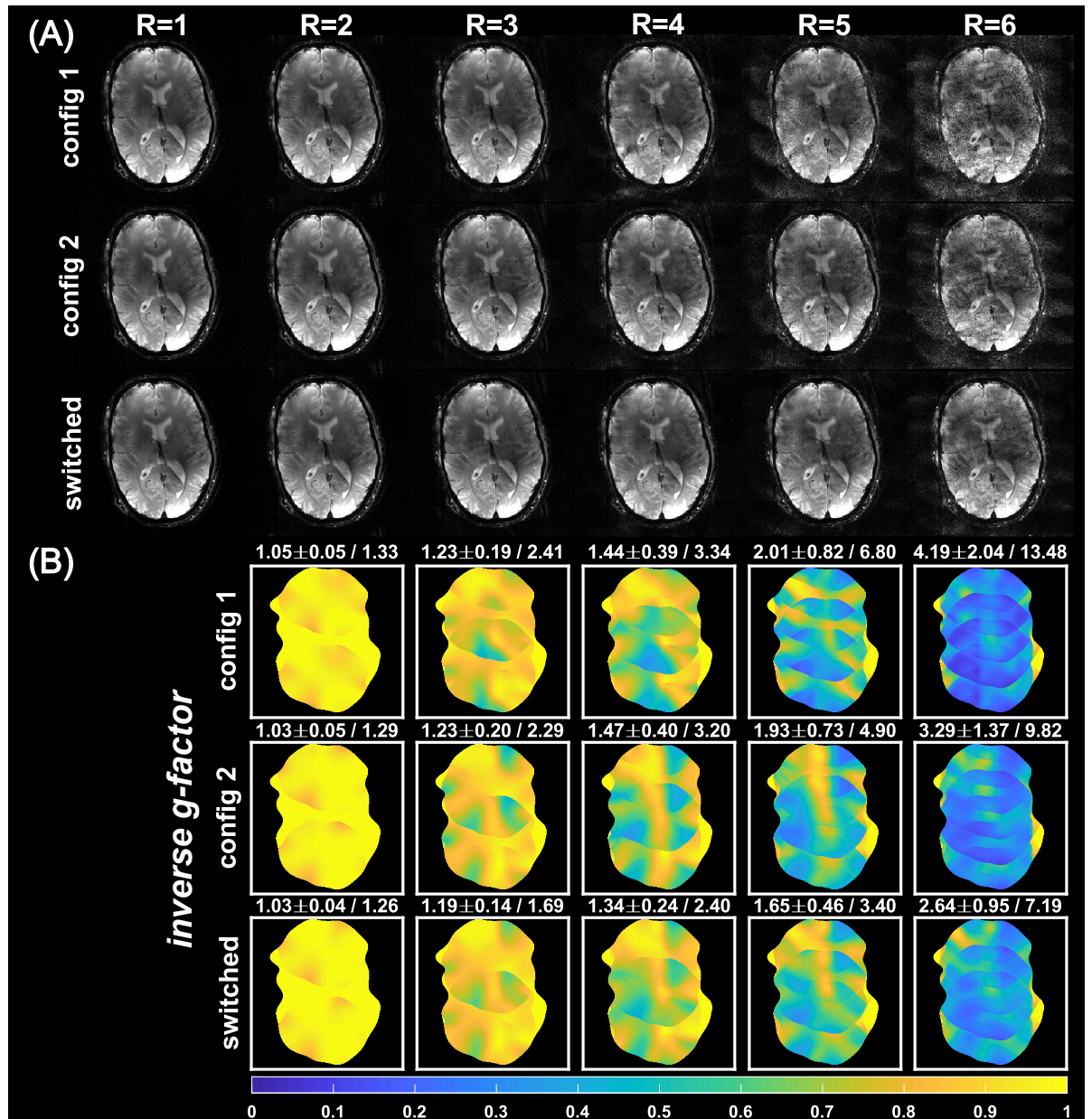
Figure 4.3.: **(A)** In vivo reconstruction results for different retrospectively applied acceleration factors, shown for static RSCs 1 ("config 1") and 2 ("config 2") with 8 sensitivity maps, respectively, as well as for the case of fast RSC switching during k-space acquisition (full RO switching, see Figure 4.2G), which effectively yields 16 multiplexed sensitivity maps. **(B)** Corresponding inverse g-factor maps (i.e., fraction of retained SNR compared to fully sampled, all on the same color scale) obtained according to equation (2.29) for the case of regular Cartesian undersampling and RSC switching. Labels indicate mean ± std / max of g-factor values for the respective maps. Reprinted with permission of John Wiley & Sons.

static cases was 3.2, while it was 2.4 for switched sensitivities, which constitutes an improvement of 25 %.

In conclusion, in the course of the presented project, tailored receive hardware, acquisition and reconstruction techniques were introduced to explore time-varying receive sensitivities as an experimental, novel degree of freedom for image encoding and reconstruction at UHF. For the presented setup, this was shown to offer the potential to improve PI, i.e., to yield lower noise amplification and reconstruction errors compared to conventional static PI.

Statement of Contribution

|	
Felix Glang	Developed and investigated the simulation and reconstruction framework for PI with time-varying sensitivities, set up the sequence, performed the MR measurements, evaluated the data, and wrote most of the manuscript.
Anton V. Nikulin	Built and tested the coil, conducted EM simulations, assisted in the MR measurements, and wrote parts of the manuscript.
Jonas Bause	Study design and performed preliminary experiments.
Rahel Heule	Study design and sequence programming assistance.
Theodor Steffen	Designed, built and tested the switching electronics.
Nikolai Avdievich	Provided assistance in building and testing the coil.
Klaus Scheffler	Conception and study design.
all authors	Proofreading of the manuscript.
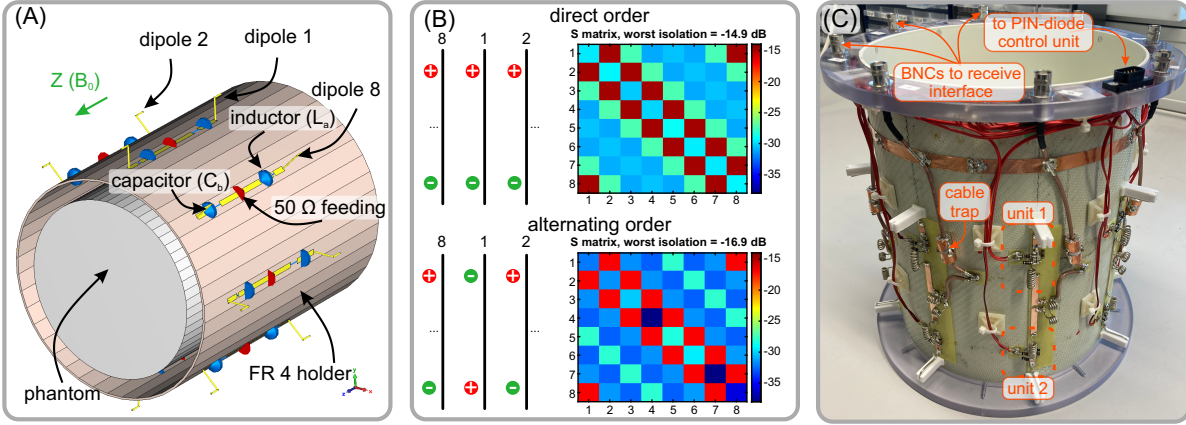
Figure 4.4.: The reconfigurable dipole array. **(A)** Geometry of the 8-element receive dipole array loaded by a homogeneous phantom. **(B)** Two scenarios of dipole driving: In the "direct" scenario, all dipoles are switched in the same manner, i.e. all inductive impedances are active at the bottom or top part of the dipoles, whereas capacitive impedances are active at the opposite part. In the "alternating" scenario, neighboring dipoles are switched alternatingly. **(C)** Photograph of the Rx dipole array coil. Reprinted with permission of John Wiley & Sons.

4.2. Publication 2

In the previous publication (section 4.1), the concept of PI with electronically modulated time-varying B_1^- has been introduced. Improvements of image quality and g-factors compared to conventional PI due to this new method could be observed, but were limited by the still somewhat similar sensitivity profiles of the two RSCs, which only yielded partially independent spatial information. Additionally, the proof-of-concept study focused only on 2D imaging, for which dynamic sensitivity modulation could only be exploited within the imaging plane. Consequently, building on this previous work, the objective of the present project was to extend the concept of time-varying B_1^- to volumetric (3D) imaging. For that, the goal was to enable PI acceleration simultaneously in the transversal plane (i.e., left-right or anterior-posterior direction) and along the z-axis (head-foot direction). This means that undersampling can be performed along both PE directions of a 3D acquisition, enabling for example acceleration patterns like $R_y \times R_z = 2 \times 2$. This is beneficial for many applications, as it allows for greater flexibility than accelerating along only one direction and makes better use of spatial coil sensitivity variations [51]. In order to achieve the required sensitivity variation along the z-axis, a new single-row receive array was conceptualized (Figure 4.4A) and constructed (Figure 4.4C). For that, the formerly used receive loop elements were replaced by 8 reconfigurable receive dipoles.

Dipole antennas have been investigated in various setups for UHF head imaging as transmit-only, receive-only or transceiver elements [102–104], showing the potential for

improved Specific Absorption Rate (SAR) efficiency in case of transmit and central SNR in case of receive, especially when combined with surface loop elements [105, 106]. Here, a novel type of receive dipole element was implemented that, like the reconfigurable loops in the previous work, enables modulation of current distribution and thus B_1^- patterns along the dipole length. To that end, electronically-controlled switchable units were placed in each dipole arm. The units were designed to change their impedance between capacitive and inductive, depending on the state of the contained PIN diodes. Details on this principle are shown in Figure 4.5. By shorting the PIN diodes in one arm (positive bias), the impedance of the switchable unit becomes inductive (Figure 4.5B), which increases the electrical length of this arm. Conversely, the PIN diode in the opposite arm is negatively biased, such that the impedance of the capacitors counteracts the inductive impedance and the total impedance of the switchable unit becomes capacitive, decreasing the electrical length of that arm. As a consequence, the maximum of the corresponding current distribution and thus the region of maximum sensitivity moves closer to the inductive impedance (Figure 4.5C). Alternating between these states again forms two distinct RSCs along the dipole's axis that can be rapidly switched (Figure 4.5C).

As in the previous publication, the proposed reconfigurable dipole array was examined by numerical electromagnetic simulations (Figures 5 and 6 of the publication), as well as phantom (Figure 6 of the publication) and in vivo measurements (Figures 7 and 8 of the publication), especially with regard to g-factor improvement. In particular, numerical simulations showed that switching between the two RSCs allows using PI acceleration factor 2 along the z-axis with acceptable g-factors (maximum 2.08), which is not possible with conventional static, symmetric dipoles as shown in the top part of Figure 4.5A (maximum g-factor 547, Figure 5 of the publication).

Another result from the simulations was that driving the dipoles in so-called "alternating" order (i.e., flipping every second dipole compared to its neighbors) provided lower noise correlation between the elements compared to the "direct" order (Figure 4.4B) and also resulted in slightly lower g-factors (Figure 5C of the publication). Interestingly, for the experimentally realized case of alternating arrangement, 2-fold acceleration along the z-axis is even possible with maximum g-factors below 6 using static only sensitivities, i.e., not switching at all during the acquisition (Figures 6-8 of the publication). At first, this appears surprising given the exploding g-factors (maximum g-factor > 500) for the case of conventional symmetric, non-reconfigurable receive dipoles (Figure 5AB of the publication). The reason for this is that the alternating order of reconfigurable dipole elements breaks the radial symmetry of sensitivity profiles with respect to the central axis of the cylindrical array. For the conventional symmetric dipoles (Figure 5AB of the publication), this symmetry leads to strong ill-conditioning, while for the alternating arrangement of asymmetric sensitivity profiles, there is sufficient sensitivity variation among the elements to support z-acceleration even in the static case. Still, as observed in the previous publication, rapid switching between the two RSCs was found to improve g-factors compared to static sensitivities only (Figure 4.6A), e.g. by a factor of 1.66, 1.65 and 2.2 for the cases of 1×2, 2×2 and 3×2 ($R_y \times R_z$) acceleration with regard to maximum g-factor in vivo, respectively. Similarly, improvements of reconstruction
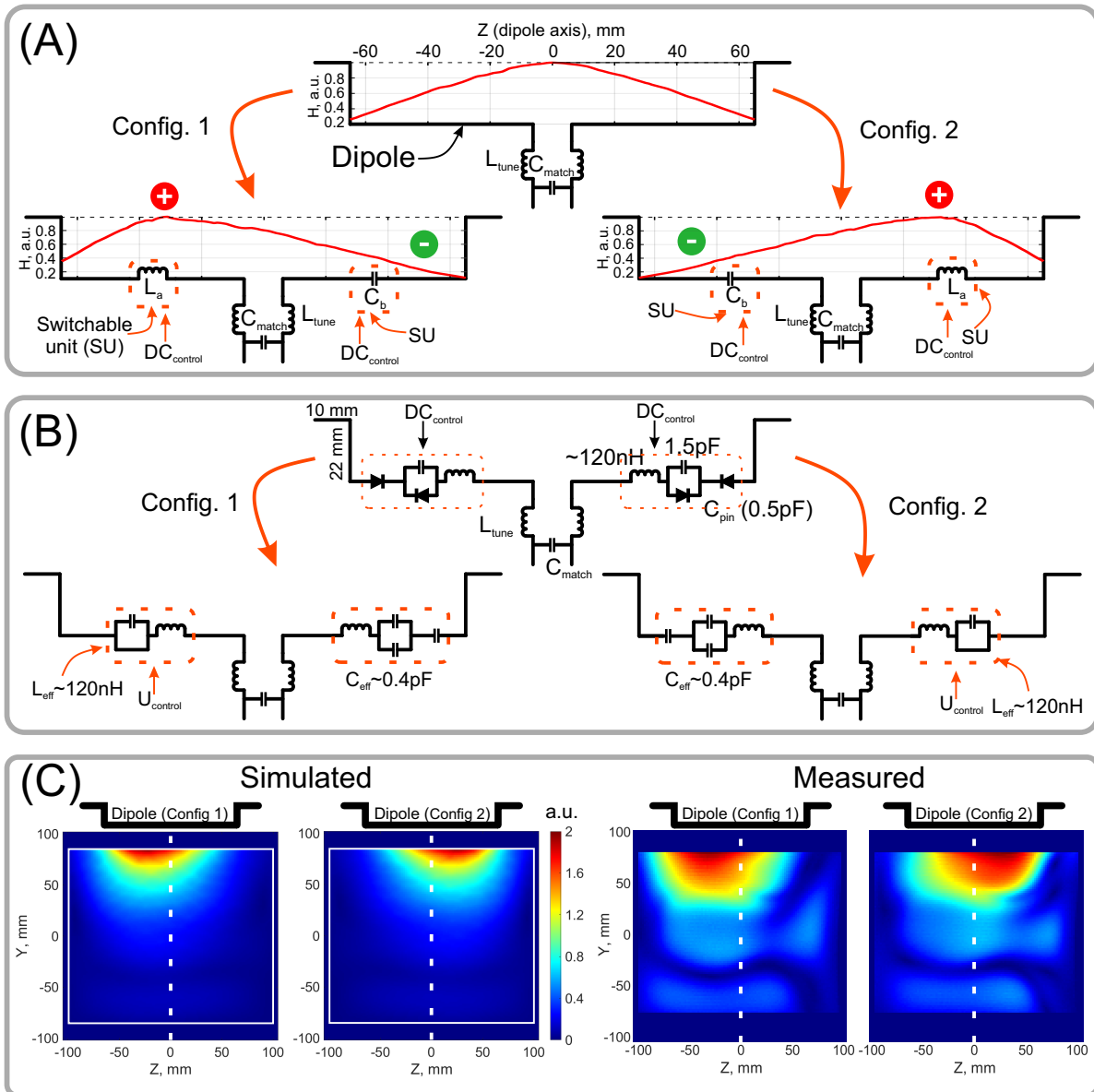
Figure 4.5.: Principle of the reconfigurable dipole antenna. **(A)** Schematic of a single conventional dipole, its symmetric magnetic field distribution H and equivalent schematics of the reconfigurable dipole with modified asymmetric field distribution. **(B)** Schematic of the reconfigurable dipole based on fast switching PIN diodes. PIN diodes allow switching between inductive and capacitive impedances in the two opposite arms as shown by the arrows. **(C)** B_1^- field patterns simulated and experimentally measured for both configurations. Reprinted with permission of John Wiley & Sons.
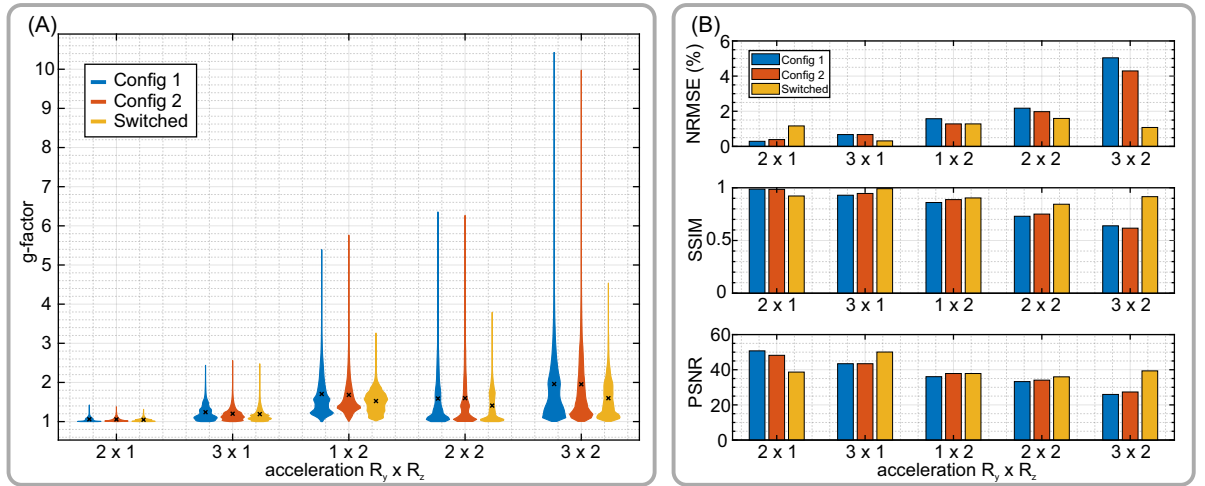
Figure 4.6.: Comparison of in vivo reconstruction results with the reconfigurable dipole array. **(A)** g-factors across the entire acquired brain volume (FOV 220 mm x 220 mm x 120 mm). **(B)** NRMSE (lower is better), SSIM (higher is better) and PSNR (higher is better) of the accelerated 3D SENSE reconstructions with respect to the fully sampled ground truth reconstructions. Reprinted with permission of John Wiley & Sons.

quality metrics with respect to non-PI-accelerated ground truth images (Figure 7A of the publication) were again found for switched compared to static sensitivities (Figure 4.6B). Taking into account the SNR loss not only due to the g-factor, but also due to the reduced acquisition time (factor $\sqrt{R_y \cdot R_z}$), according to equation (2.28), it was found that $R_y \times R_z = 2 \times 2$ acceleration with switched RSCs yields comparable total SNR as in the case of 1×2 acceleration with static sensitivities only. Thus, the g-factor improvements due to switching can ideally allow a 2-fold reduction in scan time with no additional SNR penalty.

In summary, it could be demonstrated that rapid sensitivity modulation along the head-foot direction can be achieved by reconfigurable dipole receive elements. Applying the modulation during image encoding effectively emulates two virtual rows of receive elements instead of the actual physical single row, and thus offers the potential to improve PI performance along this direction. Thus, building on the insights gained in the previous publication, this work forms a next step of exploring time-varying receive sensitivities as a novel, experimental degree of freedom for potentially accelerated MR imaging at UHF.

Statement of Contribution

Anton V. Nikulin*	Conception of the reconfigurable dipoles, built and tested the coil, conducted EM simulations, assisted in the MR measurements, and wrote most of the manuscript.
Felix Glang*	Set up sequence and reconstruction, performed the MR measurements, evaluated simulation and MR data, and wrote parts of the manuscript.
Nikolai Avdievich	Provided assistance in building and testing the coil.
Dario Bosch	Provided assistance in operating the scanner.
Theodor Steffen	Designed, built and tested the switching electronics.
Klaus Scheffler	Conception and study design, wrote parts of the manuscript.
all authors	Proofreading of the manuscript.

---

*A. V. Nikulin and F. Glang contributed equally to this work.

4.3. Publication 3

Despite the promising potential of CEST MRI as an imaging modality that is sensitive to molecular microenvironment, it generally suffers from various problems. The probably most striking one is the inherently long acquisition time due to the typical sequence structure of alternating RF saturation and imaging blocks that need to be repeated for every frequency offset $\Delta\omega$ (see section 2.3, Figure 2.6). Both correction of field inhomogeneities (B_0 and, particularly at UHF, B_1^+) and separation of the convoluted signal contributions usually require sufficiently densely sampled Z-spectra, i.e., a large number of acquired frequency offsets and potentially even multiple B_1 saturation amplitude levels. Depending on the protocol, the duration of the RF saturation blocks can account for more than $80\,\%$ of the total acquisition time [107]. Because of that, solely focusing on accelerating the imaging blocks (e.g. by PI, compressed sensing [108] and similar techniques) has only limited potential for reduction of the overall scan duration. Additionally, performing all the required corrections and contrast extraction steps often requires complex mathematical modeling, which results in time-consuming postprocessing that has to be conducted manually and off-line (i.e., on a separate computer that is not part of the MRI scanner system).

In the presented publication, it was striven to address both the complicated postprocessing and the long acquisition times due to repeated acquisitions of CEST-weighted images by introducing a linear projection-based parameter estimation method. In the spirit of a first-order Taylor expansion, the complicated non-linear mapping function from raw acquired Z-spectral data to contrast parameters of interest (here: Lorentzian fit amplitudes), which involved spline interpolation and non-linear least squares fitting, was approximated by a linear mapping. This process consisted of finding the optimal linear combination of acquired raw images that resemble the desired contrast as closely as possible. Like that, generating CEST contrast can be expressed in analogy to the discrete Fourier transform as projecting the raw acquired spectra onto appropriate weight vectors (Figure 4.7). Finding such weight vector coefficients could be formulated as a linear regression problem. Being a data-driven supervised learning approach, the method makes use of previously acquired and conventionally evaluated data, and generalization to new, unseen data is investigated.

In a second step, employing the so-called 'Least Absolute Shrinkage and Selection Operator (LASSO) regression' approach [109], the linear regression model was extended by L1 regularization, which promotes sparsity of the regression coefficients by exploiting redundancies in the acquired frequency offsets and B_1 amplitude levels. Hence, the target contrasts could be approximated from only a subset of originally acquired CEST-weighted images, where the subset selection was guided by the LASSO regularization. This offers the possibility to completely omit certain repetitions of the CEST sequence and thus a direct reduction of acquisition time.

Data for the study were acquired from six healthy subjects and one patient with a brain tumor (glioblastoma WHO grade IV) at a 7T MRI scanner using a previously established 3D CEST MRI protocol [65, 110, 111]. Conventional contrast generation was performed involving B_0 inhomogeneity correction [112], PCA denoising [113], B_1 inhomogeneity
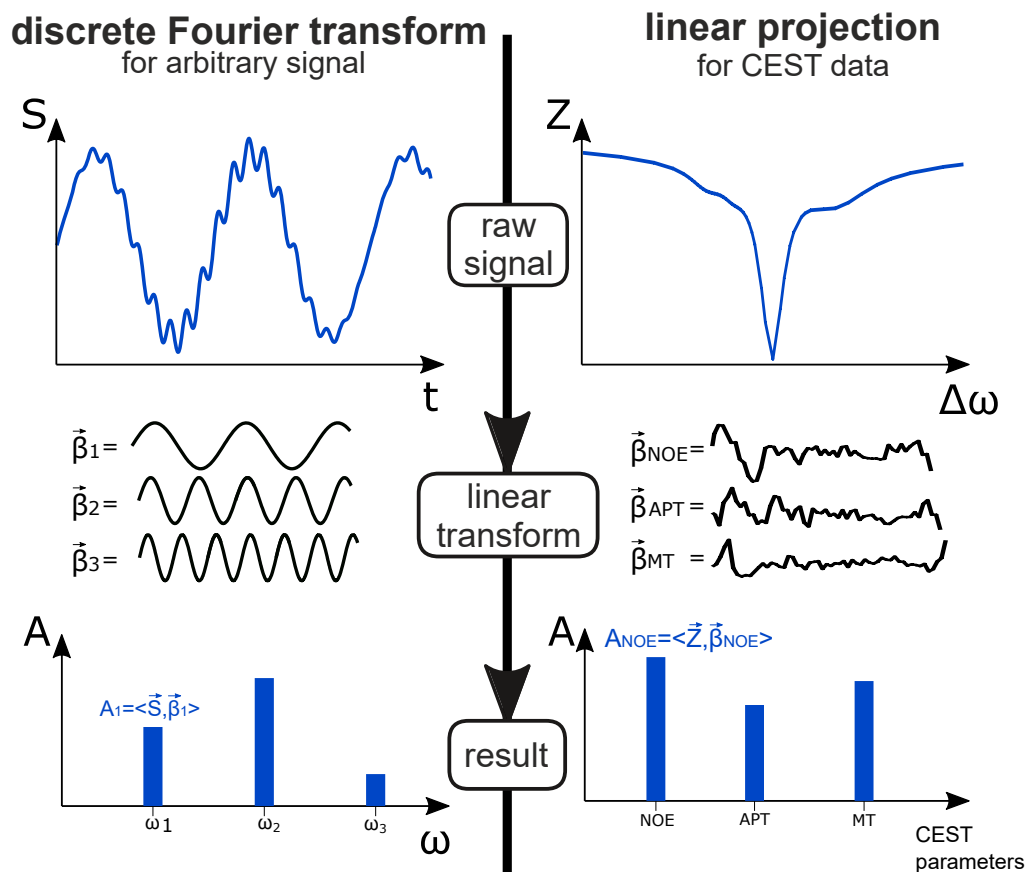
Figure 4.7.: Analogy of discrete Fourier transform and the proposed linear projection approach for CEST evaluation. For the Fourier transform, a signal vector $S(t)$ is projected onto basis vectors $\vec{\beta}_1, ..., \vec{\beta}_n$ consisting of the respective harmonics to yield the Fourier coefficients $A_1, ..., A_n$ for different frequencies. In case of linear CEST evaluation, acquired raw data are projected onto coefficient vectors to yield desired target contrasts like APT, NOE and ssMT amplitudes. The optimal coefficients can be found by linear regression from conventionally evaluated training data. Reprinted with permission of John Wiley & Sons.

correction [66] and non-linear least squares fitting of a five-pool Lorentzian model (water, amide, rNOE, amine and ssMT) [66, 72–74].

As outlined in the Theory section of the publication, the target parameters y, i.e., Lorentzian amplitudes corresponding to each CEST pool as well as off-resonance ΔB_0, were approximated as linear projections of acquired raw data $\mathbf{x}$ onto regression coefficients $\boldsymbol{\beta}$ as $y = \mathbf{x} \cdot \boldsymbol{\beta} + \varepsilon$, taking noise into account as ε. Expressing this for multiple target parameters and input/target pairs leads to the formulation as general linear model $\mathbf{Y} = \mathbf{XB}$ (see section 2.1, equation (2.9)) with input data matrix $\mathbf{X}$, target data matrix $\mathbf{Y}$ and matrix of regression coefficients $\mathbf{B}$. Given a set of known input-target pairs (in the context of supervised learning also called "training data"), the optimal regression coefficients could be obtained by application of the pseudo-inverse as described in section 2.1. For reduction of required measurements (frequency offsets and B_1 amplitude levels) that are needed to map to a multivariate target (i.e., multiple target amplitude parameters simultaneously), direct application of standard LASSO regression (equation (5) in the publication) is not possible, as it only supports a single univariate target parameter at a time. The result would thus be multiple different reduction schemes that are only suited for one particular target parameter, respectively, but not for the others. Instead, a single common reduction scheme that enables prediction of all targets simultaneously is desirable. For achieving that, the row-sparsity-enforcing L2-L1 LASSO ("rowLASSO") [114], which is a special case of the multivariate group LASSO [115], was set up for the given problem, resulting in the optimization problem

$$\hat{\mathbf{B}}_{\text{rowLASSO}} = \arg\min_{\mathbf{B}} \left(||\mathbf{Y} - \mathbf{XB}||_F^2 + \lambda||\mathbf{B}||_{2,1} \right) \ \text{with} \ ||\mathbf{B}||_{2,1} = \sum_{i=1}^{N} \sqrt{\sum_{j=1}^{M} |B_{ij}|^2} \ , \tag{4.2}$$

which could be solved numerically [116]. Depending on the value of the regularization parameter λ, the L2-L1 regularization enforces entire rows of $\mathbf{B}$ to become zero, such that the corresponding inputs do not contribute to the prediction of any target parameter and can thus be completely omitted. Data and code for demonstration of the methods introduced in this work have been made publicly available.[6]

In a first step, generalization of the linear model from training to test data was assessed by obtaining regression coefficients based on the data of five healthy subjects and applying them to a sixth healthy test dataset. It was found that the linear predictions largely agreed with the conventionally evaluated reference contrasts, yielding a NRMSE of 11 %, 4.8 %, 3.9 % and 15 % (for APT, NOE, ssMT and amine amplitudes, respectively) and Root Mean Squared Error (RMSE) of 0.035 ppm for ΔB_0 (Figure 1 of the publication). In contrast to non-linear models like neural networks, the obtained linear regression coefficients are amenable to direct human interpretation as weighting factors for each point in the input spectra that are needed to produce the desired target values. Indeed, physically plausible patterns of the coefficients were found both from real data (Figure 4 of the publication) and in simulations with artificial data (Figures S2-S7 of
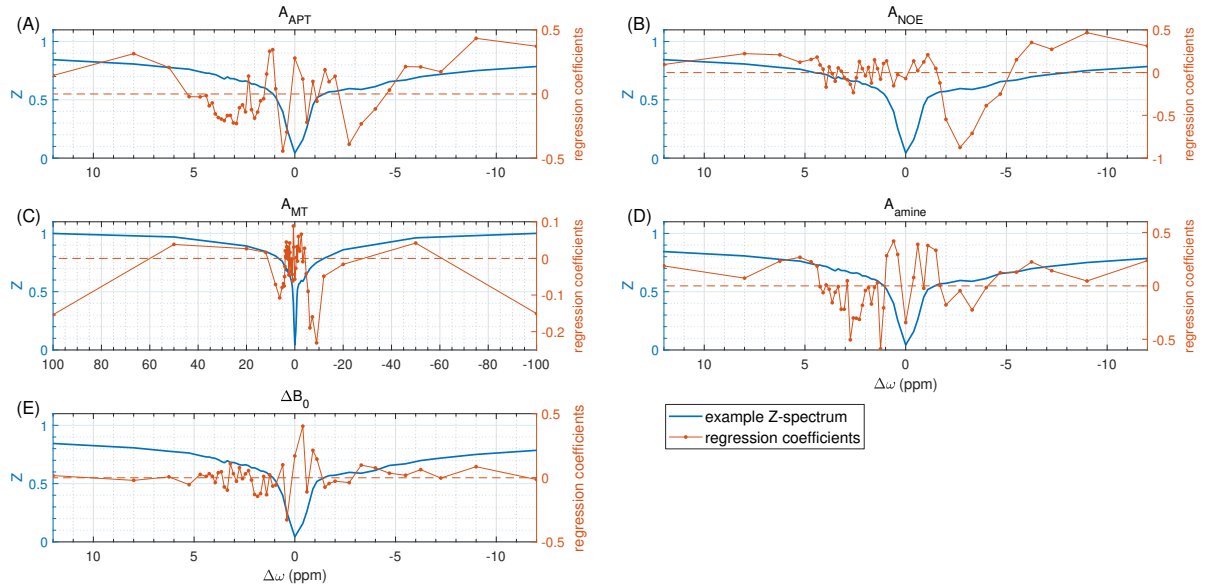
---

[6]`https://github.com/fglang/linearCEST/`

Figure 4.8.: Coefficient vectors (columns of **B**) used to generate linear projection contrast maps of **(A)** APT, **(B)** NOE, **(C)** ssMT, **(D)** amine amplitudes, and **(E)** ΔB_0. Coefficients are plotted here exemplarily for the high-power input data. Coefficients are obtained by linear regression with training data generated from 5 healthy subject measurements. In blue, an example of the corresponding voxel-wise input is given. Contrast parameters in each voxel are then obtained by a simple dot product between input and coefficient vectors. In this example, no LASSO regularization was applied, i.e., the full Z-spectra were used for linear mapping. Modified and reprinted with permission of John Wiley & Sons.

the publication), as they showed strong weightings around the respective CEST resonances (Figure 4.8). The observed oscillatory sign switches of the coefficients could be interpreted as forming weighted combinations of various spectral regions to compensate for concomitant effects.

In a next step, input reduction by the rowLASSO procedure was investigated. By analyzing the performance of increasingly regularized models, i.e. retaining gradually fewer inputs, it was found that the method outperforms randomly subsampled input lists (Figure 5 of the publication). By retaining an optimized list of 39 out of originally 110 inputs (acceleration factor of 2.8), linear projections were still possible with NRMSE= 15 %, 6.7 % and 5.9 % for APT, NOE and ssMT amplitudes and RMSE=0.06 ppm for ΔB_0 (Figure 7 of the publication).

Additionally, the rowLASSO-reduced linear prediction method was compared to conventional Lorentzian fits from regularly undersampled frequency offset lists (Figure 6 of the publication). Undersampled conventional fitting was observed to perform better for moderate acceleration up to factor 2, while for higher acceleration of factor 3,

rowLASSO predicitons of APT, NOE and ssMT amplitudes matched the reference data more closely.

Finally, applicability of the method to pathology was investigated by applying linear models trained on only healthy data to the glioblastoma patient dataset. Overall, the general contrast of the reference parameter maps could still be matched by both full and rowLASSO-reduced (acceleration factor 2.8) linear models (Figure 4.9), especially preserving the clinically interesting APT hyperintensity in the tumor that has been reported previously [79]. Furthermore, the proposed method was tested on a 3T dataset that was used in a previous work for investigating deep learning based CEST data evaluation (deepCEST) [117]. Also in this case, rowLASSO-reduced linear projection (acceleration factor $55/18 \approx 3$) generalized from healthy training data to a glioblastoma test dataset with NRMSE=15 %, 10 % and 9.9 %, and RMSE=0.04 ppm for APT, NOE, and ssMT amplitudes and ΔB_0, respectively. It was found that the deepCEST neural network introduced in this previous study yielded lower NRMSE than the new linear method in all cases, however does not offer input reduction and thus no potential for accelerated acquisition.

In summary, in the course of this project, a data-driven supervised learning-based CEST evaluation technique was established, which employs a linear mapping as fast and interpretable computation step incorporating B_0 and B_1 correction as well as contrast generation. By obtaining regression coefficients from conventionally acquired data, the method generalized from healthy subject training data to unseen test data of both healthy subjects and tumor patients. The introduced rowLASSO regularization enabled a reduction of required measurements, i.e., frequency offsets and B_1 amplitude levels, by a factor of ~ 3. This could potentially be directly translated to a corresponding speed-up of CEST acquisitions. Input reduction was performed only retrospectively in this work, but initial results from prospectively accelerated acquisitions guided by rowLASSO appear promising [118]. In view of the facilitated computations and the potential for accelerated acquisitions, this work might hopefully contribute to the perspective of bringing CEST MRI closer to clinical application.
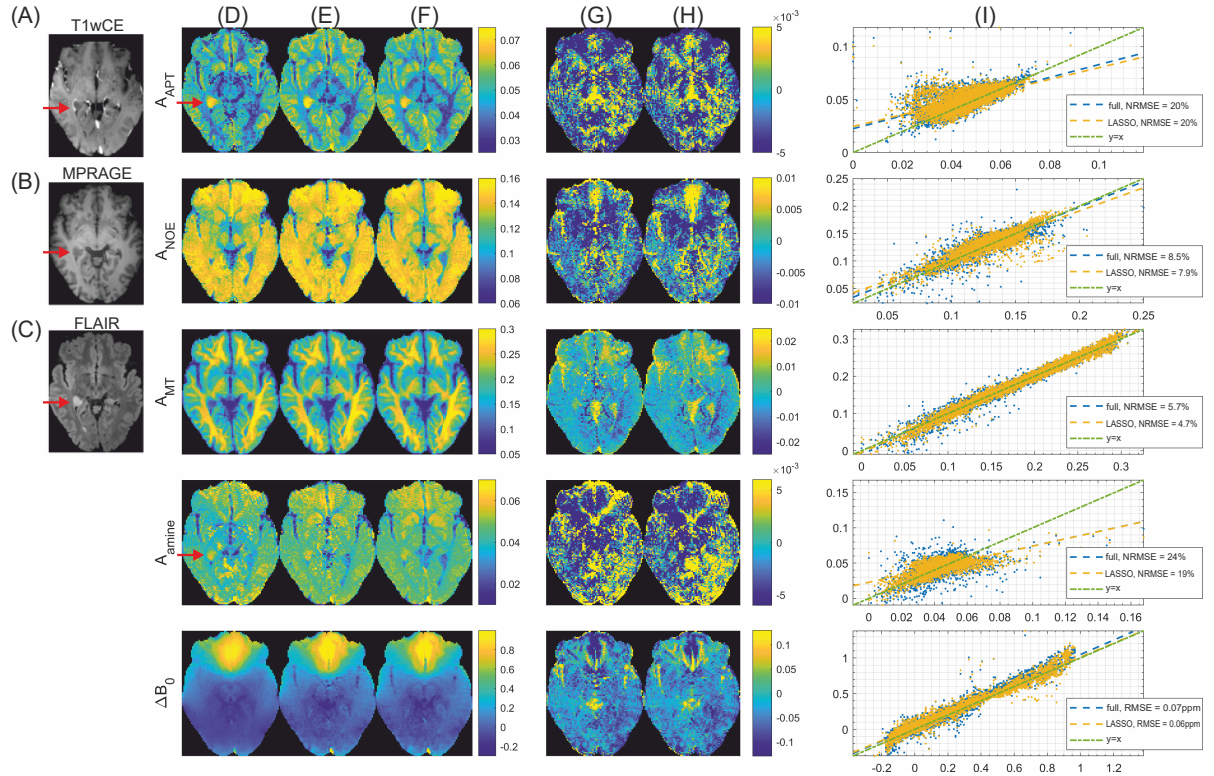
Figure 4.9.: Results of linear projection and LASSO in a tumor patient test dataset. Clinical contrasts: **(A)** T1 weighted contrast-enhanced, **(B)** MPRAGE and **(C)** FLAIR. **(D)** Reference Lorentzian fit results. Red arrows indicates the glioblastoma. **(E**) Contrast maps obtained by linear projection with coefficients obtained from 5 healthy subject datasets. **(F)** LASSO result for 39 retained inputs, corresponding to a reduction factor of $R = 2.8$. **(G,H)** Difference maps to reference for linear projection and LASSO result, respectively. For the amplitude parameters, relative differences to the reference are given in %. **(G)** Voxel-wise scatter plots of linear prediction and LASSO result versus reference with legends indicating NRMSE between predictions and reference. Reprinted with permission of John Wiley & Sons.

Statement of Contribution

Felix Glang	Implemented and investigated the linear projection and LASSO method for CEST MRI, evaluated the data, and wrote most of the manuscript
Moritz S. Fabian	Assisted in the investigation of the method and in the MR measurements, wrote parts of the manuscript.
Alexander German	Recruited subjects and performed MR measurements.
Katrin M. Khakzar	Optimized the conventional evaluation pipeline.
Angelika Mennecke	Performed MR measurements and optimized the conventional evaluation pipeline.
Andrzej Liebert	Optimized the pTx saturation.
Kai Herz	Assisted with sequence programming.
Patrick Liebig	Sequence adaption for 7 T.
Burkhard S. Kasper	Recruitment and design of patient study.
Manuel Schmidt	Recruitment and design of patient study.
Enrique Zuazua	Advice on theoretical backgrounds.
Armin M. Nagel	Study design.
Frederik B. Laun	Study design.
Arnd Dörfler	Recruitment and design of patient study.
Klaus Scheffler	Study design.
Moritz Zaiss	Conception and study design, wrote parts of the manuscript.
all authors	Proofreading of the manuscript.

4.4. Publication 4

The previous publication dealt with CEST, which is one example of the multitude of known MRI contrast mechanisms that can be exploited for addressing questions in a biophysical context. Traditionally, discovery of novel MRI contrasts as well as conventional sequence parameter optimization mostly happened by trial-and-error, potentially involving laborious human interaction with the scanner or appropriate simulations. For the latter, a theoretical description of the underlying MR physics, i.e., a model, is required to capture the targeted contrast effects, for example the Bloch [13] or Bloch-McConnell equations [63]. One recent example for that is the MRzero framework [119], which uses supervised-learning based on a differentiable Bloch simulation to automatically generate sequences that yield a certain desired target contrast "from zero", i.e., not using knowledge of human MRI experts. However, such a theoretical model inevitably requires limiting assumptions, possibly neglecting concomitant effects and imperfections that would occur in reality. Additionally, only parameters within the scope of the chosen model can be investigated or optimized for, which obviously precludes finding truly new contrast mechanisms.

In the present project, a paradigm-shift to these approaches was aimed at by investigating in a model-free way whether a certain target contrast can be generated by MRI. To that end, a real-world MRI optimization framework was implemented, in which a search algorithm repeatedly updates and executes a parametrized sequence directly on a real MR scanner, thus basing the optimization only on automated explorative measurements. The goal was thus to overcome the need for any theoretical model, which is why the framework was named "MR-double-zero". In this way, human interaction is reduced to merely providing appropriate samples, desired target contrast and sequence parametrization.

As a proof-of-principle, to mimic a real discovery, it was pretended that the CEST effect of creatine guanidine protons would be unknown and needs to be "re-discovered" by the proposed framework. The objective was to jointly optimize RF preparation parameters and image post-processing to map to absolute creatine concentration as a target in appropriately prepared sample solutions. To make sure the framework would not just simply exploit known T_1 or T_2 contrasts, which could vary with metabolite concentration, the relaxation times for each sample vial were adjusted to constant in vivo-like values by adding suitable amounts of agar and contrast agent (Figure 3 of the publication) [120]. Moreover, samples were created that contained various concentrations of glucose additionally to the creatine, representing a confounding CEST pool.

The implemented workflow of real-world scanner optimization is illustrated in Figure 4.10. The scanner is controlled by the optimization algorithm that runs on an offline computer (not part of the scanner system). Sequences are defined in Pulseq [121], sent to the scanner via local network and are executed there by a suitable Pulseq interpreter. Acquired data automatically flow back to the offline computer via the local network, get reconstructed and a contrast prediction $\mathbf{P}$ for the current iteration is formed. The deviation (Mean Squared Error (MSE)) between $\mathbf{P}$ and the given target contrast $\mathbf{T}$ (here: known absolute creatine concentration in the sample vials) informs the optimization

$$P = MRI\,(\widehat{seq}) \cdot \widehat{\beta}$$

$$\widehat{\beta} = MRI\,(\widehat{seq})^{+} \cdot T$$

$$MRI\,(\widehat{seq}) = \begin{pmatrix} | & | & | \\ Img1 & Img2 & 1 \\ | & | & | \end{pmatrix}$$
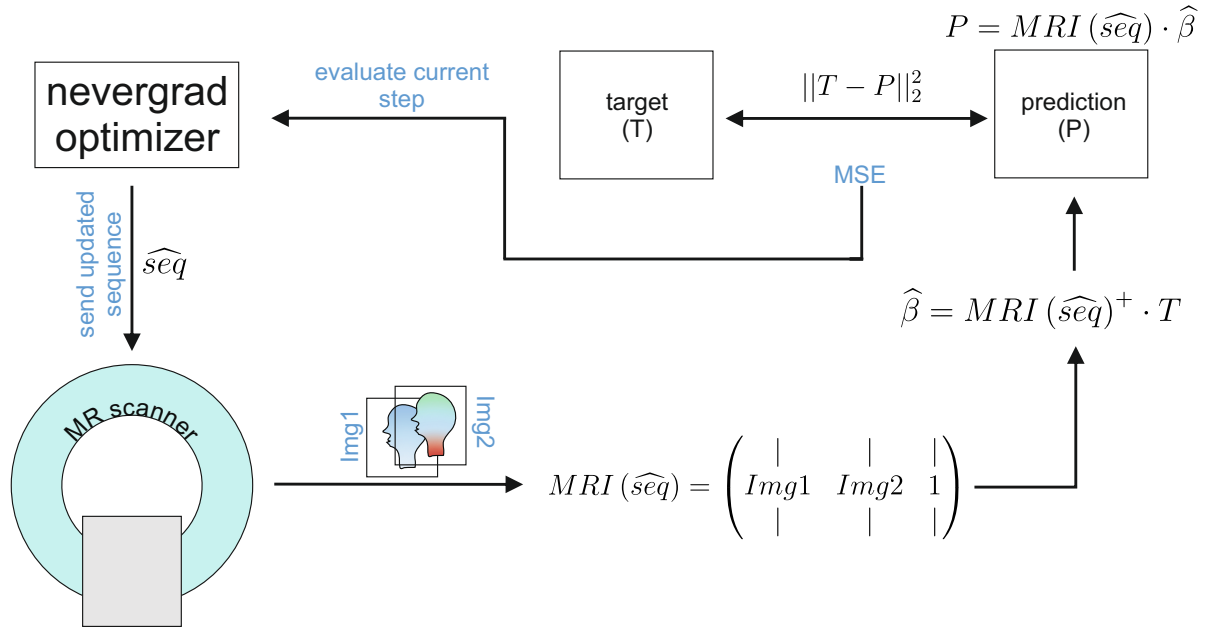
Figure 4.10.: Diagram of the MR-double-zero sequence development workflow. The optimizer sends the parametrized sequence (seq) to a real MR scanner. The acquired data (in the depicted case for $N = 2$ images: $\mathbf{Img}_1$ and $\mathbf{Img}_2$) get flattened into the matrix $\mathbf{MRI}$(seq), which is used to determine coefficients $\hat{\beta}$ from linear regression of $\mathbf{MRI}$(seq) to the target. With these coefficients, the prediction (P) is determined and the deviation from the target ($\mathbf{T}$) flows back to the optimizer. Our pipeline implements this using so called .seq-files of the Pulseq standard [121] that are played out at the scanner by a Pulseq interpreter sequence. Reprinted with permission of Elsevier Inc.

algorithm how to update the sequence for the next iteration. The sequence employed for optimization consisted of multiple (enumerated by $n = 1, \ldots, N$) RF-prepared 2D GRE imaging blocks, with the amplitudes $B_{1,n}$, frequency offsets $\Delta\omega_n$ and number of pulses np_n of the preparation pulse train before each imaging block as free parameters (seq) that can be varied by the optimizer. RF pulse duration, duty cycle as well as imaging parameters were kept constant. With this parametrization, a large range of off-resonant magnetization preparation schemes can be explored. For mapping the acquired data to the target creatine concentration maps, in this work, linear regression (see section 2.1) was employed. After executing the sequence on the scanner, the N reconstructed RF-prepared images $\mathbf{Img}_n(B_{1,n}, \Delta\omega_n, np_n)$ were arranged in a design matrix as $\mathbf{MRI}(\text{seq}) = [\mathbf{Img}_1, \ldots, \mathbf{Img}_N, \mathbf{1}]$ and regression coefficients $\boldsymbol{\beta}$ that map to the target $\mathbf{T}$ were obtained via $\hat{\boldsymbol{\beta}} = \mathbf{MRI}(\text{seq})^+ \cdot \mathbf{T}$. Predicted concentrations based on this regression could subsequently be calculated as $\mathbf{P} = \mathbf{MRI}(\text{seq}) \cdot \hat{\boldsymbol{\beta}}$. Finally, the prediction error $||\mathbf{T} - \mathbf{P}||_2^2$ was passed as objective function value to the optimizer. With this formulation, the optimizer has to find sequence parameters that enable the best possible linear mapping of image intensities to the target. Optionally, to enable a more flexible mapping function, the design matrix could be augmented by appending columns of non-linearly transformed image intensities, e.g. $\mathbf{Img}_n^2, \mathbf{Img}_n^3, \ldots$, forming for example a polynomial regression model, which is still linear in the coefficients $\boldsymbol{\beta}$ (see section 2.1).

As the entire sequence optimization problem involving real acquired data is difficult (non-convex, noisy, potentially ill-conditioned, neither analytical nor stable numerical derivatives available), the CMA-ES algorithm [122] implemented in nevergrad [123] was used, which is known to be suited for this class of problems.

In a first step, the shape of the real world data-based "loss landscape", in which the optimization algorithm needs to operate, was investigated. For that, a reference image with certain parameters seq = $(B_1, \Delta\omega, np)$ was acquired. Next, a series of images was acquired, for which two of the three parameters (e.g. $\Delta\omega$ and np) were kept fixed and the remaining one (e.g. B_1) was linearly stepped in a certain reasonable range. Then, the MSE loss between these images and the reference image was calculated, yielding a 1D cut through the "loss landscape" in the 3D parameter space. From these investigations (Figure 2 of the publication), it could be concluded that the loss function may have multiple local minima, but potentially might be smooth enough to permit successful optimization.

An example of an MR-double-zero optimization result for samples that contained both creatine and glucose is shown in Figure 4.11 and the corresponding loss and parameter evolution (retrospectively sorted according to loss) is displayed in Figure 4.12. The optimization was terminated after 300 iterations, which took $\approx 3\,\text{h}$. Indeed, an RF preparation scheme for $n = 2$ images and corresponding linear regression coefficients were found that enabled an accurate mapping to creatine concentration, even for a test vial that was not included in but masked out during the optimization. The discovered parameters involve one image with saturation close to the expected resonance frequency of creatine guanidine protons ($\Delta\omega \approx 2\,\text{ppm}$ [124]), and the second image with different saturation duration (due to different number of pulses np) and amplitude B_1 on the same side of the water resonance (positive ppm). This concept is different from conventional
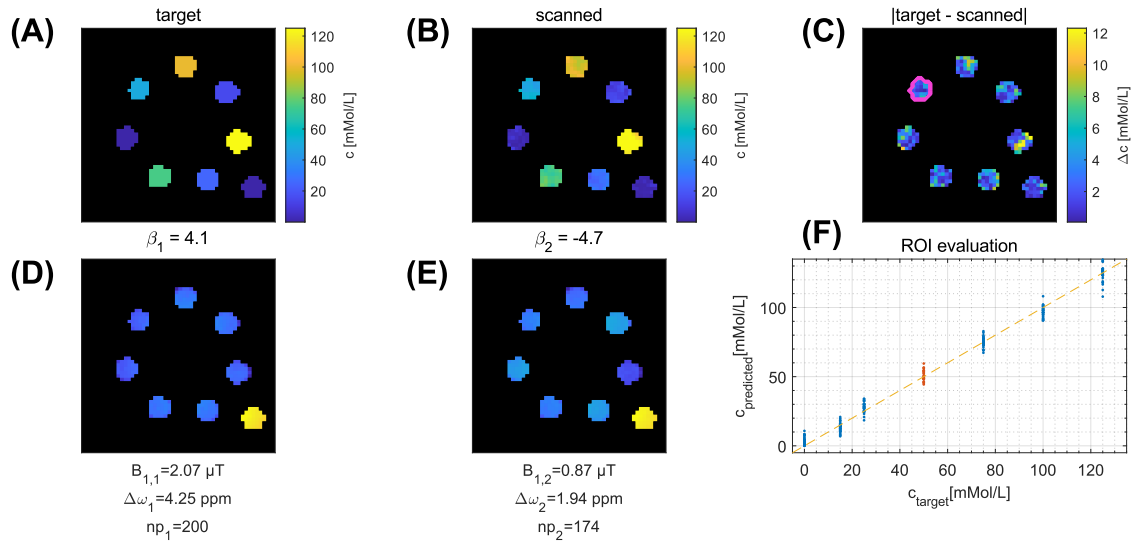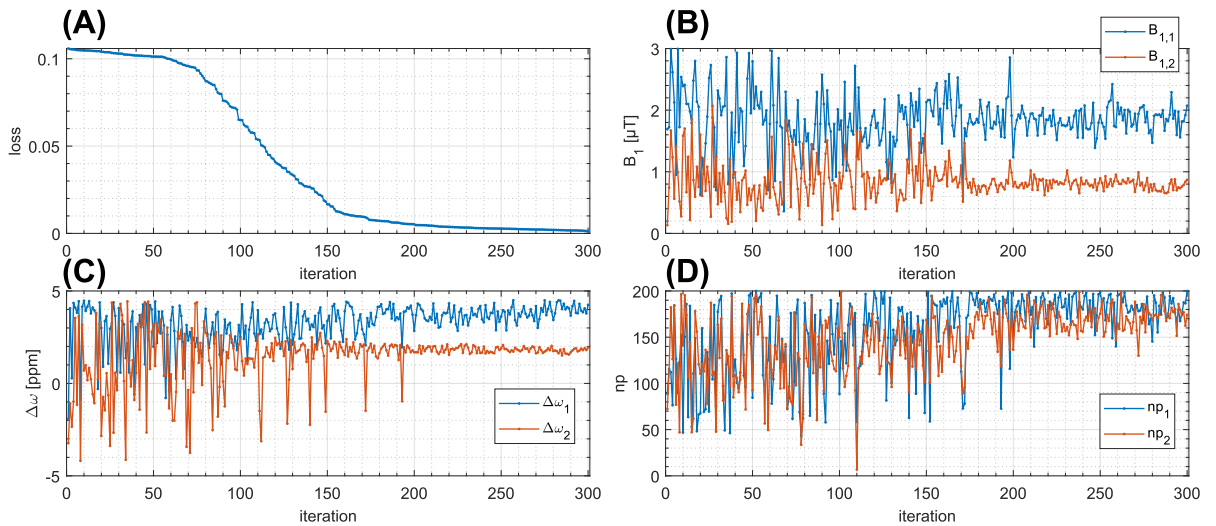
Figure 4.11.: Optimization result of MR-double-zero for samples that contained different levels of glucose concentration as a confounding factor to the targeted creatine mapping. The first row shows: **(A)** the target, **(B)** the experimentally derived and **(C)** the difference in concentrations. Second row shows the two images **(D, E)** with respective sequence parameters given below. In **(F)** the predicted and target data are scattered for ROIs within the different vials. The test vial (50 mMol/L) that was not included in the optimization process is highlighted in (C) and (F). Subscripts 1 and 2 refer to the image number for all parameters. Modified and reprinted with permission of Elsevier Inc.

Figure 4.12.: Optimization process of MR-double-zero for samples that contained different levels of glucose concentration as a confounding factor to the targeted creatine mapping, leading to the results shown in Figure 4.11. **(A)** shows the loss for the explored sequence parameters shown in **(B)**, **(C)** and **(D)**. Iterations were retrospectively sorted by loss instead of the actual time course of acquisition. Subscripts 1 and 2 refer to the image number for all parameters. Modified and reprinted with permission of Elsevier Inc.

asymmetry evaluation for CEST effects (which would here involve measurements at $\Delta\omega = \pm 2\,\text{ppm}$) and seems to enable appropriate labeling and isolation of the desired creatine concentration information independent of the glucose contamination.

Still, for multiple runs of MR-double-zero with the same settings, samples and targets, as well as using non-augmented compared to augmented design matrices (up to cubic polynomial order), different strategies are obtained that yield similar mapping performance (shown in the Supplementary Information of the publication). Some of these closely resembled the traditional asymmetry metric (subtracting two images saturated at opposite sides of the water resonance), whereas others exhibited a less intuitive, seemingly novel saturation scheme. The observation that different solutions are found is likely due to the stochastic nature of the employed CMA-ES algorithm, which results in finding different local minima for different runs. However, as all found strategies yield similar loss, it can be concluded that there exist multiple different options that enable a similarly good extraction of the creatine concentration.

Acquiring $n = 3$ instead of $n = 2$ images as well as using cubic instead of linear regression was both found to yield better performance, i.e., lower loss (Figure 5 and Supplementary Information of the publication). Among these, augmenting the mapping function from linear to cubic regression brought a larger improvement than increasing the number of images per iteration from 2 to 3. As running an optimization with $n = 3$ images takes significantly longer and requires a larger number of free parameters to be optimized (namely 9 instead of 6), the cubic regression with $n = 2$ can be considered superior.

In summary, in the course of this project, a tool for sequence parameter search on a real MR scanner by means of an automatic data flow pipeline and a derivative-free optimization algorithm was implemented, reducing the need for human interaction. For running it, no theoretical model is required; instead, the sought-for effect has to be represented by appropriately prepared samples. As a first proof-of-principle, the framework could be shown to "re-discover" the known CEST effect of creatine by finding a somewhat novel acquisition and linear mapping scheme to isolate and quantify its concentration. To conclude, MR-double-zero has been introduced as an unconventional way of MRI methods development that can already provide some new insights into sequence design and, speculatively, even novel and accelerated discoveries.

Statement of Contribution

Felix Glang*	Study design, performed measurements, set up code for optimization, evaluated data, and wrote the manuscript.
Sebastian Mueller*	Study design, performed measurements, prepared the model solutions, evaluated data, and wrote the manuscript.
Kai Herz	Provided assistance with the Pulseq framework.
Alexander Loktyushin	Provided assistance with the Pulseq framework and scanner interface.
Klaus Scheffler	Study design.
Moritz Zaiss	Study design.
all authors	Proofreading of the manuscript.

---

*S. Mueller and F. Glang contributed equally to this work.

5. Conclusion and Outlook

As a main part of this PhD project, electronically modulated time-varying receive sensitivities were explored as a novel method to improve PI for human MRI at 9.4 T. In Publications 1 (section 4.1) and 2 (section 4.2), prototype coil arrays with reconfigurable loop and dipole elements were demonstrated for this purpose. In addition, suitable switching schemes and reconstruction methods for the novel temporal degree of freedom of the sensitivity profiles were investigated. A key finding was that rapid switching during the acquisition of k-space lines, i.e. on the order of the ADC dwell time in the microsecond range, effectively makes the sensitivity profiles of the different coil configurations virtually simultaneously available for spatial encoding. For a given acceleration factor, this additional spatial information in the SENSE reconstruction was found to result in lower g-factors, i.e., noise amplification and smaller reconstruction artifacts, compared to static sensitivities only. As with conventional static coil arrays, the acceleration performance of reconfigurable coils depends critically on the spatial separation of the sensitivity profiles, both among elements and among switchable configurations. Moving from the receive loops in Publication 1 to the receive dipoles in Publication 2 already represented a certain improvement in the spatial independence of the configurations. Additionally, this opened up the possibility of using 2D PI for 3D acquisitions, including acceleration along the head-foot direction, with only a single row of receive elements, which is impossible with traditional coils. Nevertheless, an important possible future research direction for this method could be to further investigate and optimize different receive element geometries in order to make the switchable sensitivity profiles as distinct as possible.

On the hardware level, the current setup for PI with time-varying sensitivities is highly experimental and far from user-friendly, as it involves additional wiring and electronics. Also, in terms of coil design, driving the PIN diodes in the setups of Publication 1 and 2 requires many Direct Current (DC) wires close to the receive elements. In the case of the reconfigurable dipoles shown in Publication 2, two pairs of wires are required per dipole. This is particularly problematic because dipoles are sensitive to parallel conductors, which severely limits the scalability of the approach to more elements, e.g. arranged in two rows. A possible solution to this problem is to build reconfigurable coaxial dipoles, such that the central conductor of the coaxial line can be used to supply DC to the PIN diodes, which strongly reduces the need for additional wires. Such coaxial dipoles have been implemented, and first promising results for a prototype 8-channel array are shown in [125]. This paves the way for possible future reconfigurable dipole coils with full head coverage, using up to 32 elements (limited by the available number of receive channels of the 9.4 T system) arranged in multiple rows.

5. Conclusion and Outlook

On the reconstruction side, a linear SENSE-type reconstruction has been used up to now, as this could be rather straightforwardly extended to include the temporal degrees of freedom for the coil sensitivities and allowed an accessible evaluation of PI performance in the form of analytically computable g-factors (see section 2.2.5). An extension to self-calibrating PI methods such as GRAPPA [36] or SPIRIT [88] is conceivable, as these tend to be more robust in situations where accurate coil sensitivity maps in image space are difficult to obtain [37]. However, no major qualitative improvements are expected, as these methods are generally subject to the same physical limitations regarding the encoding capability of coil sensitivities as SENSE [126]. Many advanced acquisition and reconstruction techniques beyond classical Cartesian PI still explicitly or implicitly include coil sensitivities, making them possible candidates for investigating whether an extension to time-varying sensitivities enabled by reconfigurable coils might be beneficial. Some options for such possible future approaches are outlined in the following.

The investigations in Publications 1 and 2 all focused on regular Cartesian trajectories, as these are widely used and facilitate PI reconstruction (see section 2.2.5). However, non-Cartesian trajectories like radial and spiral can have several advantageous properties, such as taking full advantage of the maximum possible performance of the gradient hardware for more efficient image encoding, reduced sensitivity to motion, or allowing ultra-short Echo Time (TE) imaging [127]. In addition, it is commonly alleged that non-Cartesian trajectories have beneficial properties with respect to PI [40]. Therefore, a further direction of research is to combine non-Cartesian trajectories with time-varying sensitivities to investigate whether this novel degree of freedom is also useful in this case. One difficulty is that for non-Cartesian trajectories, the PI reconstruction problem must be solved iteratively (see section 2.2.5). For the popular CG SENSE method [42], it is known that image quality and noise amplification strongly depend on the number of iterations[8] [128]. This makes the choice of an appropriate termination criterion crucial when analyzing the performance of non-Cartesian PI. First preliminary work on this idea has been carried out by purely theoretical and retrospective numerical experiments, using previously acquired sensitivity maps from Publication 1. It could be shown that rapid sensitivity modulation has the potential to improve PI for radial and spiral trajectories to a certain degree [129], i.e. to allow earlier convergence of the iterative algorithm and thus reduce noise amplification and reconstruction artifacts. An example of this is shown in Figure 5.1 for radial and spiral trajectories. It was found that radial trajectories may be particularly suitable for being combined with time-varying sensitivities, as they resulted in the earliest convergence of the employed conjugate gradient algorithm and thus the lowest g-factors of all cases considered. This was consistent with the condition numbers of the respective encoding matrices. In addition, radial trajectories seemed to benefit not only from fast switching during readout (i.e., within a spoke, "RO switching", Figure 5.1(A), fourth row), but also from slower switching between spokes ("shot switching", Figure 5.1(A), third row), which is less demanding to implement experimen-

---

[8]In fact, it has been found by numerical investigations that terminating the conjugate gradient algorithm at an early iteration, as commonly done in MRI reconstruction methods, effectively constitutes a non-linear reconstruction method, even though the underlying reconstruction problem is linear.

tally. The observed g-factors below 1 imply a denoising effect of the early terminated conjugate gradient algorithm at the expense of slight image blurring.

As this work is purely theoretical so far, the next and ongoing steps are experimental realization and investigation. This requires a flexible sequence implementation that can handle both non-Cartesian trajectories and the necessary trigger outputs to external hardware to control the sensitivity switching of the coil. Such a sequence could already be implemented in the open Pulseq standard [121]. In addition, corrections for gradient system imperfections and B_0 inhomogeneities may be required, as these are known to degrade image quality in long readout sequences such as spiral, especially at UHF [131].

Extending this direction of investigation of time-varying receive sensitivities, the question arises if they could be combined with 3D non-Cartesian trajectories such as 3D radial [132] or 3D cones [133], or even with freely optimized non-Cartesian trajectories as recently proposed [49, 134–136]. In the course of the present project, free optimization of 2D non-Cartesian trajectories was investigated with the goal of minimizing g-factors for conventional static PI while still complying with the gradient system constraints, i.e. maximum possible amplitude and slew rate [49]. An exemplary result of such an optimized trajectory measured at a 3 T human MRI scanner (Siemens Healthineers) is shown in Figure 5.2.

Building on these attempts, a joint optimization of sensitivity switching patterns and free non-Cartesian trajectories may be an interesting future direction. Even more speculatively, the approach could, at least in theory, be combined with nonlinear gradient imaging such as FRONSAC [93] or Spread MRI [94], thus moving further in the direction of exotic but potentially advantageous spatial encoding techniques. However, apart from foreseeable significant challenges at the hardware level, all these ideas are much more computationally demanding than the cases shown so far, and require careful selection, implementation, and evaluation of reconstruction methods.

Departing from the linear reconstruction theory underlying all the methods discussed so far, the application of compressed sensing in MRI [108, 137] has received much attention. Based on prior knowledge about the statistics of typical imaged objects, such as sparsity in certain transform domains like wavelets, images can be reconstructed from much fewer samples than required by the Nyquist criterion, allowing even higher acceleration factors than conventional PI. A key requirement for a successful application of compressed sensing is incoherence between the encoding matrix and the sparsifying transform matrix, which in the case of MRI can be achieved by random k-space undersampling patterns [108]. However, such highly irregular trajectories require major sequence modifications and are difficult to realize with respect to all three spatial directions [138]. Alternatively, chirp RF pulses have been demonstrated to introduce the required incoherence while allowing to stick to regular Cartesian trajectories [139]. Inspired by that, it could be conjectured that random sensitivity switching during sampling of regular Cartesian trajectories could provide a degree of incoherence that could then be exploited for compressed sensing without the need for major sequence modifications.

An even more recent trend in MRI acceleration, as in virtually every other field, is the application of deep learning [140] methods to reconstruction [141–143]. The currently most popular physics-inspired deep reconstruction networks [144, 145] can be
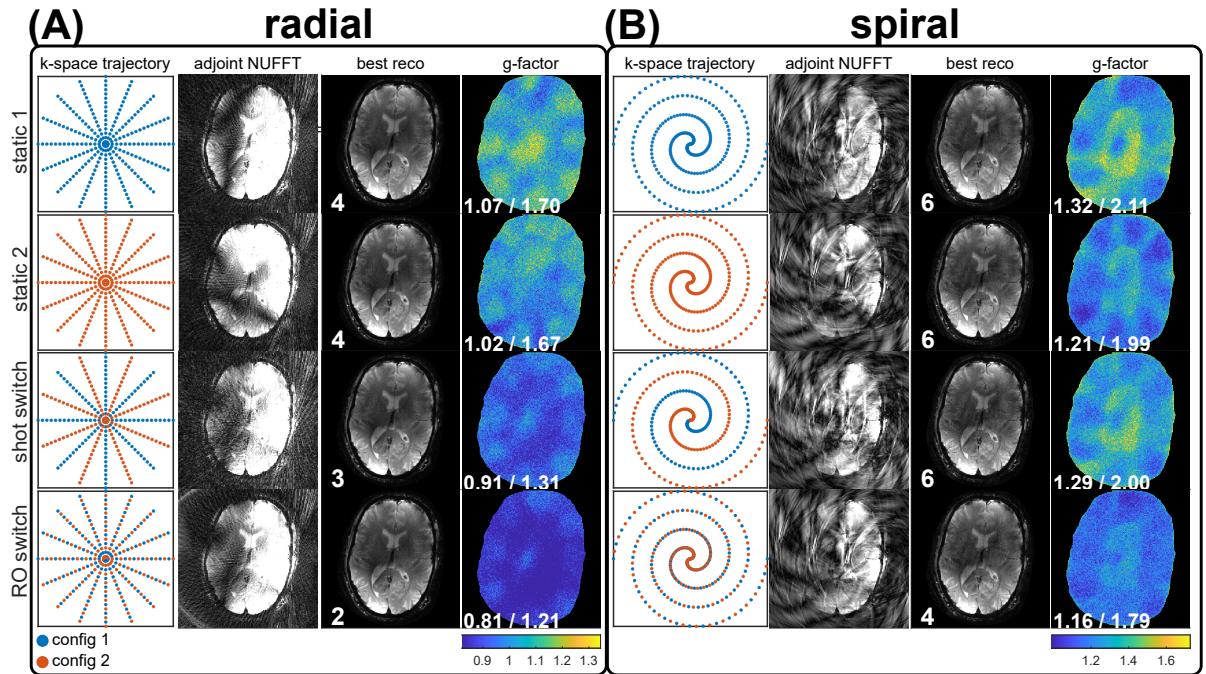
Figure 5.1.: Non-Cartesian PI with time-varying sensitivities: Reconstruction results for accelerated ($R = 4$) **(A)** radial and **(B)** spiral trajectories and different sensitivity switching modes as schematically indicated in the respective first column. Results are shown for static configurations of the reconfigurable coil array in the first two rows, for switching between RF excitations ("shot switch") in the third row, and for rapid switching during readout ("RO switch") in the fourth row. Shown is an adjoint NUFFT reconstruction [130] of a single channel, i.e, no PI applied to demonstrate the aliasing caused by undersampling (second column); the CG SENSE [42] results with the lowest reconstruction error (third column; number of required iterations shown at bottom left); and g-factors for the same iteration (fourth column; numbers indicate mean / max). Figure adapted from [129].

(A) k-space trajectory

(B) final iteration

(C) Cartesian Nyquist

(D) g-factor

mean=1.94, max=2.87

(E) difference

NRMSE = 11.17 %
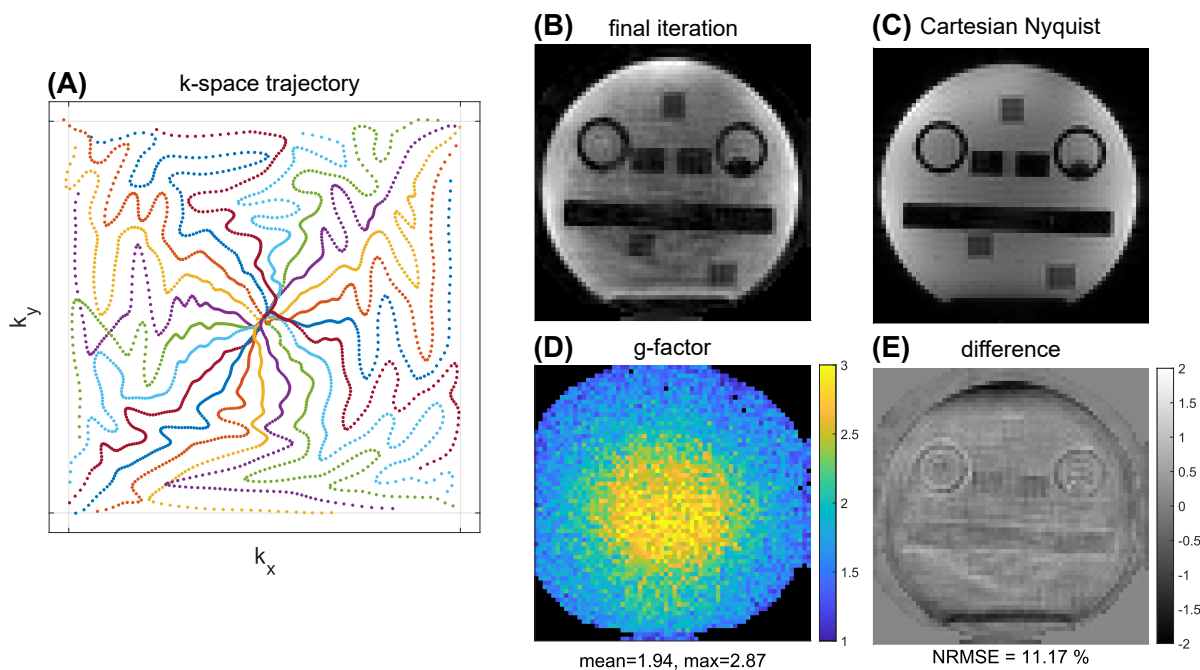
Figure 5.2.: Optimization of free non-Cartesian 2D k-space trajectories. The design method is based on MRzero [119], i.e., a gradient descent-like numerical optimization on a differentiable Bloch simulation that was extended by a PI-capable CG SENSE [42] reconstruction. The objective function was set up to find a trajectory that enables accurate reconstruction close to a Nyquist-sampled reference reconstruction, while yielding low g-factors and respecting gradient hardware constraints. Shown are **(A)** the obtained trajectory, **(B)** the resulting reconstructed image compared to **(C)** a Cartesian Nyquist-sampled reference reconstruction, as well as **(D)** the g-factor map for the free trajectory and **(E)** the difference map of (B) and (C). All data shown were acquired at a 3 T human MRI scanner. Figure adapted from [49].

seen as a generalization of compressed sensing, where instead of predefined regularization terms such as wavelets or total variation, a data-driven regularization is learned based on the statistics of a given training dataset. Such approaches have led to superior image quality at impressive acceleration factors [146]. Since these methods generally still rely on a SENSE-type encoding matrix as a backbone, incorporating time-varying receive sensitivities into such networks is in principle possible and an interesting step for further investigation. However, there is growing evidence that deep learning reconstruction methods may suffer rather from the necessarily limited coverage of their training data, i.e. the different structures seen during training and application of the networks [147, 148], than from the limited spatial information content of the coil sensitivities. An indication of this is the observation that deep reconstruction networks can reconstruct images for acceleration factors much higher than the number of coils, which is impossible with classical linear PI [146]. This is made possible by the strong reliance on prior knowledge about typical image structures introduced by the training data. In the worst case, this reliance can lead to severe instabilities [149] and so-called hallucinations [150], where e.g. pathological structures may erroneously disappear in the output images [151]. Consequently, for such highly complicated and non-linear methods, it is questionable whether reconfigurable coils can significantly contribute to alleviate their major limitations.

In terms of future plans for coil design, the reconfigurable coil arrays built so far as proof-of-principle have 8 elements, whereas typical state-of-the-art head coils for MRI at 7 T or higher have 32 [90], 64 [152] or even 128 [153] elements. However, when increasing the number of reconfigurable elements, the results of the ultimate intrinsic SNR theory [154] should be considered. According to this, it has been shown in the context of PI that adding more and more receive channels cannot reduce g-factors below a certain threshold, the "ultimate intrinsic g-factor" [155, 156]. The reason is that the spatial appearance of coil sensitivity profiles is governed by electrodynamics, specifically the RF wavelength, which depends inversely on B_0. Since this determines the length scale on which the sensitivity profiles can vary in space, adding more receive elements beyond a certain number only provides redundant information and thus can no longer contribute to spatial encoding. Consequently, for larger numbers of reconfigurable receive elements, the relative benefit of switching between configurations is expected to become smaller as the ultimate g-factor limit is approached. Nevertheless, reconfigurable coils may open up interesting possibilities for approaching the ultimate SNR with as few elements as possible, given the limited number of available ADC channels. A related insight from the theory of ultimate intrinsic SNR is that the achievable PI acceleration, allowing for feasible g-factors, grows with B_0 as the RF wavelength decreases, and coil sensitivity profiles show distinct spatial patterns that characterize the onset of wave behavior, deviating from near-field behavior at lower B_0 [157]. Since the formation of distinct sensitivity configurations of the reconfigurable coils relies on such wavelength effects at 9.4 T, it was found in simulations that the approach does not work for human head imaging at 3 T, where the configurations would be virtually identical. Here, it may be a speculative idea to investigate larger reconfigurable elements for body imaging, where the ratio of wavelength to object size may approach a regime where sufficient sensitivity

modulation may be achievable. At 7 T, simulations for human head geometry showed a promising degree of modulation, so the approach could in principle be translated to this field strength, which is gaining increasing clinical relevance [158].

Finally, leaving the realm of PI, there are first considerations to use reconfigurable dipole antennas not for MR signal reception, but for RF transmission, i.e. exciting magnetization. In this context, so-called Parallel Transmission (pTx) systems with multiple independent transmit channels and coil elements are used, especially at UHF to mitigate the inherent B_1^+ inhomogeneities [159–161]. Interestingly, certain formulations of pTx pulse design to achieve a desired spatial pattern of excited magnetization have a strong mathematical similarity to SENSE when B_1^- and B_1^+ are interchanged [162]. For example, ill-conditioning due to spatially overlapping B_1^+ patterns in pulse design leads to amplified RF pulse amplitudes and thus undesirably high SAR, analogous to the amplification of noise in SENSE reconstructions. This even makes it possible to formulate a "pTx g-factor" [163] that quantifies the SAR amplification due to the limited number and spatial independence of B_1^+ patterns. Consequently, it is hoped that, analogous to the observations made in publications 1 and 2, rapid switching of reconfigurable transmit elements could effectively emulate a larger number of virtual transmit elements and thus allow for lower SAR caused by designed pTx pulses. This would be particularly desirable given the high cost of the RF power amplifiers required to increase the number of transmit channels.

In Publication 3, a data-driven linear projection-based evaluation method for multiparametric CEST MRI was proposed that includes correction of B_0 and B_1^+ inhomogeneities as well as contrast generation in a simple and fast computation step. Both the generation and application of the linear regression coefficients are fast (fractions of a second) compared to conventional evaluation (several minutes) or neural network training (several hours). Therefore, the method may be promising for fast online computations running directly on the scanner system.

The presented linear model can be considered as the simplest possible supervised learning-based regression method, which has the advantage of direct interpretability and straightforward inclusion of sparsity-promoting regularizations such as LASSO. Reducing the number of required frequency offsets of a CEST protocol, as enabled by the LASSO method, may be considered the most promising and effective CEST acceleration method, since the RF saturation phase typically accounts for a significant fraction of the total sequence duration. For this reason, accelerating only the image encoding part of a CEST sequence, e.g. by a factor of two, does not directly translate into a twofold acceleration of the entire sequence, since the RF saturation blocks still have to be executed for each readout. Such imaging acceleration methods for CEST MRI have been proposed in various works using parallel imaging [65, 74, 164], keyhole imaging techniques [165], fast readouts like EPI [107, 166], compressed sensing [167–169], or sparsity exploiting methods [170]. In contrast, reducing the required frequency offsets by a factor of two directly halves the total scan time. For even stronger acceleration, both offset reduction and accelerated readouts as mentioned above could in principle be combined synergistically. However, since the omission of offsets in Publication 3 was performed retrospectively, i.e., by removing data points from a more densely sampled Z-spectrum

acquisition in post-processing, further investigations and validation studies are required on prospectively reduced offset lists. This would ideally involve applying the method also in different pathologies, in order to assess the robustness and generalization capability of the method in more realistic settings.

The linear regression used in Publication 3 can be seen as a baseline model in the context of emerging data-driven methods in the field of CEST MRI against which more sophisticated non-linear models can be compared. For example, neural networks have been used to map from $3\,\mathrm{T}$ Z-spectra to contrast parameters obtained at $9.4\,\mathrm{T}$ [171] and to accelerate contrast generation at $3\,\mathrm{T}$ [117] or $7\,\mathrm{T}$ [172], the latter of which has also been explicitly compared to the proposed linear model. Despite the advantages of the linear model, such as intrinsic interpretability and straightforward incorporation of input feature reduction via LASSO, it unsurprisingly shows lower prediction accuracy compared to more complicated non-linear models such as neural networks. Consequently, investigations on combining similar feature reduction approaches with neural networks as in [117, 171, 172] is an interesting future research direction. The simplest attempt would be to simply train a neural network on input Z-spectral data previously reduced by a linear LASSO procedure as in Publication 3, mapping to contrast parameters generated from the original full data. Such an approach is not guaranteed to yield a reduced offset list that is optimal for the neural network, which may be able to extract more or at least different types of correlations among the retained Z-spectral points. Nevertheless, first experiments with this approach have shown encouraging results. Alternatively, input feature reduction, e.g. by appropriate regularization such as L1-L2, could be directly incorporated into the neural network training procedure. However, training such a network is a much more difficult, i.e. non-convex and locally non-differentiable, optimization problem than solving the linear LASSO objective (equation (4.2)), and has been found to lead to severe convergence problems. Still, various approaches to overcome such problems and to integrate feature reduction in neural networks have been proposed in the literature [173–178] and offer an interesting direction to explore in future work. Given the plethora of published methods in the field of machine learning, there is plenty of room for continued exploration of different methods in the context of CEST MRI to find optimal and parsimonious ways to acquire only the minimum data required to obtain the desired information. An example of such an ongoing approach, building on the linear LASSO method presented in Publication 3, is "comprehenCEST" [179, 180], where the idea is to concurrently analyze data from a large number of reported CEST protocols. The goal is then to find a comprehensive but sparsely sampled and thus feasibly fast protocol that covers the most insightful CEST labeling and allows the design of hypothesis generating clinical pilot studies. In this context, exploring variational autoencoders[9] [182], which are a popular method in the field of machine learning, for CEST data might be an interesting future option with the hope of finding insightful latent space representations of relevant contrast information.

As a common feature of the four Publications included in this thesis, all presented methods rely on linear models (see section 2.1). In the case of PI with time-varying

---

[9]or their disentangled modification [181]

sensitivities, as investigated in Publications 1 and 2, linear reconstruction (see section 2.2.4) allows a closed-form analytical assessment of the reconstruction quality, i.e., g-factors and SNR, on which these works rely heavily. As discussed above, this is not the case for more complicated methods such as compressed sensing and deep learning, where the non-linearity and required iterative procedures impede a meaningful comparison of reconstruction methods and results. The g-factor has been introduced in section 2.2.5 as a measure of voxel variance, which can be seen as a measure of uncertainty in the reconstructed images. Uncertainty quantification, i.e. a probabilistic way to assess the trustworthiness of a prediction (which may be a reconstructed image or a CEST parameter), is a highly relevant topic especially in the context of medical imaging [183]. As an active area of research, such a probabilistic extension to enable uncertainty quantification has recently been demonstrated in neural networks for CEST MRI [117, 172]. In contrast, for the linear models used in Publication 3 for CEST MRI, uncertainty quantification is readily possible based on the analytical expression for the covariance matrix of the regression parameters (equation (2.6)): Suppose the prediction y_0 of the linear model for an input vector $\mathbf{x}_0$ is $y_0 = \mathbf{x}_0^T \hat{\boldsymbol{\beta}}$ with the least squares estimate of the regression coefficients $\hat{\boldsymbol{\beta}}$ as in equation (2.5). The variance of this prediction is $\mathrm{cov}(y_0) = \mathrm{cov}(\mathbf{x}_0^T \hat{\boldsymbol{\beta}}) = \mathbf{x}_0^T \mathrm{cov}(\hat{\boldsymbol{\beta}}) \mathbf{x}_0 \stackrel{(2.6)}{=} \sigma^2 \mathbf{x}_0^T (\mathbf{X}^T \mathbf{X})^{-1} \mathbf{x}_0$, using basic properties of the covariance matrix. The true noise variance σ^2 is unknown, but can be estimated from the regression residuals as $s^2 = ||\mathbf{y} - \mathbf{X}\hat{\boldsymbol{\beta}}||_2^2 / (n-k-1)$, so that the prediction uncertainty becomes [2]

$$\hat{\sigma}_{y_0} = s\sqrt{\mathbf{x}_0^T (\mathbf{X}^T \mathbf{X})^{-1} \mathbf{x}_0}. \tag{5.1}$$

An example of using this expression in CEST MRI is shown in Figure 5.3 and compared to the deepCEST [117] neural network approach. For demonstration purposes, in this Figure a simulated implant-like B_0 perturbation in the form of a magnetic dipole field has been applied to the input Z-spectra of a glioblastoma patient dataset, effectively shifting them along the frequency axis. When this B_0 shift exceeds the range of shifts seen in the training data, predictions become erroneous (Figure 5.3(E,F)). However, for both the neural network and the linear model, increased uncertainties in the corresponding regions of strong B_0 perturbation indicate a loss of confidence in these predictions (Figure 5.3(G,H)), making it possible to detect potential failure due to corrupted data in the absence of ground truth data. In this case, as well as in other tentative experiments, the uncertainties of the linear model obtained in this way have shown a remarkable similarity to the uncertainties of the neural network. Further analysis of the potential of such linear covariance matrix-based approaches for uncertainty quantification in comparison or synergy with neural networks may be of interest for future investigations.

Linear regression was also used in Publication 4, where it mapped the acquired data to the defined target contrast at each iteration during MR-double-zero optimization. In general, any mapping function from acquired data to target could be used in this framework (e.g. non-linear regression models, neural networks etc.), forming a joint optimization of data acquisition and post-processing. Still, the linear regression with optional polynomial augmentation used here was found to be suitable as a first attempt
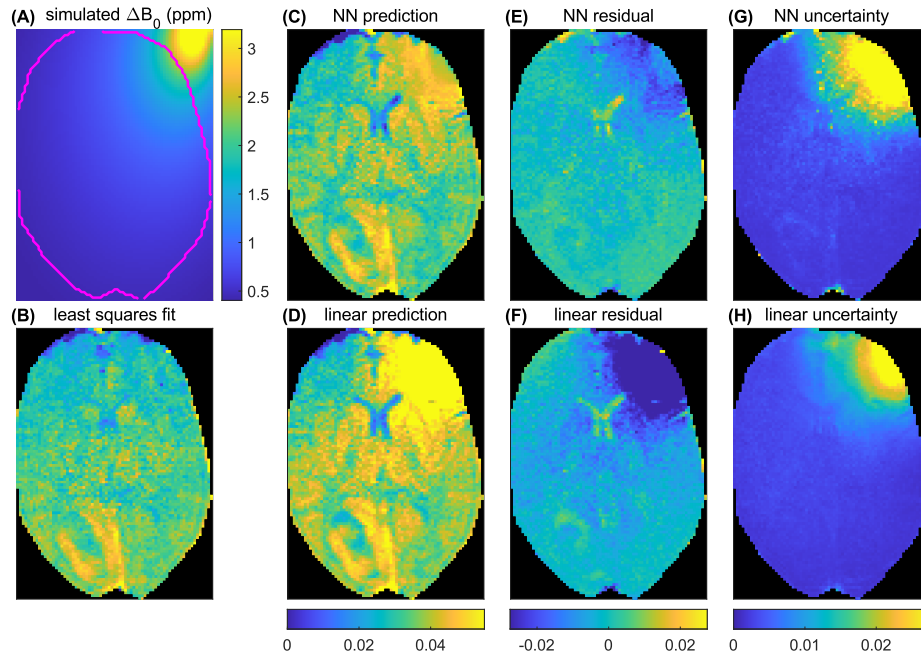
Figure 5.3.: Examples of uncertainty quantification by the deepCEST 3T neural network [117] and the linear regression method introduced in Publication 3. For demonstration, an implant-like B_0 artifact was simulated by placing a magnetic dipole in the upper right corner of the displayed slice of a glioblastoma patient dataset. **(A)** The simulated off-resonance map caused by the dipole field. **(B)** Conventional Lorentzian fit result, shown here is the APT peak amplitude. **(C)** The deepCEST prediction and **(D)** linear prediction, as well as the respective prediction errors with respect to the fit result for **(E)** deepCEST and **(F)** linear model. **(G)** Uncertainty map of deepCEST and **(H)** linear model, obtained from equation (5.1). The dataset and neural network were also used in [71, 117].

because it is fast and simple to obtain (a single pseudo-inversion step), while allowing the outer sequence parameter optimization to find an acquisition scheme that suits the prescribed linear mapping.

The MR-double-zero approach of Publication 4 can be seen as a highly experimental framework and proof-of-principle for automatic, exploratory, and model-free MR sequence optimization based on real-world data acquisition. This represents a largely unexplored approach in the field of MRI and can be seen as a paradigm shift from conventional sequence optimization, which traditionally involves theoretical models and extensive human interaction with the scanner. Still, in the specific context of RF pulse design, a similar approach has already been implemented in 1995 to refine an optimized RF pulse under realistic experimental conditions [184]. More recently, a Bayesian optimization approach based on real-time scanner acquisitions has been proposed for MR spectroscopy [185].

The results of Publication 4 can be interpreted as a proof-of-principle that MR-double-zero has "rediscovered" the supposedly unknown CEST effect of creatine and enabled quantitative concentration mapping with only two acquisitions. In contrast, conventional approaches for concentration mapping of CEST agents typically require a larger number of presaturated images [186–188]. Thus, the framework could be seen as offering potential for two types of acceleration: On the one hand, in speeding up the discovery of new contrast mechanisms compared to the traditional trial-and-error approach, and on the other hand, in terms of the scan time required by the final optimized sequence.

Since the proof-of-principle shown in Publication 4 was performed only in phantom experiments, first experiments have been conducted to apply the framework in vivo [189]. For demonstration purposes, the task was to optimize the tissue contrast of a spoiled GRE sequence in the human brain. Since accurate tissue segmentation masks as a target are difficult to obtain rapidly in vivo[10], a suitable objective function had to be established, ideally reference-free, i.e. depending only on the acquired image at each iteration. For example, spatial gradient entropy has been used as a surrogate for perceived image quality in optimization-based methods for correcting motion [190] or phase artifacts [191]. Inspired by that, Hartigan's dip test [192] was used as a reference-free quality metric for tissue contrast between Gray Matter (GM) and White Matter (WM), which is a measure of non-unimodality of the image intensity histograms. The desired tissue contrast would ideally appear as a bimodal distribution in the histogram, which could be quantified by the used dip metric. Investigations of such reference-free quality metrics may be a worthwhile direction of further research.

On a technical level, MR-double-zero can be seen as an advanced, data-driven search in a defined sequence parameter space to investigate whether a given contrast can be obtained via MRI. In contrast, a classical equispaced grid search quickly becomes infeasible in higher dimensions due to combinatorial explosion. For the investigated setting, a reasonable convergence could be observed for 300 iterations, even when going from 6 to 9 free parameters. Since only a small subspace of all possible sequence parameters

---

[10]In an extreme case, a new segmentation mask would be required for each iteration during optimization due to the inevitable subject motion.

5. Conclusion and Outlook

was covered in these first experiments, this observation seems promising for extending the approach to larger problems, which, however, requires further investigation. A central aspect for ongoing research in this regard is the chosen optimization algorithm and its properties and limitations, which need to be carefully studied. The problem posed by numerical optimization based on real scanner data is very complicated from an optimization point of view, as it involves a non-convex, noisy, potentially multimodal objective function with no stable derivatives. The chosen CMA-ES optimization algorithm belongs to the class of Evolution Strategies, i.e. stochastic, nature-inspired black-box optimizers, and has been shown to outperform a large number of other algorithms for the same class of difficult functions on larger dimensional search spaces [193]. However, in this survey only up to $d = 40$ dimensional test functions were considered, and it was noticed that within a budget (i.e., number of allowed function evaluations) of $100 \cdot d$, even the best algorithm could solve only 25% of the considered problems. The original CMA-ES implementation is recommended only for $d \leq 100$ [194]. Although modifications of this algorithm have been proposed to improve convergence in higher dimensions [195–197], these are usually tested on rather artificial test functions such as high-dimensional ellipsoids and still require a budget that scales at least linearly with the number of dimensions d. One function evaluation in MR-double-zero corresponds to generating a new Pulseq sequence file, sending it to the scanner, executing it, sending the acquired data back to an off-line computer, reconstructing it, and attempting to map it to the target. In the current implementation, this process takes approximately $30\,\text{s}$ plus the pure sequence run time due to overheads like network communication, which in principle could be further reduced. However, for higher-dimensional sequence optimization problems, the required budget is expected to quickly become infeasible due to the extensive scan time required. For example, the optimization of a variable flip angle train with, e.g., 128 free parameters (one parameter per k-space line) was found to be very challenging at the current stage. One way to overcome this may be to use appropriately chosen parameterizations of such a flip angle train (or other parameters of the sequence), e.g., spline functions, which effectively control a large number of parameters by a smaller number of basis coefficients. This has also been proposed for the design of non-Cartesian trajectories [135], pTx pulses [198], and MR fingerprinting schedules [199], and may be an interesting next step to explore. A preliminary numerical experiment with such an approach is shown in Figure 5.4.

Because MR-double-zero does not rely on any theoretical model of MRI contrast mechanisms, a speculative application of the framework might be to use it to automatically test hypotheses about whether and how a given target contrast could be generated by an appropriately designed MRI method. Even more speculatively, it could be used to design novel tailored MRI methods in a medical context. For example, data acquisition and post-processing could be automatically optimized to map to a known diagnosis, outcome, etc., rather than retrospectively searching for such correlations in conventionally acquired, already existing data.

Finally, as a model-free method, the framework may be suited for investigating or gaining insensitivity to system imperfections such as eddy currents, gradient delay, and amplifier heating, which are difficult to model. For example, first steps towards learning-
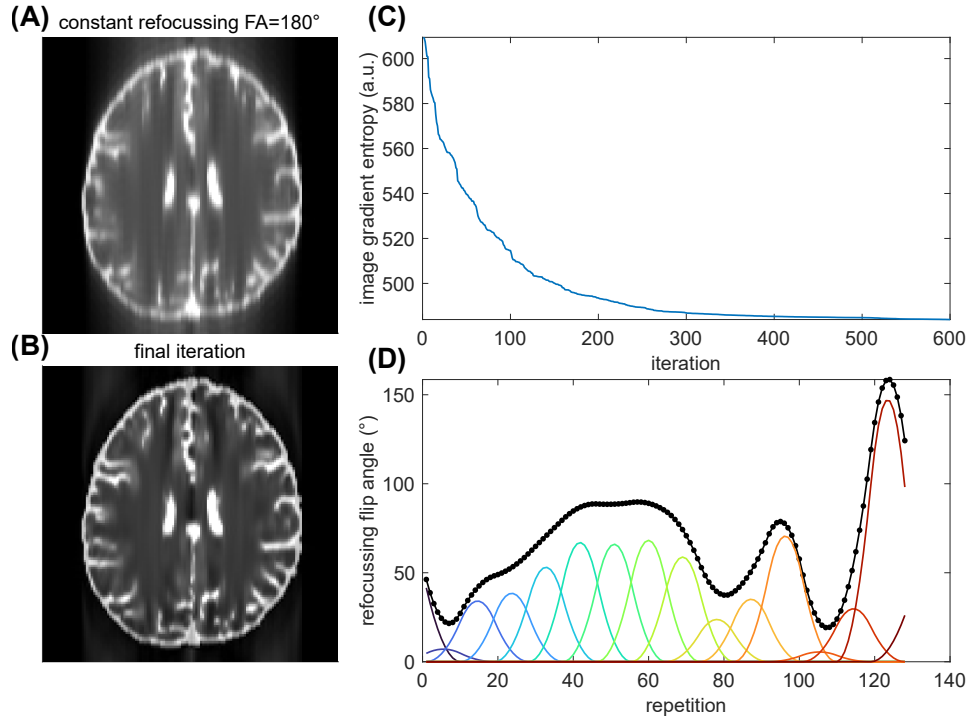
Figure 5.4.: Investigation of MR-double-zero optimization of the refocusing FA train for a single-shot TSE, similar to the approach in [200, 201]. **(A)** In a conventional centric reordered TSE sequence, the T_2 decay over the echo train leads to significant image blurring. Using a variable FA train, i.e., a different refocusing FA for each k-space line, this blurring can be reduced. As a reference-free quality metric, image gradient entropy as in [190, 191] was used here for the CMA-ES optimizer. The resulting final image and FA evolution are shown in **(B)** and **(D)**, respectively. **(C)** shows the evolution of the cost function values when sorted descending. To reduce the number of free parameters and thus make optimization feasible, the FA evolution of the 128 refocusing pulses was parametrized by 16 quadratic B-splines as shown in (D). Instead of a real scanner acquisition, a phase graph-based MRI simulation [202] was used for this preliminary investigation.

5. Conclusion and Outlook

based compensation of eddy current effects have been taken based on the original MRzero framework [119], currently only by model-based simulations [203]. A future step envisioned in this project is the possible translation to MR-double-zero-like optimization on a real system with limited gradient performance.

In summary, several new and unconventional MRI methods have been investigated in the course of this thesis. In Publications 1 to 3, a central goal was to explore ways to reduce the inherently long acquisition times, which can be seen as one of the most severe limitations of MRI. In Publications 1 and 2, this was attempted by combining novel hardware, i.e., the reconfigurable coils, with an appropriate acquisition and reconstruction scheme. This approach explicitly exploits the RF wavelength effects at UHF MRI of 9.4 T, which are generally considered to be rather a nuisance factor. Publication 3 proposed a data processing method for CEST MRI that has the potential to reduce the number and thus the duration of acquisitions required to obtain the desired contrasts, for the investigated case by a factor of ~ 3. Finally, and most experimentally, Publication 4 demonstrated proof-of-principle for an automated sequence optimization framework based on live acquisitions on a real scanner.

The different approaches taken in all these projects highlight the variety and interrelationship of aspects such as hardware components, sequences, reconstruction and data processing algorithms, which should ideally work in synergy to get the best out of the MRI methodology as a whole. This also suggests that there is plenty of room to explore and hopefully improve each of these aspects and their combinations. It should be emphasized, however, that all of the presented methods are basic research and thus have no immediate benefit, e.g., in clinical applications of MRI. The path from the basic methodological research presented here to such practical utility is long and uncertain. In this respect, as implied throughout this section, the work presented here may hopefully provide a basis for future projects branching out in different directions of potentially improving MRI methodology.

A. Publication List

Journal Articles

[A] Zaiss, M.; Deshmane, A.; Schuppert, M.; Herz, K.; **Glang, F.**; Ehses, P.; Lindig, T.; Bender, B.; Ernemann, U.; Scheffler, K. *DeepCEST: 9.4 T Chemical Exchange Saturation Transfer MRI Contrast Predicted from 3 T Data – a Proof of Concept Study.* Magnetic Resonance in Medicine 2019, 81 (6), 3901–3914. https://doi.org/10.1002/mrm.27690.

[B] **Glang, F.**; Deshmane, A.; Prokudin, S.; Martin, F.; Herz, K.; Lindig, T.; Bender, B.; Scheffler, K.; Zaiss, M. *DeepCEST 3T: Robust MRI Parameter Determination and Uncertainty Quantification with Neural Networks—Application to CEST Imaging of the Human Brain at 3T.* Magnetic Resonance in Medicine 2020, 84 (1), 450–466. https://doi.org/10.1002/mrm.28117.

[C] Loktyushin, A.; Herz, K.; Dang, N.; **Glang, F.**; Deshmane, A.; Weinmüller, S.; Doerfler, A.; Schölkopf, B.; Scheffler, K.; Zaiss, M. *MRzero - Automated Discovery of MRI Sequences Using Supervised Learning.* Magnetic Resonance in Medicine 2021, 86 (2), 709–724. https://doi.org/10.1002/mrm.28727.

[D] **Glang, F.**; Fabian, M. S.; German, A.; Khakzar, K. M.; Mennecke, A.; Liebert, A.; Herz, K.; Liebig, P.; Kasper, B. S.; Schmidt, M.; Zuazua, E.; Nagel, A. M.; Laun, F. B.; Dörfler, A.; Scheffler, K.; Zaiss, M. *Linear Projection-Based Chemical Exchange Saturation Transfer Parameter Estimation.* NMR in Biomedicine 2022, e4697. https://doi.org/10.1002/nbm.4697.

[E] Columbus, D.; Arunachalam, V.; **Glang, F.**; Avram, L.; Haber, S.; Zohar, A.; Zaiss, M.; Leskes, M. *Direct Detection of Lithium Exchange across the Solid Electrolyte Interphase by ^7Li Chemical Exchange Saturation Transfer.* J. Am. Chem. Soc. 2022, 144 (22), 9836–9844. https://doi.org/10.1021/jacs.2c02494.

[F] Birk, F.; **Glang, F.**; Loktyushin, A.; Birkl, C.; Ehses, P.; Scheffler, K.; Heule, R. *High-Resolution Neural Network-Driven Mapping of Multiple Diffusion Metrics Leveraging Asymmetries in the Balanced Steady-State Free Precession Frequency Profile.* NMR in Biomedicine 2022, 35 (6), e4669. https://doi.org/10.1002/nbm.4669.

[G] **Glang, F.***; Mueller, S.*; Herz, K.; Loktyushin, A.; Scheffler, K.; Zaiss, M. *MR-Double-Zero – Proof-of-Concept for a Framework to Autonomously Discover MRI Contrasts.* Journal of Magnetic Resonance 2022, Volume 341, 107237. https://doi.org/10.1016/j.jmr.2022.107237.

[H] **Glang, F.**; Nikulin, A. V.; Bause, J.; Heule, R.; Steffen, T.; Avdievich, N.; Scheffler, K. *Accelerated MRI at 9.4 T with Electronically Modulated Time-Varying Receive Sensitivities.* Magnetic Resonance in Medicine 2022, 88 (2), 742–756. https://doi.org/10.1002/mrm.29245.

[I] Avdievich, N. I.; Nikulin, A. V.; Ruhm, L.; Magill, A. W.; **Glang, F.**; Henning, A.; Scheffler, K. *A 32-Element Loop/Dipole Hybrid Array for Human Head Imaging at 7 T.* Magnetic Resonance in Medicine 2022, 88 (4), 1912–1926. https://doi.org/10.1002/mrm.29347.

[J] Hunger, L.; Rajput, J. R.; Klein, K.; Mennecke, A.; Fabian, M. S.; Schmidt, M.; **Glang, F.**; Herz, K.; Liebig, P.; Nagel, A. M.; Scheffler, K.; Dörfler, A.; Maier, A.; Zaiss, M. *DeepCEST 7 T: Fast and Homogeneous Mapping of 7 T CEST MRI Parameters and Their Uncertainty Quantification.* Magnetic Resonance in Medicine 2023, 89 (4), 1543–1556. https://doi.org/10.1002/mrm.29520.

[K] Nikulin, A. V.*; **Glang, F.***; Avdievich, N.; Bosch, D.; Steffen, T.; Scheffler, K. *Reconfigurable Dipole Receive Array for Dynamic Parallel Imaging at Ultra-High Magnetic Field.* Magnetic Resonance in Medicine 2023, 90 (4), 1713-1727. https://doi.org/10.1002/mrm.29745.

[L] Nikulin, A. V.; Bosch, D.; Solomakha, G.; **Glang, F.**; Scheffler, K.; Avdievich, N. *Double-Row 16-element Folded-End Dipole Transceiver Array for 3D RF Shimming of the Human Whole Brain at 9.4 T.* NMR in Biomedicine 2023, 36 (10), e4981. https://doi.org/10.1002/nbm.4981.

[M] Dang, H. N.; Endres, J.; Weinmüller, S.; **Glang, F.**; Loktyushin, A.; Scheffler, K.; Doerfler, A.; Schmidt, M.; Maier, A.; Zaiss, M. *MR-zero meets RARE MRI: Joint Optimization of Refocusing Flip Angles and Neural Networks to Minimize T2-Induced Blurring in Spin Echo Sequences.* Magnetic Resonance in Medicine 2023, 90 (4), 1345-1362. https://doi.org/10.1002/mrm.29710.

* these authors contributed equally to the respective work

Book Chapters

1. Zaiss, M.; **Glang, F.**; Herz, K. *Chapter 25 - Chemical Exchange Saturation Transfer (CEST) MRI as a Tunable Relaxation Phenomenon.* In Advances in Magnetic Resonance Technology and Applications; Choi, I.-Y., Jezzard, P., Eds.; Advanced Neuro MR Techniques and Applications; Academic Press, 2021; Vol. 4, pp 387–401. https://doi.org/10.1016/B978-0-12-822479-3.00040-3.

First Author Conference Contributions

[i] **Glang, F.**; Deshmane, A.; Martin, F.; Herz, K.; Scheffler, K.; Zaiss, M. *Can a Neural Network Predict B_0 Maps from Uncorrected CEST-Spectra?* Proc. Intl. Soc. Mag. Reson. Med. 27 (2019); Montreal (QC, Canada), 2019; #4995.

[ii] **Glang, F.**; Deshmane, A.; Prokudin, S.; Martin, F.; Herz, K.; Lindig, T.; Bender, B.; Scheffler, K.; Zaiss, M. *DeepCEST 3T: Robust Neural Network Prediction of 3T CEST MRI Parameters Including Uncertainty Quantification.* Proc. Intl. Soc. Mag. Reson. Med. 28 (2020); Virtual, 2020; #0509.

[iii] **Glang, F.**; Fabian, M. S.; Deshmane, A.; Herz, K.; Scheffler, K.; Zaiss, M. *CEST-Lasso: L1-Regularized Linear Projection Based CEST Evaluation and Feature Selection for Reduced Acquisition Time*; 8. International Workshop on Chemical Exchange Saturation Transfer Imaging (CEST 2020), 2020.

[iv] **Glang, F.**; Buckenmaier, K.; Bause, J.; Loktyushin, A.; Avdievich, N.; Scheffler, K. *Investigations on Accelerated Imaging at 9.4T with Electronically Modulated Time-Varying Receive Sensitivities.* Proc. Intl. Soc. Mag. Reson. Med. 29 (2021); Virtual, 2021; #0910.

[v] **Glang, F.**; Fabian, M.; German, A.; Khakzar, K.; Mennecke, A.; Laun, F.; Kasper, B.; Schmidt, M.; Doerfler, A.; Scheffler, K.; Zaiss, M. *Linear Projection-Based CEST Reconstruction – the Simplest Explainable AI.* Proc. Intl. Soc. Mag. Reson. Med. 29 (2021); Virtual, 2021; #1454.

[vi] **Glang, F.**; Loktyushin, A.; Herz, K.; Dang, H. N.; Deshmane, A.; Weinmüller, S.; Doerfler, A.; Maier, A.; Schölkopf, B.; Scheffler, K.; Zaiss, M. *Advances in MRzero – Supervised Learning of Parallel Imaging Sequences Including Joint Non-Cartesian Trajectory and Flip Angle Optimization.* Proc. Intl. Soc. Mag. Reson. Med. 29 (2021); Virtual, 2021; #4200.

[vii] **Glang, F.** M.; Nikulin, A. V.; Bause, J.; Heule, R.; Steffen, T.; Avdievich, N.; Scheffler, K. *Accelerated MRI at 9.4 T with Electronically Modulated Time-Varying Receive Sensitivities*; Proceedings of the DS-ISMRM Annual Meeting 2022; Aachen (Germany), pp 23–29.

[viii] **Glang, F.**; Nikulin, A.; Bause, J.; Heule, R.; Steffen, T.; Avdievich, N.; Scheffler, K. *Advances in Accelerated Imaging at 9.4T with Electronically Modulated Time-Varying Receive Sensitivities.* Proc. Intl. Soc. Mag. Reson. Med. 30 (2022); London (UK), 2022; #0104.

[ix] **Glang, F.**; Nikulin, A.; Avdievich, N.; Bosch, D.; Steffen, T.; Scheffler, K. *Dynamic Dipole Receive Coils for Improved 3D Parallel Imaging at Ultra-High Magnetic Field.* In Proc. Intl. Soc. Mag. Reson. Med. 31 (2023); Toronto (ON, Canada), 2023; #3284.

A. Publication List

[x] **Glang, F.**; Iyyappan Valsala, P.; Nikulin, A. V.; Avdievich, N.; Steffen, T.; Scheffler, K. *Investigations on Non-Cartesian Parallel Imaging with Time-Varying Receive Sensitivities.* In Proc. Intl. Soc. Mag. Reson. Med. 31 (2023); Toronto (ON, Canada), 2023; #5848.

Other Conference Abstracts

[xi] Loktyushin, A.; Herz, K.; **Glang, F.**; Schölkopf, B.; Scheffler, K.; Zaiss, M. *MRI Zero: Fully Automated Invention of MRI Sequences Using Supervised Learning*; 36th Annual Scientific Meeting of the European Society for Magnetic Resonance in Medicine and Biology (ESMRMB 2019), Rotterdam, 2019; pp S119–S120. https://doi.org/10.1007/s10334-019-00754-2.

[xii] Zaiss, M.; Martin, F.; **Glang, F.**; Herz, K.; Deshmane, A.; Bender, B.; Lindig, T.; Scheffler, K. *DeepCEST: 9.4 T Spectral Super Resolution from 3 T CEST MRI Data - Optimization of Network Architectures.* In Proc. Intl. Soc. Mag. Reson. Med. 27 (2019); Montreal (QC, Canada), 2019; #4016.

[xiii] Dang, H. N.; Loktyushin, A.; **Glang, F.**; Herz, K.; Doerfler, A.; Schölkopf, B.; Scheffler, K.; Maier, A.; Zaiss, M. *Autoencoding T1 Using MRzero for Simultaneous Sequence Optimization and Neural Network Training*; 37th Annual Scientific Meeting of the European Society for Magnetic Resonance in Medicine and Biology (ESMRMB 2020), Virtual, 2020; pp S27–S28. https://doi.org/10.1007/s10334-020-00874-0.

[xiv] Fabian, M. S.; **Glang, F.**; Khakzar, K. M.; German, A.; Mennecke, A.; Zaiss, M. *Linear Projection-Based 7T CEST Reconstruction*; 8. International Workshop on Chemical Exchange Saturation Transfer Imaging (CEST 2020), 2020.

[xv] Klein, K.; **Glang, F.**; German, A.; Mennecke, A.; Maier, A.; Schmid, M.; Dörfler, A.; Zaiss, M. *Deep Learning with Uncertainty Quantification for Acceleration of 7T CEST Acquisition and Reconstruction*; 8. International Workshop on Chemical Exchange Saturation Transfer Imaging (CEST 2020), 2020.

[xvi] Mueller, S.; **Glang, F.**; Scheffler, K.; Zaiss, M. *pH Mapping of Brain Tissue by a Deep Neural Network Trained on 9.4T CEST MRI Data – pH-DeepCEST.* In Proc. Intl. Soc. Mag. Reson. Med. 28 (2020); Virtual, 2020; #3130.

[xvii] Birk, F.; **Glang, F.**; Loktyushin, A.; Birkl, C.; Ehses, P.; Scheffler, K.; Heule, R. *NN-Driven Mapping of Multiple Diffusion Metrics at High to Ultra-High Resolution Using the BSSFP Frequency Profile*; Proceedings of the DS-ISMRM Annual Meeting 2021; Zürich (Switzerland), pp S78–S81.

[xviii] Birk, F.; **Glang, F.**; Birkl, C.; Scheffler, K.; Heule, R. *Quantification of Multiple Diffusion Metrics from Asymmetric Balanced SSFP Frequency Profiles Using Neural Networks.* In Proc. Intl. Soc. Mag. Reson. Med. 29 (2021); Virtual, 2021; #2437.

[xix] Dang, H. N.; Endres, J.; Weinmüller, S.; Loktyushin, A.; **Glang, F.**; Scheffler, K.; Doerfler, A.; Maier, A.; Zaiss, M. *Removing T2 Blurring in RARE Sequences by Using a DenseNet*; Proceedings of the DS-ISMRM Annual Meeting 2021; Zürich (Switzerland), pp S82–S83.

A. Publication List

[xx] Dang, H. N.; Weinmüller, S.; Loktyushin, A.; **Glang, F.**; Dörfler, A.; Maier, A.; Schölkopf, B.; Scheffler, K.; Zaiss, M. *MRzero with dAUTOMAP Reconstruction– Automated Invention of MR Acquisition and Neural Network Reconstruction.* In Proc. Intl. Soc. Mag. Reson. Med. 29 (2021); Virtual, 2021; #0333.

[xxi] Fabian, M. S.; **Glang, F.**; Khakzar, K. M.; Mennecke, A. B.; German, A.; Schmidt, M.; Kasper, B.; Dörfler, A.; Laun, F. B.; Zaiss, M. *Reduction of 7T CEST Scan Time and Evaluation by L1-Regularised Linear Projections.* In Proc. Intl. Soc. Mag. Reson. Med. 29 (2021); Virtual, 2021; #1452.

[xxii] Hunger, L. E.; German, A.; **Glang, F.**; Khakzar, K. M.; Dang, N.; Mennecke, A.; Maier, A.; Laun, F.; Zaiss, M. *DeepCEST: 7T Chemical Exchange Saturation Transfer MRI Contrast Inferred from 3T Data via Deep Learning with Uncertainty Quantification.* In Proc. Intl. Soc. Mag. Reson. Med. 29 (2021); Virtual, 2021; #1451.

[xxiii] Loktyushin, A.; Herz, K.; Dang, N.; **Glang, F.**; Deshmane, A.; Weinmüller, S.; Doerfler, A.; Schölkopf, B.; Scheffler, K.; Zaiss, M. *MRzero — Automated Invention of MRI Sequences Using Supervised Learning.* In Proc. Intl. Soc. Mag. Reson. Med. 29 (2021); Virtual, 2021; #4199.

[xxiv] Weinmüller, S.; Dang, H. N.; Loktyushin, A.; **Glang, F.**; Doerfler, A.; Maier, A.; Schölkopf, B.; Scheffler, K.; Zaiss, M. *MRzero Sequence Generation Using Analytic Signal Equations as Forward Model and Neural Network Reconstruction for Efficient Auto-Encoding.* In Proc. Intl. Soc. Mag. Reson. Med. 29 (2021); Virtual, 2021; #1761.

[xxv] Choi, S.; Heule, R.; Leks, E.; **Glang, F.**; Yu, X.; Scheffler, K. *Calibration Kernels with Alternative Sampling Scheme (CASS) for Parallel Imaging: SENSE Meets CASS.* In Proc. Intl. Soc. Mag. Reson. Med. 30 (2022); London (UK), 2022; #2445.

[xxvi] Dang, H. N.; Endres, J.; Weinmüller, S.; **Glang, F.** M.; Loktyushin, A.; Dörfler, A.; Maier, A.; Zaiss, M. *Joint Optimization of Flip Angle Design and DenseNet Parameters for Reduced T2 Blurring in TSE Sequences*; Proceedings of the DS-ISMRM Annual Meeting 2022; Aachen (Germany), pp 14–15.

[xxvii] Dang, H. N.; Endres, J.; **Glang, F.**; Weinmüller, S.; Loktyushin, A.; Scheffler, K.; Doerfler, A.; Maier, A.; Zaiss, M. *Solving T2-Blurring: Joint Optimization of Flip Angle Design and DenseNet Parameters for Reduced T2 Blurring in TSE Sequences.* In Proc. Intl. Soc. Mag. Reson. Med. 30 (2022); London (UK), 2022; p 2602.

[xxviii] Endres, J.; Dang, H. N.; **Glang, F.** M.; Herz, K.; Loktyushin, A.; Weinmüller, S.; Zaiss, M. *Fast Analytical Simulation of Pulseq MRI Sequence Definitions*; Proceedings of the DS-ISMRM Annual Meeting 2022; Aachen (Germany), pp 82–83.

[xxix] Endres, J.; Dang, H. N.; **Glang, F.**; Loktyushin, A.; Weinmüller, S.; Zaiss, M. *Automatic Reconstruction of Arbitrary MRI Sequences Based on Phase Distribution Graphs.* In Proc. Intl. Soc. Mag. Reson. Med. 30 (2022); London (UK), 2022; #2350.

[xxx] Endres, J.; Dang, H. N.; **Glang, F.**; Loktyushin, A.; Weinmüller, S.; Zaiss, M. *Phase Distribution Graphs for Differentiable and Efficient Simulations of Arbitrary MRI Sequences.* In Proc. Intl. Soc. Mag. Reson. Med. 30 (2022); London (UK), 2022; #0750.

[xxxi] Hunger, L.; Rajput, J.; Fabian, M. S.; Mennecke, A. B.; **Glang, F.** M.; Schmitt, M.; Dörfler, A.; Maier, A.; Zaiss, M. *DeepCEST: Fast Mapping of 7T CEST MRI Parameters with Uncertainty Quantification*; Proceedings of the DS-ISMRM Annual Meeting 2022; Aachen (Germany), pp 10–11.

[xxxii] Hunger, L.; Rajput, J.; Klein, K.; Mennecke, A.; Fabian, M.; Schmidt, M.; **Glang, F.**; Herz, K.; Liebig, P.; Nagel, A.; Scheffler, K.; Dörfler, A.; Maier, A.; Zaiss, M. *DeepCEST: Fast Mapping of 7T CEST MRI Parameters with Uncertainty Quantification*; 9th International Workshop on Chemical Exchange Saturation Transfer Imaging (CEST 2022); #12.

[xxxiii] Kamm, L.; Fabian, M.; **Glang, F.**; Herz, K.; Zaiss, M. *ComprehenCEST: A Clinically Feasible CEST Protocol to Cover All Existing CEST Preparation Schemes by Snapshot Readout and Reduction of Overhangs*; 9th International Workshop on Chemical Exchange Saturation Transfer Imaging (CEST 2022); #56.

[xxxiv] Kamm, L.; Fabian, M. S.; Herz, K.; **Glang, F.** M.; Dörfler, A.; Zaiss, M. *ComprehenCEST: A Clinically Feasible CEST Protocol to Cover All Existing CEST Preparation Schemes by Snapshot Readout and Reduction of Overhangs*; Proceedings of the DS-ISMRM Annual Meeting 2022; Aachen (Germany), pp 92–93.

[xxxv] Mueller, S.; **Glang, F.** M.; Herz, K.; Loktyushin, A.; Scheffler, K.; Zaiss, M. *MR-Double-Zero: Proof-of-Concept for a Framework to Autonomously Discover MRI Contrast*; Proceedings of the DS-ISMRM Annual Meeting 2022; Aachen (Germany), pp 12–13.

[xxxvi] Mueller, S.; **Glang, F.**; Herz, K.; Scheffler, K.; Zaiss, M. *MR-Double-Zero - Can a Machine Discover New MRI Contrasts, Such as Metabolite Concentration?* In Proc. Intl. Soc. Mag. Reson. Med. 30 (2022); London (UK), 2022; #0103.

[xxxvii] Weinmüller, S.; Dang, H. N.; Endres, J.; **Glang, F.** M.; Loktyushin, A.; Zaiss, M. *A Blurring-Free 3D Snapshot Readout for Fast CEST- or Relaxation-Prepared MRI*; Proceedings of the DS-ISMRM Annual Meeting 2022; Aachen (Germany), pp 6–7.

A. Publication List

[xxxviii] Zaiss, M.; Weinmüller, S.; Dang, H. N.; Endres, J.; Hu, Z.; Hanson, L. G.; **Glang, F.** *MRIpulseq: Learning MR Sequence Programming with Pulseq through Simulation and Measurement.* In MRI Together 2022: Global workshop on open, reproducible, and inclusive MR research; Online, 5 Dec 2022 - 8 Dec 2022.

[xxxix] Mueller, S.; **Glang, F.**; Scheffler, K.; Zaiss, M. *MR-Double-Zero in Vivo: Model-Free and Live MRI Contrast Optimization Running a Loop over a Real Scanner with a Real Subject.* In Proc. Intl. Soc. Mag. Reson. Med. 31 (2023); Toronto (ON, Canada), 2023; #6655.

[xl] Solomakha, G.; **Glang, F.**; Steffen, T.; Scheffler, K.; Avdievich, N. *Reconfigurable Coaxial Receive Dipoles for Dynamic Parallel Imaging of Human Brain at 9.4T.* In Proc. Intl. Soc. Mag. Reson. Med. 31 (2023); Toronto (ON, Canada), 2023; #4099.

[xli] West, D.; **Glang, F.**; Endres, J.; Zaiss, M.; Hajnal, J. V.; Malik, S. J. *Overcoming System Imperfections Using End-to-End MR Sequence Design.* In Proc. Intl. Soc. Mag. Reson. Med. 31 (2023); Toronto (ON, Canada), 2023; #0061.

B. Appended Publications

B.1. Publication 1

Glang, F.; Nikulin, A. V.; Bause, J.; Heule, R.; Steffen, T.; Avdievich, N.; Scheffler, K.
Accelerated MRI at 9.4 T with Electronically Modulated Time-Varying Receive Sensitivities.
Magnetic Resonance in Medicine 2022, 88 (2), 742–756.

RESEARCH ARTICLE

Accelerated MRI at 9.4 T with electronically modulated time-varying receive sensitivities

Felix Glang[1] | **Anton V. Nikulin[1,2]** | **Jonas Bause[1]** | **Rahel Heule[1,2]** | **Theodor Steffen[1]** | **Nikolai Avdievich[1]** | **Klaus Scheffler[1,2]**

[1]Magnetic Resonance Center, Max Planck Institute for Biological Cybernetics, Tübingen, Germany

[2]Department of Biomedical Magnetic Resonance, Eberhard Karls University Tübingen, Tübingen, Germany

Correspondence
Felix Glang, Magnetic Resonance Center, Max Planck Institute for Biological Cybernetics, Tübingen, Germany.
Email: felix.glang@tuebingen.mpg.de

Purpose: To investigate how electronically modulated time-varying receive sensitivities can improve parallel imaging reconstruction at ultra-high field.

Methods: Receive sensitivity modulation was achieved by introducing PIN diodes in the receive loops, which allow rapid switching of capacitances in both arms of each loop coil and by that alter B_1^- profiles, resulting in two distinct receive sensitivity configurations. A prototype 8-channel reconfigurable receive coil for human head imaging at 9.4T was built, and MR measurements were performed in both phantom and human subject. A modified SENSE reconstruction for time-varying sensitivities was formulated, and g-factor calculations were performed to investigate how modulation of receive sensitivity profiles during image encoding can improve parallel imaging reconstruction. The optimized modulation pattern was realized experimentally, and reconstructions with the time-varying sensitivities were compared with conventional static SENSE reconstructions.

Results: The g-factor calculations showed that fast modulation of receive sensitivities in the order of the ADC dwell time during k-space acquisition can improve parallel imaging performance, as this effectively makes spatial information of both configurations simultaneously available for image encoding. This was confirmed by in vivo measurements, for which lower reconstruction errors (SSIM = 0.81 for acceleration $R = 4$) and g-factors (max g = 2.4; $R = 4$) were observed for the case of rapidly switched sensitivities compared to conventional reconstruction with static sensitivities (SSIM = 0.74 and max g = 3.2; $R = 4$). As the method relies on the short RF wavelength at ultra-high field, it does not yield significant benefits at 3T and below.

Conclusions: Time-varying receive sensitivities can be achieved by inserting PIN diodes in the receive loop coils, which allow modulation of B_1^- patterns. This offers an additional degree of freedom for image encoding, with the potential for improved parallel imaging performance at ultra-high field.

KEYWORDS

B_1^- modulation, coil sensitivities, parallel imaging, reconfigurable RF coil, SENSE, ultra-high field

1 | INTRODUCTION

Parallel imaging (PI) is among the most successful techniques for accelerating MRI acquisition. Based on the phased array receiver coil,[1] it uses spatial information provided by the different sensitivities of multiple local RF receive coils to complement gradient-based Fourier encoding. For this reason, less k-space samples than required by the Nyquist criterion for a single receive channel need to be acquired, which allows omitting sequence repetition steps and thus results in accelerated acquisition. Currently, most applications of PI rely on SENSE[2] or GRAPPA[3] reconstruction. However, since the invention of these techniques, there has been extensive research on better understanding and exploiting the spatial encoding capabilities of receive arrays and their interaction with Fourier encoding, resulting in a large variety of advanced methods and algorithms.[4–7]

Common to all of these methods is that achievable acceleration and reconstruction quality are linked to the spatial patterns of receive sensitivity profiles. As the sensitivities of different coils are never completely spatially independent, their image-encoding capability is fundamentally limited. In the case of linear reconstruction methods like SENSE, for higher acceleration factors, the matrix inversions required for reconstruction become increasingly ill-conditioned, which results in noise amplification and reconstruction artifacts.[2] For this reason, efforts have been made in hardware design to improve coil arrays for optimized PI performance,[8–12] particularly by increasing the number of elements.[13]

Apart from this, applying fast field modulations during image encoding has been proposed to improve accelerated imaging, such as by additional sinusoidal gradients in wave-CAIPI,[14] oscillating second-order nonlinear shim gradients in the case of fast rotary nonlinear spatial acquisition (FRONSAC),[15] or oscillating nonlinear local field modulations in spread MRI.[16] In all of these methods, the additional field modulations lead to better k-space coverage by complementing conventional Fourier and sensitivity encoding, which improves the condition of the image reconstruction problem. In the present work, we investigated whether modulations of the receive coil sensitivities (B_1^-) during image encoding can be used in a similar way to improve PI.

This idea is also inspired by the work on rotating RF coils,[17–20] for which it has been shown that the increased number of distinct sensitivity profiles created by physically rotating coil arrays helps to improve PI reconstructions. Instead of physical rotation, in this work, receive sensitivities are electronically modulated by adding fast switchable PIN diodes to the receive circuitry, which allow

reconfiguring capacitances in the individual receive coils, and by that alter B_1^-. This results in two distinct receive sensitivity configurations (RSC) that can be switched during an MR sequence. The RSC switching during k-space acquisition is a user-defined degree of freedom for sequence design, additionally to conventional RF pulses, gradients and ADC blocks, which will affect the acquired signal and therefore reconstructed images. To demonstrate this concept, a prototype 8-channel receiver array with switchable RSCs was built, and measurements on a 9.4T human MR scanner were performed both in phantom and in vivo to assess sensitivity patterns and PI reconstructions.

Preliminary results of this idea have been presented previously,[21] in which varactor diodes were used for continuous modulation of capacitances and therefore B_1^-. It was found that fast switching between the two extreme states of the varactors yielded highest potential for PI improvement, whereas the intermediate states contributed less to spatial encoding. Because the required switching speed could not be experimentally realized with varactors, the subsequent investigations presented here are focused on fast-switching PIN diodes with only two distinct states.

2 | THEORY

2.1 | Image reconstruction with time-varying sensitivities

In the presence of time-varying receive sensitivities, the multichannel MR data acquisition process (neglecting relaxation and field inhomogeneity–related effects) can be described by a modified SENSE[2] forward model as follows:

$$s_\beta(t) = \int c_\beta(\boldsymbol{r}, t)\, m(\boldsymbol{r})\, \exp(i\boldsymbol{k}(t) \cdot \boldsymbol{r})\mathrm{d}\boldsymbol{r}, \qquad (1)$$

which relates the measured signal time course $s_\beta(t)$ in the β-th receive channel to the effective magnetization image $m(\boldsymbol{r})$ that is determined by tissue and sequence properties. Here, $c_\beta(\boldsymbol{r}, t)$ denotes the complex-valued spatial receive sensitivity of the β-th channel with an explicit time dependence, and $\boldsymbol{k}(t) = \gamma \int_0^t \boldsymbol{g}(t')\, \mathrm{d}t$, is the k-space trajectory that is determined by the linear gradient waveforms $\boldsymbol{g}(t)$. A similar model has been proposed for image reconstruction with rotating coil arrays.[17,18]

For practical application, the forward model (Eq. 1) can be discretized to yield the linear equation $\boldsymbol{s} = \boldsymbol{E}\boldsymbol{m}$, where $\boldsymbol{s} \in \mathbb{C}^{N_c \cdot N_k}$ is the vector of acquired samples from all N_c receive channels and N_k k-space sampling locations, and $\boldsymbol{m} \in \mathbb{C}^{N_x \cdot N_y}$ is the image on an $N_x \times N_y$ grid in image space that is to be reconstructed. Image and acquired signal are related via the encoding operator $\boldsymbol{E} \in \mathbb{C}^{(N_c \cdot N_k) \times (N_x \cdot N_y)}$,

which has the form

$$E_{(\beta,\kappa),\rho} = c_\beta \left(\boldsymbol{r}_\rho, t_\kappa \right) \exp \left(\mathrm{i} \boldsymbol{k} \left(t_\kappa \right) \cdot \boldsymbol{r}_\rho \right), \qquad (2)$$

with discrete voxel locations $\boldsymbol{r}_\rho$ and time points t_κ. The 2D formulation presented here can be straightforwardly extended to 3D.

A solution of the linear reconstruction problem can be obtained by pseudo-inversion of the encoding operator as $\boldsymbol{m}_{\mathrm{reco}} = \left(\boldsymbol{E}^H \widetilde{\boldsymbol{\Psi}}^{-1} \boldsymbol{E} \right)^{-1} \boldsymbol{E}^H \widetilde{\boldsymbol{\Psi}}^{-1} \boldsymbol{s}$. Here, the sample noise covariance matrix $\widetilde{\boldsymbol{\Psi}} \in \mathbb{C}^{(N_c \cdot N_k) \times (N_c \cdot N_k)}$ accounts for noise correlations between different channels, and including it in the reconstruction ensures an optimal SNR reconstruction.[2] In the case of time-varying RSCs, noise correlation for each configuration needs to be measured separately to form the sample noise correlation matrix.

For large matrix sizes or 3D reconstructions, however, storing and directly inverting the encoding operator $\boldsymbol{E}$ is computationally unfeasible. Depending on the used k-space trajectory and sensitivity time course, there are different possibilities for viable reconstruction algorithms. In the most general case of arbitrary trajectories and/or sensitivity time courses, the encoding operator can be expressed as $\boldsymbol{E} = \boldsymbol{PFS}$. Let N_s denote the number of distinct RSCs, then the matrix $\boldsymbol{S} \in \mathbb{C}^{(N_s \cdot N_c \cdot N_x \cdot N_y) \times (N_x \cdot N_y)}$ performs point-wise multiplication with all possible sensitivity maps of each coil and configuration in image space; $\boldsymbol{F} \in \mathbb{C}^{(N_s \cdot N_c \cdot N_k) \times (N_s \cdot N_c \cdot N_y)}$ performs block-wise discrete Fourier transform of coil and configuration images according to the chosen k-space trajectory; and $\boldsymbol{P} \in \mathbb{C}^{(N_c \cdot N_k) \times (N_s \cdot N_c \cdot N_k)}$ selects only those k-space samples of each RSC that are actually acquired. The operator $\boldsymbol{F}$ can be efficiently implemented as fast Fourier transform (FFT) in the case of Cartesian and nonuniform FFT[22] in the case of non-Cartesian trajectories, and the linear reconstruction can be solved iteratively, such as with the conjugate-gradient algorithm as in Pruessmann et al.[23]

In the special case of Cartesian trajectories and a small number of distinct RSCs that are switched in a regular pattern during k-space acquisition, the modified SENSE reconstruction outlined previously can be decomposed into small subproblems corresponding to unfolding of aliased voxel groups in image space. In contrast to conventional SENSE with static sensitivities, not only the k-space undersampling pattern but also the RSC switching pattern determines where in the coil images aliasing occurs and which sensitivity weighting the superimposed voxels have. A simple example for regular switching between two RSCs is provided in the Supporting Information.

Parallel imaging performance with time-varying sensitivities is assessed via the g-factor

$$g_\rho = \sqrt{ \left(\boldsymbol{E}^H \widetilde{\boldsymbol{\Psi}}^{-1} \boldsymbol{E} \right)^{-1}_{\rho,\rho} \left(\boldsymbol{E}^H \widetilde{\boldsymbol{\Psi}}^{-1} \boldsymbol{E} \right)_{\rho,\rho} }, \qquad (3)$$

which describes noise amplification in the voxel ρ due to suboptimal conditioning of the encoding operator.[2] In cases in which direct analytical calculation of the g-factor is infeasible, it can be approximated by the pseudo–multiple replica method.[24]

3 | METHODS

3.1 | Geometry of the reconfigurable coil

Conventional receive head arrays consist of electrically small loop coils.[1,12] At ultrahigh field, the length of a typical loop coil becomes comparable to the wavelength, and as a consequence, the current distribution along the loop length becomes nonuniform.[25] Commonly, to decrease the electrical size of a coil, and thus make the current distribution more uniform, a set of equal capacitors is distributed along the loop.[25] In addition, these capacitors can be used to dynamically alter the current distribution within the loop and provide different RSCs.

To study the behavior of the proposed reconfigurable loop coil, we used finite element method–based simulations in CST Studio Suite 2021 (Dassault Systemes). At first, we modeled a conventional single rectangular coil of 120×50 mm loaded by a homogeneous ($\varepsilon_r = 58.3$, $\sigma = 0.64$ S/m) cylindrical phantom of 170 mm in diameter. In this conventional loop, we distributed nine capacitors of 6.2 pF and one capacitor of 5.1 pF to tune the coil to about 400 MHz. As a result, we obtained a uniform current distribution (Figure 1A). At ultrahigh field, however, the B_1^- pattern becomes asymmetrical within the transverse plane[26] (Figure 1B). Two states of the loop are created by increasing the values of the distributed capacitors at one arm of the loop and decreasing them at the other side, while keeping the coil resonance frequency constant. This creates two different current distributions and receive sensitivity distributions shown in Figure 1B. Such alteration of distributed capacitor values creates a so-called loopole coil[27] (i.e., a structure that supports both loop-like and dipole-like currents). These two types of currents produce substantially different field profiles, which in turn is beneficial for improving PI. The required alteration of current distribution can be done with PIN diodes.

To simulate the two states of the loop (with PIN diodes), we conducted two independent full-wave

FIGURE 1 A, Surface current distribution in a loop-like coil for three configurations. Left: uniform current of a conventional loop coil; middle: loop with high current (HC) in the left arm and low current (LC) in the right arm; right: loop coil with HC in the right arm. The resonance frequency of these three configurations remains about identical at 400 MHz. B, Corresponding simulated sensitivity profiles (B_1^- field) in a central transverse plane (front view)
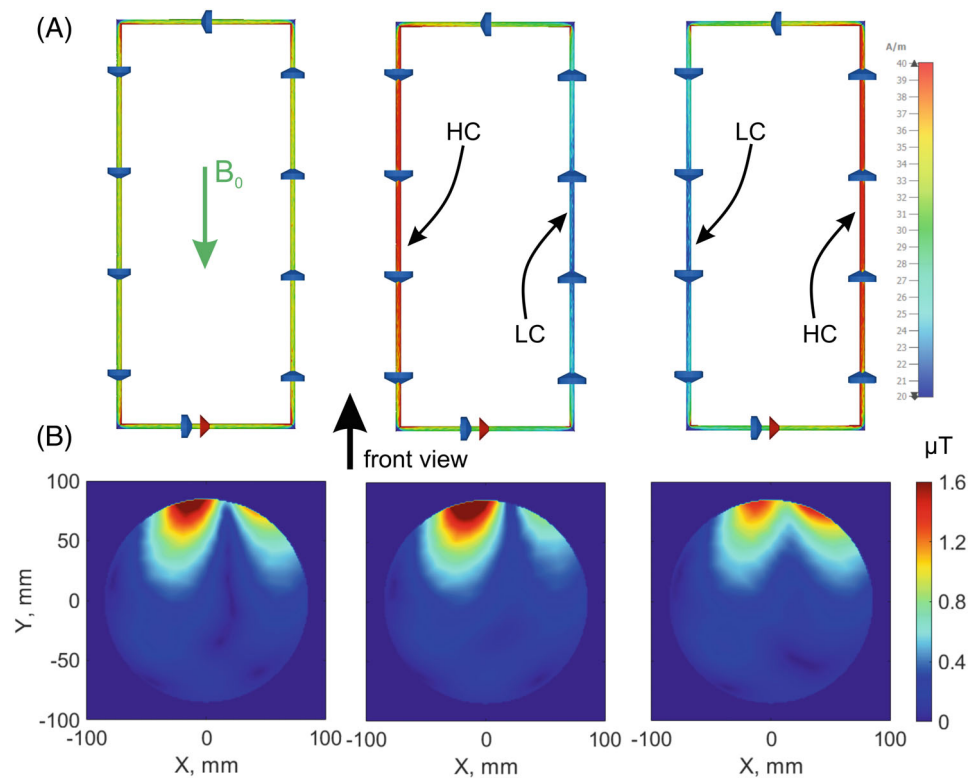
simulations with two sets of capacitors mimicking the states. In Figure 1A, high current occurs in the arm with the high capacitance (21.8 pF), whereas low current occurs in the arm containing low capacitance (2.3 pF). This current distribution creates the asymmetries in the H-field distribution, as the higher current leads to higher H-field around the modified arm. This modified current distribution provides modified sensitivity profiles (B_1^- field) compared with the conventional loop coils of the same size (Figure 1B).

Note that, even though the uniform current distribution creates a symmetrical H-field distribution (Supporting Information Figure S3), B_1^- becomes asymmetrical at ultrahigh fields.[26] For the case of high current in the left arm, this asymmetry gets amplified, whereas for high current in the right arm it gets counteracted. Therefore, uniform current and high current in the left arm provide similarly looking sensitivity patterns, whereas high current in the right arm provides a distinctly different pattern.

Here we chose the capacitors to provide a ratio of approximately 1.9:1 between the currents in the two arms of the loop. It is important to note that further increase of this ratio requires either an unrealistically small capacitance (below the parasitic capacitance of the coil itself), or very high capacitance, which would decrease the resonance frequency of the coil.

3.2 | Prototype

The proposed reconfigurable receive-only array consists of eight rectangular loops of 120 x 50 mm, each made from copper tined wire of 1.5 mm diameter, arranged symmetrically on a fiberglass cylinder of 210 mm diameter (Figure 2B). The loop width was chosen to minimize coupling between the receive elements without spoiling the sensitivity profile of the array. The crosstalk between adjacent elements measured on a vector network analyzer (Keysight 5063A; Keysight Technologies) was at the level of −10 dB. Each loop was connected to the receive interface through a cable trap as shown in Figure 2A,B. The receive interface contains eight low-noise preamplifiers (WMA9RA; Wantcom). Each element is equipped with an active detuning (AD) circuit, which detunes the receive coil when applying DC current during transmission.

To reconfigure the loop, we designed a switchable unit consisting of a PIN-diode (MA4P504-1072 T; MACOM), series capacitor of 20 pF, and a small capacitor of 1.5 pF … 2.4 pF ("B size" capacitors; Dalian Dalicap Tech) connected in parallel, as depicted in Figure 2A. When the PIN diodes are negatively biased in one of the arms (C_a or C_b), the effective capacitance of each switchable unit becomes about 2.5 pF. At the same time, the PIN diodes in the second arm of the loop are shorted. Consequently, the effective capacitance of each switchable unit becomes
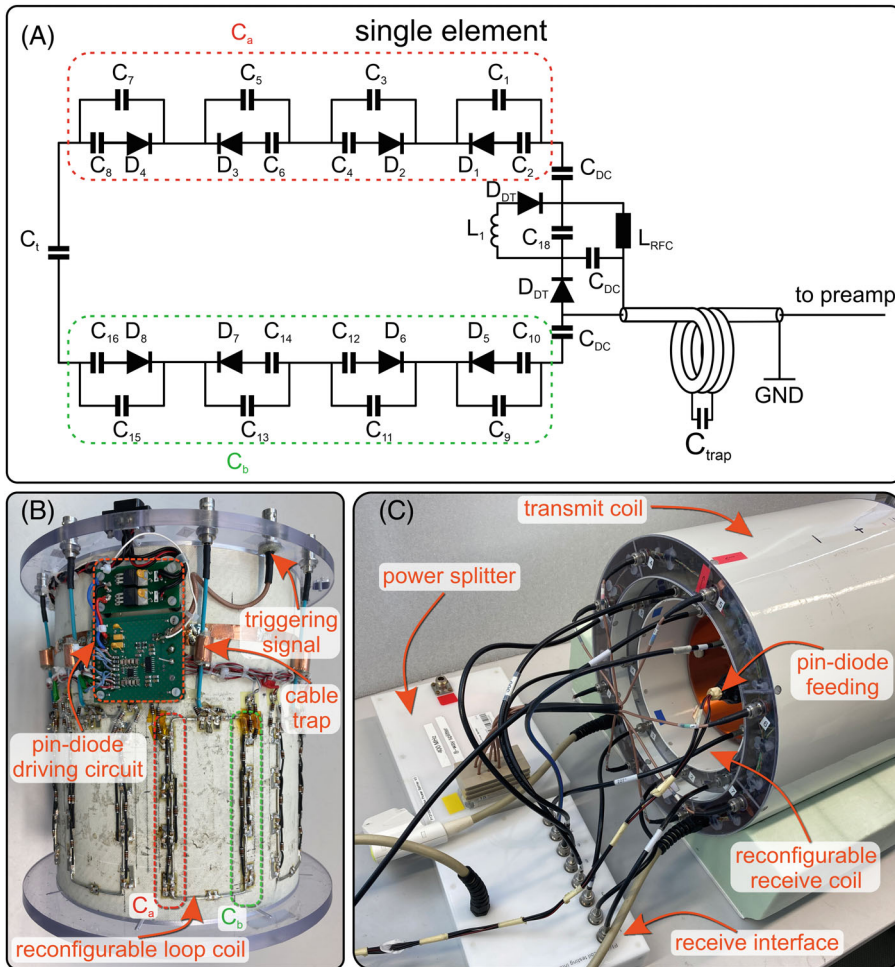
FIGURE 2 A, Circuit diagram of a single receive loop of the experimental receive array prototype, showing four switchable units, which consist of a PIN diode and two capacitors, on each arm of the loop. Alternating between forward and reverse bias of the PIN diodes yields two distinct B_1^- patterns that can be rapidly switched. B,C, Photos of the experimental setup

about 22 pF. To control the PIN diodes, we designed a driver that can negatively bias or short the PIN diodes. To change the state of this switchable unit, we applied a rectangular pulse with an offset of 1.5 V and a peak-to-peak amplitude voltage of 3 V. To feed the PIN diodes, we used DC voltage of 6 V delivered to each PIN diode using RF choke inductors (330 nH, 9230 Series; Bourns) (not shown in Figure 2A). It is important to note that when the switchable units in one arm are negatively biased, the PIN diodes in the second arm are shorted to tune the coil at the working frequency of 400 MHz. In addition, each loop contains one capacitor C_t used for frequency adjustment if the resonant frequency is unidirectionally below or beyond 400 MHz in both configurations of the switchable unit. This capacitor is in the range of 10 to 15 pF depending on the element.

As a transmit-only coil, we used an array of eight conventional loops (130×100 mm) uniformly distributed around the circumference of 280 mm in diameter. The adjacent loops were decoupled using transformer decoupling.[28] The active detuning circuits were implemented in each loop to detune the array coil in receive mode. Finally, each element of the array was connected through a cable

trap to the power splitter to excite a circularly polarized mode.

3.3 | Magnetic resonance imaging

Measurements were performed on a 9.4T human whole-body MR scanner (Siemens Healthineers) using a 2D multislice RF and spoiled gradient-echo sequence (TR = 20 ms, TE = 8 ms, flip angle = 20°, matrix size = 256×256, FOV = 220×220 mm, slice thickness = 5 mm, in-plane resolution ∼0.86 mm isotropic, 10 slices, resulting in an acquisition time of 51.2 seconds). Data were acquired in a homogeneous cylindrical phantom of 170 mm diameter, which contained a solution of 0.9698 g/mL Saccharose, 0.0307 g/mL NaCl and 0.1% Dowicil, and had the material parameters ε_r = 58.3, σ = 0.64 S/m. In vivo data were acquired in a healthy subject after written informed consent and under approval of the local ethics committee.

Switching of RSCs during the sequence was controlled by the trigger output of the scanner system. With that, different switching patterns could be implemented with the

only restriction that trigger outputs had to be defined on the gradient raster time (10 μs). Fully sampled reference scans for both static RSCs of the PIN diode setup were acquired. Noise calibration scans for both RSCs were performed by repeating the reference scans with the flip angle set to 0.

To capture the dynamic RSC switching during k-space acquisition, 20/40-fold readout oversampling was applied for an ADC dwell time of 20/40 μs, resulting in an effective dwell time of 1 μs and a bandwidth of about 195/98 Hz/pixel. Starting at the beginning of each ADC block, RSCs were switched every 10/20 μs. From that, images of the RSC switching dynamics with a time resolution of 1 μs could be obtained by the following procedure: Let $s[j]$, $j = 1, \ldots, \alpha \cdot N_x$ denote the k-space samples collected at ADC index j, where $\alpha = 20, 40$ is the oversampling factor and N_x the matrix size. These data can be reordered to form α sub-k-spaces $s^{(n)}[r] = s[n : \alpha : n + (N_x - 1) \cdot \alpha]$ with $n = 1, \ldots, \alpha$ and $r = 1, \ldots, N_x$, using *MATLAB* notation for indexing. In words, the n-th sub-k-space is formed by retaining every α th sample of each ADC block, starting with the n-th sample. Every sub-k-space obtained in that way corresponds to one time point in the repetitive switching dynamics; thus, Fourier transform of $s^{(n)}$ yields a series of time-resolved images $m^{(n)}$. The k-space locations corresponding to $m^{(n)}$ are shifted by $(n - 1) \cdot \Delta k / \alpha$ with $n = 1, \ldots, \alpha$ and $\Delta k = 1/\text{FOV}$ due to the readout gradient being active during acquisition of the oversampled ADC block. To compensate for the induced linear phase in image space, $m^{(n)}$ is multiplied by a phase factor of the form $\exp\left(-2\pi i \cdot \frac{(n-1)}{\alpha} \cdot \frac{x}{N_x}\right); x = -\frac{N_x}{2}, \ldots, \frac{N_x}{2} - 1$. By means of this procedure, the oversampling allows multiplexing of α different time steps of the switching dynamics during a single k-space acquisition. A schematic of the procedure is shown in Supporting Information Figure S1.

3.4 | Data evaluation

To estimate the receive sensitivities of both configurations, 8-channel k-space data from both reference scans were prewhitened with the corresponding noise correlation matrices and concatenated along the coil axis to form a 16-channel data set. From that, coil sensitivity maps for all coils and RSCs were estimated via ESPIRIT,[6] using the central 24 k-space lines.

The impact of different RSC switching patterns on g-factors was evaluated using Eqs. 2 and 3, with sensitivity maps of both RSCs obtained from the phantom measurement. To enable direct computation of the matrix inverse in Eq. 3, the sensitivity maps originally acquired with a matrix size of 256×256 were downsampled to 96×96.

For the in vivo measurement, images of the switching dynamics with a time resolution of 1 μs were obtained according to the procedure described previously. By averaging over the time steps corresponding to one RSC, coil images of both RSCs were generated to form a virtual 16-channel data set. Retrospective undersampling and SENSE reconstructions were performed for this data set as well as for data sets obtained from the respective static RSCs only, representing the conventional static SENSE case. Parallel imaging reconstructions for all these cases were compared to fully sampled reference reconstructions by means of normalized RMS error (NRMSE), SSIM, and peak SNR ratio (PSNR). g-Factors for both the switched and the static data sets were calculated and compared according to Eq. 3.

4 | RESULTS

Switching the PIN diodes while the ADC is open (i.e., during acquisition of a k-space line) was found to cause spurious signal fluctuations in a timespan of up to 8 μs around the switching event, resulting in image artifacts, as shown in Figure 3. An example of the fluctuations in k-space is shown in Supporting Information Figure S4. The artifact can be strongly reduced in postprocessing by a low-rank + sparse decomposition (robust PCA[29,30]) of the time series in image space. Details on this correction are given in Supporting Information Figures S5 and S6. Alternatively, the artifact can be removed by excluding corrupted samples from the reconstruction, which, in contrast to the robust PCA correction, reduces overall SNR (Supporting Information Figure S6). We are currently investigating the nature of these fluctuations and possible hardware modifications to solve this issue.

Fully sampled single coil images of each RSC are displayed in Figure 4A. It can be seen that the two reconfigurable coil states lead to distinct spatial sensitivity patterns, where configuration 1 shows a single localized region of high sensitivity close to each coil, and configuration 2 exhibits two lobes of high sensitivity. For both configurations, due to the wave behavior of RF at ultra-high field, the sensitivities form different complex patterns of constructive and destructive interference inside the object. Figure 4B,C shows that the different RSCs also lead to different noise correlations among the channels. Both configurations yield different spatial SNR distributions in coil-combined images (Figure 4D–F), where configuration 2 (Figure 4E) gives higher SNR in the center due to the presence of the dipole-like currents, while the average and peak SNR are similar for both configurations. Figure 4 shows that channels 5 and 7 reveal reduced signal in configuration 2 compared with the other channels
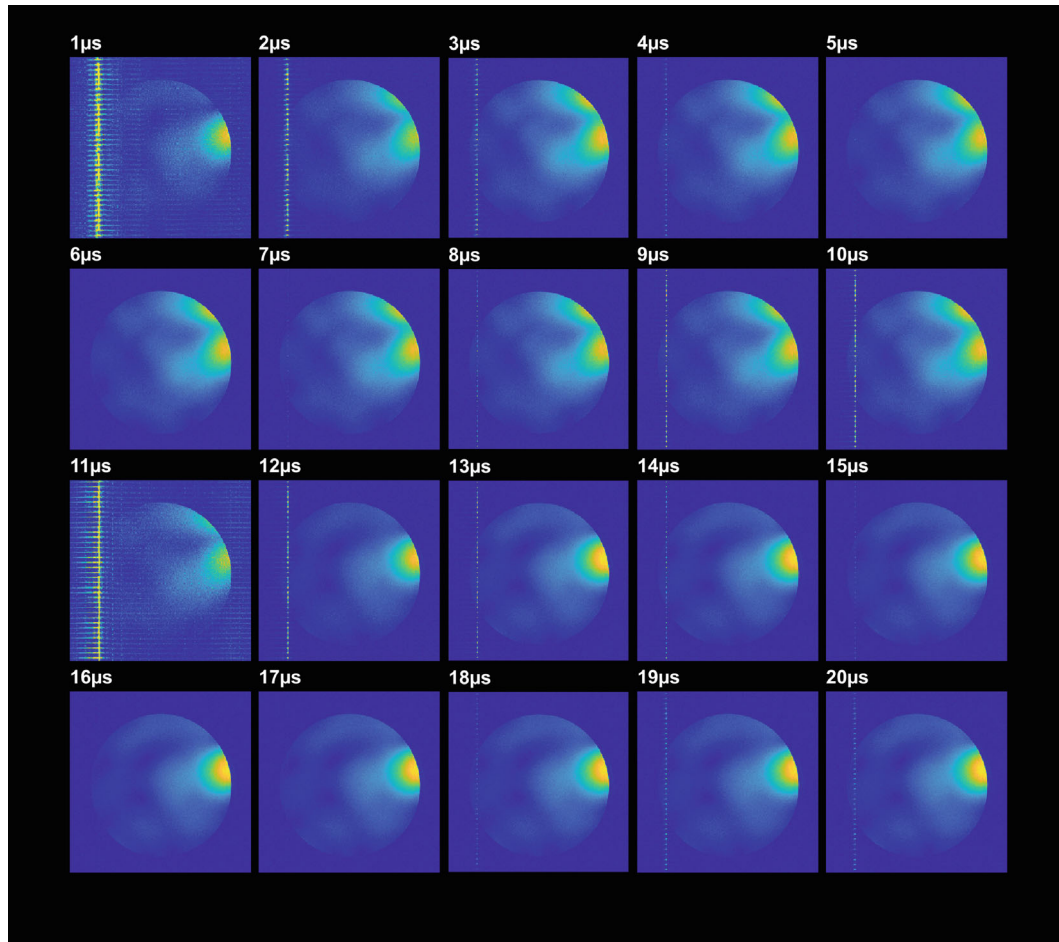
FIGURE 3 Images of the receive sensitivity configuration (RSC) switching dynamics acquired with a time resolution of 1 μs. The RSCs are switched every 10 μs, such that 1–10 μs corresponds to RSC 1 and 11–20 μs to RSC 2

in both configurations. This can be explained by inaccuracies of the self-built prototype regarding cross-talk among elements, tuning and signal attenuation, as well as exact positioning of the phantom inside the coil.

4.1 | g-Factor simulations for different switching patterns

Figure 5 demonstrates how RSC switching during k-space acquisition affects PI properties by showing the effect of different switching patterns on zero-filled inverse FFT reconstruction of a single coil image. The forward acquisition process according to Eq. 2 was simulated with a numerical phantom, and the sensitivities estimated from the phantom measurement that is shown in Figure 4. As shown in Figure 5A, switching RSCs for every phase-encoding (PE) step ("PE switching") results in two-fold aliasing. It is shown in the Supporting Information that the central ghost is weighted by the sum of the two individual sensitivities of each RSC, whereas

the peripheral ghost is weighted by their difference. For two-fold acceleration and PE switching (Figure 5B), there are four strongly overlapping ghosts in the PE direction, which can be understood by noting that the respective partial k-spaces that are weighted by the same RSC (only orange or only blue points in the figure) are effectively 4-fold undersampled. In case of fast RSC switching during acquisition of readout (RO) lines with two-fold oversampling, such that every other ADC sample is weighted by the same RSC ("full RO switching"), non-overlapping ghosts appear in the oversampled RO direction. The corresponding case for 2-fold acceleration and full RO switching is shown in Figure 5D, yielding additional aliasing in the PE direction. In contrast, switching after every second ADC sample (Figure 5E, "half RO switching"), which is similar to applying no read oversampling, the ghosts caused by switching also overlap in the RO direction. By alternating the switching for every other PE step in a CAIPI[31]-like pattern (Figure 5F, "CAIPI switching"), the ghosts caused by switching can be shifted along the PE direction to yield different overlap than in the case of Figure 5E. Looking at
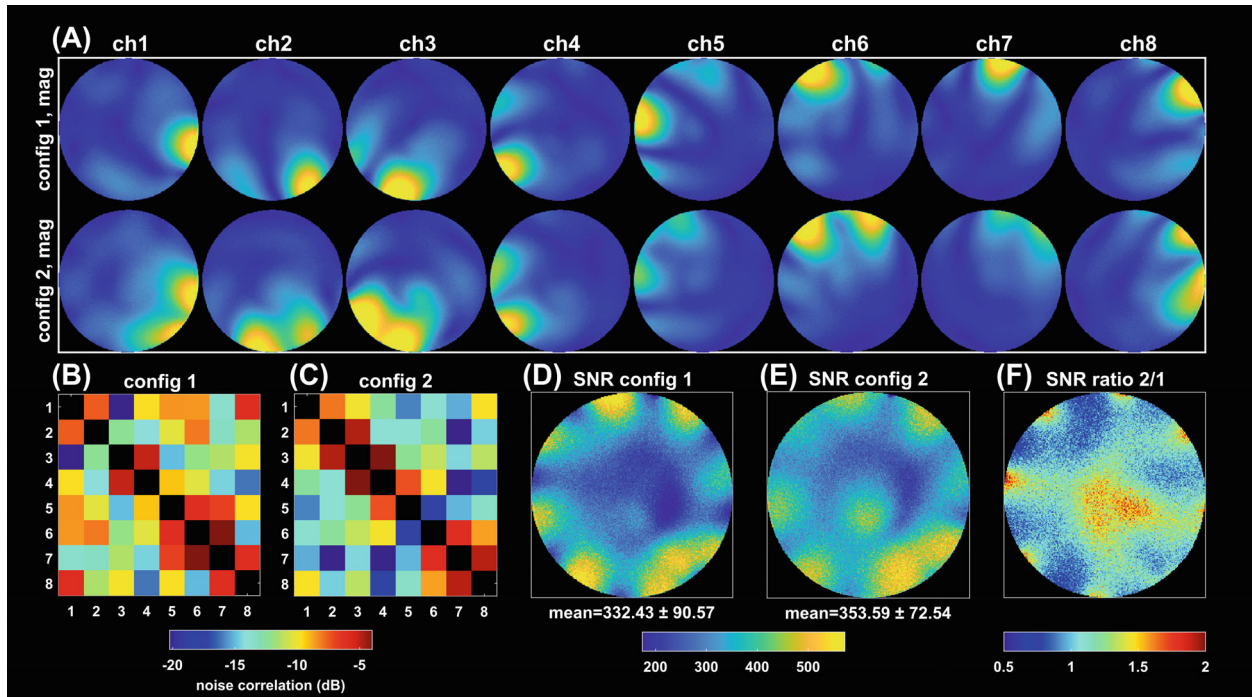
FIGURE 4 A, Fully sampled single coil images for both RSCs acquired in a homogeneous phantom. Note that in addition to the intensity weighting by the receive sensitivities (B_1^-), transmit inhomogeneity affects the spatial intensity patterns (B_1^+ pattern of circularly polarized mode). B,C, Noise covariance matrix for RSC 1 (B) and RSC 2 (C) obtained from two separate noise calibrations scans with flip angle (FA) set to zero. D,E, The SNR for a sum-of-squares coil combination for RSC 1 (D) and RSC 2 (E), calculated via the pseudo-replica method. F, Voxel-wise ratio of SNRs of RSC 2 and RSC 1

the partial k-spaces for each RSC, the last three switching patterns (Figure 5D,E) resemble 2D acceleration patterns along two PE directions in the case of 3D imaging.

Theoretical g-factor calculations for different RSC switching patterns and acceleration factors were performed according to Eqs. 2 and 3, with the sensitivities estimated from the phantom measurement shown in Figure 4. In Figure 6, exemplary g-factor maps for $R = 4$ are displayed. PE switching turns out to yield higher average g-factors than the single static RSCs only, respectively, meaning that there is no PI improvement expected from such RSC switching patterns, regardless of whether switching happens for every line (Figure 6D), every second line, (Figure 6E) or once in the middle of k-space (Figure 6F). This observation can be understood from the aliasing pattern in Figure 5B, where it could be seen that switching along the undersampled direction creates additional overlapping ghosts that need to be disentangled by the SENSE reconstruction. This results in even stronger ill-conditioning than in the case of no RSC switching (Figure 6A,B). Consequently, instead of PE switching, it is preferable to use the configuration that provides better g-factor for all k-space lines. In contrast, RO switching improves g-factors compared with the static RSCs: In case of full RO switching (Figure 6F), g-factors are identical

to the hypothetical case of having all sensitivities of both RSCs statically active at the same time (Figure 6C), thus, in terms of relative PI-related SNR loss, acting like a virtual 16-channel array instead of the actual physical 8 channels.

This can be also explained from the aliasing pattern in Figure 5C,D, where due to the non-overlapping ghosts in RO direction, a single-channel image contains information of both RSCs simultaneously (as sum and difference for each ghost, respectively, which can be easily disentangled). Full RO switching can therefore be seen as a form of time-division multiplexing of RSCs, similar to the results described in Trakic et al.[18] Slower RO switching (Figure 6H) and CAIPI switching patterns (Figure 6F) result in similar, only slightly higher g-factors than full RO switching (Figure 6G). This is because for these switching patterns, there is no strong overlap of the ghosts caused by switching and the ones caused by undersampling (Figure 5E,F), as opposed to the case of PE switching (Figures 5B and 6D).

g-Factor results for different switching patterns and multiple acceleration factors are summarized in Figure 7. PE switching appears to bring no improved PI performance compared with static coil sensitivities (except from slight reduction of maximum g-factor for $R = 4$ and $R = 5$), whereas RO switching can improve g-factors up to the level
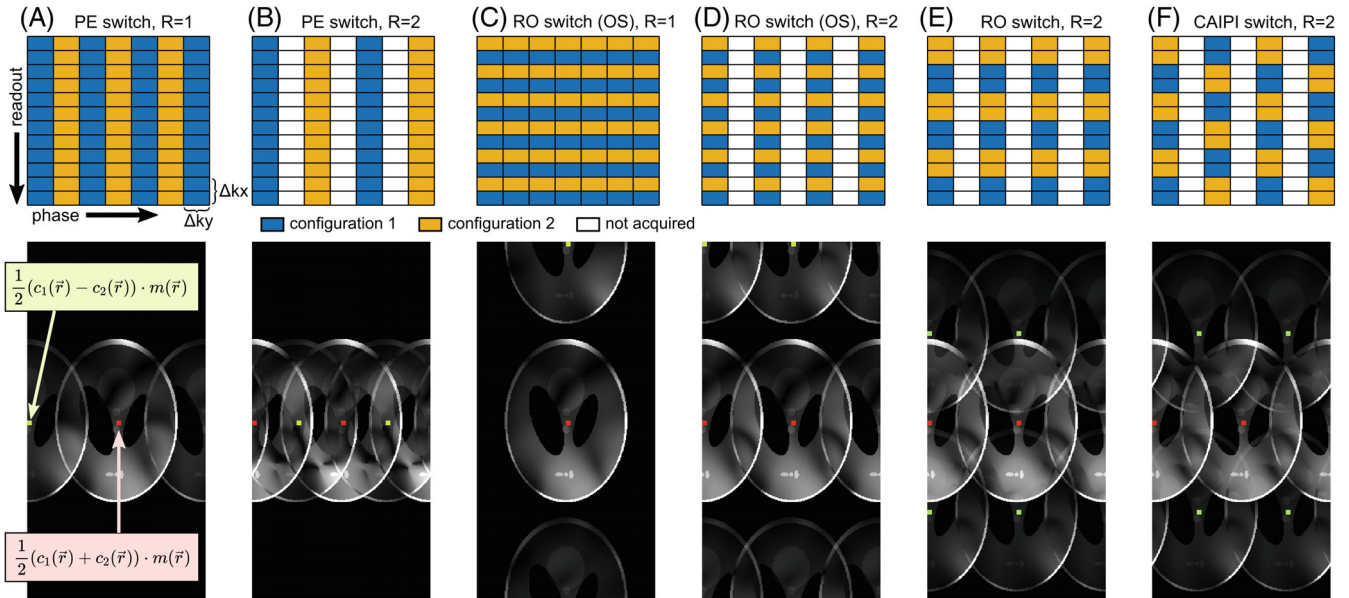
FIGURE 5 Examples of the effect of different RSC switching patterns on plain FFT reconstruction, shown here exemplarily for a single coil image of a numerical phantom. The first row shows the switching pattern schematically in k-space (i.e., which RSC is active at which time point). Note that the readout direction is two-fold oversampled. The second row shows the corresponding FFT reconstructions and overlaid colored markers representing the point-spread function (markers are enlarged for better visibility). Colors of the markers indicate sensitivity weighting of the respective ghost: Red indicates weighted by the sum, and green indicates weighted by the difference of the RSC profiles. A, Switching along the phase-encoding direction ("PE switching") (i.e., alternating between RSCs for every readout line). Even though a full k-space is acquired, 2-fold aliasing occurs. B, PE switching with 2-fold undersampling ($R = 2$), resulting in additional aliasing. C, Switching along the readout direction ("RO switching") (i.e., alternating between RSCs for every ADC sample). This causes ghosts along the readout direction, which do not overlap due to the read oversampling, such that full sensitivity information of both RSCs is simultaneously available. D, Readout switching with 2-fold acceleration, causing additional aliasing in the PE direction. E, RO switching for every second ADC sample (equivalent to applying no read oversampling and alternating for every sample) causes overlapping ghosts in the RO direction. F, Shifting the switching pattern in k-space for every other readout line in a CAIPI-like fashion shifts the ghosts caused by switching along the PE direction, resulting in different overlaps compared with (E)

of having all RSCs active at the same time. Because of these results, in vivo measurements were focused on realizing full RO switching.

4.2 | In vivo results

Fully sampled single coil images together with ESPIRIT sensitivity maps are displayed in Supporting Information Figure S2. To eliminate the switching artifact shown in Figure 3 for the measurement with switched RSCs during acquisition, corrupted data samples close to the switching events were removed from the reconstruction. The PI reconstruction results from retrospectively undersampled data sets of the switched and the static RSC measurements together with corresponding inverse g-factor maps are shown in Figure 8. Difference maps to fully sampled reference reconstructions together with reconstruction quality metrics are shown in Figure 9. Up to an acceleration factor of $R = 3$, there is no visible

difference between switched and static reconstructions, all showing low reconstruction errors with NRMSE below 1.5%, SSIM above 0.8, and PSNR above 36 (Figure 9B–D). For $R = 4$, reconstructions from the static RSCs start to show increased noise amplification and artifacts outside of the brain, which is less pronounced in the switched case (Figures 8A and 9A). For even higher accelerations of $R = 5$ and $R = 6$, the difference between static and switched reconstructions becomes more obvious, with the static reconstructions being severely corrupted, whereas the switched reconstructions are also affected by artifacts, but to a smaller extent. This is also reflected in the quality metrics in Figure 9B–D.

Similar observations can be made for g-factors (Figure 8B). Overall, mean and maximum g-factors are lower for the switched case compared with the static cases (eg, for $R = 4$: max g = 2.4 for switched compared with 3.34 and 3.20 for static RSCs). The difference in g-factors between switched and static becomes more pronounced for higher acceleration factors here as well.
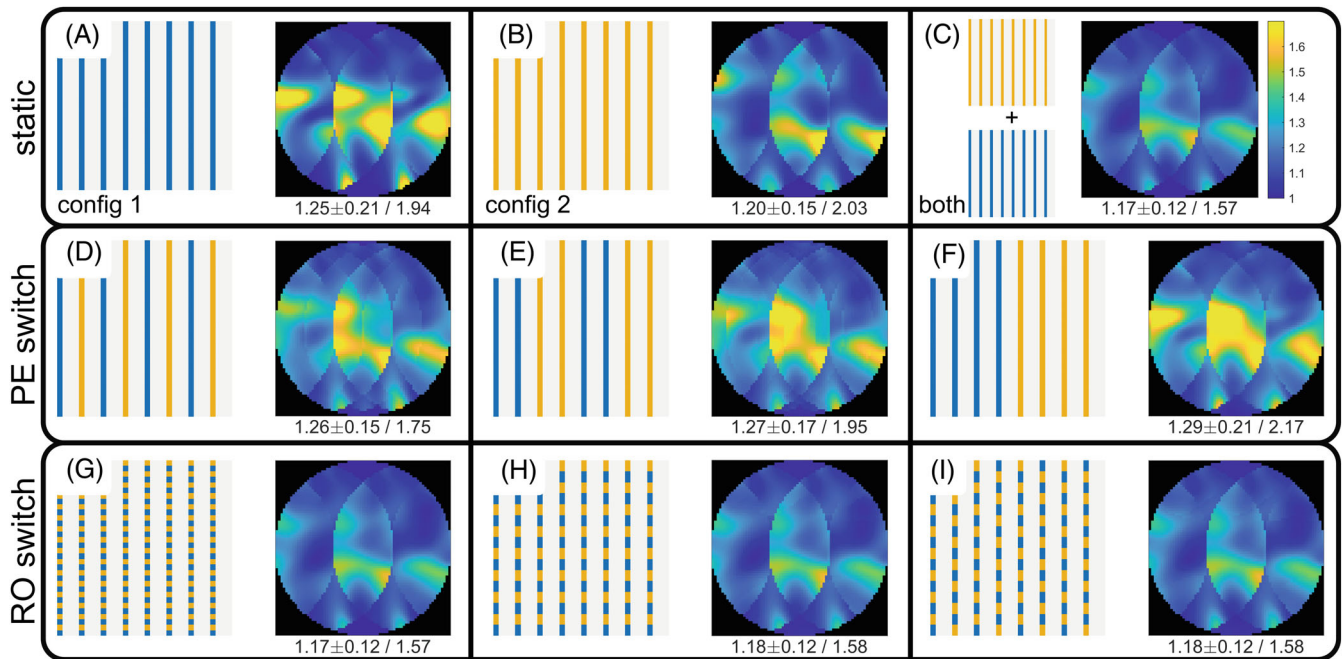
FIGURE 6 Theoretical g-factor maps according to Eq. 3 for different RSC switching patterns and 4-fold acceleration ($R = 4$) with sensitivity maps of both RSCs estimated from the phantom measurement shown in Figure 4A. A,B, Only static RSC1 (A) and RSC2 (B). C, Hypothetical case of combining all sensitivity maps from both RSCs to effectively form a 16-element instead of the physical 8-element receive array. D,E, The PE switching for every (D) and every two (E) acquired lines. F, Switching only once in the center of k-space (similar to partial Fourier imaging for each RSC) yields worse g-factors than the static configurations. G–I, In contrast, RO switching for every ADC sample (G), for every second ADC sample (H), or for every second ADC sample with additional CAIPI-like shifting (I) of the switching pattern for every second acquired line improves g-factors compared to the static configurations. In case (G), g-factors are identical to case (C), as fast RO switching with oversampling acts as time-division multiplexing of both RSCs. Labels indicate mean $\pm$ SD/max of g-factor values for the respective maps. Color scales for all maps are identical

FIGURE 7 Violin plots of theoretical g-factor calculation results for different acceleration factors R and RSC switching patterns. Cross markers indicate the respective mean values of the g-factor maps. Shown results correspond to the switching patterns in Figure 6A–D,G–I
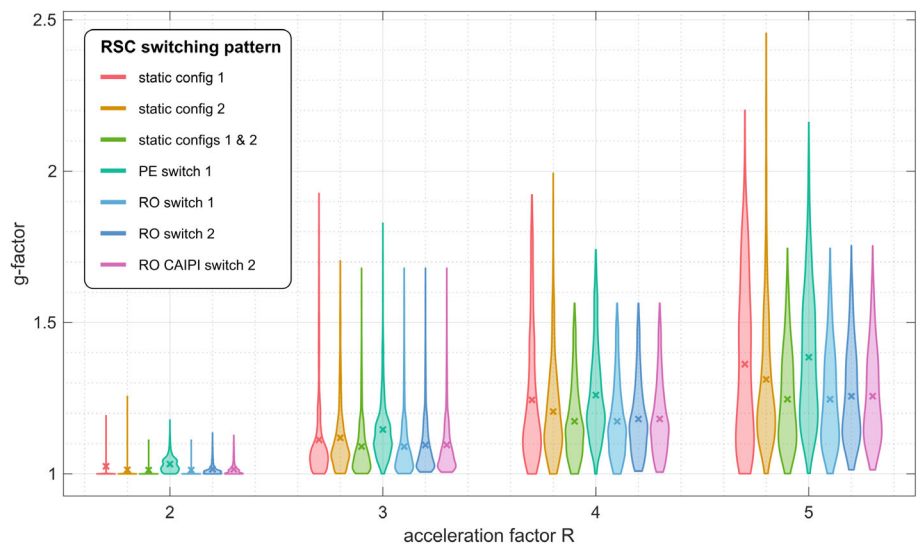
5 | DISCUSSION

In this work, it was shown that time-varying receive sensitivities can be realized by switchable PIN diodes in the receive loops, which alter capacitances and thus B_1^-.

The switching pattern of RSCs during k-space acquisition constitutes a novel degree of freedom for sequence design, offering the potential of improved PI performance. It was found that fast switching of RSCs during acquisition of oversampled k-space readout lines yields the
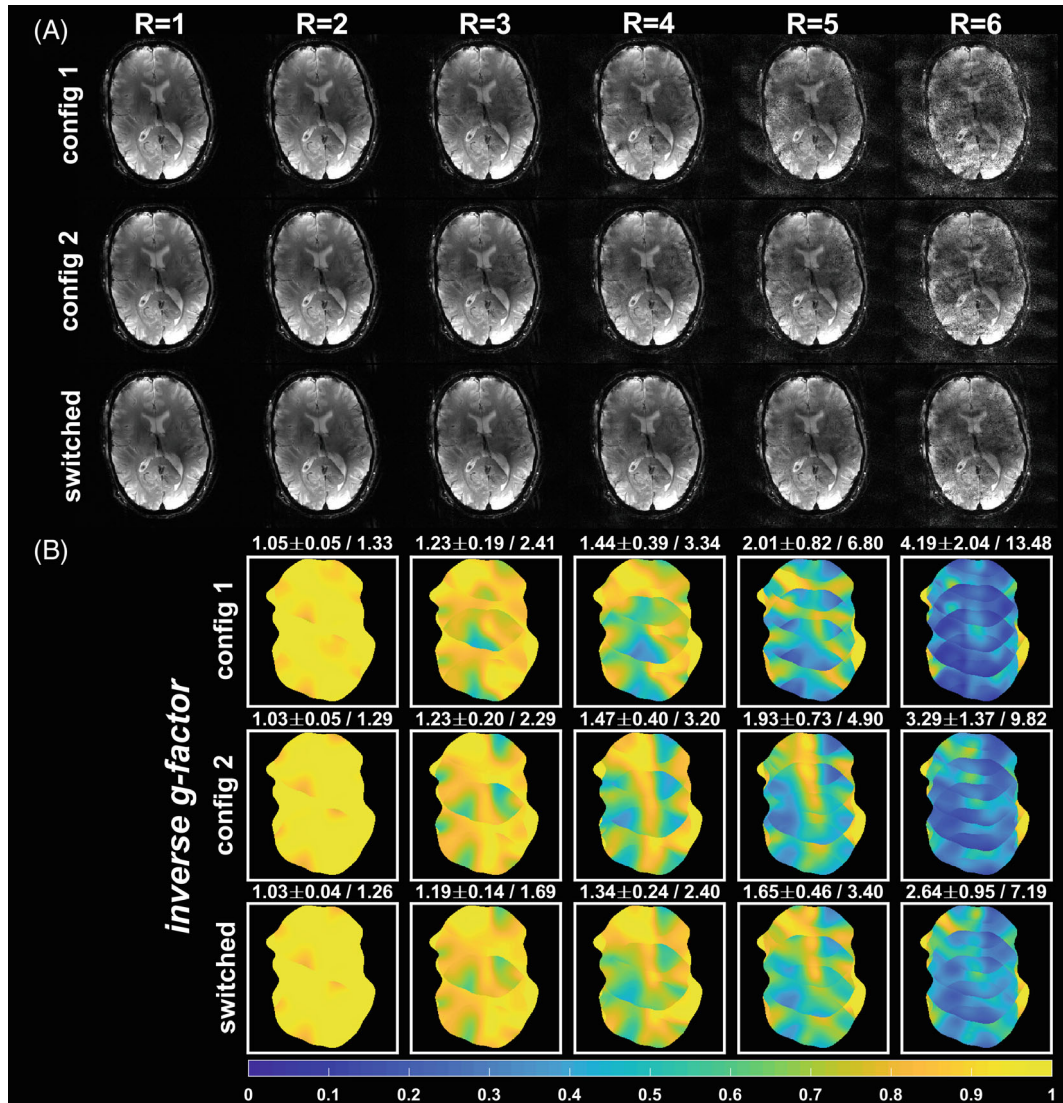
FIGURE 8 A, In vivo reconstruction results for different retrospectively applied acceleration factors, shown for static RSCs 1 ("config 1") and 2 ("config 2") with eight sensitivity maps, respectively, as well as for the case of fast RSC switching during k-space acquisition (full RO switching; see Figures 5D and 6G), which effectively yields 16 multiplexed sensitivity maps. B, Corresponding inverse g-factor maps (i.e., fraction of retained SNR compared with fully sampled, all on the same color scale) obtained according to Eq. 3 for the case of regular Cartesian undersampling and RSC switching. Labels indicate mean $\pm$ SD/max of g-factor values for the respective maps

same g-factors as a hypothetical receiver array with double the number of coils, such that the sensitivities of all RSCs are active at the same time. This observation corresponds to the time-division multiplexing SENSE reconstruction proposed for a rotating receive coil,[18] in which oversampled acquisition with a single rotating receive element could emulate multiple effective receive elements. It should be emphasized that the apparent doubling of receive channels observed here for full RO switching holds only for g-factors, which are a relative quantity describing PI-related SNR loss, and not for absolute SNR. In terms of absolute SNR, a static 16-element array would give a factor of $\sqrt{2}$ higher SNR compared with the dynamic 8-element array with two time-division-multiplexed RSCs, because

the 16-element array could acquire double the number of data samples at a time. Thus, the presented dynamic 8-element array exhibits hybrid receive characteristics of a static 8-element and a static 16-element array. Regarding absolute SNR, it acts like a static 8-element array, whereas in terms of spatial encoding capability (i.e., regarding g-factors, conditioning of the reconstruction problem, and imaging artifacts), it acts like a static 16-element array.

Switching RSCs during an ADC block was found to cause spurious signals visible in a time interval of up to 8 μs around a switching event, which manifested as a line-shaped artifact along the PE direction in the reconstructed images. As shown in the Supporting Information, this artifact can be strongly reduced in
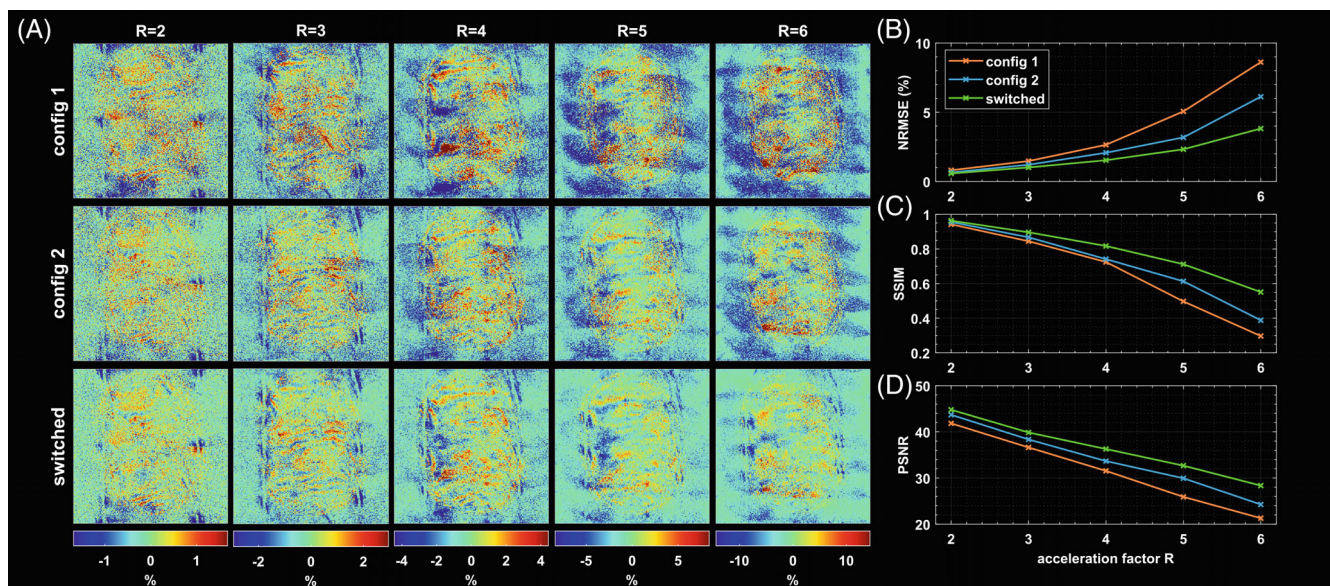
FIGURE 9 Comparison of undersampled reconstructions shown in Figure 8 with the fully sampled reference (first column in Figure 8) by means of difference maps (A) as well as normalized RMS error (NRMSE, lower is better) (B), SSIM (higher is better) (C), and peak SNR (PSNR, higher is better) (D). Color scales are fixed for each acceleration factor

postprocessing by applying a low-rank + sparse decomposition (robust PCA). Alternatively, removing the artifact completely would require discarding 50% of the acquired data samples, which would result in an SNR penalty of $\sqrt{2}$ compared with the ideal case of retaining all samples. In contrast, the robust PCA correction does not cause an SNR penalty (Supporting Information Figure S6). Although the robust PCA correction appears to work reliably, addressing this issue on the hardware level would be desirable, and further investigations are required. One possibility might be to reduce the Q-factor of the PIN-diode driver to mitigate ringing. In addition, we consider adding band-pass filters to the receive coil chain that pass signal at 400 MHz. Another potential solution would be to use extremely fast PIN-diodes with a carrier lifetime below 1 μs. However, faster PIN diodes provide higher series resistance in forward bias, which finally would lead to further degrading in SNR.

The demonstrated "full RO switching" (i.e., effectively switching RSCs between every acquired k-space sample of a two-fold oversampled ADC block) yields the best g-factors of all possible switching patterns. Even faster switching with stronger oversampling does not improve g-factors, as this only increases the distance of the already non-overlapping ghosts in Figure 5C along the extended FOV, which does not yield additional image-encoding information. Similarly, all other switching patterns that involve slower switching necessarily lead to overlapping ghosts, and thus result in a g-factor penalty.

Still, also for full RO switching, the observed improvements of g-factors and reconstruction quality compared

with the static RSCs (i.e., conventional SENSE) are moderate. The main limitation is here that sensitivity profiles of both RSCs are still similar to a certain extent and thus yield only partially independent spatial information. Consequently, future work will focus on new ideas to modify receive circuitry or geometry, to achieve stronger B_1^- modulations.

As for all SENSE-based methods, the presented approach requires explicit sensitivity estimation in image space for all RSCs. This does not require additional scan time compared with a conventional prescan as used for static PI, as coil sensitivities of both RSCs can be simultaneously estimated from a prescan acquired with full RO switching that yields unaliased low-resolution images multiplexed from both RSCs.

In the present work, only Cartesian k-space trajectories were considered. As it is known that non-Cartesian trajectories can have favorable PI properties due to incoherent aliasing and better exploitation of coil sensitivity variations,[32] combining RSC switching with trajectories like radial or spiral might be an interesting next step. First insights from combining the proposed RSC switching with a wave-like trajectory[14] are given in Supporting Information Figure S8. Furthermore, advanced nonlinear reconstruction methods like compressed sensing[33] or deep learning[34] might benefit from the additional degree of freedom in signal encoding offered by RSC switching. Combining such methods with time-varying sensitivities is left to future research.

Ultimately, the maximum achievable PI acceleration for conventional linear reconstruction, which still allows

for acceptable g-factors and reconstruction quality, is fundamentally limited by electrodynamics, as the maximum possible spatial variation of coil sensitivities is determined by the RF wavelength at certain B_0.[35,36] In general, our approach benefits from the shorter RF wavelength at higher B_0 fields, which results in stronger spatial variation of sensitivity patterns both for single elements and between RSCs. Electromagnetic simulation of the same loop coil at 3T shows that there is only very small variation between RSCs, such that no gain in PI performance can be expected (Supporting Information Figure S7). Because 7T MRI is increasingly gaining relevance for clinical imaging, we expect our approach to be most suitable for improving image quality or accelerating high-resolution 7T imaging.

In principle, the proposed method can be extended to a higher number of receive channels (e.g., 32). This would require optimization of a single element to obtain the most efficient ratio in currents, and thus most beneficial modulation of sensitivity profiles. However, PI performance for high acceleration factors is expected to saturate with increasing number of switchable receive elements or distinct configurations per element, as the ultimate intrinsic SNR limit is approached.[35,36] Still, assuming a limited number of available receive channels, the proposed method of sensitivity multiplexing might be a way to improve PI applications without expensive modifications to the scanner's receive chain.

6 | CONCLUSIONS

The reconfigurable receive coil array with fast switching PIN diodes offers an additional degree of freedom for image encoding by enabling time-varying receive sensitivities. This can improve PI performance (i.e., yield lower g-factors and smaller reconstruction artifacts compared with static receive elements). Possible improvements depend crucially on how configurations are switched during k-space acquisition and on spatial independence of the different receive profiles.

DATA AVAILABILITY STATEMENT
Additional details on the presented design are openly available at https://github.com/fglang/switchedSENSE

ORCID
Felix Glang https://orcid.org/0000-0003-3506-4947
Anton V. Nikulin https://orcid.org/0000-0001-5640-8281
Rahel Heule https://orcid.org/0000-0002-4589-6483
Nikolai Avdievich https://orcid.org/0000-0001-7608-0869
Klaus Scheffler https://orcid.org/0000-0001-6316-8773

REFERENCES
1. Roemer PB, Edelstein WA, Hayes CE, Souza SP, Mueller OM. The NMR phased array. *Magn Reson Med.* 1990;16:192-225.
2. Pruessmann KP, Weiger M, Scheidegger MB, Boesiger P. SENSE: sensitivity encoding for fast MRI. *Magn Reson Med.* 1999;42:952-962.
3. Griswold MA, Jakob PM, Heidemann RM, et al. Generalized autocalibrating partially parallel acquisitions (GRAPPA). *Magn Reson Med.* 2002;47:1202-1210.
4. Uecker M, Hohage T, Block KT, Frahm J. Image reconstruction by regularized nonlinear inversion—joint estimation of coil sensitivities and image content. *Magn Reson Med.* 2008;60:674-682.
5. Lustig M, Pauly JM. SPIRiT: iterative self-consistent parallel imaging reconstruction from arbitrary k-space. *Magn Reson Med.* 2010;64:457-471.
6. Uecker M, Lai P, Murphy MJ, et al. ESPIRiT—an eigenvalue approach to autocalibrating parallel MRI: where SENSE meets GRAPPA. *Magn Reson Med.* 2014;71:990-1001.
7. Shin PJ, Larson PEZ, Ohliger MA, et al. Calibrationless parallel imaging reconstruction based on structured low-rank matrix completion. *Magn Reson Med.* 2014;72:959-970.
8. Shajan G, Kozlov M, Hoffmann J, Turner R, Scheffler K, Pohmann R. A 16-channel dual-row transmit array in combination with a 31-element receive array for human brain imaging at 9.4 T. *Magn Reson Med.* 2014;71:870-879.
9. Avdievich NI, Giapitzakis I-A, Bause J, Shajan G, Scheffler K, Henning A. Double-row 18-loop transceive–32-loop receive tight-fit array provides for whole-brain coverage, high transmit performance, and SNR improvement near the brain center at 9.4T. *Magn Reson Med.* 2019;81:3392-3405.
10. Weiger M, Pruessmann KP, Leussler C, Röschmann P, Boesiger P. Specific coil design for SENSE: a six-element cardiac array. *Magn Reson Med.* 2001;45:495-504.
11. de Zwart JA, Ledden PJ, Kellman P, van Gelderen P, Duyn JH. Design of a SENSE-optimized high-sensitivity MRI receive coil for brain imaging. *Magn Reson Med.* 2002;47:1218-1227.
12. Ledden PJ, Mareyam A, Wang S, van Gelderen P, Duyn J. 32 channel receive-only SENSE array for brain imaging at 7T. *Proceedings of the 15th Annual Meeting of ISMRM* Berlin, Germany, 2007.
13. Gruber B, Stockmann JP, Mareyam A, et al. A 128-channel head coil array for cortical imaging at 7 tesla. *Proceedings of the 29th Annual Meeting of ISMRM [Virtual]*. 2021.
14. Bilgic B, Gagoski BA, Cauley SF, et al. Wave-CAIPI for highly accelerated 3D imaging. *Magn Reson Med.* 2015;73:2152-2162.
15. Wang H, Tam LK, Constable RT, Galiana G. Fast rotary nonlinear spatial acquisition (FRONSAC) imaging. *Magn Reson Med.* 2016;75:1154-1165.

16. Scheffler K, Loktyushin A, Bause J, Aghaeifar A, Steffen T, Schölkopf B. Spread-spectrum magnetic resonance imaging. *Magn Reson Med.* 2019;82:877-885.

17. Li M, Zuo Z, Jin J, et al. Highly accelerated acquisition and homogeneous image reconstruction with rotating RF coil array at 7T—a phantom based study. *J Magn Reson.* 2014;240:102-112.

18. Trakic A, Wang H, Weber E, et al. Image reconstructions with the rotating RF coil. *J Magn Reson.* 2009;201:186-198.

19. Li M, Weber E, Jin J, et al. Radial magnetic resonance imaging (MRI) using a rotating radiofrequency (RF) coil at 9.4 T. *NMR Biomed.* 2018;31:e3860.

20. Li M, Jin J, Zuo Z, et al. In vivo sensitivity estimation and imaging acceleration with rotating RF coil arrays at 7 tesla. *J Magn Reson.* 2015;252:29-40.

21. Glang F, Buckenmaier K, Bause J, Loktyushin A, Avdievich NI, Scheffler K. Investigations on accelerated imaging at 9.4T with electronically modulated time-varying receive sensitivities. *Proceedings of the 29th Annual Meeting of ISMRM [Virtual].* 2021. #0910.

22. Fessler JA, Sutton BP. Nonuniform fast Fourier transforms using min-max interpolation. *IEEE Trans Signal Process.* 2003;51:560-574.

23. Pruessmann KP, Weiger M, Börnert P, Boesiger P. Advances in sensitivity encoding with arbitrary k-space trajectories. *Magn Reson Med.* 2001;46:638-651.

24. Robson PM, Grant AK, Madhuranthakam AJ, Lattanzi R, Sodickson DK, McKenzie CA. Comprehensive quantification of signal-to-noise ratio and g-factor for image-based and k-space-based parallel imaging reconstructions. *Magn Reson Med.* 2008;60:895-907.

25. Mispelter J, Lupu M, Briguet A. *NMR Probeheads for Biophysical and Biomedical Experiments.* Imperial College Press and Distributed by World Scientific Publishing; 2006.

26. Vaidya MV, Collins CM, Sodickson DK, Brown R, Wiggins GC, Lattanzi R. Dependence of and field patterns of surface coils on the electrical properties of the sample and the MR operating frequency. *Concepts Magn Reson Part B Magn Reson Eng.* 2016;46:25-40.

27. Lakshmanan K, Cloos M, Brown R, Lattanzi R, Sodickson DK, Wiggins GC. The "Loopole" antenna: a hybrid coil combining loop and electric dipole properties for ultra-high-field MRI. *Concepts Magn Reson Part B Magn Reson Eng.* 2020;2020:e8886543.

28. Avdievich NI. Transceiver-phased arrays for human brain studies at 7 T. *Appl Magn Reson.* 2011;41:483-506.

29. Candes EJ, Li X, Ma Y, Wright J, Candès EJ, Li X, Ma Y, Wright J. Robust principal component analysis?. *Journal of the ACM*. 2021;58:1-37. https://doi.org/10.1145/1970392.1970395

30. Aravkin A, Becker S, Cevher V, Olsen P. A variational approach to stable principal component pursuit. *Proceedings of the Conference on Uncertainty in Artificial Intelligence (UAI)*; AUAI Press; 2014.

31. Breuer FA, Blaimer M, Mueller MF, et al. Controlled aliasing in volumetric parallel imaging (2D CAIPIRINHA). *Magn Reson Med*. 2006;55:549-556.

32. Wright KL, Hamilton JI, Griswold MA, Gulani V, Seiberlich N. Non-Cartesian parallel imaging reconstruction. *J Magn Reson Imaging.* 2014;40:1022-1040.

33. Lustig M, Donoho D, Pauly JM. Sparse MRI: the application of compressed sensing for rapid MR imaging. *Magn Reson Med.* 2007;58:1182-1195.

34. Hammernik K, Klatzer T, Kobler E, et al. Learning a variational network for reconstruction of accelerated MRI data. *Magn Reson Med.* 2018;79:3055-3071.

35. Ohliger MA, Grant AK, Sodickson DK. Ultimate intrinsic signal-to-noise ratio for parallel MRI: electromagnetic field considerations. *Magn Reson Med.* 2003;50:1018-1030.

36. Wiesinger F, Boesiger P, Pruessmann KP. Electrodynamics and ultimate SNR in parallel MR imaging. *Magn Reson Med.* 2004;52:376-390.

SUPPORTING INFORMATION

Additional supporting information may be found in the online version of the article at the publisher's website.

Figure S1. Schematic of the procedure to obtain multiplexed coil images of two receive sensitivity configurations (RSCs) by rapid switching during k-space acquisition, as described in the Methods section. The top row shows a schematic ADC block, corresponding to a readout line in k-space. Strong readout oversampling (oversampling factor α) is applied such that every effective k-space sample (black boxes) is subdivided into α samples with a dwell time of 1 μs. The switchable receive array is controlled by a sequence-defined trigger to toggle RSCs every $\alpha/2$ samples. The acquired signal can be reordered into sub-k-spaces $s^{(n)}$ by retaining every αth sample, starting at the n-th sample (second row). Fast Fourier transform (FFT) of these sub-k-spaces yields images of the RSC switching dynamics with a time resolution of 1 μs (third row). To obtain correct phase information for these images, the linear phase induced by the readout gradient during oversampling must be compensated (fourth row). Averaging over the time steps corresponding to one RSC yields multiplexed high-SNR coil images of both RSCs (fifth row). The ADC samples close to the switching events (indicated by gray crosses in the first row) are affected by signal fluctuations and can be removed from the averaging to remove the artifact that is observed otherwise

Figure S2. Individual coil images and sensitivity maps obtained via ESPIRIT (magnitude and phase) from an in vivo measurement using the prototype receive array with two fast switchable RSCs. For the shown images, fully sampled datasets were acquired for both RSCs separately

Figure S3. Simulated H-field distributions (first row) corresponding to different surface current distributions (second row) as in Figure 1

Figure S4. Demonstration of the signal fluctuations caused by fast PIN diode switching in k-space (top) and image space (bottom). Displayed are the central k-space lines (real parts only) corresponding to the first five images of the time-resolved switching dynamics shown in Figure 3. The acquired data show a strong sinusoidal corruption close to the switching (at t = 1 μs) that decays over time,

which corresponds to a localized spike in the frequency spectrum (i.e., image space). Note that the shown k-space data have been interpolated by zero-padding for better visibility of sinusoidal time courses

Figure S5. Correction of switching artifact by robust principal component analysis (robust PCA). A, Images of the RSC switching dynamics acquired with a time resolution of 1 μs. The RSCs are switched every 10 μs, such that 1–10 μs corresponds to RSC1 and 11–20 μs corresponds to RSC 2 (time steps in microseconds, indicated by white numbers). B, Low-rank component L of the image series obtained by robust PCA. C, Sparse component S obtained by robust PCA. Regularization weights for robust PCA were chosen such that rank(L) = 2

Figure S6. Comparison of two methods (discarding samples and robust PCA) to reduce the image artifact caused by fast PIN diode switching. A, The SNR for the case of including all acquired data. B, The SNR after discarding corrupted data samples close to the switching events (50% of the total number of samples). C, The SNR after reconstruction with robust PCA correction as shown in Figure 3. D,E, The corresponding relative decrease in SNR with respect to (A). F,G, Corresponding histograms. All SNR maps were obtained by generating $N = 200$ pseudo replica

Figure S7. Simulation of the proposed reconfigurable loop coil at 3T. Shown are B_1 fields for the case of a conventional loop (top), high capacitance in the left and low capacitance in the right arm (bottom left) and vice versa (bottom right)

Figure S8. Theoretical g-factor maps for a four-fold accelerated ($R=4$) 2D wave trajectory (8 cycles, amplitude $R/2 \cdot \Delta k_y$, 2-fold oversampling) and with sensitivity maps of both RSCs estimated from the phantom measurement, as in Figure 6 in the main text. Results are given for (A) static RSC1, (B) static RSC 2, (C) the case of switching RSCs for every ADC sample and (D) every second ADC sample. Second row shows exemplary three lines of the trajectory in k-space, where color of the markers indicates applied RSC. Numbers below the g-factor maps indicate mean ± std / max of g-factor values across the images.

B.2. Publication 2

Nikulin, A. V.; Glang, F.; Avdievich, N.; Bosch, D.; Steffen, T.; Scheffler, K.
Reconfigurable Dipole Receive Array for Dynamic Parallel Imaging at Ultra-High Magnetic Field.

RESEARCH ARTICLE

Magnetic Resonance in Medicine

Reconfigurable dipole receive array for dynamic parallel imaging at ultra-high magnetic field

Anton V. Nikulin[1,2,3] | Felix Glang[1] | Nikolai I. Avdievich[1] |
Dario Bosch[1,2] | Theodor Steffen[1] | Klaus Scheffler[1,2]

[1]High-Field MR Center, Max Planck Institute for Biological Cybernetics, Tübingen, Germany

[2]Department for Biomedical Magnetic Resonance, University of Tübingen, Tübingen, Germany

[3]Center of Photonics and 2D Materials, Moscow Institute of Physics and Technology, Dolgoprudny, Russia

Correspondence
Anton V. Nikulin, High-Field MR Center, Max Planck Institute for Biological Cybernetics, Tübingen, Germany.
Email: a.v.nikulin@live.ru

Purpose: To extend the concept of 3D dynamic parallel imaging, we developed a prototype of an electronically reconfigurable dipole array that provides sensitivity alteration along the dipole length.

Methods: We developed a radiofrequency array coil consisting of eight reconfigurable elevated-end dipole antennas. The receive sensitivity profile of each dipole can be electronically shifted toward one or the other end by electrical shortening or lengthening the dipole arms using positive-intrinsic-negative-diode lump-element switching units. Based on the results of electromagnetic simulations, we built the prototype and tested it at 9.4 T on phantom and healthy volunteer. A modified 3D SENSE reconstruction was used, and geometry factor (g-factor) calculations were performed to assess the new array coil.

Results: Electromagnetic simulations showed that the new array coil was capable of alteration of its receive sensitivity profile along the dipole length. Electromagnetic and g-factor simulations showed closely agreeing predictions when compared to the measurements. The new dynamically reconfigurable dipole array provided significant improvement in geometry factor compared to static dipoles. We obtained up to 220% improvement for 3×2 ($R_y \times R_z$) acceleration compared to the static configuration case in terms of maximum g-factor and up to 54% in terms of mean g-factor for the same acceleration.

Conclusion: We presented an 8-element prototype of a novel electronically reconfigurable dipole receive array that permits rapid sensitivity modulations along the dipole axes. Applying dynamic sensitivity modulation during image acquisition emulates two virtual rows of receive elements along the z-direction, and therefore improves parallel imaging performance for 3D acquisitions.

KEYWORDS
coil sensitivities, parallel imaging, reconfigurable RF coil, SENSE, ultra-high field MRI

Anton V. Nikulin and Felix Glang contributed equally to this work.

1 | INTRODUCTION

Acceleration of imaging speed has been one of the most important and challenging aims in MRI within the last three decades.[1–3] Approximately two decades ago, the landscape for rapid MRI changed dramatically with the invention of parallel imaging techniques such as SENSE, Simultaneous acquisition of spatial harmonics, GRAPPA, and others.[2–4] Faster scanning is of utmost importance for all clinical MRI applications to guarantee feasibility and patient comfort, as well as to avoid potential subject motion and allow dynamic imaging of contrast changes (e.g., in angiography or functional MRI).

Fundamental problem of all acceleration techniques is the decrease in image SNR with increasing imaging speed.[5] SNR of accelerated parallel imaging is inevitably decreased by $\sqrt{R}$, where R is the acceleration factor, compared to fully sampled non-accelerated scanning.[2] An additional SNR penalty, characterized by the so-called geometry factor (g-factor), is caused by partially dependent or overlapping receive sensitivity profiles.[2] A common way of minimizing the g-factor is increasing the number of elements in the RF array. Receive (Rx) array coils with an element count of 64[6] and higher, that is, 96[7] and 128,[8] have been shown to substantially minimize g-factor values. However, the number of elements in the Rx-array is limited by the number of available Rx-channels of an MRI scanner. An additional limit of parallel imaging is the number of array elements that can be arranged around the object. Increasing the number of elements whereas keeping the same size of the array housing is associated with a corresponding decrease of the element's size, and, therefore, a decrease in the magnetic field penetration depth. The latter leads to an increase of the relative contribution of the noise produced by the array element itself (e.g., losses in conductor, electronic components, and radiation) in comparison to the sample noise, and hence, can compromise SNR.[9]

Recently, we proposed a novel type of parallel imaging acquisition based on the dynamic modulation of the sensitivity profiles of local RF receive coils at ultra-high field strength.[10] Conventional parallel imaging relies on static sensitivity patterns of local receive coils, which is then used to accelerate image acquisition. This principle can be fundamentally expanded if these static sensitivity profiles are rapidly modulated during signal acquisition. Dynamic modulation virtually increases the number of array elements without decreasing their size, and therefore, improves parallel imaging and preserves elements' SNR. In previous works,[10] we presented a novel approach based on dynamically altering the receive sensitivity profile of surface loop elements using fast-switching positive-intrinsic-negative (PIN)-diodes or varactor diodes

during acquisition. This shifts the current distribution along the loop length and leads to two distinct receive sensitivity patterns within a single receive element during signal reception.[10] The spatial difference between the two distinct configurations within a single coil element decreases the g-factor compared to a single and static receive sensitivity profile. However, our previous design allows to alter the receive sensitivity profile only in the transverse plane, but not along the z-axis, which is allowed in the new design based on reconfigurable dipoles.

In this work, we proposed a novel elevated-end reconfigurable RF Rx array coil design based on short folded-end dipole elements.[11,12] The key idea of the folded-end dipole is moving the ends of the antenna, which generate the highest electrical field and lowest current, away from the tissue. As a result, the RF coil resonant frequency is much less sensitive to change of loading produced by variation of the human head size. In addition, using the folded-end dipole design, we load only the central part of the antenna where the current distribution is more uniform. This extends the distribution of the RF magnetic field in the longitudinal direction. The previously described shape of the folded-end dipole[11,12] is just one of the possible ways of making the folded-end dipole antenna more compact. In this work, to make the adjustment of the RF coil more convenient, we elevated the dipoles ends and bent them in the opposite direction compared to the original design.[11] By switching between inductive and capacitive impedance inserted in both dipole's arms, we could increase or shorten the electrical lengths of each arm, and thereby, alter the receive sensitivity pattern of the dipole element by shifting the maximum of the current along the dipole length toward one or the other end of the dipole. Therefore, one physical element supports two asymmetrical RF field patterns, which can be switched within ~1 μs using fast PIN-diodes. By dynamically switching the sensitivity profiles during acquisition, a single dipole element produces two virtual elements and significantly improves performance of parallel imaging for acceleration in planes, which include the head-to-feet (along the magnet axis) dimension. As a proof of concept, we developed and tested both using phantom and in vivo a novel reconfigurable 8-element receive RF dipole array coil for brain imaging at 9.4 T.

2 | METHODS

2.1 | The basic principle and design of the reconfigurable dipole antenna

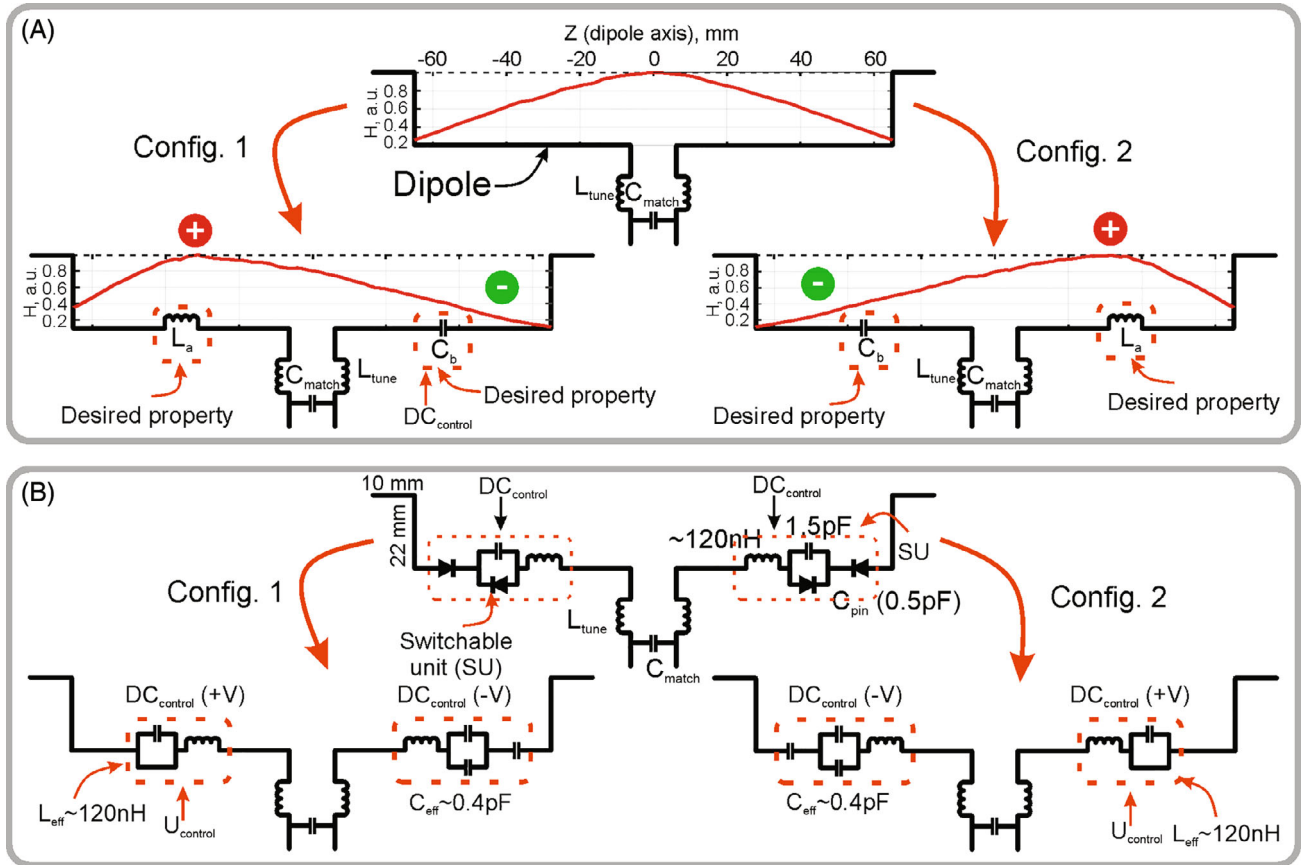Figure 1A shows the principle of the reconfigurable dipole antenna element, which is based on manipulation of the

FIGURE 1 Principle of the reconfigurable dipole antenna. (A) Schematic of the single conventional dipole, its magnetic field, H, distribution and equivalent schematics of the reconfigurable dipole with modified field distribution. (B) Schematic of the reconfigurable dipole based on fast switching positive-intrinsic-negative (PIN)-diodes. PIN-diodes allow switching between inductive and capacitive impedances (properties) in two opposite arms as shown by the arrows.

current distribution along the dipole length. For that purpose, we inserted a home-made electronically controlled switchable unit (SU) shown in Figure 1B (dashed line). This SU can change its impedance between capacitive and inductive, in each arm of the dipole depending on the applied DC voltage. During acquisition SUs are activated in such a way that one arm of the dipole has an inserted inductor while the other arm has a capacitor (Figure 1A). Because electrical lengths of the dipole arms become different, the electrical center (maximum of the current) moves toward the inductive impedance. This effect was shown previously in fractionated dipoles.[13] The effect was used to adjust the electrical length of the dipole while keeping the physical length unchanged. As a result, the maximum of the RF magnetic field generated by the dipole also moves from the center of the dipole to the middle of the left or the right arm. By dynamically altering the dipole's sensitivity profile during the MRI acquisition, one can reduce the g-factors and therefore, improve accelerated 3D imaging.

Figure 1B shows the proposed design of the reconfigurable dipole element. In this design, electronically

controlled SUs based on PIN-diodes are inserted in each arm of the dipole. If the PIN diode is shorted (positively biased), the impedance of SU becomes inductive, which effectively increases the dipole electrical length. When the PIN diode is negatively biased, the impedance of the capacitors compensates the inductive impedance and the whole impedance of SU becomes capacitive, which corresponds to a decrease in the electrical length.

2.2 | Electromagnetic simulations

In simulations, we considered an array of 8 elevated-end dipole[11] elements equally distributed around a cylindrical surface with diameter of 210 mm as shown in Figure 2A. Each dipole had a "loaded" (closest to the sample part of the dipole) straight part of 130 mm and 10-mm elevated-ends placed at the height of 22 mm from the flat part of the dipole. The total length of the dipole antenna measured 150 mm. In the middle of each dipole, we placed the 50 Ω feeding port and the matching circuit as shown in Figure 1A. The flat parts of the dipoles were
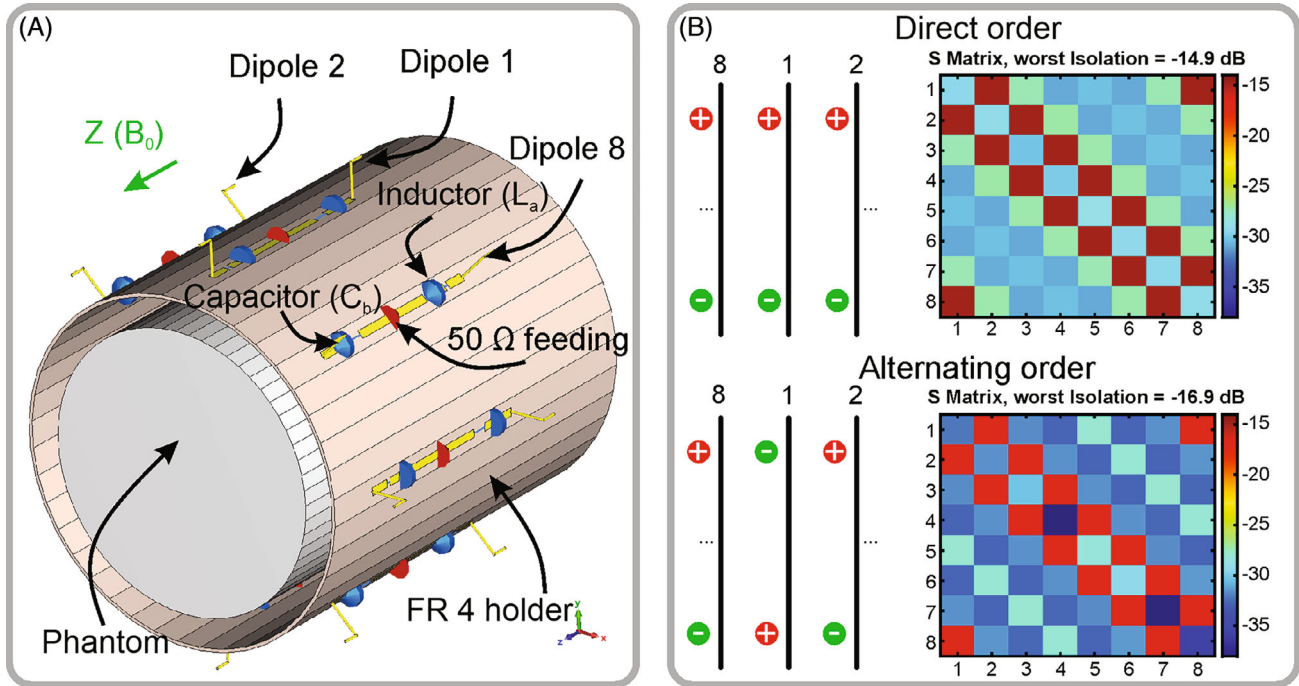
FIGURE 2 Details of the reconfigurable dipole array. (A) Geometry of the 8-element receive dipole array loaded by the homogeneous phantom. (B) Two different scenarios of dipole driving. Here, "+" shows the maximum of the current, whereas "−" shows its minimum as shown in Figure 1A.

modeled as planar copper (lossy copper: $\sigma = 5.8 \times 10^7$) strips of 0.035 mm in thickness and 5 mm in width. The elevated-ends of each dipole were modeled using lossy copper wire with 1.5-mm radius. In the middle of one arm in each dipole we placed an inductor of 120 nH, whereas a capacitor of 0.5 pF was placed in the opposite arm (Figure 2A). Each capacitor also included a series inductor of 1 nH and resistor of 0.08 Ω. The dipoles were equally distributed around the FR4 (CST Studio Suite 2021 material library: $\varepsilon_r = 4.3$; tg δ = 0.025) holder of 210 mm in diameter, 2 mm in thickness, and 265 mm in length.

To simulate the RF coil, we used the frequency domain solver of the commercial software CST Studio Suite 2021 (Dassault Systèmes). The mesh optimization was performed at 400 MHz with 15 to 20 optimization passes. The convergence threshold was set to 0.02 as all s-parameters criteria. The simulations of the 8-elements array were performed in the frequency range of 380 to 420 MHz with 15 frequency points. The number of mesh cells was in the range of 378 to 640 thousand tetrahedrons. The coil was simulated in the presence of a homogeneous cylindrical phantom ($\varepsilon_r = 58.3$, $\sigma = 0.64$ S/m at 400 MHz) of 170 mm in diameter and 200 mm in length. In addition, we tested two different driving scenarios of the dipoles (Figure 2B). These scenarios are called "direct" and "alternating" order. In the "direct" driving scenario, all dipoles are switched in the same manner (i.e., all inductive impedances are active at the bottom or top part of the dipoles) whereas capacitive

impedances are active at the opposite part. In the "alternating" scenario, all dipoles are switched in the way that when the first dipole has the inductive impedance at the top part and capacitive at the bottom, the next dipole has the opposite configuration.

To tune and match each dipole to 400 MHz (^{1}H frequency at 9.4 T), we used co-simulations (CST Schematic). Depending on the design (alternating or direct order) as shown in Figure 1B, each dipole was tuned in co-simulations by a series inductor L_{tune} in the range of 15 to 52 nH and matched by a parallel capacitor C_{match} in the range of 7.5 to 12 pF depending on the setup. The final circuit is shown in Figure 2A,B. After that, field combine task was performed to obtain the receive fields from all independent channels. The simulated B_1^- maps were obtained from H-field monitors using an embedded CST macro. All field maps were obtained for 1 W of stimulated power at the coil input.

2.3 | G-factor simulations

Parallel imaging in MRI leads to an inevitable SNR loss by a factor of $\sqrt{R}$ compared to a full Nyquist-sampled acquisition, where R denotes the acceleration factor. The receive coil sensitivities, which are used to complement Fourier encoding, are not completely spatially independent. This leads to local noise amplification in the parallel

imaging reconstruction, depending on the spatial patterns of sensitivity profiles, which is quantified by the so-called g-factor.[2]

In case of SENSE reconstruction, the g-factor in a voxel ρ can be calculated analytically as

$$g_\rho = \sqrt{(E^H E)^{-1}_{\rho,\rho} (E^H E)_{\rho,\rho'}}, \qquad (1)$$

where

$$E_{(\gamma,k),\rho} = S_\gamma(\boldsymbol{r}_\rho) \cdot \exp(i\boldsymbol{k}(t_k) \cdot \boldsymbol{r}_\rho), \qquad (2)$$

is the encoding operator consisting of the coil sensitivities S_γ of the γ-th coil at spatial location $\boldsymbol{r}_\rho$ and a discrete Fourier operator according to the applied k-space trajectory $\boldsymbol{k}$ at time point t_k.[2] As shown previously,[10] this encoding operator can be extended to allow for time-varying receive sensitivities as $E_{(\gamma,k),\rho} = S_\gamma(\boldsymbol{r}_\rho, t_k) \cdot \exp(i\boldsymbol{k}(t_k) \cdot \boldsymbol{r}_\rho)$. Note that Eq. (1) is derived from the general image noise matrix (equation [17] in Pruessmann et al.),[2] assuming decorrelated multi-channel data such that the noise covariance matrix Ψ is the identity.[14] For regular Cartesian undersampling patterns, Eq. (1) decomposes into multiple small sub-blocks, such that the full encoding operator E can be replaced by sensitivity matrices S containing only the coil sensitivity values of aliased voxel groups from all channels.[2,10]

We found previously[10] that time-varying sensitivities bring the largest g-factor improvement if sensitivities are switched rapidly for every analog-to-digital converter (ADC) sample of a two-fold oversampled acquisition (i.e., during a k-space readout line). In this case, g-factors are identical to the hypothetical case of having all sensitivities of the dynamic configurations statically active as "virtual receive channels" at the same time. This can be seen as a form of time-division multiplexing.[15–17]

For assessing g-factors from electromagnetic (EM) simulations, in the present work, receive sensitivities were calculated from the simulated RF magnetic field as $B_1^- = (B_{1,x} - iB_{1,y})*/2$[18,19] and used to form the encoding operator and calculate g-factors according to Eqs. (2) and (3).

2.4 | Coil assembly

The dipoles were made of printed circuit board (PCB) and wires (Figure 3). In contrast to the original design,[11] the dipole design did not include a closely located RF shield. As shown in the original work, the shield reduces SNR.[11] The dipole PCBs were manufactured in our institutional workshop using FR4 printed circuit board (PCB: 020103E11, Bungard) of 0.5 mm in thickness. These PCBs were glued on a fiberglass holder made by Klaus Hoppe

Werbetechnik Design. In the ends of each PCB we soldered elevated-ends held by 3D printed polyethylene terephthalate glycol (PETg with Ultimaker S5 from Ultimaker B.V.) standoffs. The final length of each fold was adjusted to tune the coil to 400 MHz. The surface-mount device (SMD) capacitors (SH-series, Exxelia SAS) were used. All inductors were self-made using 1-mm copper wire, 4 turns of 3.5 mm in inner diameter for the tuning circuit, and 8 turns of 3.5 mm in inner diameter for the switchable unit (Figure 3A,C). For the switchable unit we used PIN-diodes (MA4P504–1072; MACOM) with a carrier lifetime of 1 μs and capacitance of 0.5 pF. The PIN-diodes were driven by a home-build complementary metal-oxide semiconductor (CMOS) driver, generating voltage of −5 V and +5 V, connected via a 7.5 Ω resistor. The CMOS driver was installed to the control unit, which was connected to the coil as shown in Figure 3B. An optical-electrical converter was used to convert the optical triggering signal to the electrical signal supported by the CMOS driver. Optical converter and the control unit were powered using 6 V non-magnetic batteries (NP7-6S, GS YUASA Battery Germany). We used 330-nH RF chokes inductors (9230 Series; Bourns) and a 330-pF capacitor for RF-blocking (Figure 3A). The DC block capacitors of 330 pF were inserted after the matching circuit to avoid the DC in the low noise amplifier (LNA) path. Each dipole was connected through the cable trap to the receive interface with 8 LNAs (WMA9RD; Wantcom) as shown in Figure 3A.

Active detuning was implemented similarly as previously described[20] using the matching capacitor, PIN-diode (MA4P7461–1072, MACOM), and inductance of the short piece (∼50 mm) of the coaxial cable (K_02252_D-60, Huber+Suhner AG) as shown in Figure 3A. When the PIN diode was shorted, the short (the cable length less than quarter of the wave length) coaxial cable formed an inductor, which was adjusted by changing the length of the cable. The inductor placed across the matching capacitor formed a high-impedance parallel resonance circuit inserted between the halves of the dipole, and the coil was detuned.

As a transmit-only coil, we used a surface loop array of 8 elements (Figure 3D), wherein all closest elements were transformer decoupled.[21] The array also included a cylindrical RF shield. The loops had a length of 130 mm, width of 100 mm, and were uniformly distributed around a cylindrical housing of 280 mm in diameter. The transmit coil was driven (Figure 3B) using a home-built 8 way-splitter with 45° between adjacent elements, which produced a circularly polarized mode. Specific absorption rate safety evaluations of the experimental setup for in vivo experiments were conducted in agreement with regulations of the local ethics committee.[22] A photo of the entire setup of transmit-only coil and receive coil is shown in Figure S1.
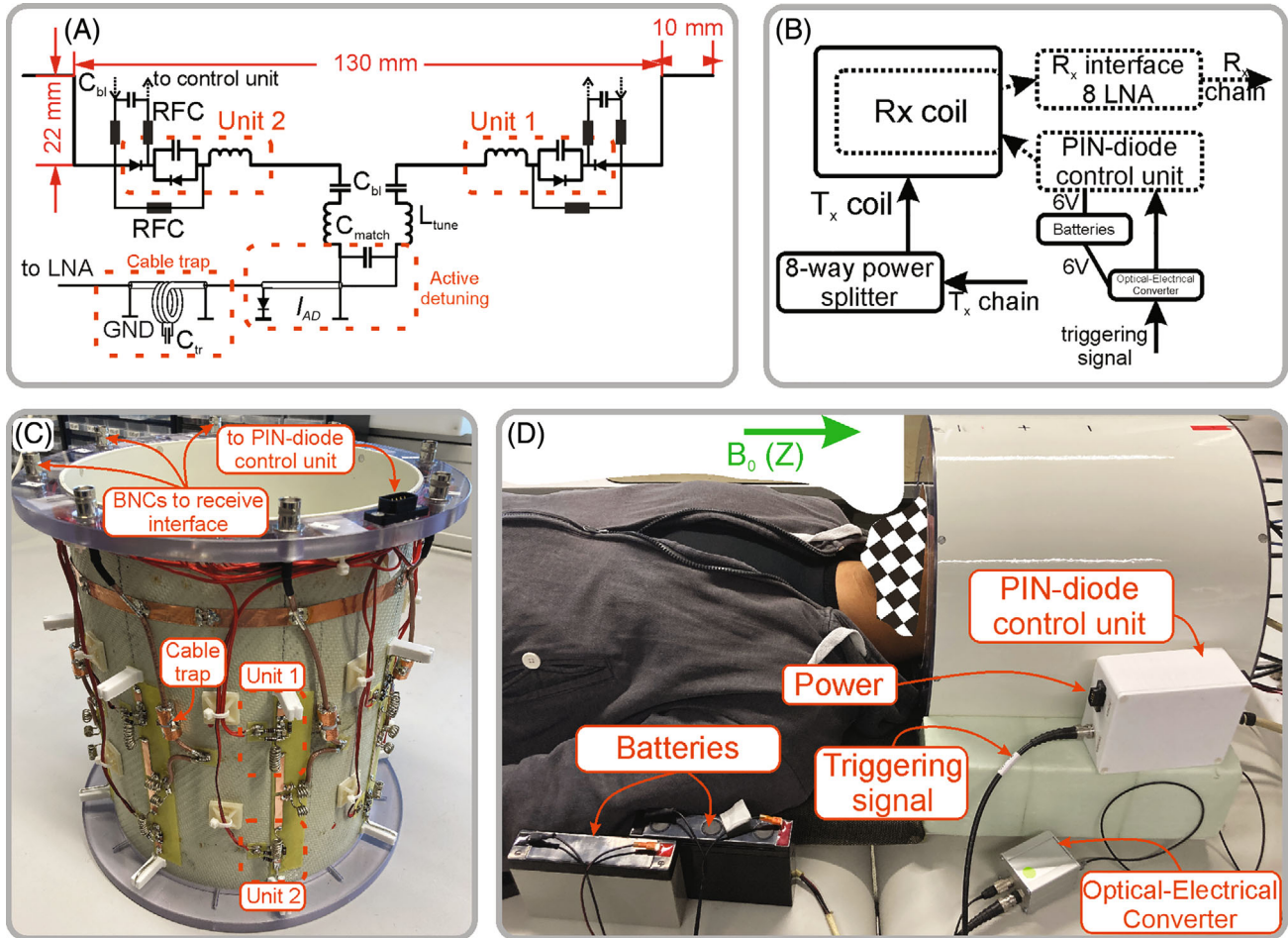
FIGURE 3 Prototype of the reconfigurable dipole array coil. (A) Detailed schematic of the dipole and positive-intrinsic-negative (PIN)-diode feeding circuit. (B) Block-diagram of the experimental setup. Here, the receive (Rx) coil is connected to the scanner's Rx chain via an interface of 8 low-noise-amplifiers (LNA). PIN diodes are powered by two batteries and controlled via the trigger output of the scanner, which is transmitted via an optical fiber to a dedicated control circuit of the coil. (C) Photograph of the Rx dipole array coil. (D) Photograph of the experimental setup.

2.5 | MR imaging

Data were acquired on a 9.4 T human whole-body MR scanner (Siemens Healthineers) using a 3D RF and gradient echo sequence (TR = 20 ms, TE = 8 ms, flip angle = 10°, slab-selective excitation, matrix size 200 × 200 × 60, FOV = 220 mm × 220 mm × 120 mm, resolution 1.1 mm × 1.1 mm × 2 mm, 20% slice oversampling, resulting in an acquisition time of 4 min 48 s).

A B_1^+ map of the transmit array was recorded using a centric-reordered 3D saturated single-shot turboFlash (3DsatTFL) sequence[23] (Figure S2).

Phantom measurements were performed in a homogeneous cylindrical phantom of 170-mm diameter, which contained a solution of 0.9698 g/mL Saccharose, 0.0307 g/mL NaCl, and 0.1% Dowicil, resulting in the same material parameters ($\sigma = 0.64$ S/m and $\varepsilon_r = 58.3$) as assumed in the simulations. In vivo data were acquired

in a healthy subject after written informed consent and under approval of the local ethics committee.

The PIN diodes of the reconfigurable dipoles were controlled via the trigger output of the scanner system, which makes switching of the sensitivity configurations a user-programmable degree of freedom during MR data acquisition. As a reference, fully sampled k-spaces were acquired for both configurations without switching. Noise calibration scans for both configurations were performed by acquiring 200 repetitions of the same sequence as used for imaging, but with the transmitter voltage set to 0.

For imaging with dynamically switched configurations, 20-fold readout oversampling was applied for an ADC dwell time of 20 μs, which results in an effective dwell time of 1 μs and a bandwidth of 250 Hz/pixel. During the ADC blocks, configurations were repeatedly switched every 10 μs. Using this procedure, multiple Nyquist-sampled k-space datasets can be obtained by

reordering the oversampled data. Each of these reordered datasets corresponds to a different time step in the repetitive switching dynamics, so that ideally half of them are weighted by one state of the receive array and half by the other. By averaging the respective images, multiplexed coil images of both receive array states are finally obtained. A detailed description of this method can be found in Glang et al.,[10] where a graphical representation of the process is also given (Figure S1 of reference Glang et al.)[10]

2.6 | Parallel imaging reconstruction and analysis

Noise decorrelation was applied to all datasets according to the noise covariance matrices as obtained from the noise calibration scans.[14] Receive sensitivities from both configurations were obtained from the acquired fully sampled data via ESPIRiT,[24] using the central 48×48 (PE1 × PE2) k-space lines. This algorithm captures the intensity variations among coil images because of B_1^- and therefore, intrinsically compensates for B_1^+ and object signal dependences, which are the same in all channels. Parallel imaging performance was assessed by retrospective undersampling of the fully sampled k-spaces and subsequent SENSE reconstruction with the obtained sensitivity maps for both the two static cases and the dynamically switched case.

The following metrics were used to compare undersampled reconstructions to fully sampled reference reconstructions: normalized root-mean-squared-error (NRMSE) defined as,

$$NRMSE(x, y) = \frac{||x - y||_2}{||x||_2}, \tag{3}$$

with the magnitude images x (reference) and y (both flattened as column vectors) of n voxels and L2 norm $||x||_2 = \sqrt{\sum_{i=1}^{n} |x_i|^2}$, structural similarity index (SSIM) defined according to[25] as,

$$SSIM(x, y) = \frac{\left(2\mu_x\mu_y + c_1\right)\left(2\sigma_x\sigma_y + c_2\right)}{\left(\mu_x^2 + \mu_y^2 + c_1\right)\left(\sigma_x^2 + \sigma_y^2 + c2\right)}, \tag{4}$$

where μ_x, μ_y and σ_x, σ_y are the means and SDs of the fully sampled and undersampled reconstructions, respectively, $c_1 = (k_1 L)^2$, $c_2 = (k_2 L)^2$, L being the dynamic range of the images, and $k_1 = 0.01, k_2 = 0.03$; and peak SNR (PSNR) defined as

$$PSNR(x, y) = 10 \cdot \log_{10}\left(\frac{\max(x)^2}{MSE(x, y)}\right), \tag{5}$$

with $MSE(x, y) = \frac{1}{n}||x - y||_2^2$.

For all reconstructions, g-factors were calculated from the sensitivity maps according to Eqs. (1) and (2).

3 | RESULTS

3.1 | Electromagnetic simulation

We simulated two scenarios of dipole driving. In both scenarios, the resonant frequency of the array was adjusted to 400 MHz. In the first "direct" driving scenario, all dipoles are switched as shown in Figure 1B. In this case, we have obtained a mean reflection coefficient S_{ii} of −29.49 dB and the worst isolation between closest adjacent elements of −14.9 dB (Figure 2B). In this scenario, because of symmetry, there is no receive field variation among the dipoles along the z-axis near the center of the cylinder, therefore, 3D acceleration is possible only in the switched configuration. As an alternative, we proposed to flip every second dipole to drive them in so-called "alternating" order (Figure 2B). This way of driving improved the isolation between the nearest neighbors. As a result, the average transmission coefficient between two adjacent elements was −16.9 dB, whereas impedance matching was −36.33 dB (Figure 2B).

Because electrical lengths of the dipole arms become different, the electrical center (maximum of the current) is moved toward the inductive impedance. As a result, the maximum of the current moves from the center of the dipole to the middle of the left or the right arm. Figure 4 shows the simulated |H|-field distribution of a dipole (130 mm in length) at a depth of 5 mm from the phantom surface. As seen in Figure 4, the field maximum follows the changes in the current distribution. Using this method, we can achieve a ratio of 1:0.4 between |H|-field picked in the opposite quarters (−31 mm and 31 mm from the dipole center) of the dipole arms. This current (H-field) difference leads to a corresponding change in B_1^- (sensitivity pattern) field. The simulated B_1^- maps in a.u. for each configuration are shown in Figure 4. Here, we normalized each B_1^- map to its maximum. As seen in the figure, the B_1^- field maximum moves from the center of the dipole (as in conventional dipole) toward the middle of each arm. Accordingly, measurements in a homogeneous phantom with a single dipole receive element (Figure 4) show two distinct spatial receive sensitivity patterns. By dynamically changing the receive field during the MRI acquisition, one can reduce the g-factors and therefore, improve accelerated 3D imaging.

In addition, we simulated case with lossy PIN diodes. In Figure S3 we showed B_1^- maps for both cases, and as seen, the effect of losses is almost negligible.
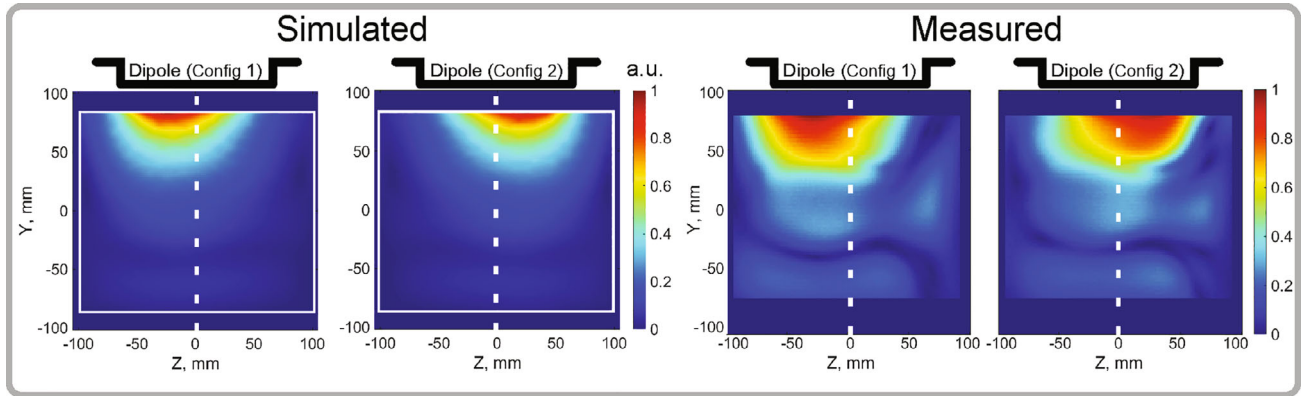
FIGURE 4 Qualitative comparison of simulated B_1^- field (receive sensitivity), and single-channel SNR maps obtained from a fully sampled gradient echo scan for both configurations. All maps are normalized to its maximum. The phantom borders are marked by the white line. Dashed line shows the dipole's geometrical center.

3.2 | G-factor simulations

Figure 5 shows simulated transversal and sagittal g-factor maps calculated for an array of conventional dipoles and a reconfigurable dipole array (Figure 5A) dynamically switched in the direct order for acceleration factor R_z of 2. Both arrays consisted of 8 elements uniformly surrounding the cylindrical phantom. Depending on the slice number along the z-direction, the improvement in g-factors varies (Figure 5B). Finally, the dynamic switching provided an overall improvement in maximum g-factor up to 263.1-fold and mean g-factor up to 9.81-fold for the acceleration factor R_z of 2. The array of conventional dipoles demonstrated unfeasibly high values of mean and maximum g-factors (Figure 5B) for acceleration in the z-direction because there is no B_1^- field variation among dipole antennas along the z-direction in the center of the phantom. The same is true for the static direct driving. Therefore, we do not consider these two scenarios in further comparison. For the alternating order scenario, the z-acceleration can be used even without switching because the B_1^- field varies among the coil elements in the z-direction.

Hence, we compare g-factors for three scenarios including direct order dynamically switched dipoles, alternating order static and dynamically switched dipoles. In all three cases, we used 8-element dipole arrays loaded with the cylindrical phantom (Figure 2A). Figure 5C shows the maximum and mean g-factors for all three cases. An overall improvement of the switched over the static scenario can clearly be seen in Figure 5C. Among the studied designs, the design with switched dipoles placed in the alternating order shows the best results. Namely, it demonstrated 2.01-fold improvement for acceleration of 1×2 ($R_y \times R_z$), 2.5-fold improvement for 2×2, and 4.02-fold improvement in case of 3×2 in maximum g-factor compared to the alternating order, but without switching. An

improvement of 5% for 1×2, 12.4% for 2×2, and 54% for 3×2 is reported for the mean g-factors compared to the alternating order coil, but without switching. For in-plane acceleration (2×1 and 3×1), all coils show comparable values of g-factors. Comparison of two switched cases shows a small (3%) improvement in the case of the alternating scenario. Although this difference in g-factors is minor, because of improvement in isolations between the channels, the design of alternating order was considered for prototype assembling. Figure 5 presents only an example of imaging accelerated in the y-z plain. Because of the cylindrical symmetry of the simulated geometry, acceleration in x-z plain produces the same results.

3.3 | Coil testing and image reconstruction

The final coil design is depicted in Figure 3. After assembling and fine-tuning on the bench, we tested the coil in the 9.4 T scanner on the phantom and in vivo.

To verify that the multiplexing procedure does not distort the obtained sensitivity patterns of the receive elements, in Figure S4 a comparison of non-switched and switched magnitude and phase maps is shown. It can be seen that the magnitude and phase patterns match for both switched and non-switched acquisitions.

Because the observation time per configuration is halved for the switched acquisitions compared to a non-switched acquisition of same duration, the SNR of the multiplexed configuration images is reduced by a factor of $\sqrt{2}$. However, by including all available data from the switched acquisition (i.e., averaging over both configuration images), a similar mean SNR as in the static cases is restored (Figure S5). This case is most relevant for parallel imaging reconstructions, where information
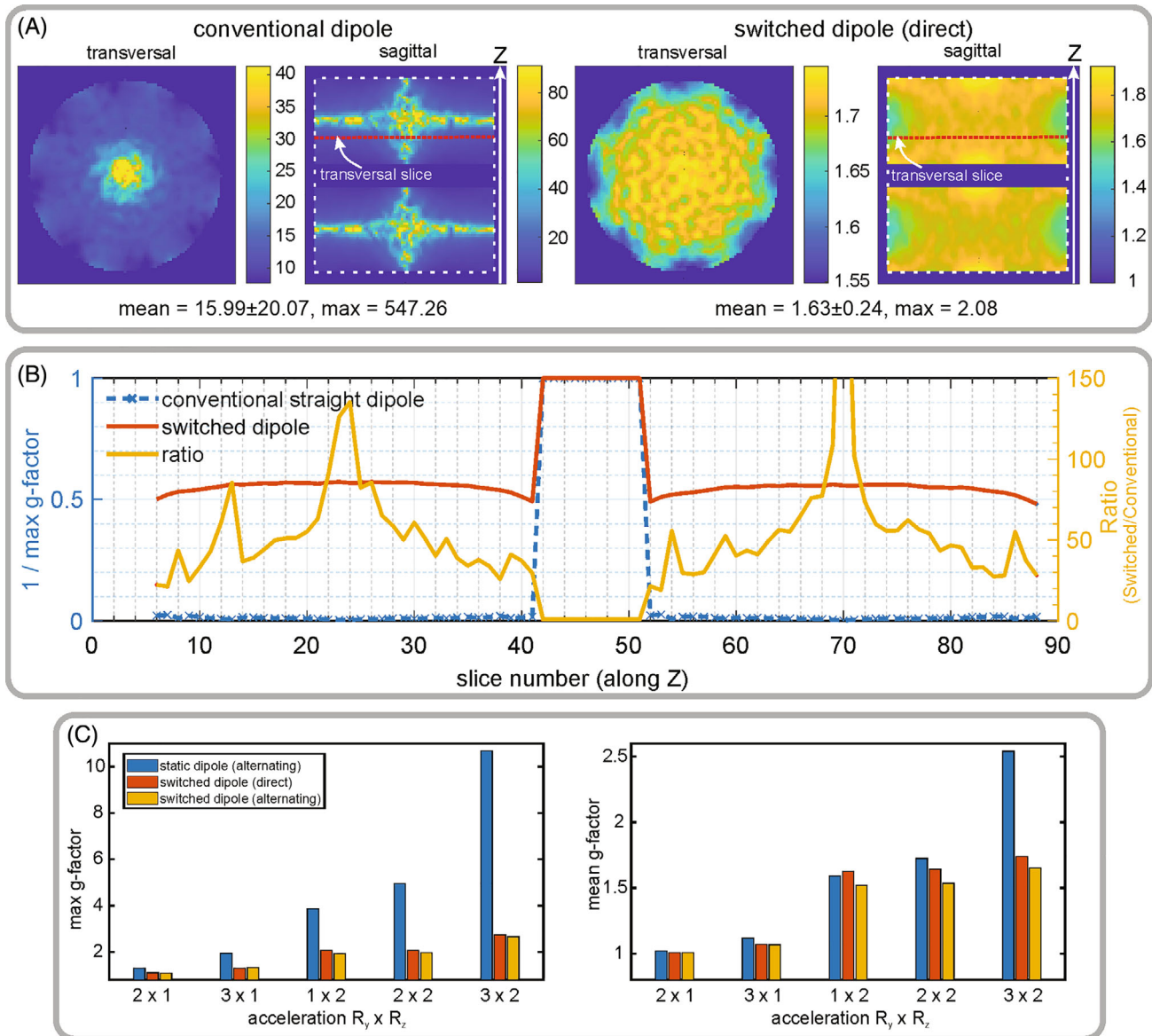
FIGURE 5 Simulated geometry-factor (g-factor) improvement. (A) Simulated transversal and sagittal g-factors maps obtained for the conventional dipole and reconfigurable dipole 8-element arrays dynamically switched in the direct order for acceleration factor R_z of 2. (B) Plot shows the distribution of the inverse maximum g-factor (higher is better) calculated for corresponding transversal slices along the dipole length. (C) Maximum and mean g-factors (lower is better) for several studied coil geometries: direct order switched dipoles, alternating order static, and switched dipoles.

from both configurations of a switched sequence is used simultaneously.

Figure 6 shows a comparison of simulated and measured g-factors all obtained using the developed 8-element array loaded by the cylindrical phantom. We evaluated two static configurations 1 and 2, and the dynamically switched configuration. In all three cases dipoles were arranged in the alternating order. The difference between configurations 1 and 2 is that inductors and capacitors at the ends of dipoles are swapped with each other. For example, if in configuration 1, dipole 1 (Figure 2A) has an inductor at the right side and capacitor at the left

side, in configuration 2, it has an inductor at the left side and capacitor at the right side. In addition, single channel images of each element for configurations 1 and 2 (Figure 1A) are shown in Figure S6. Figure 6A shows an evaluation of maximum g-factors. This evaluation demonstrates that the switched scenario yields following improvements in the maximum g-factor: 2.46-fold for acceleration of 1×2 ($R_y \times R_z$), 3.32-fold for 2×2, and 4.41-fold for 3×2 compared to the static scenario. Figure 6B shows improvement in mean g-factors of 8% for acceleration of 1×2 ($R_y \times R_z$), 15.7% for 2×2, and 33% for 3×2 compared to the static scenario. We report this
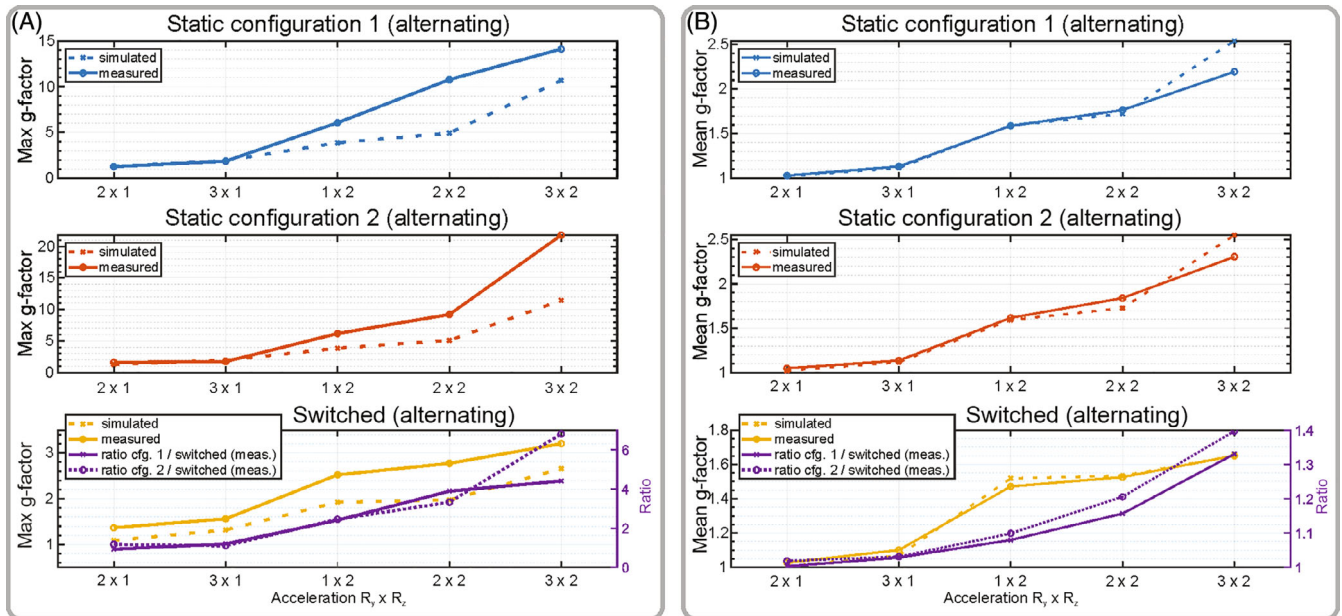
FIGURE 6 Comparison of the measured and simulated geometry-factors (g-factors) (phantom). (A) Maximum g-factors (lower is better) obtained for three simulated and measured configurations (i.e. two static configurations 1 and 2) and the dynamically switched configuration. For all three configurations dipoles were arranged in the alternating order. (B) Mean g-factors for three simulated and measured configurations (static 1, static 2, and dynamically switched). In addition, Figure 6A,B show ratios of the maximum and mean g-factors measured for the dynamically switched dipole to that of both static configurations.

improvement compared to the worst case among static 1 or 2 configurations (Figure 6).

3.4 | In vivo imaging

In Figure 7, in vivo parallel imaging results are compared for the cases of two static configurations and the case of rapidly switched alternating configuration for different acceleration patterns. As seen in the figure, higher acceleration leads to increased g-factors (Figure 6B). Switching sensitivities yielded an improvement of maximum g-factors of 1.66-fold for 1×2 ($R_y \times R_z$), 1.65-fold for 2×2, and 2.2-fold for 3×2 acceleration compared to the worst static configuration case (Figure 8). In terms of mean g-factor, the developed coil demonstrated an improvement of 7% for 1×2 ($R_y \times R_z$), 11.8% for 2×2, and 21.5% for 3×2 acceleration compared to the static worst configuration case (Figure 8). Similar observations can be made when choosing the first accelerated direction as left–right instead of anterior–posterior, this is, $R_x \times R_z$ acceleration (Figures S7 and S8).

Figure 9A shows the g-factor obtained in vivo as a "violin" plot, where the peak value shows the maximum g-factor, and the width of each bar indicates the number of voxels of the corresponding g-factor across the entire acquired brain volume. Finally, the mean value for each case is shown by the black cross.

Figure 9B further compares the accelerated 3D SENSE reconstructions with the fully sampled ground truth. Here, the benefit of sensitivity switching is especially pronounced for high acceleration factors. For instance, in case of 2×3-fold ($R_y \times R_z$) acceleration, switching reduces NRMSE by a factor of 4 (75% improvement), increases SSIM by a factor of 1.43 (43% improvement), and increases PSNR by a factor of 1.44 (44% improvement) compared to the better of the static cases, respectively.

4 | DISCUSSION

In this work, we developed and evaluated a novel concept of a dynamic Rx RF array coil based on reconfigurable elevated-end dipoles[11] for accelerated 3D parallel imaging of the human brain at 9.4 T. An array of conventional static dipoles arranged in a single row does not support 3D acceleration because there is no sensitivity variation among the dipoles along the z-direction (the axis of the magnet). In contrast, because of switching between the inductive and capacitive impedance placed in each arm of the reconfigurable dipoles, the receive sensitivity profile can be dynamically shifted along the z-direction during the acquisition phase, which provides two virtual dipoles. As a result, the developed one-row array coil has two effective (virtual) rows and is, therefore, capable of 3D acceleration.

FIGURE 7 In vivo results obtained with the proposed coil array. Top left box: Fully sampled images. Other boxes: Retrospectively undersampled 3D SENSE reconstructions. In each box, transversal, coronal, and sagittal views are shown for the static configurations 1 and 2 (first two rows in each box) as well as for the dynamically switched case (bottom row in each box). Labels indicate the applied acceleration pattern in the two-phase encoding directions as $R_y \times R_z$.
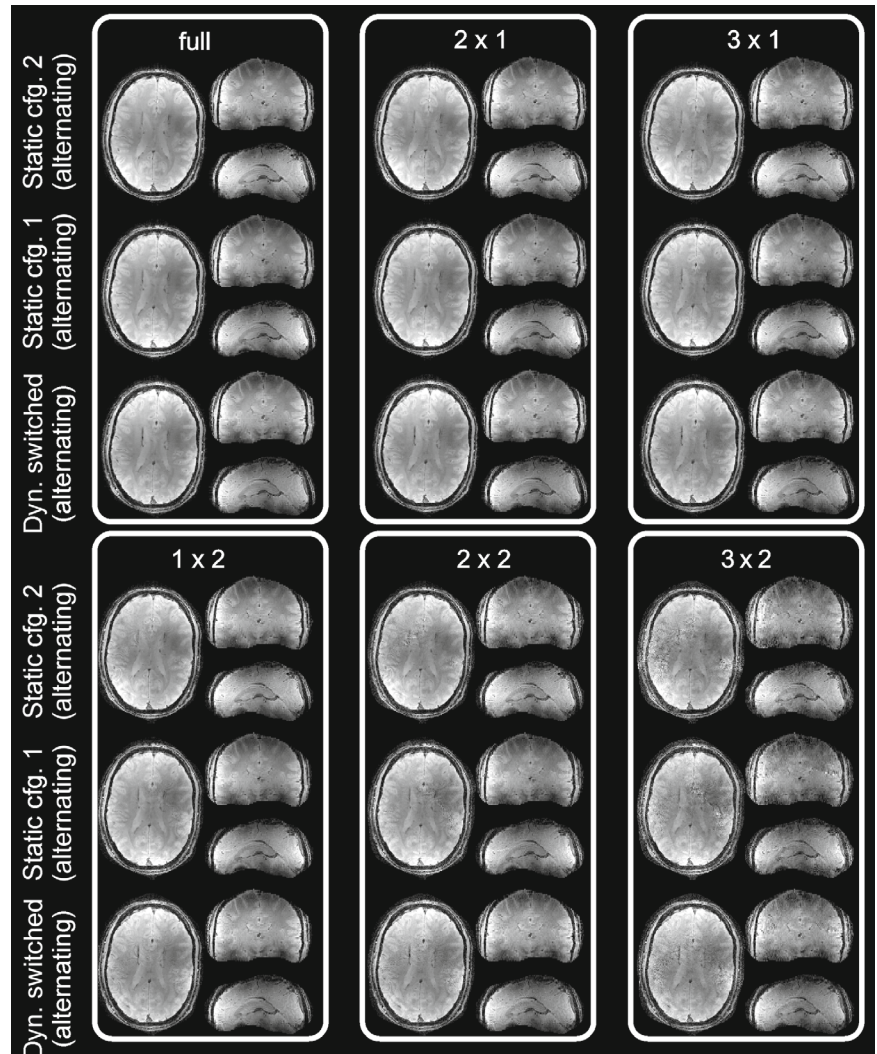
We suggested two scenarios of dipole arrangement, namely "direct" and "alternating." Despite having comparable parallel imaging improvement in both scenarios, the alternating order showed an improvement in isolation compared to the direct-order. This improvement in isolation can be important for further increasing the number of elements in a row. Finally, the dynamically switched alternating order dipoles demonstrated the best improvement of g-factors in vivo, that is, up to 2.2-fold for 3×2 ($R_y \times R_z$) acceleration, compared to the static alternating order configuration. This improvement in g-factor allows using higher acceleration factors with the reconfigurable RF coil without additional g-factor penalty compared to the non-reconfigurable RF coil. For example, in case of 3×2 ($R_y \times R_z$) acceleration, g-factor for the reconfigurable coil was comparable to the non-reconfigurable coil with a lower acceleration factor of 1×2 ($R_y \times R_z$). Because of this improvement of g-factors, one could obtain comparable overall SNR for the static configuration (non-reconfigurable) accelerated by 1×2 ($R_y \times R_z$) and

switched configuration (reconfigurable) accelerated by 2×2 ($R_y \times R_z$). As a result, when switching the sensitivities of the proposed RF coil one can shorten the acquisition time by a factor of 2 without additional SNR penalty. Such an improvement in scanning time can be particularly beneficial in high-resolution 3D anatomical brain imaging sequences like the popular MPRAGE[26] or MP2RAGE.[27]

The proposed concept of reconfigurable receive dipoles can be also very useful for accelerated MRI at 7 T. This fact is of great importance taking into account recent clearances of two commercial 7 T MRI scanners for diagnostic imaging and a growing number of 7 T MRI machines over the world (more than 100). According to recent findings of the ultimate intrinsic SNR theory, maximum SNR deeper in the human body or near the brain center at 7 T and above can be obtained only by combining complementary conductive structures carrying different current patterns, for example, loops and dipole antennas.[28,29] Following these theoretical findings, we recently developed two novel 32-element dipole/loop combined array designs,[20,30] and
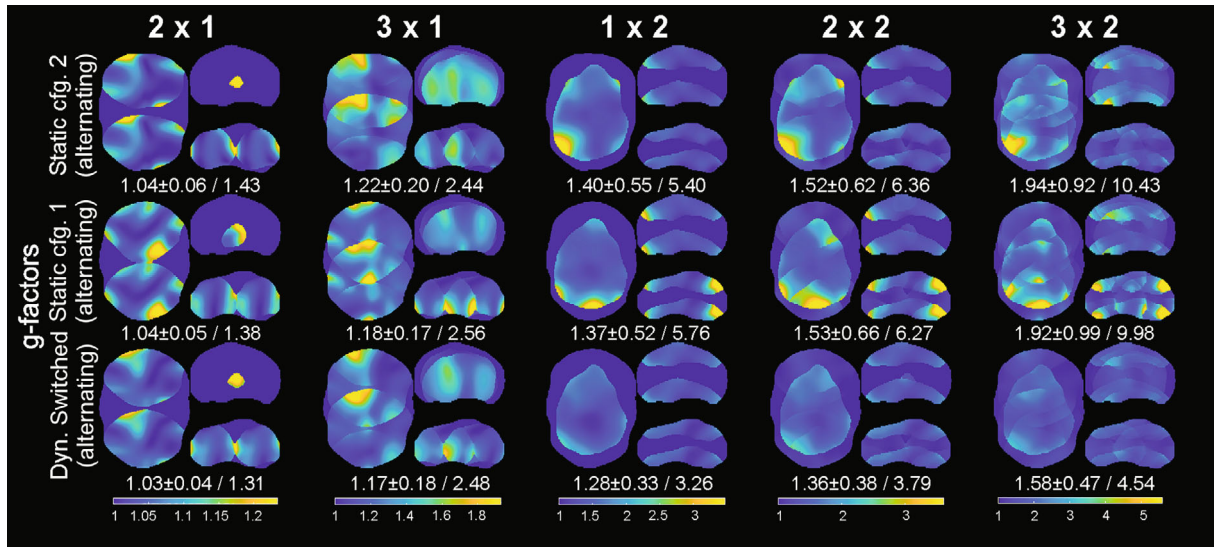
FIGURE 8 In vivo geometry-factor (g-factor) maps obtained with the proposed coil array. Columns correspond to different $R_y \times R_z$ acceleration patterns and rows show the results for static configurations 1, 2, and the dynamically switched case, respectively. As in Figure 7, for all cases a transversal, coronal and sagittal slice are shown. Labels indicate mean $\pm$ SD/max of g-factor values across the entire acquired brain volume (FOV = 220 mm $\times$ 220 mm $\times$ 120 mm).
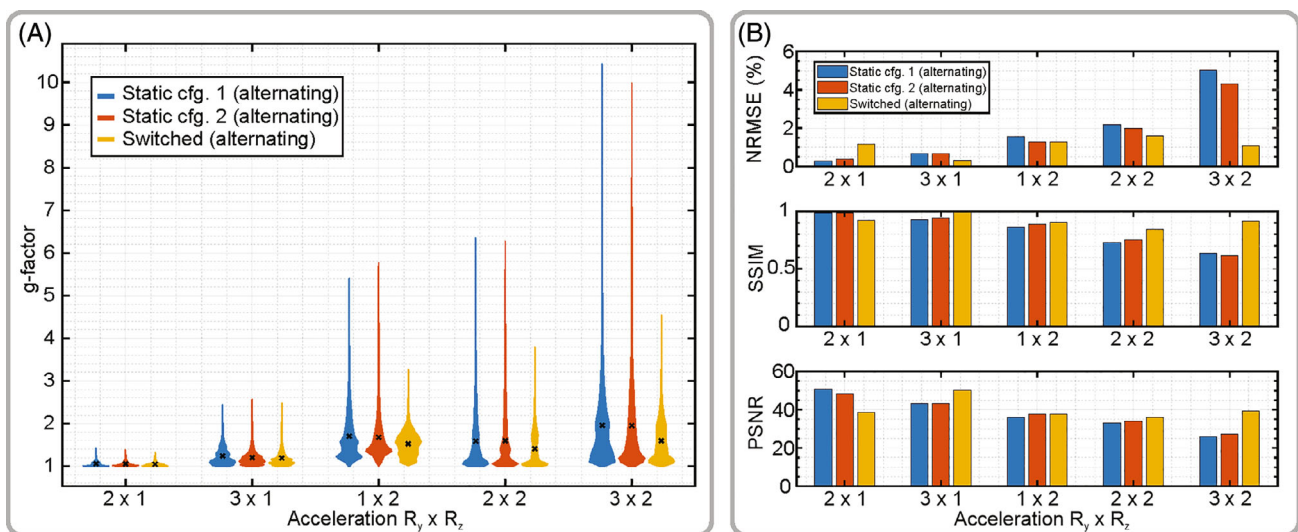

FIGURE 9 Comparison of the in vivo reconstruction results. (A) Geometry-factors (g-factors) across the entire acquired brain volume (FOV = 220 mm $\times$ 220 mm $\times$ 120 mm). (B) Normalized root-mean-squared error (NRMSE, lower is better), structural similarity index (SSIM, higher is better) and peak SNR (PSNR, higher is better) of the accelerated 3D SENSE reconstructions with respect to the fully sampled ground truth reconstructions.

wherein our new findings can be potentially applied to improve parallel imaging. For both dipole/loop designs, the 3D parallel imaging can be further improved by using reconfigurable dipoles that can effectively increase the number of virtual rows of dipoles to 2 (first design) or 4 (second design). Use of dipole antennas was also demonstrated for imaging of the human body at 3 T.[31] Therefore, the developed technique of dynamic Rx dipoles can be also applied for 3 T human body imaging.

Comparing g-factors between simulation and phantom measurement (Figure 6), for the measured maximum g-factor value we have observed underestimation of our simulation by 18.3% to 40.4% depending on the acceleration factor. In contrast, we have observed good agreement between measured and simulated results in terms of mean g-factors. This can be explained by the fact that g-factor hot spots appear at the edges of the imaged object, and therefore, maximum g-factor values are very sensitive to

the choice of image mask. For the mean value this problem is mitigated.

The ability to undersample a 3D k-space in the two phase encoding directions (e.g., acceleration patterns like 2×2) is favorable for parallel imaging compared to accelerating along a single direction (e.g., 4×1), as the former makes use of the spatial coil sensitivity information in two instead of only one direction.[32]

As a drawback, the presented setup requires additional electronics for controlling the PIN diodes and wires delivering the DC to the dipoles. These wires can interact with the dipoles and therefore, have to be mounted with care. However, this can be improved, for example, if the DC is guided through the same coaxial cable connected to the dipoles. This might reduce the number of extra wires and minimize residual interactions with electronics. EM simulations suggest that the proposed reconfigurable dipoles are applicable also at 7 T and higher fields such as 10.5 T and 11.7 T, but become less efficient at lower fields.

The proposed approach of dynamically switched Rx-elements is applicable to all types of MRI sequences, as the switching provides an additional degree of freedom during image encoding. In the present case, coil sensitivity variation along the z-axis is achieved by the two reconfigurable states of the dipoles, whereas in-plane (x/y) there is almost no sensitivity variation between the configurations. Consequently, for the in-plane acceleration, dynamic switching provides no significant benefit over static configurations. However, more advanced reconfigurable receive dipole element geometries can allow modulation of B_1^- both in-plane and along the z-axis to further improve parallel imaging performance.

5 | CONCLUSIONS

We presented an 8-element prototype of a novel electronically reconfigurable dipole receive array that permits rapid sensitivity modulations along the dipole's axes. Applying dynamic sensitivity modulation during image acquisition emulates two virtual rows of receive elements along the z-direction, and therefore, improves parallel imaging performance for 3D acquisitions. As a result, the dynamically switched dipoles demonstrated a significant improvement of g-factors in vivo, that is, up to 2.2-fold for $3 \times 2\,(R_y \times R_z)$ acceleration, compared to the static configuration.

ORCID
Anton V. Nikulin https://orcid.org/0000-0001-5640-8281
Felix Glang https://orcid.org/0000-0003-3506-4947
Nikolai I. Avdievich https://orcid.org/0000-0001-7608-0869
Dario Bosch https://orcid.org/0000-0002-6537-6370
Klaus Scheffler https://orcid.org/0000-0001-6316-8773

REFERENCES
1. Roemer PB, Edelstein WA, Hayes CE, Souza SP, Mueller OM. The NMR phased array. *Magn Reson Med*. 1990;16:192-225. doi:10.1002/mrm.1910160203
2. Pruessmann KP, Weiger M, Scheidegger MB, Boesiger P. SENSE: sensitivity encoding for fast MRI. *Magn Reson Med*. 1999;42:952-962. doi:10.1002/(SICI)1522-2594(199911)42:5<952::AID-MRM16>3.0.CO;2-S
3. Griswold MA, Jakob PM, Heidemann RM, et al. Generalized autocalibrating partially parallel acquisitions (GRAPPA). *Magn Reson Med*. 2002;47:1202-1210. doi:10.1002/mrm.10171
4. Sodickson DK, Manning WJ. Simultaneous acquisition of spatial harmonics (SMASH): fast imaging with radiofrequency coil arrays. *Magn Reson Med*. 1997;38:591-603. doi:10.1002/MRM.1910380414
5. Wiesinger F, Van De Moortele PF, Adriany G, De Zanche N, Ugurbil K, Pruessmann KP. Parallel imaging performance as a function of field strength – an experimental investigation using electrodynamic scaling. *Magn Reson Med*. 2004;52:953-964. doi:10.1002/MRM.20281
6. Keil B, Blau JN, Biber S, et al. A 64-channel 3T array coil for accelerated brain MRI. *Magn Reson Med*. 2013;70:248-258. doi:10.1002/MRM.24427
7. Wiggins GC, Polimeni JR, Potthast A, Schmitt M, Alagappan V, Wald LL. 96-channel receive-only head coil for 3 tesla: design optimization and evaluation. *Magn Reson Med*. 2009;62:754-762. doi:10.1002/MRM.22028
8. Gruber B, Stockmann JP, Keil B, Ghotra A, Feinberg DA, Wald LL. A 128-channel head coil array for cortical imaging at 7 tesla. *2021 Int Conf Electromagn Adv Appl ICEAA 2021*. Published online August 9 2021:367. doi:10.1109/ICEAA52647.2021.9539808
9. Kumar A, Edelstein WA, Bottomley PA. Noise figure limits for circular loop MR coils. *Magn Reson Med*. 2009;61:1201-1209. doi:10.1002/MRM.21948
10. Glang F, Nikulin AV, Bause J, et al. Accelerated MRI at 9.4 T with electronically modulated time-varying receive sensitivities. *Magn Reson Med*. 2022;88:742-756. doi:10.1002/MRM.29245
11. Avdievich NI, Solomakha G, Ruhm L, Scheffler K, Henning A. Evaluation of short folded dipole antennas as receive elements of ultra-high-field human head array. *Magn Reson Med*. 2019;82:811-824. doi:10.1002/MRM.27754
12. Avdievich NI, Solomakha G, Ruhm L, Henning A, Scheffler K. Unshielded bent folded-end dipole 9.4 T human head transceiver array decoupled using modified passive dipoles. *Magn Reson Med*. 2021;86:581-597. doi:10.1002/MRM.28711

13. Raaijmakers AJE, Italiaander M, Voogt IJ, et al. The fractionated dipole antenna: a new antenna for body imaging at 7 tesla. *Magn Reson Med*. 2016;75:1366-1374. doi:10.1002/MRM.25596

14. Pruessmann KP, Weiger M, Börnert P, Boesiger P. Advances in sensitivity encoding with arbitrary k-space trajectories. *Magn Reson Med*. 2001;46:638-651. doi:10.1002/MRM.1241

15. Trakic A, Wang H, Weber E, et al. Image reconstructions with the rotating RF coil. *J Magn Reson*. 2009;201:186-198. doi:10.1016/J.JMR.2009.09.009

16. Porter JR, Wright SM, Famili N. A four-channel time domain multiplexer: a cost-effective alternative to multiple receivers. *Magn Reson Med*. 1994;32:499-504. doi:10.1002/MRM.1910320412

17. MacNamara E, Hou T, Fisher G, Williams S, Raftery D. Multiplex sample NMR: an approach to high-throughput NMR using a parallel coil probe. *Anal Chim Acta*. 1999;397:9-16. doi:10.1016/S0003-2670(99)00387-6

18. Collins CM, Li S, Smith MB. SAR and B1 field distributions in a heterogeneous human head model within a birdcage coil. Specific energy absorption rate. *Magn Reson Med*. 1998;40:847-856. doi:10.1002/MRM.1910400610

19. Hoult DI. The principle of reciprocity in signal strength calculations a mathematical guide. *Inc Concepts Magn Reson*. 2000;12:173-187. doi:10.1002/1099-0534(2000)12:4

20. Avdievich NI, Nikulin AV, Ruhm L, Magill AW, Henning A, Scheffler K. Double-row dipole/loop combined Array for human whole brain imaging at 7 T. *NMR Biomed*. 2022;35:e4773. doi:10.1002/NBM.4773

21. Avdievich NI, Pan JW, Baehring JM, Spencer DD, Hetherington HP. Short echo spectroscopic imaging of the human brain at 7T using transceiver arrays. *Magn Reson Med*. 2009;62:17-25. doi:10.1002/MRM.21970

22. Hoffmann J, Henning A, Giapitzakis IA, et al. Safety testing and operational procedures for self-developed radiofrequency coils. *NMR Biomed*. 2016;29:1131-1144. doi:10.1002/NBM.3290

23. Bosch D, Bause J, Geldschläger O, Scheffler K. Optimized ultrahigh field parallel transmission workflow using rapid presaturated TurboFLASH transmit field mapping with a three-dimensional centric single-shot readout. *Magn Reson Med*. 2023;89:322-330. doi:10.1002/MRM.29459

24. Uecker M, Lai P, Murphy MJ, et al. ESPIRiT—an eigenvalue approach to autocalibrating parallel MRI: where SENSE meets GRAPPA. *Magn Reson Med*. 2014;71:990-1001. doi:10.1002/MRM.24751

25. Wang Z, Bovik AC, Sheikh HR, Simoncelli EP. Image quality assessment: from error visibility to structural similarity. *IEEE Trans Image Process*. 2004;13:600-612. doi:10.1109/TIP.2003.819861

26. Mugler JP, Brookeman JR. Three-dimensional magnetization-prepared rapid gradient-echo imaging (3D MP RAGE). *Magn Reson Med*. 1990;15:152-157. doi:10.1002/MRM.1910150117

27. Marques JP, Kober T, Krueger G, van der Zwaag W, Van de Moortele PF, Gruetter R. MP2RAGE, a self bias-field corrected sequence for improved segmentation and T1-mapping at high field. *Neuroimage*. 2010;49:1271-1281. doi:10.1016/J.NEUROIMAGE.2009.10.002

28. Lattanzi R, Wiggins GC, Zhang B, Duan Q, Brown R, Sodickson DK. Approaching ultimate intrinsic signal-to-noise ratio with loop and dipole antennas. *Magn Reson Med*. 2018;79:1789-1803. doi:10.1002/MRM.26803

29. Pfrommer A, Henning A. The ultimate intrinsic signal-to-noise ratio of loop- and dipole-like current patterns in a realistic human head model. *Magn Reson Med*. 2018;80:2122-2138. doi:10.1002/MRM.27169

30. Avdievich NI, Nikulin AV, Ruhm L, Magill AW, Henning ASKA. 32-element loop/dipole hybrid Array for human head imaging at 7T. *Magn Reson Med*. 2022;88:1912-1926. doi:10.1002/mrm.29347

31. Haghnejad AA, Malik SJ, Padormo F, et al. Transceive surface array of dipole antennas for multi-transmit imaging at 3T. *Proc Intl Soc Mag Reson Med*. 2016;(figure 2);24:3174.

32. Weiger M, Pruessmann KP, Boesiger P. 2D SENSE for faster 3D MRI. *Magma*. 2002;14:10-19. doi:10.1007/BF02668182

SUPPORTING INFORMATION

Additional supporting information may be found in the online version of the article at the publisher's website.

FIGURE S1. Photo of the experimental setup, showing the shielded outer transmit-only coil (8 surface loop elements), the inner receive coil (8 reconfigurable dipole elements), and the phantom. The receive insert was partially pulled out for better visibility.

FIGURE S2. B_1^+ map of the 8-element transmit loop array in the homogeneous phantom, acquired using a centric-reordered 3D saturated single-shot turboFlash (3DsatTFL) sequence.[20]

FIGURE S3. Simulation results for a single dipole. (A) Simulated setup. (B) B_1- field profiles in μT. (C) B_1- field in μT in the central sagittal plane (lossless case $R = 0$). (D) B_1- field in μT in the central sagittal plane (lossy case $R = 1.2\,\Omega$).

FIGURE S4. Comparison of static and multiplexed acquisitions of the two configurations of the reconfigurable dipole coil. First row: magnitude and phase maps for the two configurations from respective static acquisitions without any switching during the sequence (dwell time 20 μs). Second row: A single "time frame" of a multiplexed (i.e., rapidly switched acquisition) obtained according to the procedure described in Glang et al.[10] (effective dwell time 1 μs). Third row: Multiplexed configuration images obtained by averaging over all time frames corresponding to the respective configuration (effective dwell time 10 μs). Results are shown exemplarily for a single channel.

FIGURE S5. Comparison of single channel SNR for the cases of non-switched and switched configurations of the reconfigurable dipole array. SNR was evaluated by voxelwise division of image intensity by the noise standard deviation measured in the no-signal regions in the corners of the image. First row: SNR maps for a non-switched sequence in (A) static configuration 1 only and (B) static

configuration 2 only. Second row: SNR maps obtained from a switched (i.e., multiplexed) sequence, enabling simultaneous reconstruction of both (C) configuration 1 and (D) configuration 2, however, at half the observation time compared to (A,B), respectively. (E) SNR map for the case of averaging over all 20 individual "time frames" obtained from the switched sequence shown in (C,D), therefore, effectively mixing the configurations. Numbers below the images correspond to mean | max of the respective maps. In addition, below the images, the corresponding effective dwell times and configuration weightings in time are graphically indicated, where each colored box represents a 1 μs sample.

FIGURE S6. Single coil GRE images for both configurations and all channels of the reconfigurable dipole array, shown in transversal (first two rows), sagittal (third and fourth row) and coronal (fifth and sixth row) slices. Image intensity has been normalized to the range [0,1]. Note that image intensity varies for different views, because the respective dipole elements have various distances from the imaging planes.

FIGURE S7. In vivo results obtained with the proposed coil array for retrospective acceleration along x (left–right) and z (head–foot). Results correspond to Figure 7 in the main text, but with the first phase encoding direction assumed to be left–right instead of anterior–posterior. Fully sampled images (leftmost column) and retrospectively undersampled 3D SENSE reconstructions for the cases of only static configurations (first two rows) as well as the rapidly switched case (third row) are shown. Labels indicate the applied acceleration pattern in two phase encoding directions as $R_x \times R_z$.

FIGURE S8. G-factor maps corresponding to the reconstruction results shown in Figure S2. Labels indicate mean $\pm$ SD/max of g-factor values across the entire acquired brain volume (FOV 220 mm $\times$ 220 mm $\times$ 120 mm). Results correspond to Figure 8 in the main text, but with the first phase encoding direction assumed to be left–right instead of anterior–posterior.

B.3. Publication 3

Glang, F.; Fabian, M. S.; German, A.; Khakzar, K. M.; Mennecke, A.; Liebert, A.; Herz, K.; Liebig, P.; Kasper, B. S.; Schmidt, M.; Zuazua, E.; Nagel, A. M.; Laun, F. B.; Dörfler, A.; Scheffler, K.; Zaiss, M.
Linear Projection-Based Chemical Exchange Saturation Transfer Parameter Estimation.

RESEARCH ARTICLE

Linear projection-based chemical exchange saturation transfer parameter estimation

Felix Glang[1] | Moritz S. Fabian[2] | Alexander German[2] | Katrin M. Khakzar[2] | Angelika Mennecke[2] | Andrzej Liebert[3] | Kai Herz[1,4] | Patrick Liebig[5] | Burkhard S. Kasper[6] | Manuel Schmidt[2] | Enrique Zuazua[7] | Armin M. Nagel[3] | Frederik B. Laun[3] | Arnd Dörfler[2] | Klaus Scheffler[1,4] | Moritz Zaiss[1,2]

[1]Magnetic Resonance Center, Max Planck Institute for Biological Cybernetics, Tübingen, Germany

[2]Department of Neuroradiology, University Hospital Erlangen, Friedrich-Alexander Universität Erlangen-Nürnberg, Erlangen, Germany

[3]Institute of Radiology, University Hospital Erlangen, Friedrich-Alexander-Universität Erlangen-Nürnberg (FAU), Germany

[4]Department of Biomedical Magnetic Resonance, Eberhard Karls University Tübingen, Tübingen, Germany

[5]Siemens Healthcare GmbH, Erlangen, Germany

[6]Department of Neurology, University Clinic of Friedrich Alexander University Erlangen-Nürnberg, Erlangen, Germany

[7]Department of Data Science, Friedrich-Alexander-Universität Erlangen, Erlangen, Germany

Correspondence
Felix Glang, Magnetic Resonance Center, Max Planck Institute for Biological Cybernetics, Tübingen, Germany.
Email: felix.glang@tuebingen.mpg.de

Isolated evaluation of multiparametric in vivo chemical exchange saturation transfer (CEST) MRI often requires complex computational processing for both correction of B_0 and B_1 inhomogeneity and contrast generation. For that, sufficiently densely sampled Z-spectra need to be acquired. The list of acquired frequency offsets largely determines the total CEST acquisition time, while potentially representing redundant information. In this work, a linear projection-based multiparametric CEST evaluation method is introduced that offers fast B_0 and B_1 inhomogeneity correction, contrast generation and feature selection for CEST data, enabling reduction of the overall measurement time. To that end, CEST data acquired at 7 T in six healthy subjects and in one brain tumor patient were conventionally evaluated by interpolation-based inhomogeneity correction and Lorentzian curve fitting. Linear regression was used to obtain coefficient vectors that directly map uncorrected data to corrected Lorentzian target parameters. L1-regularization was applied to find subsets of the originally acquired CEST measurements that still allow for such a linear projection mapping. The linear projection method allows fast and interpretable mapping from acquired raw data to contrast parameters of interest, generalizing from healthy subject training data to unseen healthy test data and to the tumor patient dataset. The L1-regularization method shows that a fraction of the acquired CEST measurements

---

is sufficient to preserve tissue contrasts, offering up to a 2.8-fold reduction of scan time. Similar observations as for the 7-T data can be made for data from a clinical 3-T scanner. Being a fast and interpretable computation step, the proposed method is complementary to neural networks that have recently been employed for similar purposes. The scan time acceleration offered by the L1-regularization ("CEST-LASSO") constitutes a step towards better applicability of multiparametric CEST protocols in a clinical context.

KEYWORDS
APT, CEST, feature selection, LASSO, linear projection, NOE

1 | INTRODUCTION

Chemical exchange saturation transfer (CEST) MRI provides interesting image contrasts based on indirect detection of low concentrated solutes through the water signal attenuation caused by chemical exchange of labile protons, which have been selectively saturated by RF irradiation. Most studies focus on the CEST effects of amide, amine, and guanidine protons related to peptides and proteins.[1] Furthermore, CEST was shown to give insights into pH[2] and the metabolite content of creatine[3] or glutamate.[4] Additionally, multiparametric CEST protocols yield contrasts related to the semisolid compartment provided by the semisolid magnetization transfer (ssMT) effect, as well as relayed nuclear Overhauser (NOE) effects that are known to correlate with protein content and conformation.[5,6] In the context of brain cancer, CEST is of clinical interest; for example, amide CEST has been shown to correlate with gadolinium enhancement,[7] and changes in NOE have been reported to correlate with histology[8] and also to be a measure for tumor therapy response.[9]

However, extraction of the CEST contrast parameters of interest often requires complex mathematical modeling, for example, by nonlinear curve fitting of Bloch–McConnell[10] or Lorentzian models.[11–14] These are time-consuming, depend on initial and boundary conditions, and thus remain difficult. Presumably, this is why simple metrics like asymmetry,[15] ratios or linear interpolations of certain points in the Z-spectra[16,17] are often preferred for CEST contrast generation. Common to all of these metrics is that they describe the target contrasts as linear expressions of acquired CEST measurements at certain offset frequencies.

Linear transforms play a tremendous role in all branches of science, and MRI is no exception. Most prominently, the Fourier transform describes the decomposition of an image into spatial frequencies, which can be acquired as gradient-encoded MR signals and reconstructed using the inverse Fourier transform. In the case of a 1D Fourier transform, the contribution of a certain harmonic frequency to a signal is expressed as linear projection of the signal onto the respective harmonic signal. The harmonic signals of different frequencies thus act as basis vectors spanning a linear space of representable signals. An example of this situation is displayed in the left column of Figure 1. Such linear transforms have the advantage of being stable, fast to calculate, and insightful for theoretical analysis.

To utilize the full potential of linear transforms for CEST data evaluation, in this work we aim to find the best linear combination of acquired points in the Z-spectrum to generate a contrast as close as possible to a desired target. Such optimal linear combination weights can be found by linear regression applied to conventionally evaluated training data, in the present case using a Lorentzian fit model. Contrast generation can then be expressed analogously to the discrete Fourier transform (Figure 1, left column) as linear projection of the raw acquired data onto the respective weight vectors (Figure 1, right column). In the context of current exploration of neural networks for such tasks,[18–21] the linear transform forms the simplest learning-based approach and by its linearity allows for direct interpretation and thus also guidance for more sophisticated approaches.

Furthermore, the linear projection approach can be extended to address the scan time issue of multiparametric CEST protocols. Isolated evaluation of in vivo CEST effects usually requires sufficiently densely sampled Z-spectra, to allow for separation of concomitant exchange effects as well as correction of field inhomogeneity. Correction of B_1 inhomogeneity, which is increasingly severe at high and ultrahigh field scanners, even requires acquisition of spectral data at multiple saturation amplitude levels.[14] The number of acquired offsets and saturation amplitudes largely determines the total CEST acquisition time, as the entire sequence needs to be repeated for each amplitude and frequency offset. However, the acquired CEST data are known to be partially redundant, which can be exploited for denoising.[22] In view of such redundancies, the question arises if the desired target contrasts could be generated from only a subset of the originally acquired data. To find such subsets, we extend the linear projection approach by automatic feature selection using the well-established least absolute shrinkage and selection operator (LASSO) technique.[23] This type of L1-regularization is known from compressed sensing MRI,[24] where it is used to enforce sparsity of reconstructed MR images in certain transform domains. In the present work, the proposed "CEST-LASSO" is set up to promote sparsity of required frequency offsets and B_1 amplitude levels simultaneously, and by doing so offers a direct reduction of acquisition time.
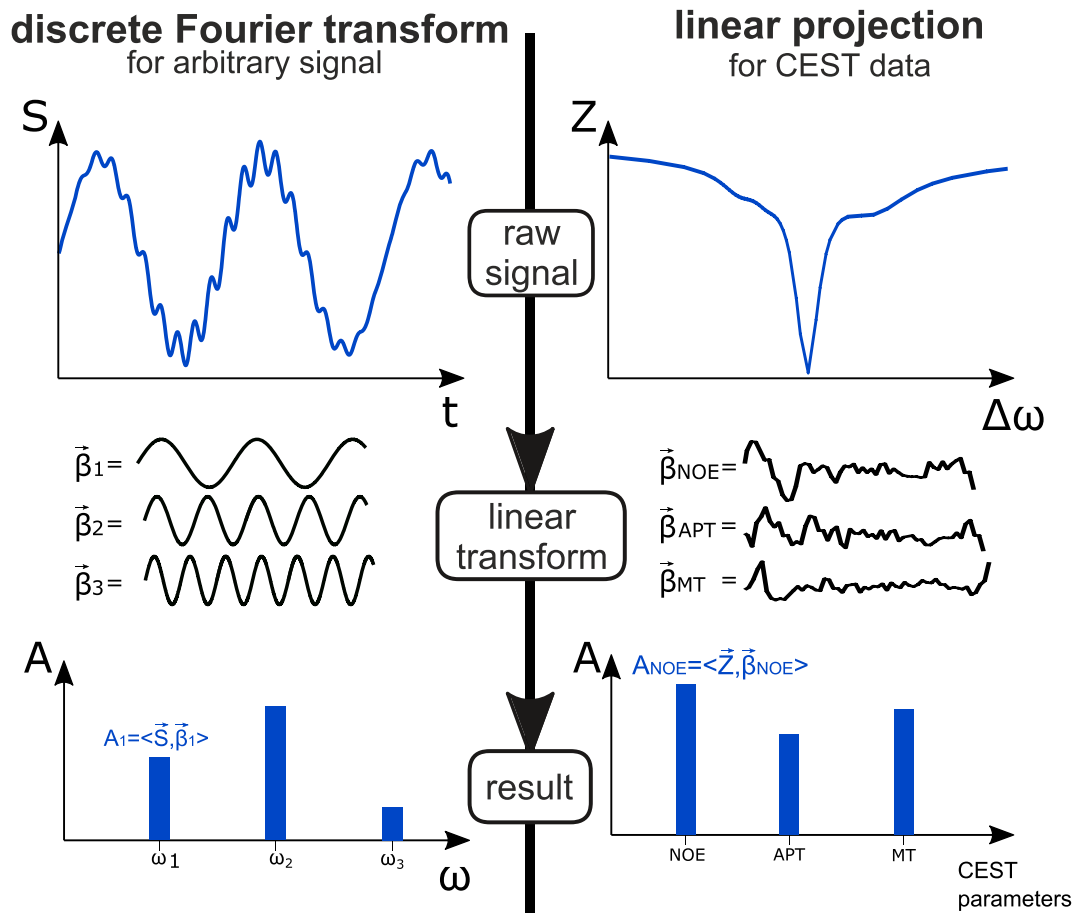
FIGURE 1　Analogy of discrete Fourier transform and the proposed linear projection approach for chemical exchange saturation transfer (CEST) evaluation. For the Fourier transform, a signal vector $S(t)$ is projected onto basis vectors $\beta_1, ..., \beta_n$ consisting of the respective harmonics to yield the Fourier coefficients $A_1, ..., A_n$ for different frequencies. In the case of linear CEST evaluation, acquired raw data are projected onto coefficient vectors to yield desired target contrasts like amide proton transfer (APT), nuclear Overhauser effect (NOE), and semisolid magnetization transfer (ssMT) amplitudes. The optimal coefficients can be found by linear regression from conventionally evaluated training data

2 | THEORY

2.1 | Linear projection

Target CEST parameters in each voxel are expressed as linear projections, that is, dot product of the acquired raw data $\vec{x}$ with N measurements, onto a vector of regression coefficients $\vec{\beta}$, as

$$y = \vec{x} \cdot \vec{\beta} = \sum_{k=1}^{N} x_k \beta_k \tag{1}$$

In the case of multiple target parameters, the vectors of regression coefficients for each of these M targets can be assembled into the coefficient matrix $\boldsymbol{B}$ $(N \times M)$, such that a vector of target parameters $\vec{y}$ can be obtained from the vector of input data $\vec{x}$ in a given voxel as a matrix–vector product

$$\vec{y} = \vec{x}\boldsymbol{B}. \tag{2}$$

Evaluating this expression for K different input vectors, for example, from multiple voxels, assembled to an input data matrix $\boldsymbol{X}$ $(K \times N)$, leads to the formulation as a general linear model

$$Y = XB \tag{3}$$

with the target data matrix Y ($K \times M$). Due to the structure of rows and columns in the defined matrices and the right-hand side multiplication of X by, the forward model Equation (3) only mixes spectral but no spatial information, such that the linear projections operate on each voxel independently. For a collection of known input-target pairs X and Y, referred to as training data from now on, the matrix of optimal regression coefficients can be obtained by solving the ordinary least squares problem, which has the global analytical solution

$$\widehat{B} = \arg\min_{B} ||Y - XB||_F^2 = \left(X^T X\right)^{-1} X^T Y = X^+ Y \tag{4}$$

with the Frobenius norm $||\cdot||_F$ and the Moore–Penrose pseudoinverse $X^+ = \left(X^T X\right)^{-1} X^T$.[25]

2.2 | LASSO

The LASSO regression objective for a single scalar target parameter y can be formulated as the L1-regularized linear least squares problem,[23]

$$\widehat{\vec{\beta}}_{\text{LASSO}} = \arg\min_{\vec{\beta}} \left(\left\| \vec{y} - X\vec{\beta} \right\|_2^2 + \lambda \left\| \vec{\beta} \right\|_1 \right) \text{ with } \left\| \vec{\beta} \right\|_1 = \sum_{i=1}^{N} |\beta_i|. \tag{5}$$

In general, there is no analytical solution for $\widehat{\vec{\beta}}_{\text{LASSO}}$. However, the optimization problem is still convex, which means that there are globally optimal solutions that can be found iteratively.[26]

Depending on the choice of the regularization parameter λ, the L1-regularization leads to a sparse solution, where a certain number of coefficients are zero. As the corresponding input components do not contribute to the linear projection (Equation (1)), they can be removed entirely from the model. In the case of CEST data, this means that the corresponding measurements (at particular frequency offsets and saturation amplitudes) do not need to be acquired at all to generate the desired target contrast parameter y by linear projection, once the regression coefficients $\vec{\beta}$ are obtained.

In the case of multiple target parameters, solutions to the standard LASSO problem (Equation (5) can be calculated for each target parameter y individually. In this case, the inputs that can be removed from the model will be different for each target parameter. Consequently, the result will be differently subsampled sets of the original inputs that are all suited for just one particular target parameter, but not a common reduction scheme that simultaneously optimizes the linear prediction of multiple target parameters. To overcome this limitation, the LASSO regularization can be modified to an instance of the multivariate group LASSO,[27] namely, the row-sparsity–enforcing L2-L1 LASSO (rowLASSO).[28]

$$\widehat{B}_{\text{rowLASSO}} = \arg\min_{B} \left(||Y - XB||_F^2 + \lambda ||B||_{2,1} \right) \text{ with } ||B||_{2,1} = \sum_{i=1}^{N} \sqrt{\sum_{j=1}^{M} |B_{ij}|^2}. \tag{6}$$

A row of the coefficient matrix B corresponds to the contribution of a particular input component to all target parameters in Equation (3). The L2-L1 norm used as regularization for the rowLASSO forces entire rows of B to become zero, which means that the corresponding input components do not contribute to any of the included target parameters and can therefore be removed. Solving the rowLASSO for CEST data thus provides a single reduced list of measurements that still allows for simultaneous generation of multiple target parameters. Denoting the number of retained inputs by N_{red} and the original number of inputs by K, the reduction factor $R = K/N_{\text{red}}$ can be defined.

The regularization term added to the ordinary least squares objective (Equation (4)) in the case of LASSO (Equation (5)) and rowLASSO (Equation (6)) is known to introduce a bias to the obtained nonzero regression coefficients in $\widehat{B}_{\text{rowLASSO}}$,[29] which can deteriorate the performance of the obtained linear model when applied to new data. This bias can be removed by refitting: a reduced input data matrix X_{red} is formed by removing all columns from X, for which the corresponding row in $\widehat{B}_{\text{rowLASSO}}$ is zero. With that, the unregularized ordinary least squares regression on the remaining inputs $\widehat{B}'_{\text{rowLASSO}} = \left(X_{\text{red}}^T X_{\text{red}}\right)^{-1} X_{\text{red}}^T Y$ is calculated. According to this procedure, the regularized problem is used only for variable selection, whereas the unregularized regression provides the final coefficient estimates. Having only a reduced input vector $\vec{x}_{\text{red}}$ at hand—for example, from an accelerated scan, for which the measurements rendered irrelevant by LASSO have been omitted—the contrast parameters can then be obtained as

$$\vec{y} = \vec{x}_{\text{red}} \widehat{B}'_{\text{rowLASSO}} \tag{7}$$

It was found throughout the present work that the refitted coefficients $\widehat{B}'_{\text{rowLASSO}}$ provided better results than the original $\widehat{B}_{\text{rowLASSO}}$.

3 | METHODS

3.1 | Data acquisition

Data were acquired from six healthy subjects and one patient with a brain tumor (glioblastoma WHO grade IV) after written informed consent at a MAGNETOM Terra 7T scanner (Siemens Healthineers AG, Erlangen, Germany) with a 32Rx/8Tx-channel head coil (Nova Medical, Wilmington, MA). All in vivo examinations were approved by the local ethics committee.

Homogeneous saturation was realized as in[30] using the MIMOSA scheme (120 Gaussian pulses, pulse duration t_p = 15 ms, interpulse delay t_d = 10 ms, duty cycle DC_{sat} = 60.56%, recovery time between previous readout and start of saturation block t_{rec} = 1 s). Two B_1 maps were acquired for circularly polarized (CP) and 90° mode, which were combined according to[31] to form the effective MIMOSA B_1 map. Two different saturation amplitude levels of B_1 = 0.72 μT and B_1 = 1.00 μT were applied. The CEST image readout was a centric reordered 3D snapshot gradient echo[32] (TE = 1.77 ms, TR = 3.70 ms, FA = 6°, FOV: 230 mm x 186.875 mm x 21 mm, matrix size: 128 x 104 x 18, GRAPPA[33] factor 2 in the first phase-encoding direction). 56 frequency offsets were acquired according to the sampling schedule given in the Appendix. With that, the total saturation time was T_{sat} = 2.99 s. The total acquisition time for Z-spectra of both B_1 values was 13 min 24 s.

3.2 | Conventional evaluation

A schematic of the employed postprocessing pipeline is shown in Figure 2. All acquired 3D volumes were coregistered onto the chosen reference volume at $\Delta\omega$ = 3.5 ppm and B_1 = 0.72 μT, to correct for subject motion, using the SPM toolbox.[34] B_0 inhomogeneity correction was applied by fitting the water peak of the Z-spectra with a smoothing spline and shifting the spectra according to the spline's minimum on the frequency axis. The obtained frequency shift in each voxel provides a relative B_0 inhomogeneity map. During postprocessing, an interpolated baseline correction[35] with the offsets acquired at ±100 ppm turned out to yield more stable results than M_0 normalization with –300 ppm, which is why the two –300 ppm scans were not considered for further evaluations. Spectra were denoised using principal component analysis (PCA),[22] retaining the first 11 principal components. After that, two-point Z-B_1-correction[14] was applied using the acquired spectra at both B_1 amplitudes and the relative MIMOSA B_1 map.
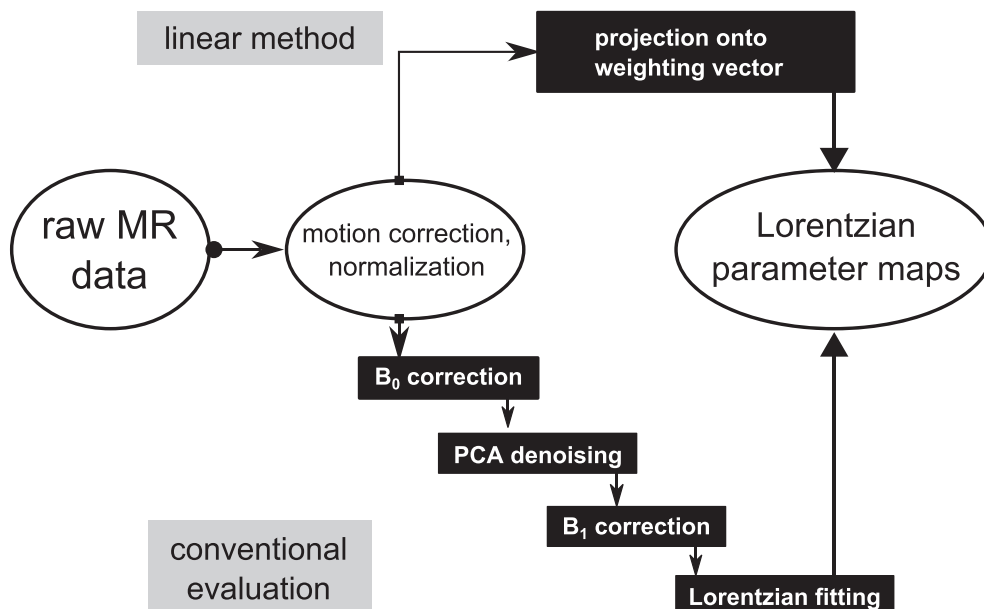

FIGURE 2 Schematic of the conventional multiparametric chemical exchange saturation transfer (CEST) data evaluation pipeline (bottom), for which the proposed linear projection-based evaluation (top) forms a shortcut. In both cases, acquired CEST data are corrected for subject motion and spectrally normalized. Conventional evaluation consists of interpolation-based B_0 and B_1 inhomogeneity correction, followed by spectral principal component analysis (PCA) denoising and nonlinear least-squares fitting of a five-pool Lorentzian model. In the case of the proposed linear approach, all of these steps are accomplished by projection onto regression coefficients previously obtained from conventionally evaluated data

Based on the models,[11–14,35] the resulting spectra were fitted using a five-pool Lorentzian model (water, amide, rNOE, amine, and ssMT, resulting in 16 free fit parameters), using the same initial and boundary conditions for all datasets. The output of the complete conventional evaluation including B_0 and B_1 correction and Lorentzian fitting was used to generate the training datasets for linear regression. All computations were carried out in MATLAB (MathWorks, Natick, MA).

3.3 | Linear regression and LASSO

Uncorrected but normalized Z-spectra of both B_1 levels were assembled to form the input data matrix X. Additionally, the B_1-MIMOSA and B_1-CP field map values in each voxel were provided as additional inputs by concatenating them to the columns of X, resulting in a total of 110 (54 + 54 + 2) input features. Lorentzian parameters from each voxel obtained by conventional fitting of B_0-corrected data and the B_0 inhomogeneity in each voxel calculated from the non-B_0–corrected data were likewise assembled in the target data matrix Y, resulting in 17 (16 + 1) target parameters.

The introduced formulation of the general linear model (Equation (3)) and LASSO methods (Equations (5) and (6)) assumes that both input data matrix X and target data matrix Y are centered, meaning they have column-wise mean zero. With that, there is no need for an additional constant intercept term.[29] Because of that, and to avoid any scaling issues, input and target matrices were standardized to column-wise mean zero and variance one before performing the least-squares and LASSO fits.

Data and code for demonstration of the method can be found at https://github.com/fglang/linearCEST/. For the linear projection method, all the necessary steps (i.e., data standardization, pseudoinverse calculation, and application to test data) can be performed in less than 50 lines of MATLAB code. Solving the linear least-squares problem by MATLAB's "pinv" function took 0.8 s on a computer with an Intel Xeon W-2145 3.7 GHz CPU, 8 cores and 32 GB RAM, and application of the regression coefficients took 0.03 s. Lorentzian fitting for all voxels of one subject dataset took 4 min 36 s. The standard LASSO (Equation (5)) and rowLASSO (Equation (6)) problems were solved using the FISTA algorithm.[26,36] For the typical data matrix sizes occurring in this work (number of inputs $N = 110$, number of targets $M = 17$, number of training voxels $K \approx 300\,000$), calculation of a solution takes approximately 0.25 s. This allows calculating many solutions for increasing values of the regularization parameter λ, such that any possible number of retained inputs, meaning arbitrary acceleration factors, can be found within minutes.

The approach of generating CEST contrast maps by linear projections from the unprocessed raw Z-spectra was first validated in a healthy subject test dataset. The data of five healthy subjects were used as training set to obtain regression coefficients $\widehat{B}$ according to Equation (4), which were then applied to a sixth healthy test dataset according to Equation (3).

Predictions of the linear and LASSO method for amplitude parameters were assessed in terms of the normalized root-mean-squared error

$$\text{NRMSE} = \frac{1}{\bar{y}} \sqrt{\frac{\sum_{j=1}^{K} \left(\widehat{y}_j - y_j\right)^2}{K}}$$

between predicted values $\widehat{y}$ and the reference parameters y with mean value $\bar{y}$. For ΔB_0 as a target parameter, non-normalized RMSE was used, because of the mean value being close to 0.

4 | RESULTS

The resulting maps in Figure 3 show that for APT, NOE, and ssMT contrasts, as well as field inhomogeneity ΔB_0, the linear projection results (Figure 3B) preserve the general contrast of the reference maps (Figure 3A) obtained by conventional evaluation, with NRMSE of 11%, 4.8%, and 3.9% (for APT, NOE, and ssMT amplitudes, respectively), and RMSE of 0.035 ppm for ΔB_0. The NRMSE between the reference and projection result for the individual CEST contrasts coincides with the observed effect strengths: the strongly pronounced ssMT effect, manifested as the highest of the Lorentzian peak amplitudes, can be best predicted by the linear projection, followed by the smaller NOE and APT effects. For the amine contrast, which is the least pronounced CEST effect in the acquired data, the linear projection result is the least accurate (NRMSE = 15%). The difference maps in Figure 3C exhibit localized deviations: in the case of the NOE and amine amplitudes, deviations occur within the anterior left region, where the MIMOSA map (Figure 3E) assumes the highest values. For the ssMT amplitude, slightly too low predictions occur in the posterior left region, where the MIMOSA map assumes the lowest values, as well as in the CSF. The projection-based maps show similar low noise as the conventionally evaluated data, for which an explicit denoising step is included. This shows that the projection approach denoises implicitly.

Results for the remaining parameters of the five-pool Lorentzian model are displayed in Figure S1. From the figure it can be seen that the linear projection works better for amplitude parameters than for peak widths and positions.
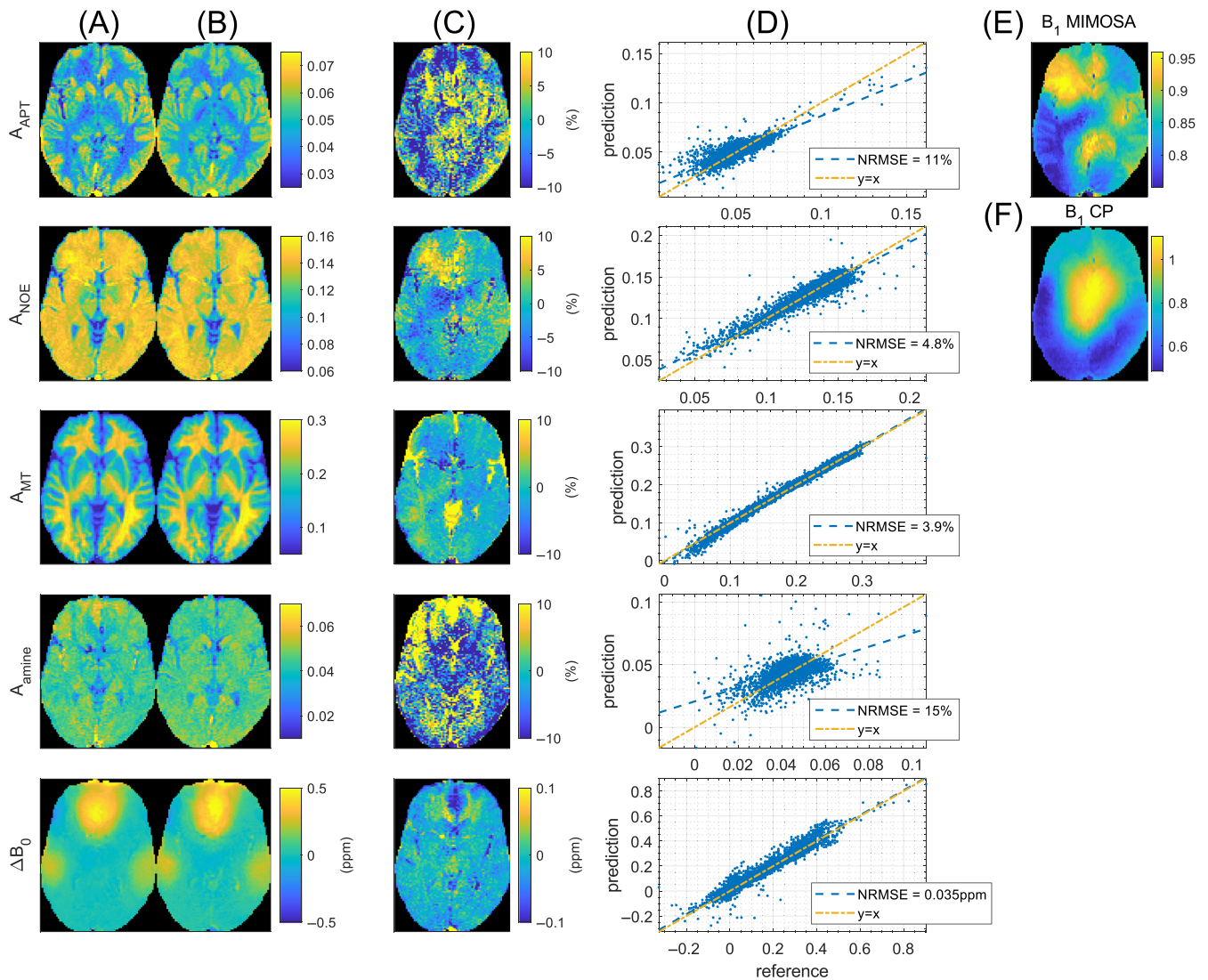
FIGURE 3 Results of linear projection in a healthy test dataset. (A) Reference Lorentzian fit results for a healthy subject dataset. (B) Contrast maps obtained by linear projection in the same subject. (C) Difference maps between reference and linear projection. For the amplitude parameters, relative differences to the reference are given in %. (D) Voxel-wise scatter plots of linear prediction results versus reference with legends indicating the normalized root mean square error (NRMSE) between prediction and reference. (E) Multiple interleaved mode saturation (MIMOSA) transmit field map (corresponding to CEST saturation RF pulses). (F) Circularly polarized (CP)-mode transmit field map (corresponding to readout RF pulses)

The linear regression coefficients **B** obtained by Equation (4) allow a directly interpretable insight into how the target contrast parameters emerge from the raw input data by linear projection. In Figure 4, the regression coefficients used to generate the contrast maps in Figure 3 are shown together with example input spectra at both B_1 amplitude levels, demonstrating how each point in the input spectra is weighted by the coefficients to produce the respective target value. In general, the coefficients for all target parameters show complex patterns with differently weighted contributions from all input points at both amplitude levels.

Still, some physically plausible patterns can be identified. For all CEST effects, there are clear weightings around the resonance frequency of the respective pool. For NOE, there are strong contributions around −3.5 ppm for both amplitude levels. For amines, the highest absolute weighting at the high amplitude level is at 2 ppm, whereas the amine weighting at the low amplitude level shows a less clear structure. For APT, there are contributions at the high amplitude level around +3.5 ppm, but also on the opposite side of the spectrum around −3.5 ppm. In the case of ssMT, the strongest contributions are located far-off-resonant at ±100 ppm for both amplitude levels, at 8 ppm and −5.5 ppm for the low amplitude level, and at +6 ppm and −9 ppm for the high amplitude level. The coefficients for ΔB_0 show complex oscillatory behavior in the spectral range between 0 ppm and ±8 ppm, with the highest values close to 0 ppm.
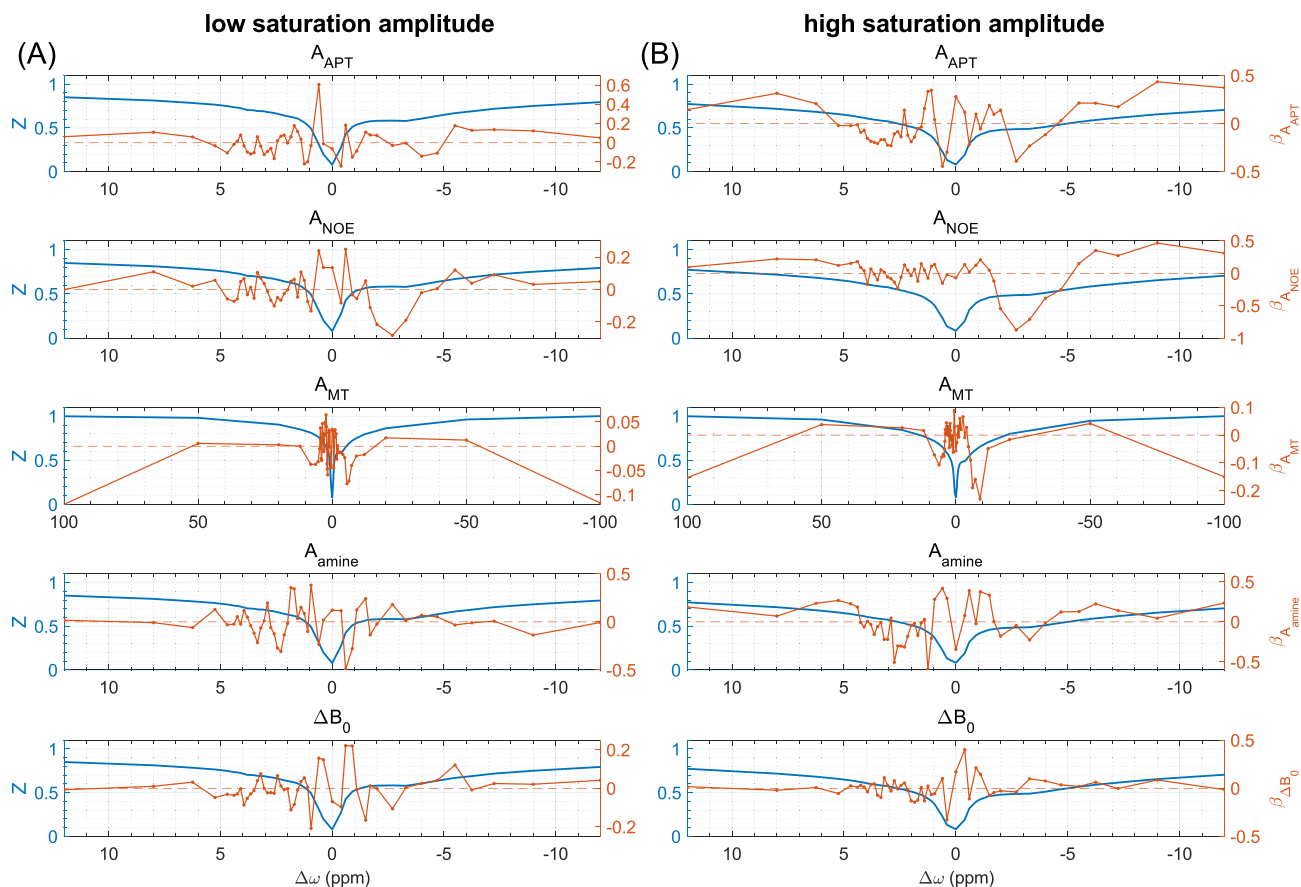
FIGURE 4 Coefficient vectors β (columns of coefficient matrix **B**) used to generate the linear projection contrast maps shown in Figure 3B. Coefficients are plotted for (A) Low- and (B) High-amplitude input data separately. The coefficients are obtained according to Equation (4) with training data generated from five healthy subject measurements. In blue, an example of the corresponding voxel-wise input is given, consisting of Z-spectra at two different saturation amplitudes and the values of the multiple interleaved mode saturation (MIMOSA) and circularly polarized (CP) B1+ field maps (not plotted). Contrast parameters in each voxel are then obtained by a simple dot product between input and coefficient vectors

More insight into the regression coefficient patterns can be gained by simulations with artificial data, which are shown in Figures S2-S7. From those figures, it can be seen that the oscillatory sign switches of the regression coefficients effectively form weighted sums of Z-spectral points around each CEST resonance that are suitable for isolating the respective amplitude parameters from concomitant effects.

As a next step, the LASSO procedure was applied to reduce the number of inputs to the linear model. As described in the Methods section, values of the regularization parameter λ were found such that the number of retained inputs (i.e., the number of nonzero rows in **B**) decreases gradually from 110 (all original inputs) to one. The models were trained again on the same five healthy subject datasets and tested on the sixth healthy subject dataset, as shown in Figure 3. The rowLASSO objective was set up here to fit the targets APT, NOE, ssMT, and amine amplitudes, and ΔB_0 simultaneously, which means that the obtained reduced input lists are a compromise to yield predictions of all of these targets at the same time. A comparison of alternative rowLASSO objectives, including one reduction set for all Lorentzian parameters (amplitudes, peak widths, and positions), as well as individual reduction sets for all parameters separately (standard LASSO), is provided in Figure S8. As a general observation, including more target parameters to be predicted simultaneously by a single reduced input list yields less accurate results than individual reduced input lists for each target parameter separately in most of the cases.

An overview of the input frequency offsets that were removed by the LASSO procedure in each step is given in Figure S9.

Figure 5 shows the influence of offset reduction on the NRMSE between the linear projection result from the rowLASSO-reduced inputs and reference data (red curve). Retaining 39 of the originally 110 inputs (corresponding to a reduction factor R = 2.8) still allows linear projections with NRMSE = 15%, 6.7%, 5.9%, and 21% for APT, NOE, ssMT, and amine amplitudes, respectively, and RMSE = 0.06 ppm for ΔB_0 over the test dataset.

For comparison, randomly subsampled lists of inputs were generated 100 times for each respective reduction factor, and linear regressions (Equation (4)) were calculated and evaluated for the randomly retained inputs (Figure 5, blue curves). For most of the reduction factors, the rowLASSO-reduced solution outperforms the average of the randomly subsampled input list solutions in terms of NRMSE. However, there are
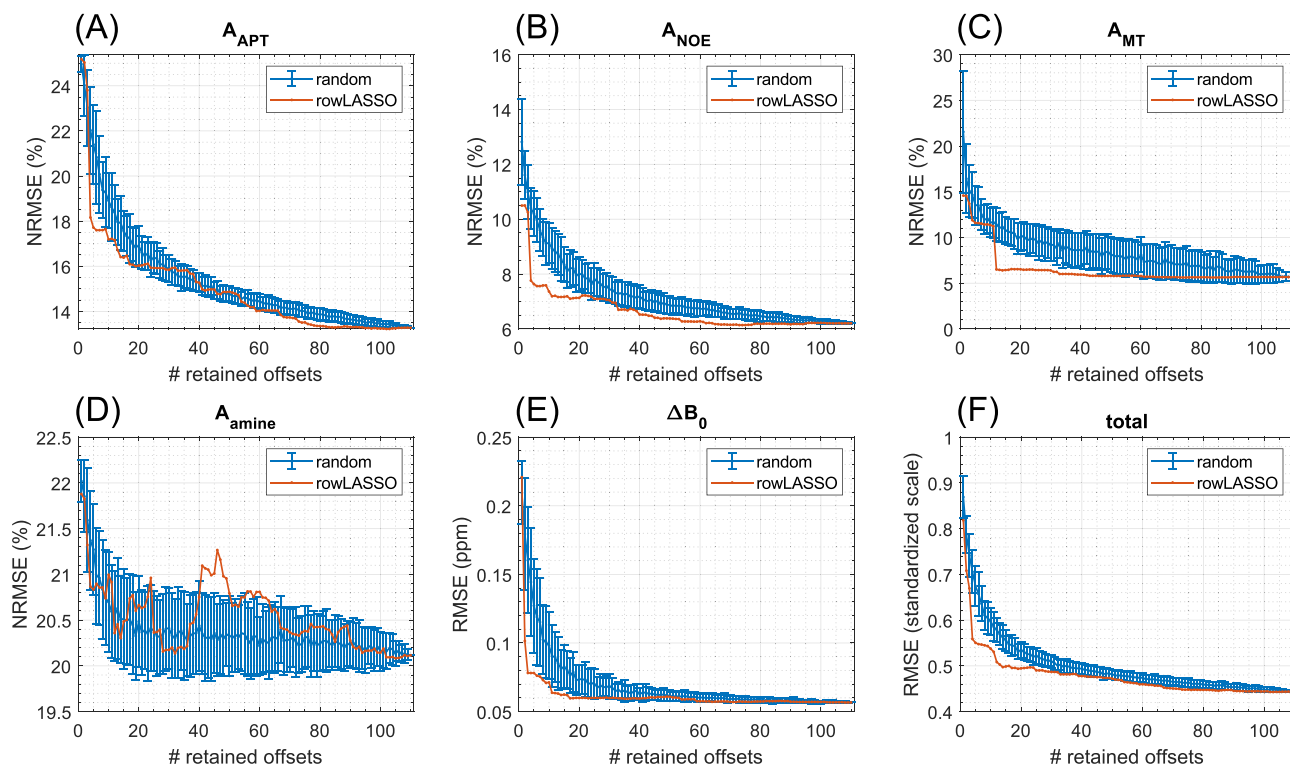
FIGURE 5 Dependence of least absolute shrinkage and selection operator (LASSO) prediction performance on offset reduction. Displayed are the normalized root mean square errors (NRMSEs) between linear projection results from a LASSO-reduced offset list and the reference Lorentzian fit results against the number of retained offsets for (A) Amide proton transfer (APT), (B) Nuclear Overhauser effect (NOE), (C) Magnetization transfer (MT), and (D) Amine amplitudes, and (E) ΔB_0. (F) NRMSE evaluated for all these target parameters simultaneously, calculated on the standardized target values to compensate for the different target scales. Blue curves show the results of random offset list reduction, evaluated 100 times, with the error bars indicating standard deviation over the random repetitions. The rowLASSO objective (Equation (6)) was set up with the target parameters APT, NOE, MT, and amine amplitudes, and ΔB_0 simultaneously

random reductions that yield better predictions than the rowLASSO solution. In these cases, the subsampled input lists may be incidentally well suited for the prediction of just one single target, whereas the rowLASSO objective is always to find a compromise that works as best as possible for all target parameters simultaneously. This can be confirmed by calculating the NRMSE for all standardized target parameters simultaneously (Figure 5F), showing the superiority of the rowLASSO solution over the random reductions, especially for very high reduction factors (number of retained offsets ≤ 20).

With regard to these results, the question arises if the conventional Lorentzian fit could be used directly to generate accurate contrast maps from a reduced number of acquired frequency offsets. To investigate this, conventionally corrected Z-spectra were retrospectively undersampled (acceleration factors: R = 3/2, i.e., removing every third offset; R = 2, i.e., removing every second offset; and R = 3, i.e., retaining every third offset) and processed by the nonlinear least squares fit. The fitted results from such reduced spectra were then compared with the linear projection results from the original uncorrected spectra of both B_1 values for the same acceleration factors. As regular undersampling in the case of the Lorentzian fit permits different undersampling patterns for each acceleration factor (e.g., for R = 2 retaining offsets 1,3,5 ... or 2,4,6 ...), the respective pattern that yielded the best results in terms of NRMSE was chosen to make the analysis less biased towards the optimized rowLASSO.

The obtained results shown in Figure 6 illustrate that, for moderate acceleration up to R = 2, the equidistantly reduced Lorentzian fit provides lower NRMSE with respect to the reference data compared with rowLASSO. However, for an acceleration of R = 3 in the case of APT, NOE, and MT amplitudes, rowLASSO performs better, which is especially visible in the degraded NOE contrast in Figure 6E and the difference maps in Figure 6F. For amine amplitudes, the reduced Lorentzian fit performs better than rowLASSO for all the considered accelerations. Overall, it is noticeable that the reduced Lorentzian fit contrast maps fluctuate for different undersampling schemes, while rowLASSO contrasts appear stable over different acceleration factors.

The maintained low NRMSE in the case of rowLASSO reduction (NRMSE ≤ 15% in APT, NOE, and MT amplitudes for R ≤ 2.8) indicates that a linear projection reconstruction of these CEST contrast maps is still possible with only a fraction of the originally acquired frequency offsets at both B_1 amplitude levels. Indeed, the obtained parameter maps for acceleration factors R = 2 (Figure 7C) and R = 2.8 (Figure 7D) show no major
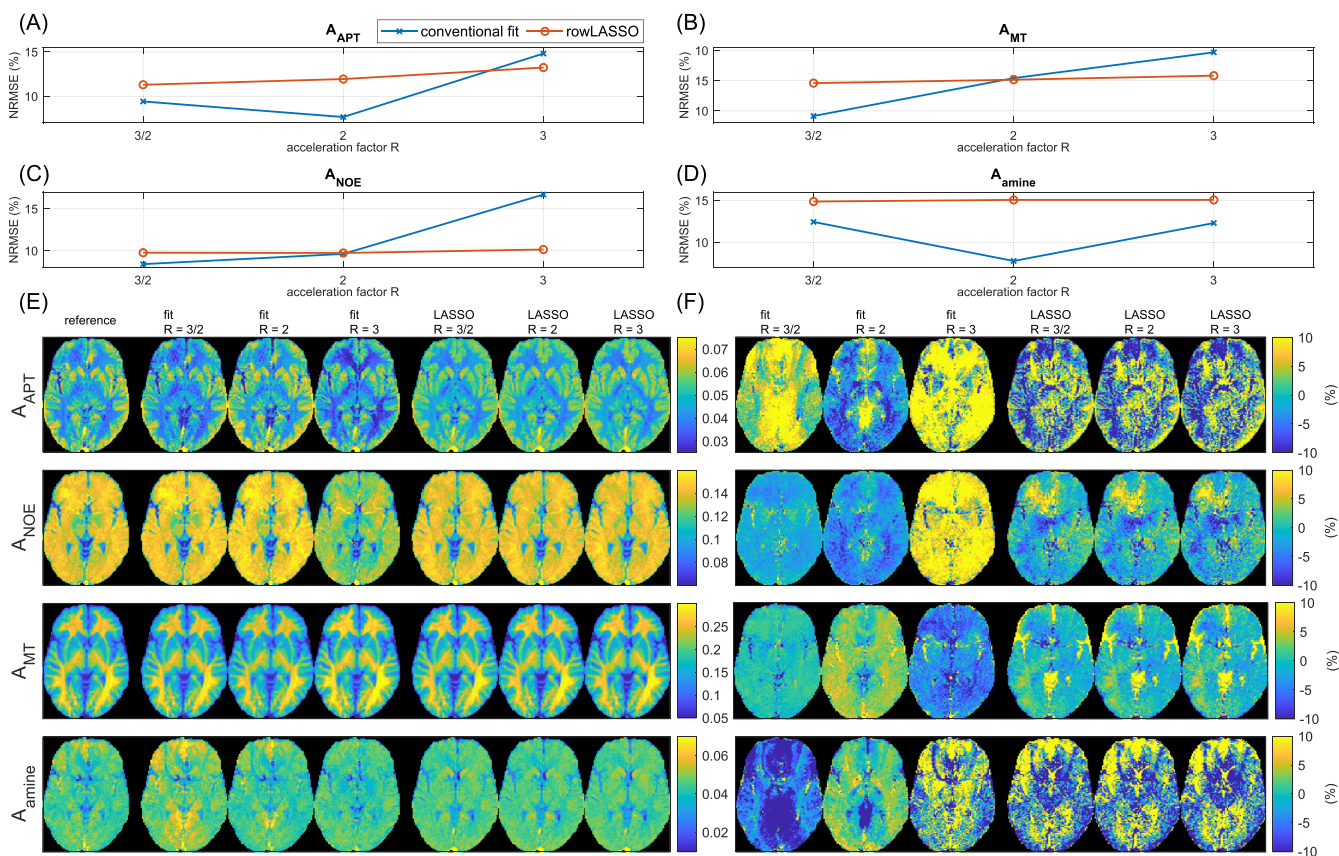
FIGURE 6 Comparison of linear projection results from reduced offset lists obtained by rowLASSO and conventional Lorentzian fits on equidistantly undersampled corrected Z-spectra. (A–D) Normalized root mean square error (NRMSE) between reference and rowLASSO linear projection results (blue curves), as well as Lorentzian fitting applied to retrospectively undersampled corrected Z-spectra (orange curves) for different acceleration factors. (E) Exemplary contrast maps from both methods (rowLASSO and conventional fit) for different acceleration factors and (F) Corresponding difference maps to the reference (fully sampled Lorentzian fit)

deviation from the full projection result (R = 1, Figure 7B) and therefore are in agreement with the reference contrasts (Figure 7A) as well. Only in the case of a very strong reduction (Figure 7E, R $\approx$ 37, only 3 inputs retained) were the obtained APT and amine contrasts severely corrupted. Remarkably, even for such a strong reduction, the NOE and ssMT amplitudes and ΔB_0 still correlate with the reference data to a certain extent, and the coarse spatial structure and even some anatomical contrast between gray and white matter (in the case of NOE and ssMT amplitudes) are roughly preserved. The rowLASSO-reduced regression coefficients used for generating the contrast maps in Figure 7B-E are displayed in Figure S10.

Having established the linear projection and rowLASSO method in healthy subject training and test datasets, as a next step, generalization of the method to pathology was investigated. Linear regression coefficients from the five healthy subject training datasets were obtained and applied to the glioblastoma patient dataset. Figure 8 shows the CEST results next to clinical contrasts for this patient. Interestingly, this tumor did not show typical gadolinium uptake (Figure 8A) as expected for glioblastoma, although amide CEST (Figure 8D, first row) showed the same hyperintensity as reported previously.[37] Despite the regression coefficients being obtained from only healthy subject data, the linear projection approach appears to generalize to tumor data, and the resulting maps (Figure 8E) still match the general contrast of the reference Lorentzian fit maps (Figure 8D), albeit with higher NRMSE (Figure 8I) than in the healthy test case (Figure 3D). In particular, the linear projections preserve the amide hyperintensity in the tumor. The same holds for the rowLASSO result with a reduction factor of R = 2.8 (Figure 8F), although with slightly reduced contrast.

Finally, the linear projection and rowLASSO approach was applied to 3T data to assess the applicability of the method in a broader clinical context. For that, data from[18] were retrospectively re-evaluated and compared with the recent deepCEST 3T approach introduced therein. Three healthy subject datasets were used for training and a glioblastoma patient (WHO grade IV) dataset for testing. The linear projections from all 55 acquired frequency offsets (Figure 9E), as well as a rowLASSO-reduced projection from 18 retained offsets (reduction factor R $\approx$ 3, Figure 9F), match the reference contrasts obtained by Lorentzian fitting (Figure 9C) with NRMSE = 14%, 8.1%, and 5.4%, and RMSE = 0.035 ppm in the case of full linear projection, and NRMSE = 15%, 10%, and 9.9%, and RMSE = 0.04 ppm in the case of rowLASSO, for APT, NOE, and ssMT
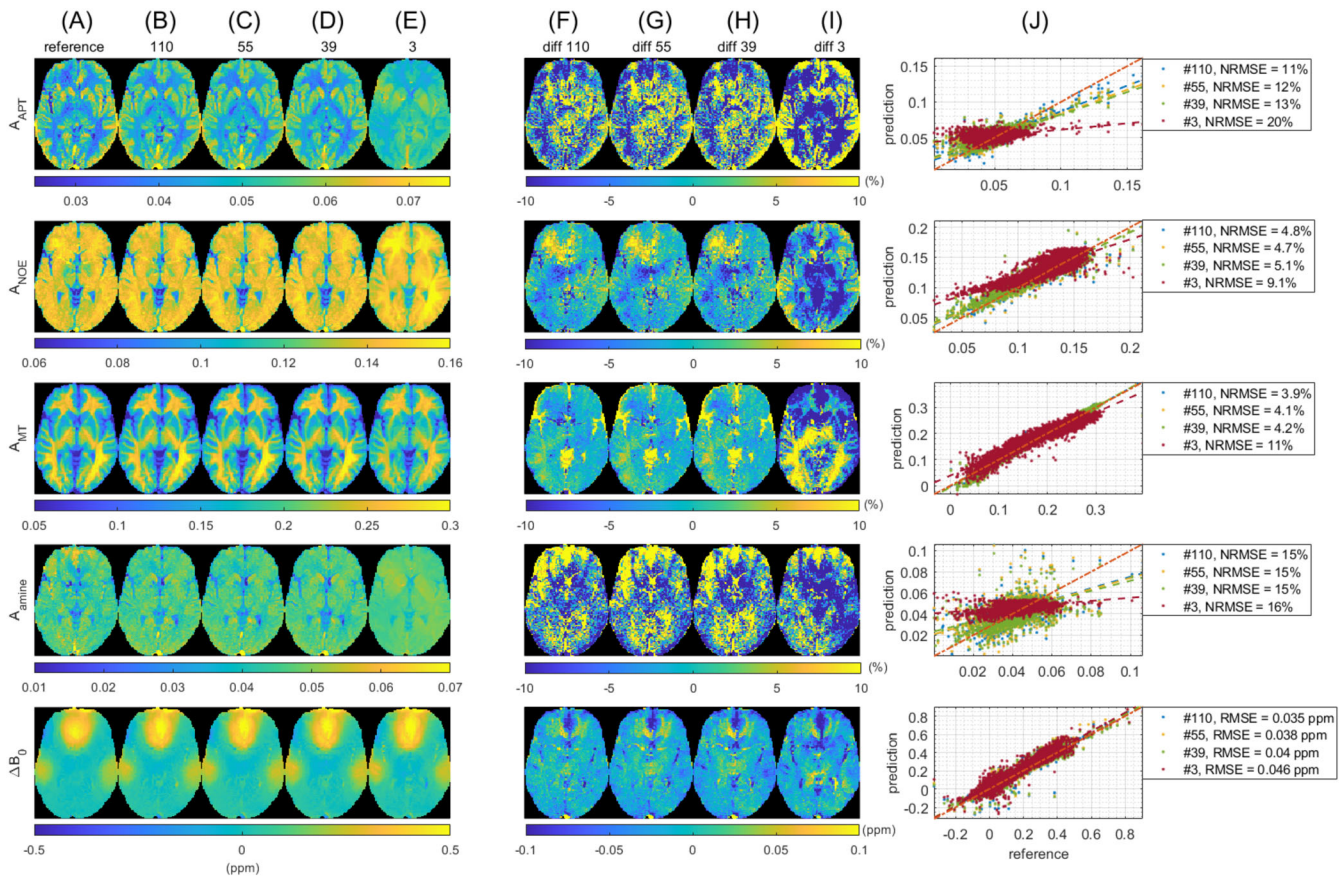
FIGURE 7 Least absolute shrinkage and selection operator (LASSO) results in a healthy test dataset. (A) Reference maps. (B) Linear projection results from the full input data (110 inputs). (C–E) LASSO-reduced projection results from 55, 39, and 3 inputs, respectively, corresponding to an acceleration of scan time by factors of 2, 2.8, and ∼37. (F–I) Difference maps between reference and projection results from the full 110 and LASSO-reduced 55, 39, and 3 inputs, respectively. For the amplitude parameters, relative differences to the reference are given in %. (J) Voxel-wise scatter plots of linear prediction results from the respective number of reduced inputs versus reference. Legends indicate the normalized root mean square error (NRMSE) between prediction and reference

amplitudes, and ΔB_0, respectively. In terms of NRMSE, the deepCEST 3T neural network (Figure 9D) performs best for all target parameters. Still, the linear and rowLASSO predictions preserve the principal contrast in the tumor region, especially the ring-shaped APT hyperintensity, which coincides with the gadolinium contrast-enhanced hyperintensity (Figure 9A).

5 | DISCUSSION

In this work, it was shown that CEST parameter maps, which would conventionally have been obtained by iterative nonlinear least squares fitting of a multipool Lorentzian model, can be obtained as simple linear projections of the acquired raw Z-spectra onto regression coefficients generated from conventionally corrected and evaluated training data. The linear projection thus integrates B_0 correction, B_1 correction, and contrast generation into a single computation step. Applying the coefficient vectors is fast (fractions of seconds) compared with conventional evaluation (>10 minutes for all required steps). Compared with the training of neural networks (several hours), obtaining solutions for the supervised learning problem (i.e., calculating the regression coefficients from a training set) is also faster by several orders of magnitude. The approach was shown to translate from healthy subject training data to a tumor patient test dataset, which was also observed in recent works on neural networks for CEST evaluation[18,19] and appears plausible as long as tumor tissue spectra can be approximated by linear combinations of healthy tissue spectra.[19]

The introduced linear projection approach has similarities with PCA methods, which were recently introduced in the field of CEST for denoising[22,38] and data-driven feature extraction.[39] For the latter method, test Z-spectra were linearly projected onto principal component vectors generated from a training dataset of healthy subject spectra. This was shown, similar to the finding in this work, to yield interesting tissue contrasts for a tumor patient dataset as well. The employed principal component basis vectors in the PCA method are independent of any target parameters obtained by conventional evaluation and only describe statistical correlations of the input Z-spectra. By contrast, the basis vectors in
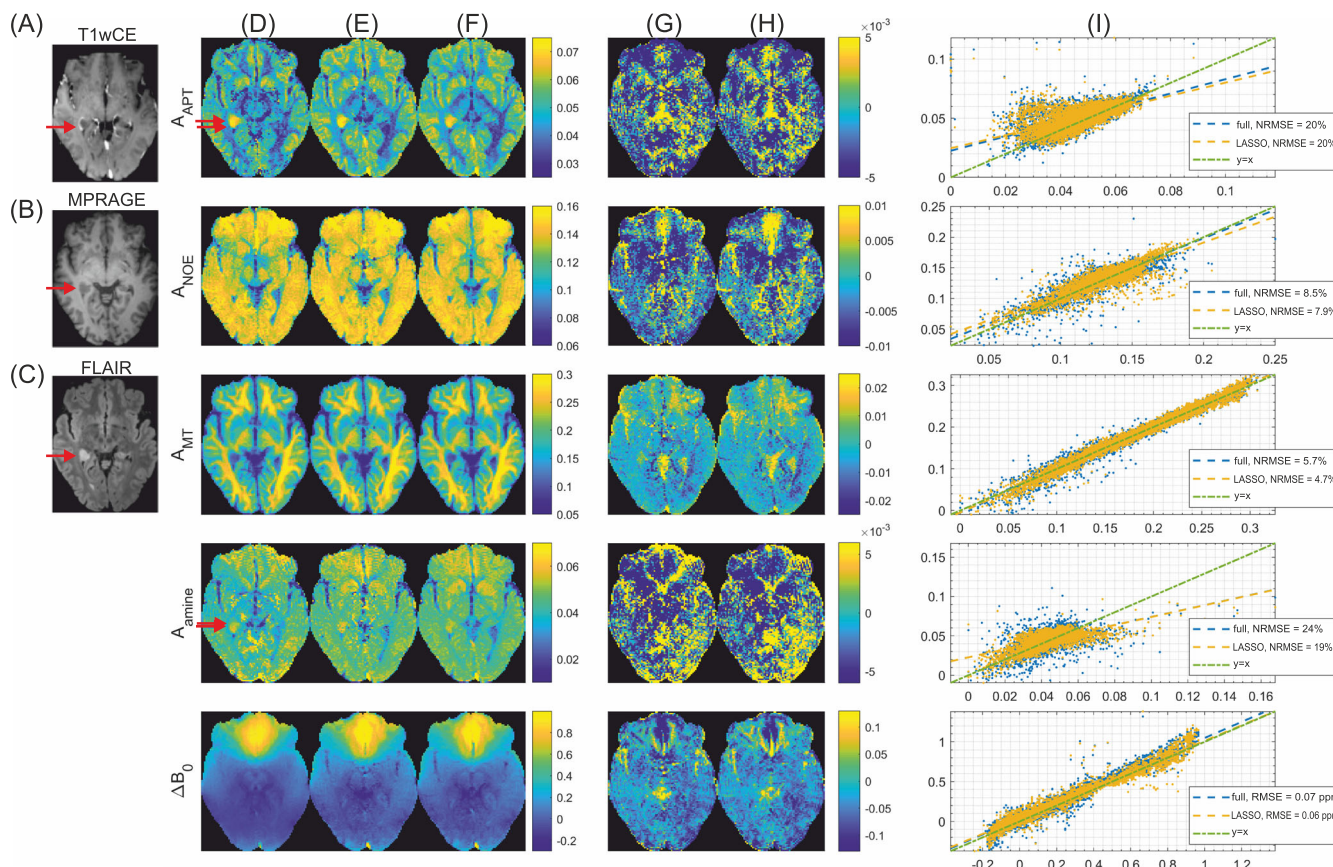
FIGURE 8 Results of linear projection in a tumor patient test dataset. Clinical contrasts: (A) T1-weighted contrast-enhanced, (B) MPRAGE, and (C) FLAIR. (D) Reference Lorentzian fit results. The red arrow indicates the glioblastoma. (E) Contrast maps obtained by linear projection with coefficients obtained from five healthy subject datasets. (F) Least absolute shrinkage and selection operator (LASSO) results for 39 retained inputs, corresponding to a reduction factor of R = 2.8. (G and H) Difference maps to reference for linear projection and LASSO results, respectively. For the amplitude parameters, relative differences to the reference are given in %. (G) Voxel-wise scatter plots of linear prediction and LASSO results versus reference with legends indicating the normalized root mean square error (NRMSE) between prediction and reference

this work (i.e., the linear regression coefficients) describe the correlations between spectra and tailored target contrast parameters defined by the conventional evaluation, making the present approach a more supervised one.

Extending the proposed linear projection method by LASSO regularization provided subsets of the original measured spectral offsets at both saturation amplitude levels, which still allowed linear mapping to the target contrast parameters. By that, potential acceleration factors for the CEST acquisition of up to R = 2.8 could be achieved with only minor impact on prediction quality compared with the full linear solution (Figures 7 and 8). The LASSO reduction method is data-driven and thus specific to the chosen CEST protocol. Consequently, the offset reduction scheme depends on B_0, B_1, and other sequence parameters, which is why new offset lists should be generated if the acquisition protocol has changed.

As shown in Figure 6, conventional Lorentzian fitting on equidistantly undersampled spectra can also be used for acceleration. However, for acceleration R = 3 in the case of APT, NOE, and MT, rowLASSO performed better than Lorentzian fitting. Even more conservatively, Goerke et al.[40] manually reduced offsets for Lorentzian fitting and reported a maximum reduction of 19% (corresponding to acceleration R ≈ 1.23) to still yield acceptable results. Better performance of undersampled conventional Lorentzian fitting might be achievable by dedicated offset list optimization instead of equispaced undersampling, but in the case of nonlinear least squares Lorentzian fitting, the required combinatorial optimization would suffer from computational complexity. The observed dependence on the sampling pattern (every first or every second removed, etc.) also indicates that detailed analysis of B_0 shifts is needed here, as these shifts have a similar influence on the effective sampling pattern.

The performance of CEST-LASSO for strong spectral undersampling is surprising, as to properly define the Lorentzian fit curve, many spectral points are necessary. However, (i) several Lorentzian parameters (e.g., the peak width and height) are correlated and the reduced training data effectively defines a subspace of the original data, so less information is needed than the full Lorentzian parameter space; and (ii) we also map solely on amplitude parameters, which again is just a part of the Z-spectral information, thus redundant data can be removed. If all parameters are reconstructed simultaneously, the performance decreases (Figure S8).
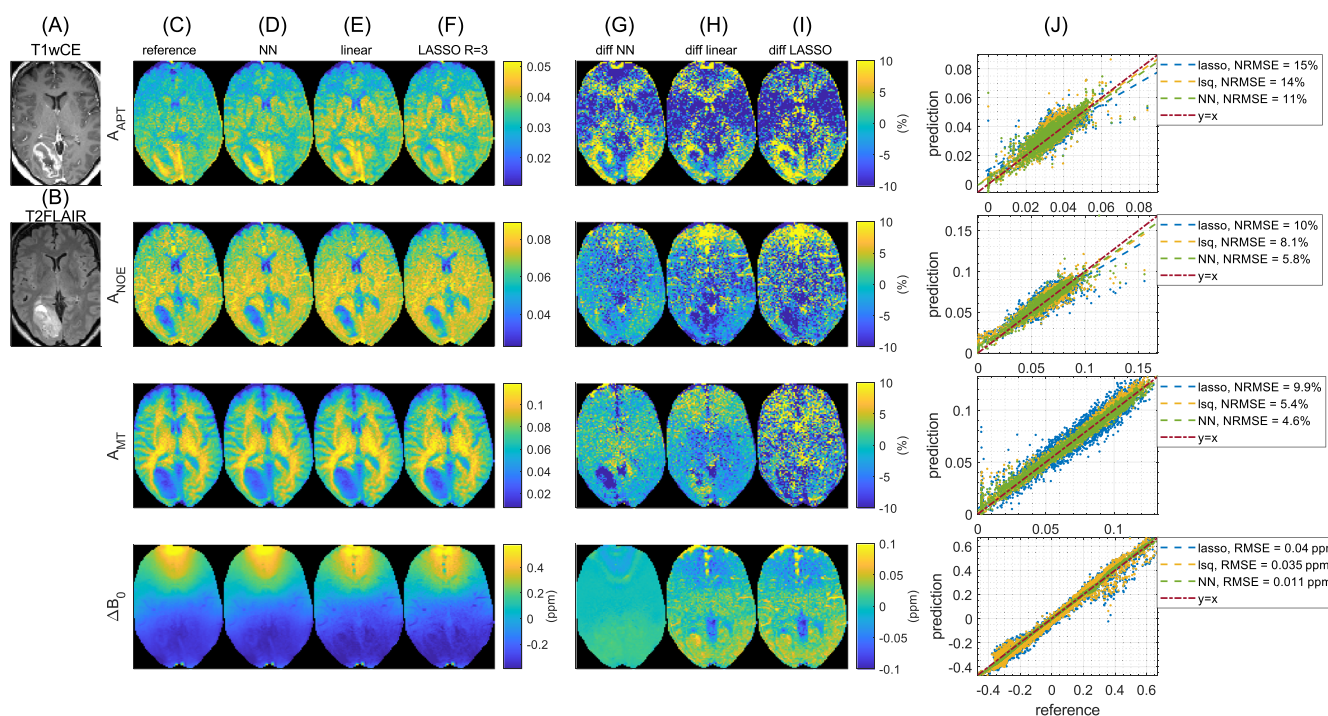
FIGURE 9 Application of the linear projection and least absolute shrinkage and selection operator (LASSO) approach to a tumor patient dataset acquired at a clinical 3T scanner and comparison with the deepCEST 3T approach. (A and B) Clinical contrasts: gadolinium-enhanced T1w and T2-FLAIR. (C) Reference Lorentzian fit results. (D) Neural network contrast predictions generated with the deepCEST 3T approach. (E) Linear projection results from all 55 acquired frequency offsets. (F) LASSO-reduced linear projection results from 18 retained frequency offsets, corresponding to a possible scan time reduction by a factor of R = 3. (G–I) Difference maps between reference and deepCEST 3T prediction, full linear projection, and LASSO-reduced linear projection, respectively. For the amplitude parameters, relative differences to the reference are given in %. (J) Voxel-wise scatter plots of the different prediction methods against Lorentzian fit reference

LASSO methods for feature selection are well established across disciplines[23,27] and known from compressed sensing MRI[24] for enforcing sparsity on the representation of MR images in certain transform domains, which allows accelerated acquisitions. The presented CEST-LASSO approach, by contrast, does not apply sparsity constraints to the image encoding, as the k-spaces of each acquisition are conventionally sampled and reconstructed, but to the number of CEST acquisitions. With that, the potential for CEST acceleration can be even greater than in the case of methods that focus only on acceleration of image encoding, as the saturation block of a CEST sequence can account for more than 80% of the total acquisition time,[41] depending on the protocol.

Most in vivo CEST studies use evenly distributed or manually tailored frequency sampling schedules that are not necessarily optimal. Addressing this issue, Tee et al.[42] apply an optimal design approach that yields optimized sampling schedules for amine quantification. In contrast to the present work, their objective is to find optimal sampling points for a predefined fixed number of acquisitions, whereas CEST-LASSO finds subsets of arbitrary length from a fixed initial sampling schedule. Consequently, the optimal design approach optimizes parameter quantification for fixed acquisition time, whereas CEST-LASSO finds compromises between parameter quantification and shorter acquisition time. The optimal design method relies on differential sensitivity analysis performed on numerically simulated spectra. Consequently, transferring this approach from phantom to in vivo CEST imaging would require an accurate Bloch–McConnell model for in vivo spectra, which is currently still not well established, as reported quantification results vary strongly among research groups.[10,43–45] By contrast, CEST-LASSO, as a more data-driven approach operating directly on measured spectra and evaluation results, is readily applicable to in vivo data.

The initial example of Figure 1 employing the analogy to Fourier transform hints at previous work performed by Yadav et al.,[46] where an actual Fourier transformation on Z-spectra was performed. This should not be confused with our approach, which finds a new data-driven linear basis, whereas Yadav et al. used the Fourier basis directly to remove low and high frequency components in the time domain.

The Lorentzian fitting method employed for generating reference data is only one of the many approaches for analyzing CEST data. Being a nonlinear least squares fit with 16 free parameters, it suffers from typical drawbacks, such as depending on initial and boundary conditions and being susceptible to noise and fluctuations. In particular, the amine contribution at +2 ppm can only be poorly extracted by both the Lorentzian fit and the proposed linear method, which also manifests in a low correspondence between the amine signals from CEST-LASSO and the reference data. The reason is that the corresponding features in the spectra are only weakly pronounced due to the relatively low applied B_1

amplitudes (0.72 μT and 1.00 μT) compared with the relatively high reported exchange rates of 700 Hz–10 kHz.[47] The resulting weak CEST labeling,[48] together with the low reported amine pool size,[49] leads to an overall small effect strength. Furthermore, the amine resonance at ~2 ppm is close to the water peak where spillover dilution effects occur. The choice of five pools is of course an oversimplification of the complex in vivo situation, which comprises many concomitant exchange effects (e.g., of –OH groups), which are not taken into account here. Nevertheless, similar five-pool Lorentzian models have been successfully applied as estimators of in vivo CEST effects before.[11,14] Similar to the observations made for the tumor patient dataset in this work, hyperintensities in tumor areas have been observed before for APT and amine contrasts obtained by Lorentzian fitting.[11,50]

Although in the present work the MIMOSA saturation scheme was employed for achieving more homogeneous saturation at 7 T, the proposed linear projection and LASSO method does not rely on this scheme and can be used for other CEST saturation schemes as well, as demonstrated for a 3T protocol without MIMOSA in Figure 3.

5.1 | Explainable AI

Recently, deep neural networks have been suggested for CEST data evaluation.[18–21] Like most deep learning methods, these are ascribed to be "black boxes" as their nested nonlinear structures do not allow interpretable insight into how inputs are mapped to targets. This makes careful assessment of such methods difficult. Addressing this issue, the recent trend of "explainable AI" aims at making machine learning systems more accessible for human interpretation.[51] In this sense, the presented linear projection approach could be considered as a simple step towards "explainable AI" applied to CEST MRI, as linear models are intrinsically interpretable,[51] which was demonstrated in Figure 4 and Figures S2-S7.

In general, the relationship between CEST contrast parameters and measured Z-spectra is nonlinear and can be described by solutions of the Bloch–McConnell differential equations or simplified Lorentzian models, as employed in this work. Given that, the proposed linear model can be interpreted as a first order approximation in the sense of a Taylor expansion of the generally unknown nonlinear function solving the inverse problem of inferring the parameters of interest from the measured data.

Resorting to a linear model instead of a nonlinear neural network thus enables interpretability (and much faster computation), however, at the expense of lower prediction performance, as shown in comparison with the deepCEST method[18] in Figure 9. This represents a general trade-off between model complexity and capacity on the one hand and simplicity and interpretability on the other.[51] Given the advantages of the linear approach in terms of speed and insight, first applying a linear model before advancing to more complex nonlinear models like neural networks might be a reasonable choice and is recommended for other learning-based CEST evaluations.

Linear models are more robust to errors in the input data than nonlinear models like neural networks.[52] Small fluctuations, which could be caused, for example, by motion in the case of CEST acquisitions, can in the worst case translate to arbitrarily high errors in the parameters predicted by a neural network. By contrast, the prediction error of a linear model in such cases is always bounded and can be estimated from the "slope" of the model (i.e., the regression coefficients). Furthermore, as there are no cross terms between different spectral input points (e.g., products like $Z(\Delta\omega_1)\cdot Z(\Delta\omega_2)$), a single corrupted frequency offset can only have limited impact on the result, which is not the case for highly entangled models like neural networks.

6 | CONCLUSION

Multiparametric CEST contrasts including field inhomogeneity correction can be well approximated by a simple linear projection of the acquired uncorrected Z-spectra onto regression coefficients fitted from conventionally evaluated data. The method translates from healthy to tumor patient datasets and is fast and interpretable, the latter being in contrast to neural networks employed for similar purposes.

Extending the approach by L1-regularization yields reduced frequency offset acquisition schedules offering a potential reduction of total scan time by factors of up to 2.8 with only moderate quality losses, compared with directly fitting subsampled Z-spectra. This could help make multiparametric CEST protocols more viable for clinical application.

DATA AVAILABILITY STATEMENT
Data and code for demonstration of the methods proposed in this study are openly available at https://github.com/fglang/linearCEST.

ORCID

Felix Glang https://orcid.org/0000-0003-3506-4947

Alexander German https://orcid.org/0000-0002-8708-6809

Angelika Mennecke https://orcid.org/0000-0001-6795-5627

Andrzej Liebert https://orcid.org/0000-0002-8450-3021

Kai Herz https://orcid.org/0000-0002-7286-1454

Patrick Liebig https://orcid.org/0000-0001-7342-3715

Enrique Zuazua https://orcid.org/0000-0002-1377-0958

Armin M. Nagel https://orcid.org/0000-0003-0948-1421

Klaus Scheffler https://orcid.org/0000-0001-6316-8773

Moritz Zaiss https://orcid.org/0000-0001-9780-3616

REFERENCES

1. Zhou J, Payen JF, Wilson DA, Traystman RJ, van Zijl PCM. Using the amide proton signals of intracellular proteins and peptides to detect pH effects in MRI. *Nat Med*. 2003;9(8):1085-1090. doi:10.1038/nm907

2. Ward KM, Balaban RS. Determination of pH using water protons and chemical exchange dependent saturation transfer (CEST). *Magn Reson Med*. 2000;44(5):799-802. doi:10.1002/1522-2594(200011)44:5%3C799::AID-MRM18%3E3.0.CO;2-S

3. Kogan F, Haris M, Singh A, et al. Method for high-resolution imaging of creatine in vivo using chemical exchange saturation transfer. *Magn Reson Med*. 2014;71(1):164-172. doi:10.1002/mrm.24641

4. Cai K, Haris M, Singh A, et al. Magnetic resonance imaging of glutamate. *Nat Med*. 2012;18(2):302-306. doi:10.1038/nm.2615

5. Zaiss M, Kunz P, Goerke S, Radbruch A, Bachert P. MR imaging of protein folding in vitro employing Nuclear-Overhauser-mediated saturation transfer. *NMR Biomed*. 2013;26(12):1815-1822. doi:10.1002/nbm.3021

6. Goerke S, Milde KS, Bukowiecki R, et al. Aggregation-induced changes in the chemical exchange saturation transfer (CEST) signals of proteins. *NMR Biomed*. 2017;30(1):e3665. doi:10.1002/nbm.3665

7. Cai K, Singh A, Poptani H, et al. CEST signal at 2 ppm (CEST@2ppm) from Z-spectral fitting correlates with creatine distribution in brain tumor. *NMR Biomed*. 2015;28(1):1-8. doi:10.1002/nbm.3216

8. Paech D, Burth S, Windschuh J, et al. Nuclear Overhauser enhancement imaging of glioblastoma at 7 Tesla: region specific correlation with apparent diffusion coefficient and histology. *PLoS ONE*. 2015;10(3):e0121220. doi:10.1371/journal.pone.0121220

9. Meissner JE, Korzowski A, Regnery S, et al. Early response assessment of glioma patients to definitive chemoradiotherapy using chemical exchange saturation transfer imaging at 7 T: response assessment to CRT with CEST. *J Magn Reson Imaging*. 2019;12:1268-1277. doi:10.1002/jmri.26702

10. Liu D, Zhou J, Xue R, Zuo Z, An J, Wang DJJ. Quantitative characterization of nuclear overhauser enhancement and amide proton transfer effects in the human brain at 7 Tesla. *Magn Reson Med*. 2013;70(4):1070-1081. doi:10.1002/mrm.24560

11. Zaiss M, Windschuh J, Paech D, et al. Relaxation-compensated CEST-MRI of the human brain at 7T: Unbiased insight into NOE and amide signal changes in human glioblastoma. *Neuroimage*. 2015;112:180-188. doi:10.1016/j.neuroimage.2015.02.040

12. Goerke S, Soehngen Y, Deshmane A, et al. Relaxation-compensated APT and rNOE CEST-MRI of human brain tumors at 3 T. *Magn Reson Med*. 2019; 29:622-632. doi:10.1002/mrm.27751

13. Deshmane A, Zaiss M, Lindig T, et al. 3D gradient echo snapshot CEST MRI with low power saturation for human studies at 3T. *Magn Reson Med*. 2019;81(4):2412-2423. doi:10.1002/mrm.27569

14. Windschuh J, Zaiss M, Meissner J-E, et al. Correction of B1-inhomogeneities for relaxation-compensated CEST imaging at 7 T. *NMR Biomed*. 2015; 28(5):529-537. doi:10.1002/nbm.3283

15. Guivel-Scharen V, Sinnwell T, Wolff SD, Balaban RS. Detection of proton chemical exchange between metabolites and water in biological tissues. *J Magn Reson*. 1998;133(1):36-45. doi:10.1006/jmre.1998.1440

16. Xu J, Zaiss M, Zu Z, et al. On the origins of chemical exchange saturation transfer (CEST) contrast in tumors at 9.4 T. *NMR Biomed*. 2014;27(4): 406-416. doi:10.1002/nbm.3075

17. Jin T, Wang P, Zong X, Kim SG. MR imaging of the amide-proton transfer effect and the pH-insensitive nuclear overhauser effect at 9.4 T. *Magn Reson Med*. 2013;69(3):760-770. doi:10.1002/mrm.24315

18. Glang F, Deshmane A, Prokudin S, et al. DeepCEST 3T: Robust MRI parameter determination and uncertainty quantification with neural networks—application to CEST imaging of the human brain at 3T. *Magn Reson Med*. 2020;84(1):450-466. doi:10.1002/mrm.28117

19. Zaiss M, Deshmane A, Schuppert M, et al. DeepCEST: 9.4 T Chemical exchange saturation transfer MRI contrast predicted from 3 T data – a proof of concept study. *Magn Reson Med*. 2019;81(6):3901-3914. doi:10.1002/mrm.27690

20. Chen L, Schär M, Chan KWY, et al. In vivo imaging of phosphocreatine with artificial neural networks. *Nat Commun*. 2020;11(1):1-10. doi:10.1038/s41467-020-14874-0

21. Li Y, Xie D, Cember A, et al. Accelerating GluCEST imaging using deep learning for B0 correction. *Magn Reson Med*. 2020;84(4):1724-1733. doi:10.1002/mrm.28289

22. Breitling J, Deshmane A, Goerke S, et al. Adaptive denoising for chemical exchange saturation transfer MR imaging. *NMR Biomed*. 2019;(11):e4133. doi:10.1002/nbm.4133

23. Tibshirani R. Regression shrinkage and selection via the lasso. *J R Stat Soc B Methodol*. 1996;58(1):267-288. doi:10.1111/j.2517-6161.1996.tb02080.x

24. Lustig M, Donoho D, Pauly JM. Sparse MRI: The application of compressed sensing for rapid MR imaging. *Magn Reson Med*. 2007;58(6):1182-1195. doi:10.1002/mrm.21391

25. Rencher AC, Schaalje GB. *Linear Models in Statistics*. 2nd ed. Wiley Interscience; 2008.

26. Beck A, Teboulle M. A Fast Iterative Shrinkage-Thresholding Algorithm for Linear Inverse Problems. *SIAM J Imaging Sci*. 2009;2(1):183-202. doi:10.1137/080716542

27. Yuan M, Lin Y. Model selection and estimation in regression with grouped variables. *J R Stat Soc Series B Stat Methodology*. 2006;68(1):49-67. doi: 10.1111/j.1467-9868.2005.00532.x

28. Obozinski G, Wainwright MJ, Jordan MI. Support union recovery in high-dimensional multivariate regression. *Ann Statist*. 2011;39(1):1-47. doi: 10.1214/09-AOS776

29. Hastie T, Tibshirani R, Friedman J. *The Elements of Statistical Learning: Data Mining, Inference, and Prediction*. second Ed. Springer Science & Business Media; 2009.

30. Liebert A, Tkotz K, Herrler J, et al. Whole-brain quantitative CEST MRI at 7T using parallel transmission methods and correction. *Magn Reson Med*. 2021;86(1):346–362. doi:10.1002/mrm.28745

31. Liebert A, Zaiss M, Gumbrecht R, et al. Multiple interleaved mode saturation (MIMOSA) for B1+ inhomogeneity mitigation in chemical exchange saturation transfer. *Magn Reson Med*. 2019;82(2):693-705. doi:10.1002/mrm.27762

32. Zaiss M, Ehses P, Scheffler K. Snapshot-CEST: Optimizing spiral-centric-reordered gradient echo acquisition for fast and robust 3D CEST MRI at 9.4 T. *NMR Biomed*. 2018;31(4):e3879. doi:10.1002/nbm.3879

33. Griswold MA, Jakob PM, Heidemann RM, et al. Generalized autocalibrating partially parallel acquisitions (GRAPPA). *Magn Reson Med*. 2002;47(6): 1202-1210. doi:10.1002/mrm.10171

34. Ashburner J, Friston KJ. Unified segmentation. *Neuroimage*. 2005;26(3):839-851. doi:10.1016/j.neuroimage.2005.02.018

35. Mennecke A, Khakzar K, German A, et al. 7 tricks for 7 T CEST: improving reproducibility of multi-pool evaluation provides insights into effects of age and early stage Parkinson's disease. Accepted at NMR Biomed; 2022.

36. tiepvupsu. tiepvupsu/FISTA. https://github.com/tiepvupsu/FISTA. Accessed May 28, 2021.

37. Paech D, Dreher C, Regnery S, et al. Relaxation-compensated amide proton transfer (APT) MRI signal intensity is associated with survival and progression in high-grade glioma patients. *Eur Radiol*. 2019;29(9):4957-4967. doi:10.1007/s00330-019-06066-2

38. Chen L, Cao S, Koehler RC, van Zijl PCM, Xu J. High-sensitivity CEST mapping using a spatiotemporal correlation-enhanced method. *Magn Reson Med*. 2020;84(6):3342-3350. doi:10.1002/mrm.28380

39. Schuppert M, Deshmane A, Herz K, Scheffler K, Zaiss M. Data-Driven Spectral Feature Extraction in 9.4T CEST MRI data of the human brain. Program Number 4995. In: *Proceedings of ISMRM 27th Annual Meeting*; 2019.

40. Goerke S, Breitling J, Korzowski A, et al. Clinical routine acquisition protocol for 3D relaxation-compensated APT and rNOE CEST-MRI of the human brain at 3T. *Magn Reson Med*. 2021;86(1):393-404. doi:10.1002/mrm.28699

41. Akbey S, Ehses P, Stirnberg R, Zaiss M, Stöcker T. Whole-brain snapshot CEST imaging at 7 T using 3D-EPI. *Magn Reson Med*. 2019;(5):1741-1752. doi:10.1002/mrm.27866

42. Tee YK, Khrapitchev AA, Sibson NR, Payne SJ, Chappell MA. Optimal sampling schedule for chemical exchange saturation transfer. *Magn Reson Med*. 2013;70(5):1251-1262. doi:10.1002/mrm.24567

43. Heo HY, Zhang Y, Jiang S, Lee DH, Zhou J. Quantitative assessment of amide proton transfer (APT) and nuclear overhauser enhancement (NOE) imaging with extrapolated semisolid magnetization transfer reference (EMR) signals: II. Comparison of three EMR models and application to human brain glioma at 3 Tesla. *Magn Reson Med*. 2016;75(4):1630-1639. doi:10.1002/mrm.25795

44. Cohen O, Huang S, McMahon MT, Rosen MS, Farrar CT. Rapid and quantitative chemical exchange saturation transfer (CEST) imaging with magnetic resonance fingerprinting (MRF). *Magn Reson Med*. 2018;80(6):2449-2463. doi:10.1002/mrm.27221

45. Perlman O, Ito H, Herz K, et al. Quantitative imaging of apoptosis following oncolytic virotherapy by magnetic resonance fingerprinting aided by deep learning. *Nat Biomed Eng*. 2021. doi:10.1038/s41551-021-00809-7

46. Yadav NN, Chan KWY, Jones CK, McMahon MT, van Zijl PCM. Time domain Removal of Irrelevant Magnetization (TRIM) in CEST Z-spectra. *Magn Reson Med*. 2013;70(2):547-555. doi:10.1002/mrm.24812

47. Liepinsh E, Otting G. Proton exchange rates from amino acid side chains— implications for image contrast. *Magn Reson Med*. 1996;35(1):30-42. doi: 10.1002/mrm.1910350106

48. Sun PZ, van Zijl PCM, Zhou J. Optimization of the irradiation power in chemical exchange dependent saturation transfer experiments. *J Magn Reson*. 2005;175(2):193-200. doi:10.1016/j.jmr.2005.04.005

49. van Zijl PCM, Lam WW, Xu J, Knutsson L, Stanisz GJ. Magnetization transfer contrast and chemical exchange saturation transfer MRI. Features and analysis of the field-dependent saturation spectrum. *Neuroimage*. 2018;168:222-241. doi:10.1016/j.neuroimage.2017.04.045

50. Zaiss M, Schuppert M, Deshmane A, et al. Chemical exchange saturation transfer MRI contrast in the human brain at 9.4 T. *Neuroimage*. 2018;179: 144-155. doi:10.1016/j.neuroimage.2018.06.026

51. Samek W, Müller KR. Towards Explainable Artificial Intelligence. In: Samek W, Montavon G, Vedaldi A, Hansen LK, Müller KR, eds. *Explainable AI: Interpreting, Explaining and Visualizing Deep Learning*. Lecture Notes in Computer Science. Springer International Publishing; 2019:5-22. doi:10. 1007/978-3-030-28954-6_1

52. Maier AK, Syben C, Stimpel B, et al. Learning with known operators reduces maximum error bounds. *Nat Mach Intell*. 2019;1(8):373-380. doi: 10.1038/s42256-019-0077-5

SUPPORTING INFORMATION

Additional supporting information may be found in the online version of the article at the publisher's website.

APPENDIX A.

Frequency offset list of the CEST acquisitions

$\Delta\omega\,(\text{ppm}) =$ −300.0, −100.0, −50.0, −20.0, −12.0, −9.0, −7.2, −6.2, −5.5, −4.7, −4.0, −3.3, −2.7, −2.0, −1.7, −1.5, −1.1, −0.9, −0.6, −0.4, 0.0, 0.4, 0.6, 0.9, 1.1, 1.2, 1.4, 1.5, 1.7, 1.8, 2.0, 2.1, 2.3, 2.4, 2.6, 2.7, 2.9, 3.0, 3.2, 3.3, 3.5, 3.6, 3.8, 3.9, 4.1, 4.2, 4.4, 4.7, 5.2, 6.2, 8.0, 12.0, 20.0, 50.0, 100.0, −300.0.

B.4. Publication 4

Glang, F.; Mueller, S.; Herz, K.; Loktyushin, A.; Scheffler, K.; Zaiss, M.

MR-Double-Zero – Proof-of-Concept for a Framework to Autonomously Discover MRI Contrasts.

MR-double-zero – Proof-of-concept for a framework to autonomously discover MRI contrasts

Felix Glang [a,1], Sebastian Mueller [a,b,1], Kai Herz [a,b], Alexander Loktyushin [a], Klaus Scheffler [a,b], Moritz Zaiss [a,c,*]

[a] *High-field Magnetic Resonance Center, Max Planck Institute for Biological Cybernetics, Tuebingen, Germany*
[b] *Department of Biomedical Magnetic Resonance, Eberhard Karls University Tuebingen, Tuebingen, Germany*
[c] *Institute of Neuroradiology, University Hospital Erlangen, Friedrich-Alexander University Erlangen-Nürnberg (FAU), Erlangen, Germany*

ARTICLE INFO

ABSTRACT

Purpose: A framework for supervised design of MR sequences for any given target contrast is proposed, based on fully automatic acquisition and reconstruction of MR data on a real MR scanner. The proposed method does not require any modeling of MR physics and thus allows even unknown contrast mechanisms to be addressed.
Methods: A derivative-free optimization algorithm is set up to repeatedly update and execute a parametrized sequence on the MR scanner to acquire data. In each iteration, the acquired data are mapped to a given target contrast by linear regression.
Results: It is shown that with the proposed framework it is possible to find an MR sequence that yields a predefined target contrast. In the present case, as a proof-of principle, a sequence mapping absolute creatine concentration, which cannot be extracted from T1 or T2-weighted scans directly, is discovered. The sequence was designed in a comparatively short time and with no human interaction.
Conclusions: New MR contrasts for mapping a given target can be discovered by derivative-free optimization of parametrized sequences that are directly executed on a real MRI scanner. This is demonstrated by 're-discovery' of a chemical exchange weighted sequence. The proposed method is considered to be a paradigm shift towards autonomous, model-free and target-driven sequence design.
© 2022 The Authors. Published by Elsevier Inc. This is an open access article under the CC BY-NC-ND license (http://creativecommons.org/licenses/by-nc-nd/4.0/).

1. Introduction

The discovery of new MRI contrasts often happened hitherto by 'trial-and-error' using educated guesses directly at the MR system. We consider here whether such a trial-and-error approach can be formulated as a machine learning or optimization approach, that still makes use of the MRI system directly. Traditionally, the design of an MR sequence yielding a certain target contrast is performed manually, often by considering an analytical description of the contrast mechanism (subsequently referred to as a 'model') and adapting parameters such as the echo time (TE) or flip angle (FA) at the scanner. This approach is inherently limited by having to describe and understand the contrast mechanism before designing

a sequence for it. In addition, this workflow requires time-consuming human interaction with the scanner.

Within this traditional approach, often a single potentially specific target, e.g. quantitative relaxation, diffusion or magnetization transfer parameters is aimed for during sequence optimization. When considering one of these targets in isolation, there are often very precise models available to describe the underlying physics, such as the Bloch, Bloch-Torrey or Bloch-McConnell equations. However, in most cases, some assumptions do have to be made to apply these models, such as ignoring concomitant effects. A more general description requires the combination of different models, which may result in models that are too large and complicated to solve, and that anyway involve making many assumptions. Furthermore, the choice of model explicitly defines the targets which one may optimize, as the only possible targets are the ones described by the model itself. This ultimately means that the entire MR experiment, including the object of interest, the MR scanner hardware and the data reconstruction need to be included into a comprehensive, universal model that, to be practical, should be evaluated within as little time as possible.

We recently proposed a self-learning framework to discover MRI sequences based on a differentiable MRI physics simulation, which was dubbed *MRzero*, because zero sequence programming experience, but only knowledge of the Bloch equations was required [1]. Progressing further, the approach presented here requires neither a model nor human interaction with the scanner; thus, we call this approach *MR-double-zero*.

Instead of starting from a theoretical model and optimizing for a certain contrast, here, the model-free learning process is based solely on the desired target contrast, and performs automated, explorative real-scanner acquisitions. This allows optimization for any given target, even if the physical contrast mechanism in the MR signal might yet be unknown. With such a target-driven approach, a pure 'optimization' can be extended to become a 'discovery', as it may now be possible to test hypotheses as to whether (and how) a certain target might become visible by exploiting MRI as a tool. The proposed method can therefore be considered as a paradigm shift towards automatic target-driven sequence design. The ability to initially find an MR sequence solely guided by a desired target is the novelty of the presented work. In a first step, it is necessary to consider a mechanism which is known to result in an alteration of the MR signal and therefore may in principle be used to generate MR contrast. To mimic the discovery of a novel MRI effect, we assume that we know about water relaxation and have relaxation-weighted sequences. We then pretend that another specific contrast mechanism, namely the chemical exchange saturation transfer effect (CEST) of creatine guanidine protons, is unknown and needs to be discovered with MR-double-zero autonomously. In contrast to classical sequence design, no signal equation or analytical model are included. Instead, only the final target, which is not even an MR signal anymore, but rather absolute creatine concentration, is provided. The necessary human interaction is reduced to creating the samples and providing a suitable target, which in the present case is a manually generated map of the known creatine concentrations. To the best of our knowledge, this is the first realization of a MR sequence optimization framework with direct and automatized data acquisition and feedback on a real MR scanner in a target-contrast-driven manner; for pulse profile optimization a similar setup was proposed by Scheffler [2].

2. Methods

2.1. Samples

Samples were prepared with varying concentration of creatine. Seven samples with different creatine concentration values (0, 15, 25, 50, 75, 100, 125 mMol/L) were created from creatine monohydrate (Fisher Scientific GmbH, Schwerte, Germany). By adding T1 contrast agent (dotarem® 500 mMol/L, Guerbet, Germany) and agarose (Carl Roth, Karlsruhe, Germany) [3] it was made sure that in quantitative T1 and T2 maps obtained from conventional sequences these samples were indiscernible as shown in Fig. 3A-D.

To add another test case, the sample at 100 mMol/L concentration was designed in a way that it actually had a significantly longer T1 value then the other samples. This was achieved by not adding any contrast agent at all to this sample. Still, agar was added such that its T2 value approximately matches that of the other samples. Quantitative T1 and T2 values can be found in Fig. 3. Full Z-spectra acquired with low power preparation [4] are shown in Supplementary Fig. 1 for the seven different samples. For comparison of classical Z-spectra and Z-values explored with the proposed framework, an overlay plot of those can be found in Supplementary Fig. 5/6.

2.2. Scanner interface

To enable real measurements for the optimization process, the MR scanner was remotely controlled by the optimizer. Pulseq [5] files were used to automatically execute the sequence of each iteration at the scanner. The actual optimization was run on a local computer (Intel Xeon W-2145 3.7 GHz CPU, 8 cores and 128 GB RAM) but not on the scanner host computer. This reduces the interaction with the scanner software to reading Pulseq files from a network drive. The Pulseq files additionally facilitate numerical simulations of the optimized sequence parameters [6]. Measurements were performed on a 3 T PRISMA scanner (Siemens Healthineers, Erlangen, Germany) using the vendor's 20Ch head coil for receive and the body coil for transmit.

2.3. Optimization process

The actual optimization is based on an RF-prepared sequence with fixed 2D gradient and RF spoiled GRE readout (TE = 3.3 ms, TR = 6.6 ms, FA = 8°, BW = 300 Hz/pixel, RO $\times$ PE = 96 $\times$ 96, FoV = 128 $\times$ 128 mm^2, slice thickness: 10 mm). The CMA-ES optimization algorithm [7] implemented in nevergrad [8] was employed to explore the sequence parameter space including possible RF-preparation events such as number of pulses, amplitude, duration, phase/frequency, and delay times. This type of stochastic optimization algorithm is particularly designed for derivative-free, non-convex, noisy optimization problems as posed by sequence optimization at a real scanner. Every sequence generated by the optimizer is executed directly at the scanner and the intermediate images flow back to the algorithm influencing the next sequence iteration.

For the present work, each sequence iteration consisted of several (indexed by $r = 1, 2, ..., R$) RF-prepared readouts with the pulse train parameters peak saturation amplitude $B_{1,r}$, frequency offset $\Delta\omega_r$ and number of pulses np_r as optimized sequence parameters (seq) with seq = $(B_{1,1}, \Delta\omega_1, np_1 | B_{1,2}, \Delta\omega_2, np_2 | ... | B_{1,R}, \Delta\omega_R, np_R)$.

Initial and boundary conditions for the optimization algorithm used with this parametrization are given in Table 1.

The duration of each Gaussian-shaped pulse was fixed to $t_p = 20$ ms and the duty cycle to DC $= t_p/(t_p + t_d) = 50\%$, i.e. a $t_d = 20$ ms gap between pulses. Still, with the number of pulses as free parameter, a large range of different total saturation times can be achieved. This choice of parametrization ensured that the explored sequences stay within the specific absorption rate limits throughout the optimization. The reconstructed images $\text{Img}_r(B_{1,r}, \Delta\omega_r, np_r)$ at each iteration were assembled in a design matrix.

$$\text{MRI(seq)} = \begin{pmatrix} \vdots & \vdots & \vdots & \vdots & \vdots \\ \text{Img}_1 & \text{Img}_2 & \cdots & \text{Img}_R & 1 \\ \vdots & \vdots & \vdots & \vdots & \vdots \end{pmatrix}$$

of shape #voxels-by-(R + 1). Only voxels within ROIs of the sample vials were considered, to avoid bias by the larger number of surrounding water-only voxels. Still, voxels within an ROI of the same size in the surrounding water were included as well.

Linear regression onto the voxel-wise targets T (shape: #voxels–by-1), was performed by pseudo-inversion of the relation $T = \text{MRI(seq)} \cdot \beta \Rightarrow \hat{\beta}(\text{seq}) = \text{MRI(seq)}^+ \cdot T$ (with the Moore-Penrose pseudo-inverse $X^+ = (X^T X)^{-1} X^T$). This mapping process is referred to as 'inner' optimization in the following. The difference between the linear prediction and the true target determined how the CMA-ES optimization algorithm updated the sequence

Table 1

Initial and boundary conditions for the creatine mapping experiments, corresponding to seq = $(B_{1,1}, \Delta\omega_1, np_1 | B_{1,2}, \Delta\omega_2, np_2)$ in the case of R = 2 images per iteration and seq = $(B_{1,1}, \Delta\omega_1, np_1 | B_{1,2}, \Delta\omega_2, np_2 | B_{1,3}, \Delta\omega_3, np_3)$ in case of R = 3 images per iteration.

	lower bound	initial value	upper bound
$B_{1,1}$	0.1 µT	1 µT	3 µT
$B_{1,2}$	0.1 µT	1 µT	3 µT
$B_{1,3}$	0.1 µT	1 µT	3 µT
$\Delta\omega_1$	−4.5 ppm	+1 ppm	+4.5 ppm
$\Delta\omega_2$	−4.5 ppm	−1 ppm	+4.5 ppm
$\Delta\omega_3$	−4.5 ppm	0 ppm	+4.5 ppm
np_1	1	80	200
np_2	1	80	200
np_3	1	80	200

parameters by solving the following non-linear minimization problem:

$$\widehat{seq} = \text{argmin}_{seq}\left(\left\|T - \text{MRI}(seq) \cdot \hat{\beta}(seq)\right\|_2^2\right)$$

$$= \text{argmin}_{seq}\left(\left\|\left(\mathbb{1} - \text{MRI}(seq) \cdot \text{MRI}(seq)^+\right) \cdot T\right\|_2^2\right)$$

With this problem formulation, the optimizer has to find sequence parameters that yield images that allow the best possible linear mapping to the target (Fig. 1). The optimization of sequence parameters is referred to as 'outer' optimization in the following.

To enable a more flexible mapping function from acquired images to targets, the design matrix MRI(seq) can be extended by non-linear transforms of the acquired images as additional features, i.e. columns. For example, by adding the squares and cubes of the acquired pixel intensities, respectively, a third-order polynomial representation is formed:

Note that, while being non-linear in the image intensities, such a representation is still linear in the regression coefficients β, which allows obtaining them by simple pseudo-inversion.

As exemplary targets, known creatine concentrations were chosen with samples prepared as described in the above section.

3. Results

As a first feasibility check, simple experiments to investigate the behavior of the MSE loss function evaluated directly at the scanner were performed. To that end, a single target image with fixed saturation parameters seq = (1 µT, +1.9 ppm, 80) was acquired. Subsequently, three series of presaturated images were acquired, for which two of the parameters were fixed to their original values, respectively, while the remaining parameter was linearly incremented. This approach explores the loss landscape along each of these three axes (B_1, $\Delta\omega$, np) individually. For each of the acquired images, MSE to the target was calculated to see if this loss function actually exhibits a minimum at the respective target parameter value. Fig. 2 shows the resulting 1D loss curves. For the saturation amplitude B_1, there is a clear global minimum at the target value and the loss curve appears smooth and largely convex. In case of the frequency offset $\Delta\omega$, there are several local minima and a more complex oscillatory behavior of the loss curve. Still, the global minimum in the explored range is located at the target value of $\Delta\omega = +1.9$ ppm. For the number of pulses np, the global minimum is at a higher number ($np \sim 100$) than the actual target value ($np = 80$), and the loss curve exhibits small periodic oscillations.

From these experiments it can be concluded that the MSE loss landscapes acquired at the real scanner with respect to a given

$$\text{MRI(seq)} = \begin{pmatrix} \vdots & \vdots & \vdots & \vdots & \vdots & \vdots & \vdots & \vdots & \vdots & \vdots & \vdots & \vdots \\ \text{Img}_1 & \text{Img}_2 & \cdots & \text{Img}_R & \text{Img}_1^2 & \text{Img}_2^2 & \cdots & \text{Img}_R^2 & \text{Img}_1^3 & \text{Img}_2^3 & \cdots & \text{Img}_R^3 & 1 \\ \vdots & \vdots & \vdots & \vdots & \vdots & \vdots & \vdots & \vdots & \vdots & \vdots & \vdots & \vdots \end{pmatrix}$$
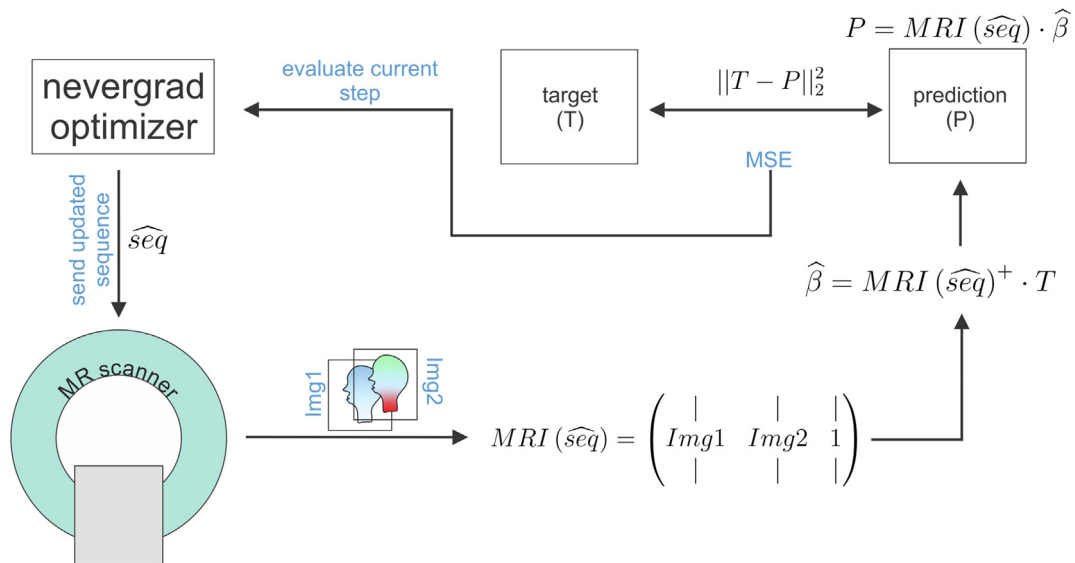
Fig. 1. Diagram of the proposed sequence development workflow termed MR-double-zero. The optimizer sends the parametrized sequence (seq) to a real MR scanner. The acquired data (in the depicted case for R = 2 images: Img$_1$ and Img$_2$) get flattened into the matrix MRI(seq) which is used to determine coefficients β from linear regression of MRI(seq) to the target. With these coefficients, the prediction (P) is determined and the deviation from the target (T) flows back to the optimizer. Our pipeline implements this using so called .seq-files of the Pulseq standard that are played out at the scanner by a Pulseq interpreter sequence.

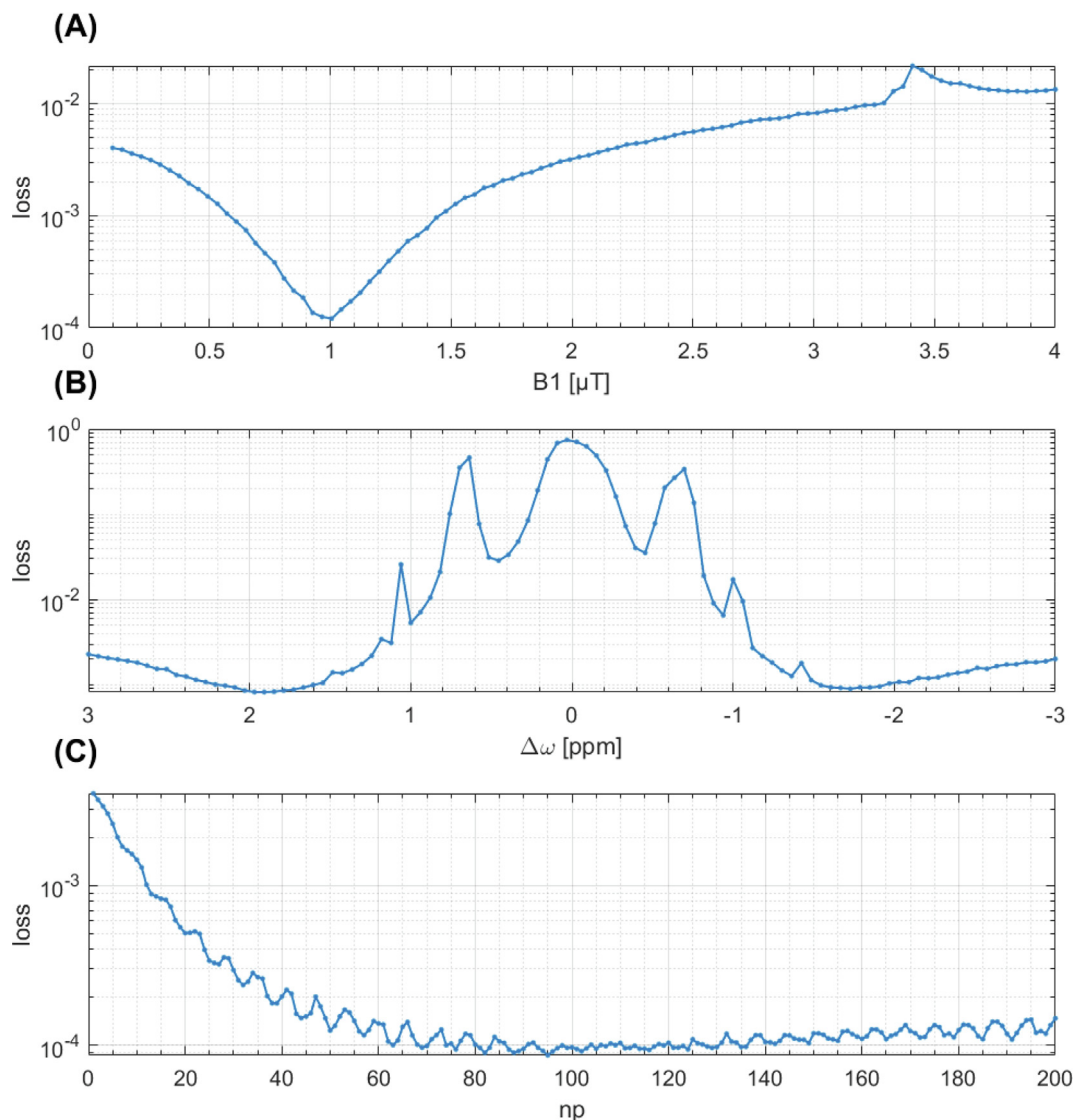**Fig. 2.** Preliminary sanity checks of the MSE loss function evaluated directly at the scanner. As a target, a CEST-weighted image with predefined parameters seq = (1 µT, +1.9 ppm, 80) was acquired. Subsequently, a set of weighted images was acquired with two of these three parameters fixed to their target values, respectively, and the remaining parameter incremented with constant step size across a predefined range. For each of these images, MSE to the original target is shown (only evaluated within the sample vials, not in the surrounding water).

target contrast may exhibit multiple local minima, but still show somewhat smooth behavior and global minima that closely reflect the ground truth parameters. This means that these target parameter values can also be found by an optimization algorithm, however, a gradient descent might get stuck in the observed local minima.

To make sure that the MR-double-zero agent has to find a new sequence concept, and that the creatine concentration cannot be inferred only from T1- or T2-weighed contrasts, the samples were built such that T1 and T2 is not governed by creatine proton exchange. This invariance can already be seen in the T1 and T2 maps in Fig. 3, and was verified by the unsuccessful linear estimation using only T1 and T2 as input (Fig. 3F). Interestingly, it was not even possible to map the vial that had longer T1 values (see Fig. 3A/C) to its target concentration.

An exemplary optimization process is depicted in Fig. 4. Due to the stochastic behavior of the optimizer, the iterations were retrospectively sorted by loss instead of acquisition number. It can be seen that with decreasing loss at some point the optimized param-

eters converge towards a specific value. Still, for different runs, different sets of parameters are found (Supplementary Figure 7), which reflects that there are different strategies to generate the same contrast. In this specific case, the optimized sequence consists of two images at + 2.09 ppm and −2.11 ppm with similar saturation strength (i.e., B_1 and np), which approximately get subtracted by the linear regression. This closely resembles the asymmetry metric, which is a classical model-based description of CEST effects [9]. If not stated differently, for all data shown in the following, the iteration that yielded smallest loss was chosen.

Fig. 4B shows the creatine concentration map generated based on the newly discovered sequence, which was formed by linear regression from the two RF-prepared images (Fig. 4D/E) with optimized sequence parameters. Remarkably, the method generalizes to the vial with 50 mMol/L, which was excluded from the 'training' procedure, i.e. not considered in the loss function during optimization (Fig. 4F).

Fig. 5 shows the optimization result for the concentration mapping experiment in which the design matrix was augmented by
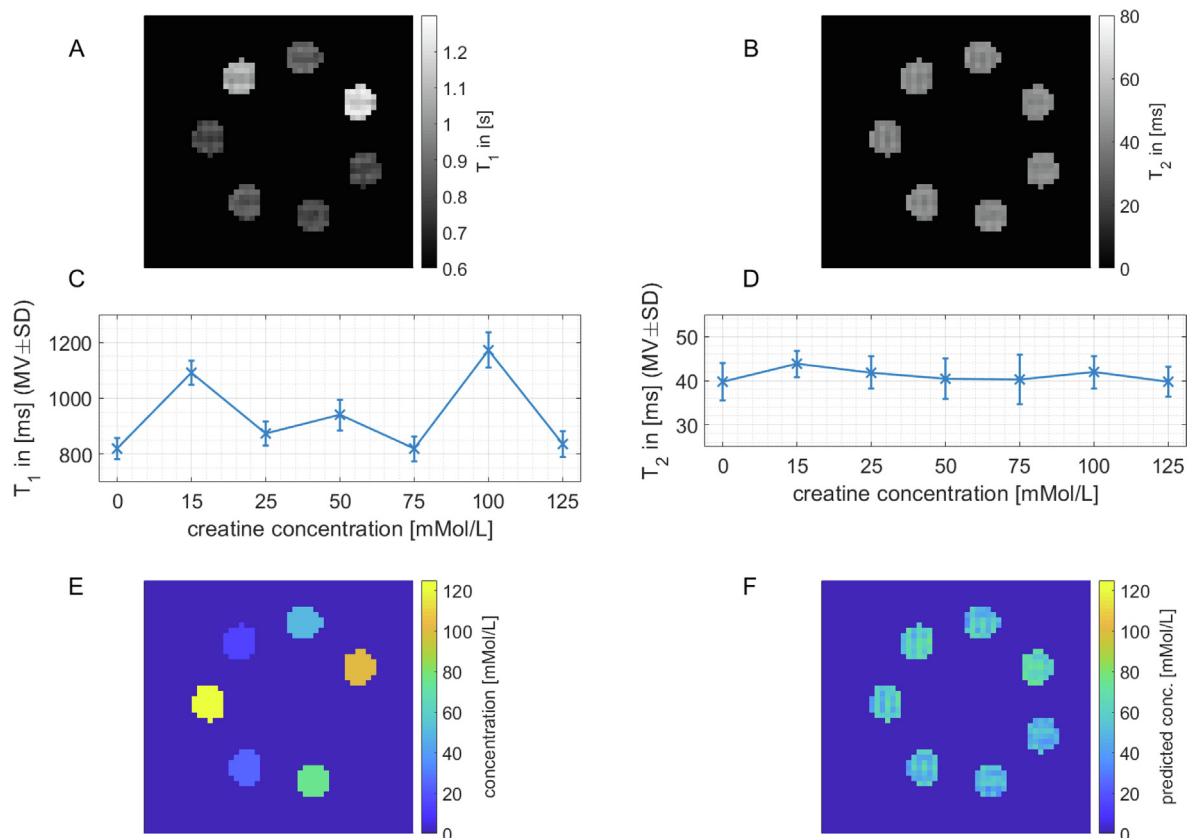
Fig. 3. Quantitative T1 and T2 maps of samples with different creatine concentration (c_{Cr}). Upper row: different concentrations cannot be distinguished directly from T1 (A) and/or T2 (B) maps. Center row: evaluation of (C) T1 and (D) T2 values in different ROIs of data shown in (A)/(B) with mean (MV) and standard deviation (SD) for each vial. Bottom row: True creatine concentrations (E) cannot be predicted by linear regression $f([T1, T2, 1]) = c_{Cr}$ from T1 and T2 (F).

square and cube terms. It can be seen that the more flexible polynomial mapping results in a more accurate mapping ($\sim$50% smaller MSE loss, see Supplementary Fig. 4) to the target concentrations, which is especially pronounced for the ROIs with no creatine (both within the sample and in the surrounding water) and the two vials with highest concentrations (for which one even had different T1). The sequence parameters found by the optimization in this case were substantially different from the ones found in the experiment with simple non-augmented design matrix (Fig. 5 vs. Fig. 4). On the one hand, the non-linear mapping function allows for different contrast extraction schemes compared to the case of a simple linear mapping, which may lead to different sequence schemes generating the input for this specific extraction. On the other hand, the stochastic optimization process itself will yield different seq-vectors for different runs in a loss-landscape with potentially multiple, equivalent local minima. This is demonstrated in Supplementary Figure 7, from which it can be seen that the observed fluctuations in the final parameters could be attributed to the stochastic nature of the chosen optimizer rather than to the influence of non-linear extensions to the design matrix.

The accuracy of predicted concentrations can be further increased by extending the sequence to three differently prepared images (Supplementary Figs. 2, 3, 4), however, at the expense of increased acquisition and thus optimization duration. Also, it was found that extending the design matrix to a third image performs similarly well as extending the design matrix by higher order terms of only two images actually acquired at the scanner. However, extending the design matrix by higher order terms only requires very little additional computation time compared to the additional scan time required for a larger number of images. A

comparison of loss curves for all shown experiments (2 scans vs. 3 scans and linear vs. polynomial regression) is given in Supplementary Fig. 4.

3.1. Samples including creatine plus glucose as confounding factor

The above experiments were conducted in samples that contained only creatine as a unique compound of interest. However, in a typical in vivo situation, multiple metabolites are present, which raises the question if this might skew the optimization process. To investigate this further, an additional set of samples was created similar to the first set that only contained creatine, but adding variable concentrations of glucose as a potential confounding factor. Indeed, when applying optimized GlucoCEST RF preparation [10], some of the creatine concentrations can no longer be distinguished by the conventional MTR$_{asym}$ approach (Supplementary Figure 8).

As demonstrated in Fig. 6, also for these samples, the proposed optimization pipeline comes up with a solution that accurately maps to creatine concentration with no apparent interference from the different glucose concentration levels. Runs with R = 3 images per iteration as well as non-linearly extended design matrix are shown in Supplementary Figures 10–12. As can be seen in Supplementary Figure 9, also for these samples, non-linear extension of the design matrix leads to lower loss values even with R = 2 images compared to only linear design matrix with R = 3 images. The concept found by MR-double-zero is qualitatively different from conventional MTR$_{asym}$, and the chosen different B$_1$ levels and offsets seem to enable the robustness against glucose contamination.
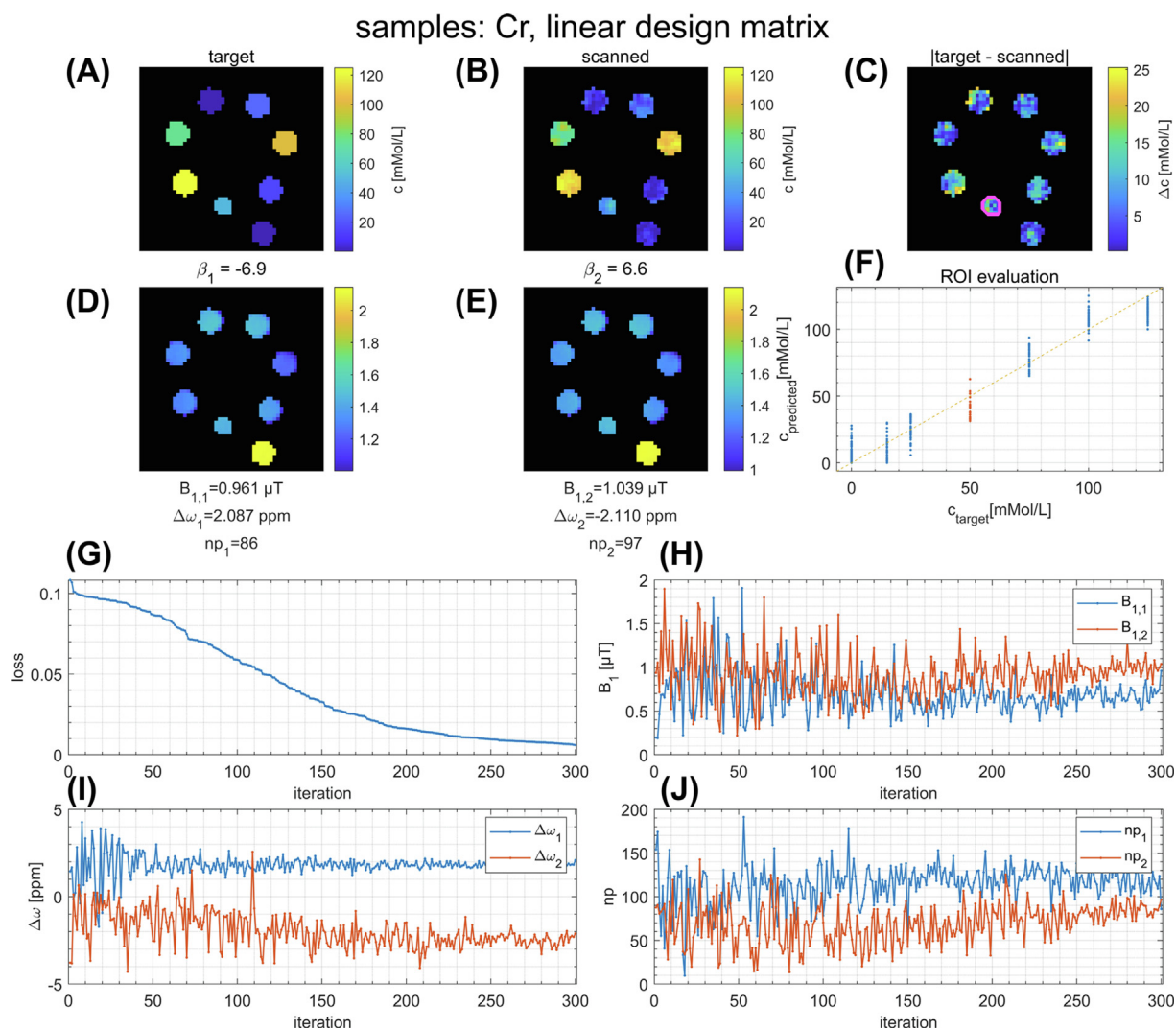
Fig. 4. Exemplary optimization process of a MR-double-zero sequence with 300 iterations (MRI scan time: 3 h). The final parameter set was here seq = $(0.96 \,\mu T, +2.09 \,ppm, 86 | 1.04 \,\mu T, -2.11 \,ppm, 97)$. The design matrix contained two images acquired with different RF-preparations. The first row shows quantitative concentration maps: (A) the target, (B) the experimentally derived and (C) the difference in concentrations. Second row shows the two images (D,E) with respective sequence parameters given below. In (F) the predicted and target data are scattered for ROIs within the different vials. The test vial (50 mMol/L) that was not included in the optimization process, is highlighted in (C) and (F). Subplots (G-J) were retrospectively sorted by loss instead of the actual time course of acquisition. (G) shows the loss for the sequence parameters shown in (H)-(J) . Subscripts 1 and 2 refer to the image number for all parameters. An animated version of this figure can be found as Supplementary Material.

4. Discussion

4.1. General comments on the proposed method

In the present work, we have shown a proof-of-principle for MRI sequence parameter optimization with the goal to discover a target contrast solely based on acquisitions at a real scanner system, without any knowledge of a theoretical signal model. In general, such an optimization problem is difficult, i.e. noisy, non-convex, high-dimensional and potentially ill-conditioned. However, the very first feasibility checks of the MSE loss function for a single parameter sweep showed that running an optimization based on real data could in principle converge towards global minima (Fig. 2). Additionally, stochastic gradient-free evolutionary algorithms like the employed CMA-ES are known to be particularly suited for this class of optimization problems [8].

MR-double-zero can be seen as advanced, sophisticated and efficient search in the MR parameter space to figure out if a certain

contrast can be generated by MRI. A grid search with S = 100 entries in each of the N = 3 dimensions would lead to $S^N = 10^5$ necessary measurements, and the problem of defining suitable grid boundaries. In contrast, the autonomous MR-double-zero learning required only 300 iterations, which took around 3 h at the MRI scanner. This is still long for an MRI scan, but fast for the discovery of a novel MRI contrast.

In general, the search space grows with the power of the number of dimensions, thus, reduction of dimensions N is an important step. The present optimization problem was reduced to the optimization of as little as $3 \cdot R$ parameters (with the number of scans per iteration $R = 2, 3$), which defined the preparation phase before R fixed 2D readouts. This is a significantly smaller subset of parameters as compared to the set of parameters required to define an entire MR sequence. Doing so, we still gave some reasonable boundaries by the definition of these few dimensions. Still, going from N·R = 6 to N·R = 9 degrees of freedom, a similar decrease of the MSE loss function was observed over the fixed number of
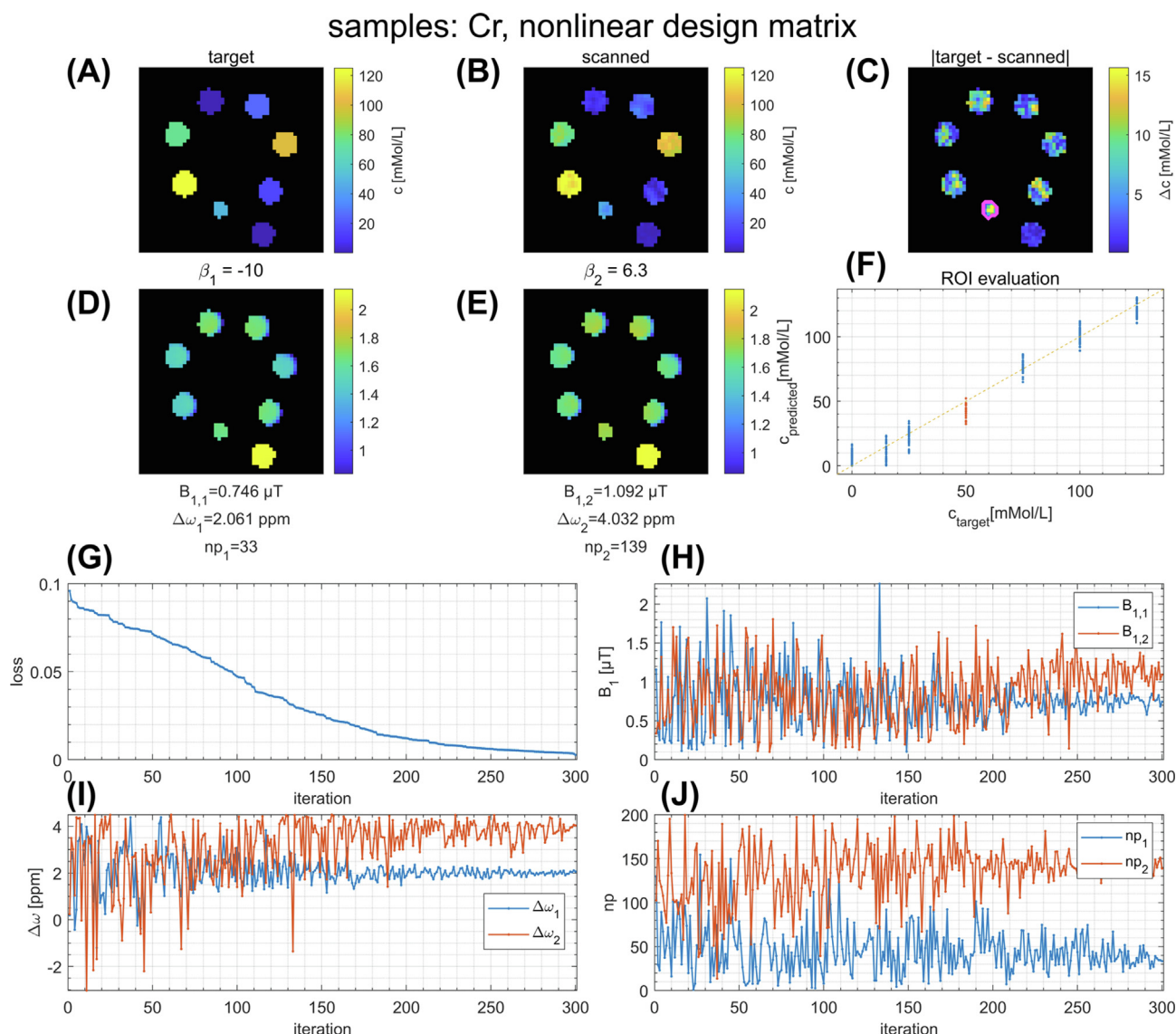
Fig. 5. Exemplary optimization process of a MR-double-zero sequence with 300 iterations (MRI scan time 3 h). The final parameter set was here seq = $(0.75 \, \mu T, +2.06 \, \text{ppm}, 33 | 1.10 \, \mu T, +4.03 \, \text{ppm}, 139)$. In contrast to Fig. 4, the design matrix contains in addition to the images (Img_1, Img_2) also the pixel-wise images squared (Img_1^2, Img_2^2) and cubed (Img_1^3, Img_2^3). The first row shows: (A) the target, (B) the experimentally derived and (C) the difference in concentrations. Second row shows the two images (C,D) with respective sequence parameters given below. In (F) the predicted and target data are scattered for ROIs within the different vials. The test vial (50 mMol/L) that was not included in the optimization process is highlighted in (C) and (F). Subplots (G-J) were retrospectively sorted by loss instead of the actual time course of acquisition. (G) shows the loss for the sequence parameters shown in (H)-(J). Subscripts 1 and 2 refer to the image number for all parameters. An animated version of this figure can be found as Supplementary Material.

300 iterations for both cases (Supplementary Fig. 4). Thus, it is conceivable that also higher-dimensional problems could be addressed by a feasible number of iterations, such that they are solvable with reasonable effort and scan time. However, this must be investigated in detail, also with regard to the hyper-parameters of the optimizer.

4.2. Contrast mapping function (inner optimization)

Note that a linear representation was assumed to map from contrast-prepared images to the target map, such that the coefficients could be directly obtained by pseudo-inversion of acquired and target data and do not need to be *learned* by the outer optimizer. For more sophisticated tasks, however, also non-linear representations like neural networks might be used instead. As a first step towards such more sophisticated mapping functions, it could be observed that augmenting the design matrix by non-linear transforms of the acquired signal intensities (here by power functions, thus forming a polynomial regression) increased the accuracy of the predicted concentrations (Supplementary Fig. 4). Potentially, the accuracy can be improved even more by adding more of such transforms e.g. 1/x, as inverse metrics have proven useful for CEST data evaluation [11]. This, however, would mean to incorporate CEST-specific knowledge into the reconstruction, which was intentionally avoided here by using polynomials as a general choice known from Taylor series expansion. Additionally, including more non-linear features comes at the risk of overfitting, as more regression coefficients are added to the representation. However, this can be avoided by monitoring MSE in a hold-out test set, which was shown to be still low in the present case (Figs. 4-6). These insights hint also to the benefits of using neural network approaches for the inner optimization that come with further challenges, and were not yet tested herein.
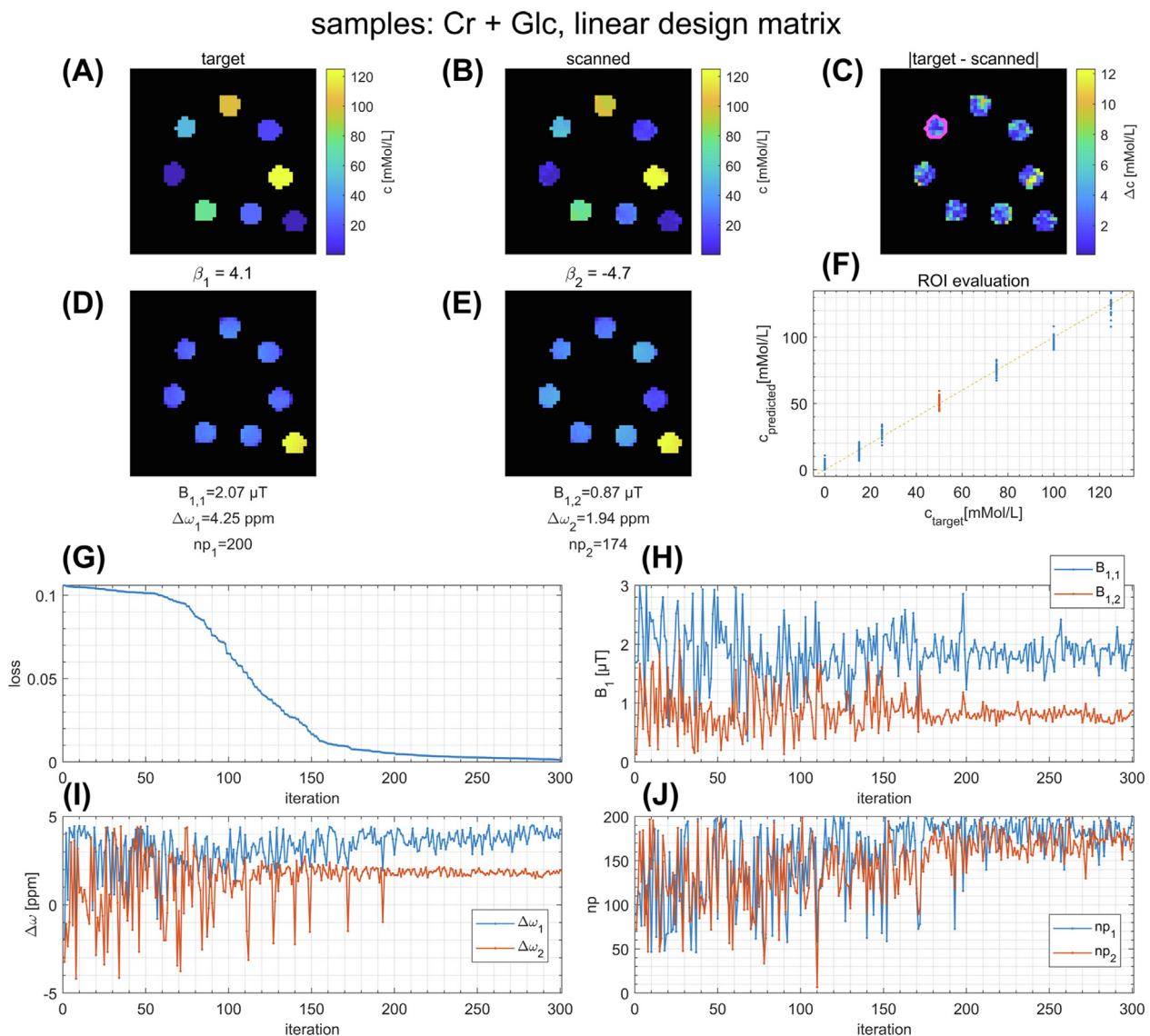
Fig. 6. Optimization process of a MR-double-zero sequence similar to the one shown in Fig. 4, but conducted on samples that contained different levels of glucose concentration as a confounding factor to the targeted creatine mapping. The final parameter set was here seq $= (2.07\ \mu T, +4.25\ \text{ppm}, 200 | 0.87\ \mu T, +1.94\ \text{ppm}, 174)$. The first row shows: (A) the target, (B) the experimentally derived and (C) the difference in concentrations. Second row shows the two images (C,D) with respective sequence parameters given below. In (F) the predicted and target data are scattered for ROIs within the different vials. The test vial (50 mMol/L) that was not included in the optimization process is highlighted in (C) and (F). Subplots (G-J) were retrospectively sorted by loss instead of the actual time course of acquisition. (G) shows the loss for the sequence parameters shown in (H)-(J) . Subscripts 1 and 2 refer to the image number for all parameters.

4.3. Discovered strategies in the context of existing methods

A CEST pool can affect T1 and T2 relaxation times, thus adding agar and contrast agent is crucial to make this direct influence negligible and the samples undiscernible in conventional contrasts. By doing this, the actual contrast of interest can be considered unknown. Still, not on-resonant preparation pulses, which would lead to T1/T2-weighting, but off-resonant pulses are chosen by MR-double-zero to encode the creatine concentration. In contrast to conventional CEST imaging, the optimized sequence required as little as two RF preparation offsets. The optimized sequence in case of the simple design matrix without additional non-linear transforms (Fig. 4) yields the parameters seq $= (0.96\ \mu T, +2.09\ \text{ppm}, 86 | 1.04\ \mu T, -2.11\ \text{ppm}, 97)$ and closely resembles the traditional asymmetry metric at 2 ppm: seq $= (B_1, +2\ \text{ppm}, np | B_1, -2\ \text{ppm}, np)$.

Interestingly, for the run with non-linear terms shown in Fig. 5, the offsets are not chosen symmetrically around the water reso-

nance, where they are typically placed in a conventional CEST measurement, but instead at seq $= (0.75\ \mu T, +2.06\ \text{ppm}, 33 | 1.10\ \mu T, +4.03\ \text{ppm}, 139)$, leading to improved prediction performance. This is interesting, as asymmetric approaches are known to be most prone to B_0 inhomogeneity artefacts [12], while same side approaches are more robust against B_0 shifts [13]. Furthermore, also different B_1 levels and number of pulses are chosen, which together can provide more insight into T1- and T2-dependent direct saturation, that has to be eliminated to achieve absolute concentration mapping [11]. Thus, MR-double-zero is not only able to find 'unknown' contrast-generating concepts, but can also learn better strategies for existing approaches and small but smart tricks for more robust preparation/detection/sampling schemes.

The finding that different methods are discovered that yield similar accuracy can be seen as a limitation that no global minimum is found. However, it actually fits perfectly to the experience that a plethora of chemical-exchange-weighted methods were published that generate similar contrast correlation [14–18].

4.4. Related work in the context of MRI

The presented method has some similarity with MR fingerprinting [19], which has also been demonstrated for CEST parameter mapping [17,20]. For the latter, only saturation pulse amplitudes (B_1) were varied in a pseudo-random manner to obtain unique signal trajectories, from which e.g. CEST pool concentrations could be inferred by means of dictionary matching. This, however, also requires the use of Bloch equations or extended phase graph formalism as a numerical model. Thus, MR-double-zero can be seen as model-free joint optimization of a fingerprinting schedule and reconstruction based on real measurements.

The idea of optimizing both acquisition and reconstruction of MRI data at the same time was already presented by others in the context of 'active acquisition' [21–22]. Jin et al. [21] split the optimization process into separately optimizing acquisition and reconstruction of MRI data by training "two deep networks that are tied together". The so-called SampleNet predicts which k-space points should be acquired next based on previous acquisitions, and the ReconNet learns the reconstruction given the provided sampling strategy. To some extent, the present approach behaves similarly, as the outer optimization (CMA-ES) optimizes the data acquisition while in the inner optimization the coefficients for linear regression are determined. Although such active acquisition policies could in principle be executed directly at a real MR scanner, in these works they are evaluated purely retrospectively on brain and knee MRI data sets. In contrast, the proposed approach optimizes a real data acquisition with live optimization. This might be beneficial as it enables full flexibility in terms of data acquisition and is not limited to any existing data that gets re-sampled.

4.5. Real-world optimization

Running optimization algorithms on real physical systems instead of theoretical models or simulations is known from other disciplines like robotics or autonomously driving cars. Particularly, reinforcement learning [23] can be applied to learning robot policies in realistic environments, e.g. [24–25]. In fact, the model and derivative-free optimization algorithm chosen in the present work reminds of the popular Q-learning algorithm [26], which learns to take appropriate actions (here: MR sequences) in a certain state (previously tested sequences) and environment (scanner and samples). Learning in realistic environments brings the benefit of including all possible real-world error sources like sensor noise, complex mechanical interactions and friction. However, a common disadvantage of all such real-world optimizations is that they are expensive, hard to reproduce exactly and usually more time-consuming (in terms of possible optimization iterations per time) than pure simulations. Because of that, it appears promising to combine simulation and real world based optimizations to hybrid approaches, which, for example, might intermittently update and improve a simulation-based optimization by real measurements.

However, also in the case of MRI, even simple systems may be challenging to model as the model has to be extended by experimental imperfections, e.g. eddy currents, gradient delays, and amplifier heating [27] in case of MR image encoding. Consequently, potential theoretical benefits of pure simulations - such as computational speed, reduced costs – are counterbalanced by the fact that simulating the real world accurately is arbitrarily complicated. This may not be an issue for some applications, but as the final goal of MRI in most cases is the real experimental implementation, it may actually be a severe bottleneck.

Moreover, instead of discovery of novel contrasts, one could exactly take such imperfections as a task for an optimization. For instance, the current off-resonant pulses could be optimized to generate a fast/robust fat-saturation, using an expensively acquired fat-artifact-free image as a target. In addition, B_0 or B_1 inhomogeneity-robust sequences optimized at the scanner are conceivable to be found. In general, not only complete novel strategies can be aimed for, but also small optimizations of existing approaches can be performed elegantly with the MR-double-zero approach. The optimization parameters are not limited to $seq = (B_1, \Delta\omega, np)$ as shown in this proof-of-concept, but could also be parameters such as echo time, repetition time or flip angle $seq = (TE, TR, FA)$. For instance, variable flip angle approaches could potentially be efficiently optimized with the proposed framework.

4.6. Future ideas and outlook

For the described proof of principle, a well know contrast mechanism was investigated. The ultimate goal could be to provide any target of interest. The proposed framework would then be used to learn how to map from the object/sample to the target by exploiting MR methodology. Here it is important, that not only the feature of interest is well-prepared in the used samples, but also to rule out correlations by 'randomizing' other properties that are not targeted, as shown in the present case for relaxation effects, as well as for the glucose contamination. In general, all contaminations against which the developed sequence should be robust, must be part of the training data established by the samples. Well-prepared samples are therefore a crucial step for the presented approach. Until now, we only showed re-discovery of a CEST contrast mechanism, but novel discoveries are in principle possible for samples already.

In contrast, for learning directly in vivo, the rather lengthy scan time in the order of several hours might be challenging, but it is still conceivable if the dimensionality can be reasonably reduced. Furthermore, one could split the learning phase into several sessions or run the optimization on multiple scanners with similar targets in parallel.

As a speculative future application, MR-double-zero might be used complementary to the radiomics approach that is of increasing popularity in the medical context of MRI [28]. Radiomics relies on using all available multi-modal imaging information to find correlations with pathology, e.g. brain tumors. Instead of looking for correlations in already existing data from conventional imaging methodologies, real-world based optimization of MR sequences and reconstructions that map to a known outcome, prognosis etc., thus explicitly designing the data generation process to correlate with the desired target information, might be a promising step towards novel, targeted MRI methods applied for medical diagnosis.

However, also well-designed experiments in samples can lead to novel concepts that can subsequently be translated for in vivo application, similar to many previous MRI breakthroughs found by 'trial-and-error' or grid search approaches in samples and in vivo in the past. The found glucose-invariant creatine mapping in the present work, by using different B1 and offsets, is such a concept that could now be investigated in more detail using human intuition, Bloch simulations, or more detailed grid-search measurements.

5. Conclusion

MR-double-zero is able to discover completely new MRI contrasts without requiring an explicit description of the underlying mechanism in form of a theoretical model. This was exemplarily demonstrated for a specific chemical-exchange-weighting, but it is conceivable that MR-double-zero could also discover yet

unknown MRI contrast correlations given suitable samples and targets are provided.

Declaration of Competing Interest

The authors declare that they have no known competing financial interests or personal relationships that could have appeared to influence the work reported in this paper.

Acknowledgements

Appendix A. Supplementary data

Supplementary data to this article can be found online at https://doi.org/10.1016/j.jmr.2022.107237.

References

[1] A. Loktyushin, K. Herz, N. Dang, et al., MRzero - Automated discovery of MRI sequences using supervised learning, Magnetic Resonance in Medicine 86 (2021) 709–724, https://doi.org/10.1002/mrm.28727.

[2] Scheffler, K. (1995). Design of B1-Insensitive and B1-Selective RF Pulses by Means of Stochastic Optimization. Journal of Magnetic Resonance Series B, 109 (2), 175-183. https://doi.org/10.1006/jmrb.1995.0007.

[3] S. Mueller, K. Scheffler, M. Zaiss, On the interference from agar in chemical exchange saturation transfer MRI parameter optimization in model solutions, NMR in Biomedicine 34 (2021) e4403.

[4] A. Deshmane, M. Zaiss, T. Lindig, et al., 3D gradient echo snapshot CEST MRI with low power saturation for human studies at 3T, Magnetic Resonance in Medicine 81 (2019) 2412–2423, https://doi.org/10.1002/mrm.27569.

[5] K.J. Layton, S. Kroboth, F. Jia, et al., Pulseq: A rapid and hardware-independent pulse sequence prototyping framework, Magnetic Resonance in Medicine 77 (2017) 1544–1552, https://doi.org/10.1002/mrm.26235.

[6] Herz K, Mueller S, Perlman O, et al. Pulseq-CEST: Towards multi-site multi-vendor compatibility and reproducibility of CEST experiments using an open-source sequence standard. Magnetic Resonance in Medicine n/a doi: 10.1002/mrm.28825.

[7] N. Hansen, A. Ostermeier, Adapting arbitrary normal mutation distributions in evolution strategies: the covariance matrix adaptation, in: In: Proceedings of IEEE International Conference on Evolutionary Computation, 1996, pp. 312–317, https://doi.org/10.1109/ICEC.1996.542381.

[8] Rapin J, Teytaud O. Nevergrad - A gradient-free optimization platform. https://GitHub.com/FacebookResearch/Nevergrad. 2018.

[9] V. Guivel-Scharen, T. Sinnwell, S.D. Wolff, R.S. Balaban, Detection of Proton Chemical Exchange between Metabolites and Water in Biological Tissues, Journal of Magnetic Resonance 133 (1998) 36–45, https://doi.org/10.1006/jmre.1998.1440.

[10] K. Herz, T. Lindig, A. Deshmane, et al., $T1\rho$-based dynamic glucose-enhanced (DGEρ) MRI at 3 T: method development and early clinical experience in the human brain, Magnetic Resonance in Medicine 82 (2019) 1832–1847, https://doi.org/10.1002/mrm.27857.

[11] M. Zaiss, J. Xu, S. Goerke, et al., Inverse Z-spectrum analysis for spillover-, MT-, and T1-corrected steady-state pulsed CEST-MRI – application to pH-weighted MRI of acute stroke, NMR in Biomedicine 27 (2014) 240–252, https://doi.org/10.1002/nbm.3054.

[12] A. Singh, M. Haris, K. Cai, et al., Chemical exchange saturation transfer magnetic resonance imaging of human knee cartilage at 3 T and 7 T, Magnetic Resonance in Medicine 68 (2012) 588–594, https://doi.org/10.1002/mrm.23250.

[13] P.Z. Sun, C.T. Farrar, A.G. Sorensen, Correction for artifacts induced by B0 and B1 field inhomogeneities in pH-sensitive chemical exchange saturation transfer (CEST) imaging, Magnetic Resonance in Medicine 58 (2007) 1207–1215, https://doi.org/10.1002/mrm.21398.

[14] J. Yuan, J. Zhou, A.T. Ahuja, Y.-X.-J. Wang, MR chemical exchange imaging with spin-lock technique (CESL): a theoretical analysis of the Z-spectrum using a two-pool $R_{1\rho}$ relaxation model beyond the fast-exchange limit, Phys. Med. Biol. 57 (2012) 8185–8200, https://doi.org/10.1088/0031-9155/57/24/8185.

[15] Z. Zu, V.A. Janve, J. Xu, M.D. Does, J.C. Gore, D.F. Gochberg, A new method for detecting exchanging amide protons using chemical exchange rotation transfer, Magnetic Resonance in Medicine 69 (2013) 637–647, https://doi.org/10.1002/mrm.24284.

[16] N.N. Yadav, C.K. Jones, J. Xu, et al., Detection of rapidly exchanging compounds using on-resonance frequency-labeled exchange (FLEX) transfer, Magnetic Resonance in Medicine 68 (2012) 1048–1055, https://doi.org/10.1002/mrm.24420.

[17] O. Perlman, K. Herz, M. Zaiss, O. Cohen, M.S. Rosen, C.T. Farrar, CEST MR-Fingerprinting: Practical considerations and insights for acquisition schedule design and improved reconstruction, Magnetic Resonance in Medicine 83 (2020) 462–478, https://doi.org/10.1002/mrm.27937.

[18] F.T. Gutjahr, E. Munz, P.M. Jakob, Positive chemical exchange contrast in MRI using Refocused Acquisition of Chemical Exchange Transferred Excitations (RACETE), Zeitschrift für Medizinische Physik 29 (2019) 184–191, https://doi.org/10.1016/j.zemedi.2018.05.005.

[19] D. Ma, V. Gulani, N. Seiberlich, et al., Magnetic resonance fingerprinting, Nature 495 (2013) 187–192, https://doi.org/10.1038/nature11971.

[20] O. Perlman, H. Ito, K. Herz, et al., Quantitative imaging of apoptosis following oncolytic virotherapy by magnetic resonance fingerprinting aided by deep learning, Nat Biomed Eng (2021) 1–10, https://doi.org/10.1038/s41551-021-00809-7.

[21] Jin KH, Unser M, Yi KM. Self-Supervised Deep Active Accelerated MRI. arXiv:1901.04547 [cs] 2019.

[22] Z. Zhang, A. Romero, M.J. Muckley, P. Vincent, L. Yang, M. Drozdzal, Reducing Uncertainty in Undersampled MRI Reconstruction With Active Acquisition, in: 2019 IEEE/CVF Conference on Computer Vision and Pattern Recognition (CVPR), 2019, pp. 2049–2053, https://doi.org/10.1109/CVPR.2019.00215.

[23] Kober J, Bagnell JA, Peters J. Reinforcement Learning in Robotics: A Survey. :38.

[24] S. Mahadevan, J. Connell, Automatic programming of behavior-based robots using reinforcement learning, Artificial Intelligence 55 (1992) 311–365, https://doi.org/10.1016/0004-3702(92)90058-6.

[25] Bagnell JA, Schneider JG. Autonomous helicopter control using reinforcement learning policy search methods. In: Proceedings 2001 ICRA. IEEE International Conference on Robotics and Automation (Cat. No.01CH37164). Vol. 2. ; 2001. pp. 1615–1620 vol.2. doi: 10.1109/ROBOT.2001.932842.

[26] C.J.C.H. Watkins, P. Dayan, Q-learning, Mach Learn 8 (1992) 279–292, https://doi.org/10.1007/BF00992698.

[27] Voelker MN, Kraff O, Goerke S, et al. The traveling heads 2.0: Multicenter reproducibility of quantitative imaging methods at 7 Tesla. NeuroImage 2021;232:117910 doi: 10.1016/j.neuroimage.2021.117910.

[28] R.J. Gillies, P.E. Kinahan, H. Hricak, Radiomics: Images Are More than Pictures, They Are Data. Radiology 278 (2016) 563–577, https://doi.org/10.1148/radiol.2015151169.

C. Appendix

C.1. Derivation of a General Analytical SENSE g-Factor Formula

In the original SENSE paper [34], Pruessmann et al. give an expression for the g-factor in the special case of regular Cartesian undersampling. Here, a general expression for arbitrary encoding schemes is derived. The g-factor in the ρ-th voxel is defined in terms of the SNR of a fully sampled reference reconstruction $\mathrm{SNR}_\rho^{\mathrm{ref}}$ and the SNR of a PI reconstruction $\mathrm{SNR}^{\mathrm{PI}}$ accelerated by factor R as ([34], equation [24])

$$g_\rho^2 = \frac{(\mathrm{SNR}_\rho^{\mathrm{ref}})^2}{(\mathrm{SNR}_\rho^{\mathrm{PI}})^2 \cdot R} = \frac{(\sigma_\rho^{\mathrm{PI}})^2}{(\sigma_\rho^{\mathrm{ref}})^2 \cdot R} \tag{C.1}$$

with the corresponding spatially-varying noise variances of PI and reference reconstructions $(\sigma_\rho^{\mathrm{PI}})$ and $(\sigma_\rho^{\mathrm{ref}})$, assuming for the second equality that the signal is identical in both images. The image noise matrix $\mathbf{X}$, whose diagonal entries contain the noise variance in each pixel, is given by ([34], equation [17]; see also section 2.2.5)

$$\mathbf{X} = (\mathbf{E}^H \mathbf{E})^{-1}, \tag{C.2}$$

where the sample noise matrix $\tilde{\boldsymbol{\Psi}}$ is eliminated by previously performed noise decorrelation as described in [42], and the encoding matrix is given by ([34], equations [5] and [19])

$$\mathbf{E}_{(\gamma,\kappa),\rho} = c_\gamma(\vec{r}_\rho) \exp\left(i\vec{k}_\kappa \cdot \vec{r}_\rho\right). \tag{C.3}$$

This yields

$$(\mathbf{E}^H \mathbf{E})_{\rho,\rho'} = \sum_{\gamma=1}^{N_c} \sum_{\kappa=0}^{N_K-1} c_\gamma^*(\vec{r}_\rho) c_\gamma(\vec{r}_{\rho'}) \exp\left(i\vec{k}_\kappa \cdot (\vec{r}_{\rho'} - \vec{r}_\rho)\right) \tag{C.4}$$

with the number of coils N_c and number of k-space samples N_K. The structure of this matrix, which can be seen as the correlation matrix of encoding basis vectors, depends strongly on the k-space trajectory $\vec{k}_\kappa$.

C. Appendix

In case of a Nyquist-sampled Cartesian k-space grid, substituting the expressions from [34], equations [D1] and [D2], for equispaced $\vec{k}_\kappa$ and $\vec{r}_\rho$ (using multi-indices $\kappa = (\kappa_x, \kappa_y)$ and $\rho = (\rho_x, \rho_y)$), which read

$$\vec{k}_\kappa = 2\pi \left(\frac{1}{\Delta x} \left(\frac{\kappa_x}{N_{K_x}} - \frac{1}{2} \right), \frac{1}{\Delta y} \left(\frac{\kappa_y}{N_{K_y}} - \frac{1}{2} \right) \right) \tag{C.5}$$

$$\vec{r}_\rho = \left(\Delta x \left(\rho_x - \frac{N_{V_x}}{2} \right), \Delta y \left(\rho_y - \frac{N_{V_y}}{2} \right) \right) \tag{C.6}$$

into equation (C.4) results in[11]

$$(\mathbf{E}_{\text{cart,full}}^H \mathbf{E}_{\text{cart,full}})_{\rho,\rho'} =$$

$$\sum_\gamma c_\gamma^*(\vec{r}_\rho) c_\gamma(\vec{r}_{\rho'}) e^{-2\pi i \left(\frac{\rho'_x - \rho_x}{2} + \frac{\rho'_y - \rho_y}{2} \right)} \sum_{\kappa_x = 0}^{N_{K_x} - 1} e^{2\pi i \frac{\kappa_x (\rho'_x - \rho_x)}{N_{K_x}}} \sum_{\kappa_y = 0}^{N_{K_y} - 1} e^{2\pi i \frac{\kappa_y (\rho'_y - \rho_y)}{N_{K_y}}} \tag{C.7}$$

Due to the orthogonality of the discrete Fourier basis (which follows from the geometric summation formula), the last two sums yield the expressions $N_{K_x} \delta_{\rho'_x, \rho_x}$ and $N_{K_y} \delta_{\rho'_y, \rho_y}$ with the Kronecker delta $\delta_{i,j}$, respectively. Consequently, for the Nyquist-sampled Cartesian case, one obtains the diagonal matrix

$$(\mathbf{E}_{\text{cart,full}}^H \mathbf{E}_{\text{cart,full}})_{\rho,\rho'} = N_k \delta_{\rho',\rho} \sum_\gamma |c_\gamma(\vec{r}_\rho)|^2 \tag{C.8}$$

with $N_K = N_{K_x} \cdot N_{K_y}$ and $\delta_{\rho',\rho} = \delta_{\rho'_x, \rho_x} \delta_{\rho'_y, \rho_y}$. The matrix inversion required to form the diagonal entries of the image noise matrix (equation (C.2)) thus becomes a simple scalar inversion of the diagonal elements:

$$(\mathbf{X}_{\text{cart,full}})_{\rho,\rho} = (\sigma_\rho^{\text{ref}})^2 = \left((\mathbf{E}_{\text{cart,full}}^H \mathbf{E}_{\text{cart,full}})^{-1} \right)_{\rho,\rho} = \frac{1}{(\mathbf{E}_{\text{cart,full}}^H \mathbf{E}_{\text{cart,full}})_{\rho,\rho}}. \tag{C.9}$$

Note that evaluating the diagonal elements ($\rho = \rho'$) in equation (C.4) for general (not necessarily regular Cartesian) sampling with number of samples $N_{K_{\text{red}}}$ yields

$$(\mathbf{E}^H \mathbf{E})_{\rho,\rho} = \sum_\gamma \sum_{\kappa=0}^{N_{K_{\text{red}}} - 1} |c_\gamma(\vec{r}_\rho)|^2 = N_{K_{\text{red}}} \sum_\gamma |c_\gamma(\vec{r}_\rho)|^2 = \frac{N_{K_{\text{red}}}}{N_K} (\mathbf{E}_{\text{cart,full}}^H \mathbf{E}_{\text{cart,full}})_{\rho,\rho}. \tag{C.10}$$

---

[11]Note that with the definitions in equation (C.5) and (C.6) one obtains for the phase term $k_{\kappa_x} r_{\rho_x} = 2\pi \left(\frac{\kappa_x \rho_x}{N_{K_x}} - \frac{\kappa_x}{N_{K_x}} \frac{N_{V_x}}{2} - \frac{\rho_x}{2} + \frac{N_{V_x}}{4} \right)$ and analogously for y. This leads to $k_{\kappa_x} (r_{\rho'_x} - r_{\rho_x}) = 2\pi \left(\frac{\kappa_x (\rho'_x - \rho_x)}{N_{K_x}} - \frac{\rho'_x - \rho_x}{2} \right)$.

The last equality follows from comparison with equation (C.8), leading to the factor $N_{K_{\text{red}}}/N_K = 1/R$. Using these insights to insert the relevant image noise matrix terms into equation (C.1) yields

$$g_\rho^2 = \frac{\mathbf{X}_{\rho,\rho}}{R \cdot (\mathbf{X}_{\text{cart,full}})_{\rho,\rho}} = \frac{(\mathbf{E}^H\mathbf{E})_{\rho,\rho}^{-1}}{R \cdot \frac{1}{(\mathbf{E}_{\text{cart,full}}^H\mathbf{E}_{\text{cart,full}})_{\rho,\rho}}} = (\mathbf{E}^H\mathbf{E})_{\rho,\rho}^{-1}(\mathbf{E}^H\mathbf{E})_{\rho,\rho}, \qquad \text{(C.11)}$$

where in the second and third equality equations (C.9) and (C.10) were used, respectively. In summary, the expression $g_\rho = \sqrt{(\mathbf{E}^H\mathbf{E})_{\rho,\rho}^{-1}(\mathbf{E}^H\mathbf{E})_{\rho,\rho}}$ with an arbitrary encoding matrix $\mathbf{E}$ yields the g-factor as ratio between the SNR of a reconstruction based on $\mathbf{E}$ and a reference Nyquist-sampled Cartesian reconstruction based on $\mathbf{E}_{\text{cart,full}}$ with the same coil sensitivities, intrinsically adjusted for the inevitable SNR loss of factor $\sqrt{R}$ due to lower total sample number.

C.2. Proof: Time-Division Multiplexing of Coil Sensitivities

The purpose of this section is to prove that, in the context of time-varying receive sensitivities, which are subject of Publications 1 and 2 of this thesis, two physically different situations result in the same SENSE g-factors:

a) Dynamically switching between two receive sensitivity configurations $c_\gamma^{(1)}(\vec{r})$ and $c_\gamma^{(2)}(\vec{r})$ of $\gamma = 1, \ldots, N_c$ coils during a two-fold oversampled k-space readout, such that neighboring k-space samples are alternatingly weighted by the two configurations ("switching along the readout direction", see Figure 4.2(G)), while applying arbitrary undersampling in the phase encoding directions

b) Using a hypothetical coil array with $2N_c$ receive channels that has all the sensitivities $c_\gamma^{(1)}(\vec{r})$ and $c_\gamma^{(2)}(\vec{r})$ statically active at the same time, while applying the same undersampling as in a) in the phase encoding directions

For the g-factor as derived in section C.1, equation (C.11), only the matrix $\mathbf{E}^H\mathbf{E}$ that is formed from the respective encoding matrix is relevant. For situation b), assuming Cartesian Nyquist sampling in the k_x direction as in equation (C.5) and arbitrary sampling in k_y, evaluating equation (C.4) yields

$$(\mathbf{E}_b^H\mathbf{E}_b)_{\rho,\rho'} = N_{K_x}\delta_{\rho'_x,\rho_x} \sum_{\alpha=1}^{2}\sum_{\gamma=1}^{N_c} c_\gamma^{(\alpha)}(\vec{r}_\rho)^* \cdot c_\gamma^{(\alpha)}(\vec{r}_{\rho'}) \underbrace{\sum_{\kappa_y=0}^{N_{K_y}-1} e^{ik_{\kappa_y}(r_{\rho'_y}-r_{\rho_y})}}_{=:\Psi_y}, \qquad \text{(C.12)}$$

where, analogously to section C.1, the orthogonality of the discrete Fourier basis that arises from regular Cartesian sampling along k_x was exploited. The term $\Psi_y = \Psi_y(\kappa_y, \rho_y, \rho'_y)$

captures the aliasing pattern due to undersampling in the PE direction. Note that in this expression, the configurations enumerated by α and channels enumerated by γ play equivalent roles, according to the hypothetical scenario of having both configurations simultaneously active at the same time.

For situation a), the sensitivity terms in the encoding matrix have an explicit time dependency as $(\mathbf{E}_a)_{(\gamma,\kappa),\rho} = c_\gamma(\vec{r}_\rho, t_\kappa) \exp\left(i\vec{k}_\kappa \cdot \vec{r}_\rho\right)$. To model two-fold readout oversampling, it is sufficient to use the Cartesian k-space coordinate definition from equation (C.5) as $k_{\kappa_x} = 2\pi\frac{1}{\Delta x}\left(\frac{\kappa_x}{N_{K_x}} - \frac{1}{2}\right)$ but with $\kappa_x = 0, \frac{1}{2}, 1, \frac{3}{2}, \ldots, N_{K_x} - \frac{1}{2}$ instead of integer indices. The alternating sensitivity switching between consecutive samples along the readout direction can then be formulated as

$$c_\gamma(\vec{r}_\rho, t_{\kappa_x,\kappa_y}) = \begin{cases} c_\gamma^{(1)}(\vec{r}_\rho) & \text{for} \quad \kappa_x = 0, 1, 2, \ldots, N_{K_x} - 1 \\ c_\gamma^{(2)}(\vec{r}_\rho) & \text{for} \quad \kappa_x = \frac{1}{2}, \frac{3}{2}, \frac{5}{2}, \ldots, N_{K_x} - \frac{1}{2} \end{cases}. \tag{C.13}$$

With that, one obtains

$$(\mathbf{E}_a^H \mathbf{E}_a)_{\rho,\rho'} = \sum_\gamma \sum_{\kappa_x} \sum_{\kappa_y} c_\gamma^*(\vec{r}_\rho, t_{\kappa_x,\kappa_y}) c_\gamma(\vec{r}_{\rho'}, t_{\kappa_x,\kappa_y}) e^{ik_{\kappa_x}(r_{\rho'_x} - r_{\rho_x})} e^{ik_{\kappa_y}(r_{\rho'_y} - r_{\rho_y})}$$

$$= \sum_\gamma e^{-2\pi i \frac{\rho'_x - \rho_x}{2}} \left\{ c_\gamma^{(1)}(\vec{r}_\rho)^* \cdot c_\gamma^{(1)}(\vec{r}_{\rho'}) \sum_{\kappa_x=0}^{N_{K_x}-1} e^{2\pi i\left(\frac{\kappa_x}{N_{K_x}}(\rho'_x - \rho_x)\right)} + \ldots \right.$$

$$\left. \ldots \quad c_\gamma^{(2)}(\vec{r}_\rho)^* \cdot c_\gamma^{(2)}(\vec{r}_{\rho'}) \sum_{\kappa_x=0}^{N_{K_x}-1} e^{2\pi i\left(\frac{\kappa_x+1/2}{N_{K_x}}(\rho'_x - \rho_x)\right)} \right\} \Psi_y$$

$$\tag{C.14}$$

where in the large curly bracket, the summation over κ_x was split into integer and non-integer terms, corresponding to the sensitivity switching defined in equation (C.13). Again, orthogonality of the discrete Fourier basis can be exploited as

$$\sum_{\kappa_x=0}^{N_{K_x}-1} e^{2\pi i\left(\frac{\kappa_x}{N_{K_x}}(\rho'_x - \rho_x)\right)} = N_{K_x}\delta_{\rho'_x,\rho_x} \tag{C.15}$$

and

$$\sum_{\kappa_x=0}^{N_{K_x}-1} e^{2\pi i\left(\frac{\kappa_x+1/2}{N_{K_x}}(\rho'_x - \rho_x)\right)} = e^{i\pi\frac{\rho'_x - \rho_x}{N_{K_x}}} N_{K_x}\delta_{\rho'_x,\rho_x} = N_{K_x}\delta_{\rho'_x,\rho_x}, \tag{C.16}$$

which corresponds to the observation that the two intertwined sub-grids in k-space formed by two-fold oversampling still satisfy the Nyquist criterion. Thus, one obtains

$$(\mathbf{E}_a^H \mathbf{E}_a)_{\rho,\rho'} = N_{K_x}\delta_{\rho'_x,\rho_x} \sum_{\gamma=1}^{N_c} \sum_{\kappa_x=0}^{N_{K_x}-1} \left(c_\gamma^{(1)}(\vec{r}_\rho)^* \cdot c_\gamma^{(1)}(\vec{r}_{\rho'}) + c_\gamma^{(2)}(\vec{r}_\rho)^* \cdot c_\gamma^{(2)}(\vec{r}_{\rho'})\right) \Psi_y. \tag{C.17}$$

Comparing equations (C.12) and (C.17), one finds $\mathbf{E}_a^H \mathbf{E}_a = \mathbf{E}_b^H \mathbf{E}_b$, so according to equation (C.11), the g-factors of scenario a) and b) are identical. $\square$

Rapid configuration switching can thus be regarded as a form of time-division multiplexing of sensitivity profiles. It is important to note, that this result holds only for g-factors, which are a relative quantity, and not for absolute SNR. Scenario b), by acquiring twice the number of samples at the same time, would give $\sqrt{2}$ times higher absolute SNR than scenario a).

References

[1] Hastie T, Tibshirani R, Friedman J. *The Elements of Statistical Learning: Data Mining, Inference, and Prediction, Second Edition.* Springer Science & Business Media, 2009. ISBN 978-0-387-84858-7

[2] Rencher AC, Schaalje GB. *Linear Models in Statistics.* Wiley-Interscience, Hoboken, N.J, 2nd ed edition, 2008. ISBN 978-0-471-75498-5

[3] Bishop CM. *Pattern Recognition and Machine Learning.* Information Science and Statistics. Springer, New York, 2006. ISBN 978-0-387-31073-2

[4] Kay S. *Fundamentals of Statistical Signal Processing: Estimation Theory.* Fundamentals of Statistical Signal Processing. Prentice-Hall, 1993. ISBN 978-0-13-042268-2

[5] Aitken AC. IV.—On Least Squares and Linear Combination of Observations. *Proceedings of the Royal Society of Edinburgh*, 1936;55:42–48. doi:10.1017/S0370164600014346

[6] Levitt MH. *Spin Dynamics: Basics of Nuclear Magnetic Resonance.* Wiley, Chichester, England; Hoboken, NJ, 2. edition edition, 2008. ISBN 978-0-470-51117-6

[7] Bernstein MA, King KF, Zhou ZJ. *Handbook of MRI Pulse Sequences.* Academic Press, Amsterdam ; Boston, 2004. ISBN 978-0-12-092861-3

[8] Brown RW. *Magnetic Resonance Imaging: Physical Principles and Sequence Design.* John Wiley & Sons, Inc., 2014. ISBN 978-0-471-72085-0

[9] Engelke F. Virtual photons in magnetic resonance. *Concepts in Magnetic Resonance Part A*, 2010;36A(5):266–339. doi:10.1002/cmr.a.20166

[10] Ehrenfest P. Bemerkung über die angenäherte Gültigkeit der klassischen Mechanik innerhalb der Quantenmechanik. *Zeitschrift für Physik*, 1927;45(7):455–457. doi:10.1007/BF01329203

[11] Nolting W. *Grundkurs Theoretische Physik 5/1.* Springer-Lehrbuch. Springer Berlin Heidelberg, Berlin, Heidelberg, 2013. ISBN 978-3-642-25402-4 978-3-642-25403-1. doi:10.1007/978-3-642-25403-1

[12] Pohmann R, Speck O, Scheffler K. Signal-to-noise ratio and MR tissue parameters in human brain imaging at 3, 7, and 9.4 tesla using current receive coil arrays. *Magnetic Resonance in Medicine*, 2016;75(2):801–809. doi:10.1002/mrm.25677

References

[13] Bloch F. Nuclear Induction. *Physical Review*, 1946;70(7-8):460–474. doi:10.1103/PhysRev.70.460

[14] Slichter CP. *Principles of Magnetic Resonance*, volume 1 of *Springer Series in Solid-State Sciences*. Springer Berlin Heidelberg, Berlin, Heidelberg, 1990. ISBN 978-3-642-08069-2 978-3-662-09441-9. doi:10.1007/978-3-662-09441-9

[15] Hoult DI. The principle of reciprocity in signal strength calculations—A mathematical guide. *Concepts in Magnetic Resonance*, 2000;12(4):173–187. doi:10.1002/1099-0534(2000)12:4⟨173::AID-CMR1⟩3.0.CO;2-Q

[16] Ilott AJ, Jerschow A. Aspects of NMR reciprocity and applications in highly conductive media. *Concepts in Magnetic Resonance Part A*, 2018;47A(2):e21466. doi:10.1002/cmr.a.21466

[17] Vaidya MV, Collins CM, Sodickson DK, Brown R, Wiggins GC, Lattanzi R. Dependence of and field patterns of surface coils on the electrical properties of the sample and the MR operating frequency. *Concepts in Magnetic Resonance Part B: Magnetic Resonance Engineering*, 2016;46(1):25–40. doi:10.1002/cmr.b.21319

[18] Lauterbur PC. Image Formation by Induced Local Interactions: Examples Employing Nuclear Magnetic Resonance. *Nature*, 1973;242(5394):190–191. doi:10.1038/242190a0

[19] Likes RS. Moving gradient zeugmatography, US patent, assignee: General Electric Co, US06067697, 1981

[20] Ljunggren S. A simple graphical representation of fourier-based imaging methods. *Journal of Magnetic Resonance (1969)*, 1983;54(2):338–343. doi:10.1016/0022-2364(83)90060-4

[21] Twieg DB. The k -trajectory formulation of the NMR imaging process with applications in analysis and synthesis of imaging methods: k -trajectory formulation of NMR imaging. *Medical Physics*, 1983;10(5):610–621. doi:10.1118/1.595331

[22] Kumar A, Welti D, Ernst RR. NMR Fourier zeugmatography. *Journal of Magnetic Resonance (1969)*, 1975;18(1):69–83. doi:10.1016/0022-2364(75)90224-3

[23] Lai CM, Lauterbur PC. A gradient control device for complete three-dimensional nuclear magnetic resonance zeugmatographic imaging. *Journal of Physics E: Scientific Instruments*, 1980;13(7):747. doi:10.1088/0022-3735/13/7/013

[24] Ahn CB, Kim JH, Cho ZH. High-Speed Spiral-Scan Echo Planar NMR Imaging-I. *IEEE Transactions on Medical Imaging*, 1986;5(1):2–7. doi:10.1109/TMI.1986.4307732

[25] Ladd ME, Bachert P, Meyerspeer M, et al. Pros and cons of ultra-high-field MRI/MRS for human application. *Progress in Nuclear Magnetic Resonance Spectroscopy*, 2018;109:1–50. doi:10.1016/j.pnmrs.2018.06.001

[26] Aja-Fernández S, Vegas-Sánchez-Ferrero G. *Statistical Analysis of Noise in MRI*. Springer International Publishing, Cham, 2016. ISBN 978-3-319-39933-1 978-3-319-39934-8. doi:10.1007/978-3-319-39934-8

[27] Macovski A. Noise in MRI. *Magnetic Resonance in Medicine*, 1996;36(3):494–497. doi:10.1002/mrm.1910360327

[28] Fessler JA. Model-Based Image Reconstruction for MRI. *IEEE Signal Processing Magazine*, 2010;27(4):81–89. doi:10.1109/MSP.2010.936726

[29] Shannon C. Communication in the Presence of Noise. *Proceedings of the IRE*, 1949;37(1):10–21. doi:10.1109/JRPROC.1949.232969

[30] Cooley JW, Tukey JW. An Algorithm for the Machine Calculation of Complex Fourier Series. *Mathematics of Computation*, 1965;19(90):297–301. doi:10.2307/2003354

[31] Roemer PB, Edelstein WA, Hayes CE, Souza SP, Mueller OM. The NMR phased array. *Magnetic Resonance in Medicine*, 1990;16(2):192–225. doi:10.1002/mrm.1910160203

[32] Carlson JW, Minemura T. Imaging time reduction through multiple receiver coil data acquisition and image reconstruction. *Magnetic Resonance in Medicine*, 1993;29(5):681–687. doi:10.1002/mrm.1910290516

[33] Sodickson DK, Manning WJ. Simultaneous acquisition of spatial harmonics (SMASH): Fast imaging with radiofrequency coil arrays. *Magnetic Resonance in Medicine*, 1997;38(4):591–603. doi:10.1002/mrm.1910380414

[34] Pruessmann KP, Weiger M, Scheidegger MB, Boesiger P. SENSE: Sensitivity encoding for fast MRI. *Magnetic Resonance in Medicine*, 1999;42(5):952–962. doi:10.1002/(SICI)1522-2594(199911)42:5⟨952::AID-MRM16⟩3.0.CO;2-S

[35] Pruessmann KP. Encoding and reconstruction in parallel MRI. *NMR in Biomedicine*, 2006;19(3):288–299. doi:10.1002/nbm.1042

[36] Griswold MA, Jakob PM, Heidemann RM, et al. Generalized autocalibrating partially parallel acquisitions (GRAPPA). *Magnetic Resonance in Medicine*, 2002;47(6):1202–1210. doi:10.1002/mrm.10171

[37] Deshmane A, Gulani V, Griswold MA, Seiberlich N. Parallel MR imaging. *Journal of Magnetic Resonance Imaging*, 2012;36(1):55–72. doi:10.1002/jmri.23639

[38] Larkman DJ, Nunes RG. Parallel magnetic resonance imaging. *Physics in Medicine and Biology*, 2007;52(7):R15–R55. doi:10.1088/0031-9155/52/7/R01

[39] Hamilton J, Franson D, Seiberlich N. Recent advances in parallel imaging for MRI. *Progress in Nuclear Magnetic Resonance Spectroscopy*, 2017;101:71–95. doi:10.1016/j.pnmrs.2017.04.002

References

[40] Wright KL, Hamilton JI, Griswold MA, Gulani V, Seiberlich N. Non-Cartesian parallel imaging reconstruction. *Journal of Magnetic Resonance Imaging*, 2014; 40(5):1022–1040. doi:10.1002/jmri.24521

[41] Kellman P, McVeigh ER. Image reconstruction in SNR units: A general method for SNR measurement†. *Magnetic Resonance in Medicine*, 2005;54(6):1439–1447. doi:10.1002/mrm.20713

[42] Pruessmann KP, Weiger M, Börnert P, Boesiger P. Advances in sensitivity encoding with arbitrary k-space trajectories. *Magnetic Resonance in Medicine*, 2001; 46(4):638–651. doi:10.1002/mrm.1241

[43] Ohliger MA, Sodickson DK. An introduction to coil array design for parallel MRI. *NMR in Biomedicine*, 2006;19(3):300–315. doi:10.1002/nbm.1046

[44] Muftuler LT, Chen G, Nalcioglu O. An inverse method to design RF coil arrays optimized for SENSE imaging. *Physics in Medicine and Biology*, 2006;51(24):6457–6469. doi:10.1088/0031-9155/51/24/012

[45] de Zwart JA, Ledden PJ, Kellman P, van Gelderen P, Duyn JH. Design of a SENSE-optimized high-sensitivity MRI receive coil for brain imaging. *Magnetic Resonance in Medicine*, 2002;47(6):1218–1227. doi:10.1002/mrm.10169

[46] Weiger M, Pruessmann KP, Leussler C, Röschmann P, Boesiger P. Specific coil design for SENSE: A six-element cardiac array. *Magnetic Resonance in Medicine*, 2001;45(3):495–504. doi:10.1002/1522-2594(200103)45:3⟨495::AID-MRM1065⟩3.0. CO;2-V

[47] Breuer FA, Blaimer M, Mueller MF, et al. Controlled aliasing in volumetric parallel imaging (2D CAIPIRINHA). *Magnetic Resonance in Medicine*, 2006;55(3):549–556. doi:10.1002/mrm.20787

[48] Bilgic B, Gagoski BA, Cauley SF, et al. Wave-CAIPI for highly accelerated 3D imaging. *Magnetic Resonance in Medicine*, 2015;73(6):2152–2162. doi:10.1002/mrm.25347

[49] Glang F, Loktyushin A, Herz K, et al. Advances in MRzero – supervised learning of parallel imaging sequences including joint non-Cartesian trajectory and flip angle optimization. In *Proc. Intl. Soc. Mag. Reson. Med. 29 (2021)*. Virtual, 2021; abstract number 4200

[50] Levine E, Hargreaves B. On-the-Fly Adaptive k-Space Sampling for Linear MRI Reconstruction Using Moment-Based Spectral Analysis. *IEEE Transactions on Medical Imaging*, 2018;37(2):557–567. doi:10.1109/TMI.2017.2766131

[51] Weiger M, Pruessmann KP, Boesiger P. 2D SENSE for faster 3D MRI. *Magnetic Resonance Materials in Physics, Biology and Medicine*, 2002;14(1):10–19. doi: 10.1007/BF02668182

[52] Scheffe M. The Cramer-Rao Bound for Parallel MRI: Optimum SNR, Minimum Error, and the g-Function. In *Second International Workshop on Parallel MRI*. Zurich, Switzerland, 2004;

[53] Pineda AR, Lew CD, Bammer R. The Geometry Factor as a Cramér-Rao Bound for Magnitude and Phase. In *Proc. Intl. Soc. Mag. Reson. Med. 14*. Seattle, Washington, USA, 2006; abstract number 2469

[54] Golub GH, Van Loan CF. *Matrix Computations*. Johns Hopkins Studies in the Mathematical Sciences. The Johns Hopkins University Press, Baltimore, fourth edition edition, 2013. ISBN 978-1-4214-0794-4

[55] Breuer FA, Blaimer M, Heidemann RM, Mueller MF, Griswold MA, Jakob PM. Controlled aliasing in parallel imaging results in higher acceleration (CAIPIRINHA) for multi-slice imaging. *Magnetic Resonance in Medicine*, 2005;53(3):684–691. doi:10.1002/mrm.20401

[56] Shajan G, Kozlov M, Hoffmann J, Turner R, Scheffler K, Pohmann R. A 16-channel dual-row transmit array in combination with a 31-element receive array for human brain imaging at 9.4 T. *Magnetic Resonance in Medicine*, 2014;71(2):870–879. doi: 10.1002/mrm.24726

[57] Hestenes MR, Stiefel E, et al. Methods of conjugate gradients for solving linear systems. *Journal of research of the National Bureau of Standards*, 1952;49(6):409–436

[58] Forsén S, Hoffman RA. Study of Moderately Rapid Chemical Exchange Reactions by Means of Nuclear Magnetic Double Resonance. *The Journal of Chemical Physics*, 1963;39(11):2892–2901. doi:10.1063/1.1734121

[59] Wolff SD, Balaban RS. Magnetization transfer contrast (MTC) and tissue water proton relaxation in vivo. *Magnetic Resonance in Medicine*, 1989;10(1):135–144. doi:10.1002/mrm.1910100113

[60] Guivel-Scharen V, Sinnwell T, Wolff SD, Balaban RS. Detection of Proton Chemical Exchange between Metabolites and Water in Biological Tissues. *Journal of Magnetic Resonance*, 1998;133(1):36–45. doi:10.1006/jmre.1998.1440

[61] Ward KM, Aletras AH, Balaban RS. A New Class of Contrast Agents for MRI Based on Proton Chemical Exchange Dependent Saturation Transfer (CEST). *Journal of Magnetic Resonance*, 2000;143(1):79–87. doi:10.1006/jmre.1999.1956

[62] Mulkern RV, Williams ML. The general solution to the Bloch equation with constant rf and relaxation terms: Application to saturation and slice selection. *Medical Physics*, 1993;20(1):5–13. doi:10.1118/1.597063

[63] McConnell HM. Reaction Rates by Nuclear Magnetic Resonance. *The Journal of Chemical Physics*, 1958;28(3):430–431. doi:10.1063/1.1744152

References

[64] Zaiss M, Bachert P. Chemical exchange saturation transfer (CEST) and MR Z -spectroscopy *in vivo* : A review of theoretical approaches and methods. *Physics in Medicine and Biology*, 2013;58(22):R221–R269. doi:10.1088/0031-9155/58/22/R221

[65] Zaiss M, Ehses P, Scheffler K. Snapshot-CEST: Optimizing spiral-centric-reordered gradient echo acquisition for fast and robust 3D CEST MRI at 9.4 T. *NMR in Biomedicine*, 2018;31(4):e3879. doi:10.1002/nbm.3879

[66] Windschuh J, Zaiss M, Meissner JE, et al. Correction of $B1$-inhomogeneities for relaxation-compensated CEST imaging at 7 T. *NMR in Biomedicine*, 2015; 28(5):529–537. doi:10.1002/nbm.3283

[67] McMahon MT, Gilad AA, Zhou J, Sun PZ, Bulte JWM, van Zijl PCM. Quantifying exchange rates in chemical exchange saturation transfer agents using the saturation time and saturation power dependencies of the magnetization transfer effect on the magnetic resonance imaging signal (QUEST and QUESP): Ph calibration for poly-L-lysine and a starburst dendrimer. *Magnetic Resonance in Medicine*, 2006; 55(4):836–847. doi:10.1002/mrm.20818

[68] Zaiss M, Angelovski G, Demetriou E, McMahon MT, Golay X, Scheffler K. QUESP and QUEST revisited - fast and accurate quantitative CEST experiments. *Magnetic Resonance in Medicine*, 2018;79(3):1708–1721. doi:10.1002/mrm.26813

[69] Liu D, Zhou J, Xue R, Zuo Z, An J, Wang DJJ. Quantitative characterization of nuclear overhauser enhancement and amide proton transfer effects in the human brain at 7 Tesla. *Magnetic Resonance in Medicine*, 2013;70(4):1070–1081. doi:10.1002/mrm.24560

[70] Woessner DE, Zhang S, Merritt ME, Sherry AD. Numerical solution of the Bloch equations provides insights into the optimum design of PARACEST agents for MRI. *Magnetic Resonance in Medicine*, 2005;53(4):790–799. doi:10.1002/mrm.20408

[71] Glang F. *CEST MRI Parameter Estimation and Uncertainty Quantification in the Human Brain via Deep Learning Approaches*. Master's thesis, University of Tuebingen & Max Planck Institute for Biological Cybernetics, Tübingen, 2019

[72] Zaiss M, Windschuh J, Paech D, et al. Relaxation-compensated CEST-MRI of the human brain at 7T: Unbiased insight into NOE and amide signal changes in human glioblastoma. *NeuroImage*, 2015;112:180–188. doi:10.1016/j.neuroimage.2015.02.040

[73] Goerke S, Soehngen Y, Deshmane A, et al. Relaxation-compensated APT and rNOE CEST-MRI of human brain tumors at 3 T. *Magnetic Resonance in Medicine*, 2019;doi:10.1002/mrm.27751

[74] Deshmane A, Zaiss M, Lindig T, et al. 3D gradient echo snapshot CEST MRI with low power saturation for human studies at 3T. *Magnetic Resonance in Medicine*,

2019;81(4):2412–2423. doi:10.1002/mrm.27569

[75] Henkelman RM, Stanisz GJ, Graham SJ. Magnetization transfer in MRI: A review. *NMR in Biomedicine*, 2001;14(2):57–64. doi:10.1002/nbm.683

[76] van Zijl PCM, Zhou J, Mori N, Payen JF, Wilson D, Mori S. Mechanism of magnetization transfer during on-resonance water saturation. A new approach to detect mobile proteins, peptides, and lipids. *Magnetic Resonance in Medicine*, 2003;49(3):440–449. doi:10.1002/mrm.10398

[77] Kingsley PB, Monahan WG. Effects of Off-Resonance Irradiation, Cross-Relaxation, and Chemical Exchange on Steady-State Magnetization and Effective Spin–Lattice Relaxation Times. *Journal of Magnetic Resonance*, 2000;143(2):360–375. doi:10.1006/jmre.2000.2018

[78] Zhou J, Payen JF, Wilson DA, Traystman RJ, van Zijl PCM. Using the amide proton signals of intracellular proteins and peptides to detect pH effects in MRI. *Nature Medicine*, 2003;9(8):1085–1090. doi:10.1038/nm907

[79] Paech D, Dreher C, Regnery S, et al. Relaxation-compensated amide proton transfer (APT) MRI signal intensity is associated with survival and progression in high-grade glioma patients. *European Radiology*, 2019;29(9):4957–4967. doi:10.1007/s00330-019-06066-2

[80] Zaiss M, Windschuh J, Goerke S, et al. Downfield-NOE-suppressed amide-CEST-MRI at 7 Tesla provides a unique contrast in human glioblastoma. *Magnetic Resonance in Medicine*, 2017;77(1):196–208. doi:10.1002/mrm.26100

[81] Jones CK, Huang A, Xu J, et al. Nuclear Overhauser enhancement (NOE) imaging in the human brain at 7T. *NeuroImage*, 2013;77:114–124. doi:10.1016/j.neuroimage.2013.03.047

[82] van Zijl PC, Lam WW, Xu J, Knutsson L, Stanisz GJ. Magnetization Transfer Contrast and Chemical Exchange Saturation Transfer MRI. Features and analysis of the field-dependent saturation spectrum. *NeuroImage*, 2018;168:222–241. doi:10.1016/j.neuroimage.2017.04.045

[83] Zaiss M, Kunz P, Goerke S, Radbruch A, Bachert P. MR imaging of protein folding in vitro employing Nuclear-Overhauser-mediated saturation transfer. *NMR in Biomedicine*, 2013;26(12):1815–1822. doi:10.1002/nbm.3021

[84] Goerke S, Zaiss M, Kunz P, et al. Signature of protein unfolding in chemical exchange saturation transfer imaging. *NMR in Biomedicine*, 2015;28(7):906–913. doi:10.1002/nbm.3317

[85] Goerke S, Milde KS, Bukowiecki R, et al. Aggregation-induced changes in the chemical exchange saturation transfer (CEST) signals of proteins. *NMR in Biomedicine*, 2017;30(1):e3665. doi:10.1002/nbm.3665

References

[86] Chen L, Wei Z, Chan KWY, et al. Protein aggregation linked to Alzheimer's disease revealed by saturation transfer MRI. *NeuroImage*, 2019;188:380–390. doi:10.1016/j.neuroimage.2018.12.018

[87] Uecker M, Hohage T, Block KT, Frahm J. Image reconstruction by regularized nonlinear inversion—Joint estimation of coil sensitivities and image content. *Magnetic Resonance in Medicine*, 2008;60(3):674–682. doi:10.1002/mrm.21691

[88] Lustig M, Pauly JM. SPIRiT: Iterative self-consistent parallel imaging reconstruction from arbitrary k-space. *Magnetic Resonance in Medicine*, 2010;64(2):457–471. doi:10.1002/mrm.22428

[89] Shin PJ, Larson PEZ, Ohliger MA, et al. Calibrationless parallel imaging reconstruction based on structured low-rank matrix completion. *Magnetic Resonance in Medicine*, 2014;72(4):959–970. doi:10.1002/mrm.24997

[90] Avdievich NI, Giapitzakis IA, Bause J, Shajan G, Scheffler K, Henning A. Double-row 18-loop transceive–32-loop receive tight-fit array provides for whole-brain coverage, high transmit performance, and SNR improvement near the brain center at 9.4T. *Magnetic Resonance in Medicine*, 2019;81(5):3392–3405. doi:10.1002/mrm.27602

[91] Ledden PJ, Mareyam A, Wang S, van Gelderen P, Duyn J. 32 Channel Receive-Only SENSE Array for Brain Imaging at 7T. In *Proc. Intl. Soc. Mag. Reson. Med. 15*. 2007;

[92] Gruber B, Stockmann JP, Mareyam A, et al. A 128-Channel head coil array for Cortical Imaging at 7 Tesla. In *Proc. Intl. Soc. Mag. Reson. Med. 29*. 2021;

[93] Wang H, Tam LK, Constable RT, Galiana G. Fast rotary nonlinear spatial acquisition (FRONSAC) imaging. *Magnetic Resonance in Medicine*, 2016;75(3):1154–1165. doi:10.1002/mrm.25703

[94] Scheffler K, Loktyushin A, Bause J, Aghaeifar A, Steffen T, Schölkopf B. Spread-spectrum magnetic resonance imaging. *Magnetic Resonance in Medicine*, 2019;82(3):877–885. doi:10.1002/mrm.27766

[95] Li M, Zuo Z, Jin J, et al. Highly accelerated acquisition and homogeneous image reconstruction with rotating RF coil array at 7T—A phantom based study. *Journal of Magnetic Resonance*, 2014;240:102–112. doi:10.1016/j.jmr.2013.11.002

[96] Trakic A, Wang H, Weber E, et al. Image reconstructions with the rotating RF coil. *Journal of Magnetic Resonance*, 2009;201(2):186–198. doi:10.1016/j.jmr.2009.09.009

[97] Li M, Weber E, Jin J, et al. Radial magnetic resonance imaging (MRI) using a rotating radiofrequency (RF) coil at 9.4 T. *NMR in Biomedicine*, 2018;31(2):e3860. doi:10.1002/nbm.3860

[98] Mispelter J, Lupu M, Briguet A. *NMR Probeheads for Biophysical and Biomedical Experiments.* published by Imperial College Press and distributed by World Scientific Publishing Co., 2006. ISBN 978-1-86094-637-0. doi:10.1142/p438

[99] Glang F, Buckenmaier K, Bause J, Loktyushin A, Avdievich N, Scheffler K. Investigations on accelerated imaging at 9.4T with electronically modulated time-varying receive sensitivities. In *Proc. Intl. Soc. Mag. Reson. Med. 29 (2021).* Virtual, 2021; abstract number 0910

[100] Candes EJ, Li X, Ma Y, Wright J. Robust Principal Component Analysis? *arXiv:0912.3599 [cs, math],* 2009;doi:10.48550/arXiv.0912.3599

[101] Aravkin A, Becker S, Cevher V, Olsen P. A variational approach to stable principal component pursuit. *arXiv:1406.1089 [math, stat],* 2014;doi:10.48550/arXiv.1406.1089

[102] Avdievich NI, Solomakha G, Ruhm L, Scheffler K, Henning A. Evaluation of short folded dipole antennas as receive elements of ultra-high-field human head array. *Magnetic Resonance in Medicine,* 2019;82(2):811–824. doi:10.1002/mrm.27754

[103] Avdievich NI, Solomakha G, Ruhm L, Henning A, Scheffler K. Unshielded bent folded-end dipole 9.4 T human head transceiver array decoupled using modified passive dipoles. *Magnetic Resonance in Medicine,* 2021;86(1):581–597. doi:10.1002/mrm.28711

[104] Avdievich NI, Nikulin AV, Ruhm L, et al. A 32-element loop/dipole hybrid array for human head imaging at 7 T. *Magnetic Resonance in Medicine,* 2022; 88(4):1912–1926. doi:10.1002/mrm.29347

[105] Lattanzi R, Wiggins GC, Zhang B, Duan Q, Brown R, Sodickson DK. Approaching ultimate intrinsic signal-to-noise ratio with loop and dipole antennas. *Magnetic Resonance in Medicine,* 2018;79(3):1789–1803. doi:10.1002/mrm.26803

[106] Pfrommer A, Henning A. The ultimate intrinsic signal-to-noise ratio of loop- and dipole-like current patterns in a realistic human head model. *Magnetic Resonance in Medicine,* 2018;80(5):2122–2138. doi:10.1002/mrm.27169

[107] Akbey S, Ehses P, Stirnberg R, Zaiss M, Stöcker T. Whole-brain snapshot CEST imaging at 7 T using 3D-EPI. *Magnetic Resonance in Medicine,* 2019;0(0). doi: 10.1002/mrm.27866

[108] Lustig M, Donoho D, Pauly JM. Sparse MRI: The application of compressed sensing for rapid MR imaging. *Magnetic Resonance in Medicine,* 2007;58(6):1182–1195. doi:10.1002/mrm.21391

[109] Tibshirani R. Regression Shrinkage and Selection Via the Lasso. *Journal of the Royal Statistical Society: Series B (Methodological),* 1996;58(1):267–288. doi:10.1111/j.2517-6161.1996.tb02080.x

References

[110] Liebert A, Zaiss M, Gumbrecht R, et al. Multiple interleaved mode saturation (MIMOSA) for B1+ inhomogeneity mitigation in chemical exchange saturation transfer. *Magnetic Resonance in Medicine*, 2019;82(2):693–705. doi:10.1002/mrm.27762

[111] Mennecke A, Khakzar KM, German A, et al. 7 tricks for 7 T CEST: Improving the reproducibility of multipool evaluation provides insights into the effects of age and the early stages of Parkinson's disease. *NMR in Biomedicine*, 2022;abstract number e4717. doi:10.1002/nbm.4717

[112] Schuenke P, Windschuh J, Roeloffs V, Ladd ME, Bachert P, Zaiss M. Simultaneous mapping of water shift and B_1 (WASABI)-Application to field-Inhomogeneity correction of CEST MRI data: Simultaneous Mapping of Water Shift and B_1 (WASABI). *Magnetic Resonance in Medicine*, 2017;77(2):571–580. doi:10.1002/mrm.26133

[113] Breitling J, Deshmane A, Goerke S, et al. Adaptive denoising for chemical exchange saturation transfer MR imaging. *NMR in Biomedicine*, 2019;0(0):e4133. doi:10.1002/nbm.4133

[114] Yuan M, Lin Y. Model selection and estimation in regression with grouped variables. *Journal of the Royal Statistical Society: Series B (Statistical Methodology)*, 2006;68(1):49–67. doi:10.1111/j.1467-9868.2005.00532.x

[115] Obozinski G, Wainwright MJ, Jordan MI. Support union recovery in high-dimensional multivariate regression. *Annals of Statistics*, 2011;39(1):1–47. doi:10.1214/09-AOS776

[116] Beck A, Teboulle M. A Fast Iterative Shrinkage-Thresholding Algorithm for Linear Inverse Problems. *SIAM Journal on Imaging Sciences*, 2009;2(1):183–202. doi:10.1137/080716542

[117] Glang F, Deshmane A, Prokudin S, et al. DeepCEST 3T: Robust MRI parameter determination and uncertainty quantification with neural networks—application to CEST imaging of the human brain at 3T. *Magnetic Resonance in Medicine*, 2020;84(1):450–466. doi:10.1002/mrm.28117

[118] Fabian MS, Glang F, Khakzar KM, et al. Reduction of 7T CEST scan time and evaluation by L1-regularised linear projections. In *Proc. Intl. Soc. Mag. Reson. Med. 29 (2021)*. Virtual, 2021; abstract number 1452

[119] Loktyushin A, Herz K, Dang N, et al. MRzero - Automated discovery of MRI sequences using supervised learning. *Magnetic Resonance in Medicine*, 2021; 86(2):709–724. doi:10.1002/mrm.28727

[120] Mueller S, Scheffler K, Zaiss M. On the interference from agar in chemical exchange saturation transfer MRI parameter optimization in model solutions. *NMR in Biomedicine*, 2021;34(1):e4403. doi:10.1002/nbm.4403

[121] Layton KJ, Kroboth S, Jia F, et al. Pulseq: A rapid and hardware-independent pulse sequence prototyping framework. *Magnetic Resonance in Medicine*, 2017; 77(4):1544–1552. doi:10.1002/mrm.26235

[122] Hansen N, Ostermeier A. Adapting arbitrary normal mutation distributions in evolution strategies: The covariance matrix adaptation. In *Proceedings of IEEE International Conference on Evolutionary Computation*. 1996; pages 312–317. doi:10.1109/ICEC.1996.542381

[123] Rapin J, Teytaud O. Nevergrad - A gradient-free optimization platform. https://GitHub.com/FacebookResearch/Nevergrad, 2018

[124] Cai K, Singh A, Poptani H, et al. CEST signal at 2 ppm (CEST@2ppm) from Z-spectral fitting correlates with creatine distribution in brain tumor. *NMR in Biomedicine*, 2015;28(1):1–8. doi:10.1002/nbm.3216

[125] Solomakha G, Glang F, Steffen T, Scheffler K, Avdievich N. Reconfigurable coaxial receive dipoles for dynamic parallel imaging of human brain at 9.4T. In *Proc. Intl. Soc. Mag. Reson. Med. 31 (2023)*. Toronto (ON, Canada), 2023; abstract number 4099

[126] Blaimer M, Breuer F, Mueller M, Heidemann RM, Griswold MA, Jakob PM. SMASH, SENSE, PILS, GRAPPA: How to Choose the Optimal Method. *Topics in Magnetic Resonance Imaging*, 2004;15(4):223. doi:10.1097/01.rmr.0000136558.09801.dd

[127] Robson MD, Gatehouse PD, Bydder M, Bydder GM. Magnetic Resonance: An Introduction to Ultrashort TE (UTE) Imaging. *Journal of Computer Assisted Tomography*, 2003;27(6):825

[128] Qu P, Zhong K, Zhang B, Wang J, Shen GX. Convergence behavior of iterative SENSE reconstruction with non-Cartesian trajectories. *Magnetic Resonance in Medicine*, 2005;54(4):1040–1045. doi:10.1002/mrm.20648

[129] Glang F, Iyyappan Valsala P, Nikulin AV, Avdievich N, Steffen T, Scheffler K. Investigations on non-Cartesian parallel imaging with time-varying receive sensitivities. In *Proc. Intl. Soc. Mag. Reson. Med. 31 (2023)*. Toronto (ON, Canada), 2023; abstract number 5848

[130] Fessler J, Sutton B. Nonuniform fast Fourier transforms using min-max interpolation. *IEEE Transactions on Signal Processing*, 2003;51(2):560–574. doi:10.1109/TSP.2002.807005

[131] Engel M, Kasper L, Barmet C, et al. Single-shot spiral imaging at 7 T. *Magnetic Resonance in Medicine*, 2018;80(5):1836–1846. doi:10.1002/mrm.27176

[132] Glover GH, Pauly JM, Bradshaw KM. Boron-11 imaging with a three-dimensional reconstruction method. *Journal of Magnetic Resonance Imaging*, 1992;2(1):47–52. doi:10.1002/jmri.1880020109

References

[133] Irarrazabal P, Nishimura DG. Fast Three Dimensional Magnetic Resonance Imaging. *Magnetic Resonance in Medicine*, 1995;33(5):656–662. doi:10.1002/mrm.1910330510

[134] Lazarus C, Weiss P, Chauffert N, et al. SPARKLING: Variable-density k-space filling curves for accelerated T2*-weighted MRI. *Magnetic Resonance in Medicine*, 2019;81(6):3643–3661. doi:10.1002/mrm.27678

[135] Wang G, Luo T, Nielsen JF, Noll DC, Fessler JA. B-Spline Parameterized Joint Optimization of Reconstruction and K-Space Trajectories (BJORK) for Accelerated 2D MRI. *IEEE Transactions on Medical Imaging*, 2022;41(9):2318–2330. doi:10.1109/TMI.2022.3161875

[136] Weiss T, Senouf O, Vedula S, Michailovich O, Zibulevsky M, Bronstein A. PILOT: Physics-Informed Learned Optimized Trajectories for Accelerated MRI. *arXiv:1909.05773 [physics]*, 2020;

[137] Lustig M, Donoho DL, Santos JM, Pauly JM. Compressed Sensing MRI. *IEEE Signal Processing Magazine*, 2008;25(2):72–82. doi:10.1109/MSP.2007.914728

[138] Lazarus C, Weiss P, Gueddari LE, et al. 3D variable-density SPARKLING trajectories for high-resolution T2*-weighted magnetic resonance imaging. *NMR in Biomedicine*, 2020;33(9):e4349. doi:10.1002/nbm.4349

[139] Pawar K, Chen Z, Zhang J, Shah NJ, Egan GF. Application of compressed sensing using chirp encoded 3D GRE and MPRAGE sequences. *International Journal of Imaging Systems and Technology*, 2020;30(3):592–604. doi:10.1002/ima.22401

[140] LeCun Y, Bengio Y, Hinton G. Deep learning. *Nature*, 2015;521(7553):436–444. doi:10.1038/nature14539

[141] Zhu B, Liu JZ, Cauley SF, Rosen BR, Rosen MS. Image reconstruction by domain-transform manifold learning. *Nature*, 2018;555(7697):487–492. doi:10.1038/nature25988

[142] Hammernik K, Klatzer T, Kobler E, et al. Learning a variational network for reconstruction of accelerated MRI data. *Magnetic Resonance in Medicine*, 2018;79(6):3055–3071. doi:10.1002/mrm.26977

[143] Aggarwal HK, Mani MP, Jacob M. MoDL: Model-Based Deep Learning Architecture for Inverse Problems. *IEEE Transactions on Medical Imaging*, 2019;38(2):394–405. doi:10.1109/TMI.2018.2865356

[144] Hammernik K, Küstner T, Yaman B, et al. Physics-Driven Deep Learning for Computational Magnetic Resonance Imaging: Combining physics and machine learning for improved medical imaging. *IEEE Signal Processing Magazine*, 2023;40(1):98–114. doi:10.1109/MSP.2022.3215288

[145] Liang D, Cheng J, Ke Z, Ying L. Deep MRI Reconstruction: Unrolled Optimization Algorithms Meet Neural Networks. *arXiv:1907.11711 [physics, stat]*, 2019;

doi:10.48550/arXiv.1907.11711

[146] Radmanesh A, Muckley MJ, Murrell T, et al. Exploring the Acceleration Limits of Deep Learning Variational Network–based Two-dimensional Brain MRI. *Radiology: Artificial Intelligence*, 2022;4(6):e210313. doi:10.1148/ryai.210313

[147] Knoll F, Hammernik K, Kobler E, Pock T, Recht MP, Sodickson DK. Assessment of the generalization of learned image reconstruction and the potential for transfer learning. *Magnetic Resonance in Medicine*, 2019;81(1):116–128. doi:10.1002/mrm.27355

[148] Hammernik K, Schlemper J, Qin C, Duan J, Summers RM, Rueckert D. Systematic evaluation of iterative deep neural networks for fast parallel MRI reconstruction with sensitivity-weighted coil combination. *Magnetic Resonance in Medicine*, 2021; 86(4):1859–1872. doi:10.1002/mrm.28827

[149] Antun V, Renna F, Poon C, Adcock B, Hansen AC. On instabilities of deep learning in image reconstruction and the potential costs of AI. *Proceedings of the National Academy of Sciences*, 2020;doi:10.1073/pnas.1907377117

[150] Bhadra S, Kelkar VA, Brooks FJ, Anastasio MA. On Hallucinations in Tomographic Image Reconstruction. *IEEE Transactions on Medical Imaging*, 2021; 40(11):3249–3260. doi:10.1109/TMI.2021.3077857

[151] Nataraj G, Otazo R. Model-Free Deep MRI Reconstruction: A Robustness Study. In *Proc. Intl. Soc. Mag. Reson. Med. 28 (2020)*. Virtual, 2020; abstract number 3590

[152] May MW, Hansen SLJD, Mahmutovic M, et al. A patient-friendly 16-channel transmit/64-channel receive coil array for combined head–neck MRI at 7 Tesla. *Magnetic Resonance in Medicine*, 2022;88(3):1419–1433. doi:10.1002/mrm.29288

[153] Gruber B, Stockmann JP, Mareyam A, et al. A 128-Channel head coil array for Cortical Imaging at 7 Tesla. In *Proc. Intl. Soc. Mag. Reson. Med. 29 (2021)*. Virtual, 2021; abstract number 0176

[154] Ocali O, Atalar E. Ultimate intrinsic signal-to-noise ratio in MRI. *Magnetic Resonance in Medicine*, 1998;39(3):462–473. doi:10.1002/mrm.1910390317

[155] Wiesinger F, Boesiger P, Pruessmann KP. Electrodynamics and ultimate SNR in parallel MR imaging. *Magnetic Resonance in Medicine*, 2004;52(2):376–390. doi:10.1002/mrm.20183

[156] Ohliger MA, Grant AK, Sodickson DK. Ultimate intrinsic signal-to-noise ratio for parallel MRI: Electromagnetic field considerations. *Magnetic Resonance in Medicine*, 2003;50(5):1018–1030. doi:10.1002/mrm.10597

[157] Wiesinger F, de Moortele PFV, Adriany G, Zanche ND, Ugurbil K, Pruessmann KP. Potential and feasibility of parallel MRI at high field. *NMR in Biomedicine*, 2006;19(3):368–378. doi:10.1002/nbm.1050

References

[158] Cosottini M, Roccatagliata L. Neuroimaging at 7 T: Are we ready for clinical transition? *European Radiology Experimental*, 2021;5(1):37. doi:10.1186/s41747-021-00234-0

[159] Katscher U, Börnert P, Leussler C, van den Brink JS. Transmit SENSE. *Magnetic Resonance in Medicine*, 2003;49(1):144–150. doi:10.1002/mrm.10353

[160] Zhu Y. Parallel excitation with an array of transmit coils. *Magnetic Resonance in Medicine*, 2004;51(4):775–784. doi:10.1002/mrm.20011

[161] Padormo F, Beqiri A, Hajnal JV, Malik SJ. Parallel transmission for ultrahigh-field imaging. *NMR in Biomedicine*, 2016;29(9):1145–1161. doi:10.1002/nbm.3313

[162] Lattanzi R, Sodickson DK, Grant AK, Zhu Y. Electrodynamic constraints on homogeneity and radiofrequency power deposition in multiple coil excitations. *Magnetic Resonance in Medicine*, 2009;61(2):315–334. doi:10.1002/mrm.21782

[163] Zhu Y. RF Power Deposition and "g-Factor" in Parallel Transmit. In *Proc. Intl. Soc. Mag. Reson. Med. 14*. Seattle, WA, USA, 2006; abstract number 599

[164] Zhang Y, Heo HY, Lee DH, et al. Chemical exchange saturation transfer (CEST) imaging with fast variably-accelerated sensitivity encoding (vSENSE). *Magnetic Resonance in Medicine*, 2017;77(6):2225–2238. doi:10.1002/mrm.26307

[165] Varma G, Lenkinski RE, Vinogradov E. Keyhole chemical exchange saturation transfer. *Magnetic Resonance in Medicine*, 2012;68(4):1228–1233. doi:10.1002/mrm.23310

[166] Mueller S, Stirnberg R, Akbey S, et al. Whole brain snapshot CEST at 3T using 3D-EPI: Aiming for speed, volume, and homogeneity. *Magnetic Resonance in Medicine*, 2020;84(5):2469–2483. doi:10.1002/mrm.28298

[167] Heo HY, Zhang Y, Lee DH, Jiang S, Zhao X, Zhou J. Accelerating chemical exchange saturation transfer (CEST) MRI by combining compressed sensing and sensitivity encoding techniques. *Magnetic Resonance in Medicine*, 2017;77(2):779–786. doi:10.1002/mrm.26141

[168] She H, Greer JS, Zhang S, et al. Accelerating chemical exchange saturation transfer MRI with parallel blind compressed sensing. *Magnetic Resonance in Medicine*, 2019;81(1):504–513. doi:10.1002/mrm.27400

[169] Heo HY, Xu X, Jiang S, et al. Prospective acceleration of parallel RF transmission-based 3D chemical exchange saturation transfer imaging with compressed sensing. *Magnetic Resonance in Medicine*, 2019;82(5):1812–1821. doi:10.1002/mrm.27875

[170] Kwiatkowski G, Kozerke S. Accelerating CEST MRI in the mouse brain at 9.4 T by exploiting sparsity in the Z-spectrum domain. *NMR in Biomedicine*, 2020;33(9):e4360. doi:10.1002/nbm.4360

[171] Zaiss M, Deshmane A, Schuppert M, et al. DeepCEST: 9.4 T Chemical exchange saturation transfer MRI contrast predicted from 3 T data – a proof of concept study. *Magnetic Resonance in Medicine*, 2019;81(6):3901–3914. doi:10.1002/mrm.27690

[172] Hunger L, Rajput JR, Klein K, et al. DeepCEST 7 T: Fast and homogeneous mapping of 7 T CEST MRI parameters and their uncertainty quantification. *Magnetic Resonance in Medicine*, 2023;89(4):1543–1556. doi:10.1002/mrm.29520

[173] Li F, Zurada JM, Liu Y, Wu W. Input Layer Regularization of Multilayer Feedforward Neural Networks. *IEEE Access*, 2017;5:10979–10985. doi:10.1109/ACCESS.2017.2713389

[174] Scardapane S, Comminiello D, Hussain A, Uncini A. Group sparse regularization for deep neural networks. *Neurocomputing*, 2017;241:81–89. doi:10.1016/j.neucom.2017.02.029

[175] Feng J, Simon N. Sparse-Input Neural Networks for High-dimensional Nonparametric Regression and Classification. *arXiv:1711.07592 [stat]*, 2019;doi:10.48550/arXiv.1711.07592

[176] Balin MF, Abid A, Zou J. Concrete Autoencoders: Differentiable Feature Selection and Reconstruction. In *Proceedings of the 36th International Conference on Machine Learning*. PMLR, 2019; pages 444–453

[177] Zhang H, Wang J, Sun Z, Zurada JM, Pal NR. Feature Selection for Neural Networks Using Group Lasso Regularization. *IEEE Transactions on Knowledge and Data Engineering*, 2020;32(4):659–673. doi:10.1109/TKDE.2019.2893266

[178] Lemhadri I, Ruan F, Tibshirani R. LassoNet: Neural Networks with Feature Sparsity. In *Proceedings of The 24th International Conference on Artificial Intelligence and Statistics*. PMLR, 2021; pages 10–18

[179] Kamm L, Fabian M, Glang F, Herz K, Zaiss M. comprehenCEST: A clinically feasible CEST protocol to cover all existing CEST preparation schemes by snapshot readout and reduction of overhangs. In *Chemical Exchange Saturation Transfer Imaging (CEST 2022)*. 2022; abstract number 56

[180] Kamm L, Fabian MS, Herz K, Glang FM, Dörfler A, Zaiss M. ComprehenCEST: A clinically feasible CEST protocol to cover all existing CEST preparation schemes by snapshot readout and reduction of overhangs. In *24. Jahrestagung Der Deutschen Sektion Der ISMRM (DS-ISMRM 2022)*. 2022; pages 92–93

[181] Higgins I, Matthey L, Pal A, et al. Beta-VAE: Learning Basic Visual Concepts with a Constrained Variational Framework. In *International Conference on Learning Representations*. 2022;

[182] Kingma DP, Welling M. Auto-Encoding Variational Bayes, 2022. doi:10.48550/arXiv.1312.6114

References

[183] Lambert B, Forbes F, Tucholka A, Doyle S, Dehaene H, Dojat M. Trustworthy clinical AI solutions: A unified review of uncertainty quantification in deep learning models for medical image analysis, 2022. doi:10.48550/arXiv.2210.03736

[184] Scheffler K. Design of B1-Insensitive and B1-Selective RF Pulses by Means of Stochastic Optimization. *Journal of Magnetic Resonance, Series B*, 1995; 109(2):175–183. doi:10.1006/jmrb.1995.0007

[185] Beracha I, Seginer A, Tal A. Adaptive Magnetic Resonance, 2022. doi:10.1101/2022.03.16.484410

[186] Meissner JE, Goerke S, Rerich E, et al. Quantitative pulsed CEST-MRI using Ω -plots: Quantitative pulsed CEST using Ω-plots. *NMR in Biomedicine*, 2015; 28(10):1196–1208. doi:10.1002/nbm.3362

[187] Rerich E, Zaiss M, Korzowski A, Ladd ME, Bachert P. Relaxation-compensated CEST-MRI at 7 T for mapping of creatine content and pH – preliminary application in human muscle tissue in vivo. *NMR in Biomedicine*, 2015;28(11):1402–1412. doi:10.1002/nbm.3367

[188] Chen L, Schär M, Chan KWY, et al. In vivo imaging of phosphocreatine with artificial neural networks. *Nature Communications*, 2020;11(1):1–10. doi:10.1038/s41467-020-14874-0

[189] Mueller S, Glang F, Scheffler K, Zaiss M. MR-double-zero in vivo: Model-free and live MRI contrast optimization running a loop over a real scanner with a real subject. In *Proc. Intl. Soc. Mag. Reson. Med. 31 (2023)*. Toronto (ON, Canada), 2023; abstract number 6655

[190] Loktyushin A, Nickisch H, Pohmann R, Schölkopf B. Blind retrospective motion correction of MR images. *Magnetic Resonance in Medicine*, 2013;70(6):1608–1618. doi:10.1002/mrm.24615

[191] Loktyushin A, Ehses P, Schölkopf B, Scheffler K. Autofocusing-based phase correction. *Magnetic Resonance in Medicine*, 2018;80(3):958–968. doi:10.1002/mrm.27092

[192] Hartigan JA, Hartigan PM. The Dip Test of Unimodality. *The Annals of Statistics*, 1985;13(1):70–84

[193] Hansen N, Auger A, Ros R, Finck S, Posik P. Comparing results of 31 algorithms from the black-box optimization benchmarking BBOB-2009. In *Proceedings of the 12th Annual Conference Companion on Genetic and Evolutionary Computation*. ACM, Portland Oregon USA. ISBN 978-1-4503-0073-5, 2010; pages 1689–1696. doi:10.1145/1830761.1830790

[194] Hansen N. The CMA Evolution Strategy, https://cma-es.github.io/

[195] Ros R, Hansen N. A Simple Modification in CMA-ES Achieving Linear Time and Space Complexity. In G Rudolph, T Jansen, N Beume, S Lucas, C Poloni, editors,

Parallel Problem Solving from Nature – PPSN X, Lecture Notes in Computer Science. Springer, Berlin, Heidelberg. ISBN 978-3-540-87700-4, 2008; pages 296–305. doi:10.1007/978-3-540-87700-4_30

[196] Shimizu H, Toyoda M. CMA-ES with coordinate selection for high-dimensional and ill-conditioned functions. In *Proceedings of the Genetic and Evolutionary Computation Conference Companion*, GECCO '21. Association for Computing Machinery, New York, NY, USA. ISBN 978-1-4503-8351-6, 2021; pages 209–210. doi:10.1145/3449726.3459575

[197] Varelas K, Auger A, Brockhoff D, et al. A Comparative Study of Large-Scale Variants of CMA-ES. In A Auger, CM Fonseca, N Lourenço, P Machado, L Paquete, D Whitley, editors, *Parallel Problem Solving from Nature – PPSN XV*, volume 11101, pages 3–15. Springer International Publishing, Cham. ISBN 978-3-319-99252-5 978-3-319-99253-2, 2018;doi:10.1007/978-3-319-99253-2_1

[198] Hao S, Fessler JA, Noll DC, Nielsen JF. Joint Design of Excitation k-Space Trajectory and RF Pulse for Small-Tip 3D Tailored Excitation in MRI. *IEEE Transactions on Medical Imaging*, 2016;35(2):468–479. doi:10.1109/TMI.2015.2478880

[199] Jordan SP, Hu S, Rozada I, et al. Automated design of pulse sequences for magnetic resonance fingerprinting using physics-inspired optimization. *Proceedings of the National Academy of Sciences*, 2021;118(40):e2020516118. doi:10.1073/pnas.2020516118

[200] Dang HN, Endres J, Glang F, et al. Solving T2-blurring: Joint Optimization of Flip Angle Design and DenseNet Parameters for Reduced T2 Blurring in TSE Sequences. In *Proc. Intl. Soc. Mag. Reson. Med. 30 (2022)*. London (UK), 2022; abstract number 2602

[201] Dang HN, Endres J, Weinmüller S, et al. MR-zero meets RARE MRI: Joint optimization of refocusing flip angles and neural networks to minimize T2-induced blurring in spin echo sequences. *Magnetic Resonance in Medicine*, 2023;90(4):1345–1362. doi:10.1002/mrm.29710

[202] Endres J, Dang HN, Glang F, Loktyushin A, Weinmüller S, Zaiss M. Phase distribution graphs for differentiable and efficient simulations of arbitrary MRI sequences. In *Proc. Intl. Soc. Mag. Reson. Med. 30 (2022)*. London (UK), 2022; abstract number 0750

[203] West D, Glang F, Endres J, Zaiss M, Hajnal JV, Malik SJ. Overcoming system imperfections using end-to-end MR sequence design. In *Proc. Intl. Soc. Mag. Reson. Med. 31 (2023)*. Toronto (ON, Canada), 2023; abstract number 0061

161

Acknowledgments

It has been a real pleasure and a great privilege for me to do my PhD in the MRZ department, to have the opportunity to learn so much, to meet so many great people and to have such a good time. So I am glad about this chance to say thank you to everyone who has been involved in this:

Thank you Klaus for being my supervisor and giving me the opportunity to work in your department, for providing such a nice working environment, for offering great freedom as well as support whenever needed.

Big thanks to Moritz for being my co-supervisor, for your enormously valuable support, for your inspiring and enthusiastic way of doing science and all sorts of other things, and for bringing out the best in people working together as a team.

I would also like to thank Reinhold Kleiner and Sebastian Kozerke for being thesis reviewers, and Fritz Schick for agreeing to be part of my thesis committee.

Working as a PhD student (as probably everywhere else) sometimes feels like oscillating between moments of success and satisfaction, but also struggle and sometimes frustration. However, even in view of these occasional strains, I have found that it is remarkably difficult to be in a bad mood for more than a few minutes in Kinderzimmer. In fact, I cannot imagine a better place to face such a task – thank you guys for being there and creating a place where working never feels like a burden, but just right.

First of all, thank you Sebastian for the great time, for all the conversations about all kinds of scientific and non-scientific things, which I really enjoy; for being the best imaginable LOOM astronaut, as well as for the countless CEST sports sessions and bike trips.

Thanks a lot Praveen – it is a great pleasure to have such a nice desk neighbor who is an expert in spirals, dinosaurs, coding, music, all kinds of computer and electronics stuff, practical jokes, kaputt- and ganzspieling.

Dario, thank you very much for your impressive knowledge and motivation to fix all kinds of scanner problems, your boundless readiness to help, for your stunning skills in e.g. blindly writing and fixing coil files, and for virtually embodying multiple core facilities in one person.

Erklärung / Declaration

Ich erkläre, dass ich die zur Promotion eingereichte Arbeit mit dem Titel:

Dynamic Parallel Imaging for Fast MRI, and Optimization of CEST Methods for Metabolic MRI

selbständig verfasst, nur die angegebenen Quellen und Hilfsmittel benutzt und wörtlich oder inhaltlich übernommene Stellen als solche gekennzeichnet habe. Ich erkläre, dass die Richtlinien zur Sicherung guter wissenschaftlicher Praxis der Universität Tübingen (Beschluss des Senats vom 25.5.2000) beachtet wurden. Ich versichere an Eides statt, dass diese Angaben wahr sind und dass ich nichts verschwiegen habe. Mir ist bekannt, dass die falsche Abgabe einer Versicherung an Eides statt mit Freiheitsstrafe bis zu drei Jahren oder mit Geldstrafe bestraft wird.

I hereby declare that I have produced the work entitled:

Dynamic Parallel Imaging for Fast MRI, and Optimization of CEST Methods for Metabolic MRI

submitted for the award of a doctorate, on my own (without external help), have used only the sources and aids indicated and have marked passages included from other works, whether verbatim or in content, as such. I declare that the guidelines for ensuring good scientific practice at the University of Tübingen (resolution of the Senate of 25.5.2000) have been observed. I swear upon oath that these statements are true and that I have not concealed anything. I am aware that making a false declaration under oath is punishable by a term of imprisonment of up to three years or by a fine.

Tübingen, den   ....

Datum / Date   Unterschrift / Signature